Environmentally-Assisted Fracture Events in High Strength Nickel-Based Superalloys



André Anjou Nordine Németh

Lincoln College

University of Oxford

A thesis submitted for the degree of

Doctor of Philosophy

Michaelmas Term 2017

"Discovery is seeing what everybody else has seen, and thinking what nobody else has thought."

Szent-Györgyi Albert

Abstract

There is significant interest in defining and quantifying the performance of polycrystalline Ni-based superalloys – particularly high strength ones produced via powder processing for turbine disc applications – at temperatures between 700 and 800°C. This is because the outer rims of a high pressure turbine disc in turbine applications for jet propulsion can experience such temperatures during a significant portion of the flight cycle while also being exposed to oxidative/corrosive gases which cause intergranular environmentally-assisted crack growth. In this work, a testing methodology involving slow strain-rate tensile tests on a electro-thermal mechanical testing device is presented which is capable of the rapid assessment of an alloys susceptibility to environmentally-assisted cracking. It makes use of miniature test pieces which are shown to be of sufficient size to characterise macroscopic properties. This approach is first validated and then utilized to perform systematic experimentation involving the control of the important microstructural and compositional variables such that the effects of others can be isolated, identified and confirmed. The need to better understand the embrittlement mechanism was addressed at the most appropriate lengthscale using high resolution characterisation techniques which are capable of providing the most revealing information including scanning and transmission electron microscopy and nanoscale secondary ion mass spectrometry. Our results have implications for alloy design efforts – rationalising the effect of heat treatment and demonstrating that for a given strength level, both more and less damage tolerant variants can be designed.

Preface

Research in this thesis has been prepared for publication as follows:

- A.A.N. Németh, D.J. Crudden, D.M. Collins, D.E.J. Armstrong, R.C.R. Reed, *Novel Techniques to Assess Environmentally-Assisted Cracking in a Nickel-based Superalloy*, Superalloys 2016, John Wiley & Sons, Inc., Hoboken, NJ, USA, 2016, pp. 801-810, doi: 10.1002/9781119075646.ch86

- A.A.N. Németh, D.J. Crudden, D.E.J. Armstrong, D.M. Collins, K. Li, A.J. Wilkinson, C.R.M Grovenor, R.C.R. Reed, *Environmentally-Assisted Grain Boundary Attack as a Mechanism of Embrittlement in a Nickel-based Superalloy*, Acta Materialia 126 (2017), pp. 449-463, doi: 10.1016/j.actamat.2016.12.039

- A.A.N. Németh, D.J. Crudden, D.M. Collins, V. Kuksenko, C.H. Liebscher, D.E.J. Armstrong, A.J. Wilkinson, R.C.R. Reed, *On the Influence of Nb/Ti Ratio on Environmentally-Assisted Crack Growth in High Strength Nickel-based superalloys*, Metallurgical and Materials Transactions A (2018), doi: 10.1007/s11661-018-4619-y

Acknowledgements

Pursuing my doctorate degree at the University of Oxford has given me everything I could ever have wanted at this early stage of my life – living within this historic and inspiring environment during the last three years has provided me with the opportunity to experience emotions ranging from great highs to difficult lows. In the end, I have come to understand that making mistakes is exactly what I have come here for. This thesis is based on the lessons learned and obstacles overcome, which are inherently linked to the support of many remarkable individuals who I wish to acknowledge.

I would like to express the deepest appreciation to my three academic advisors: **Professor Roger Reed**, **Professor David Armstrong**, and **Dr. David Crudden**. I am eternally grateful for their advice, patience, and ability to challenge me. I am also extremely grateful to my industrial supervisor, **Dr. Mark Hardy** of Rolls-Royce plc. His meticulous comments were an enormous help to me. I would also like to acknowledge the generous financial support provided by Rolls-Royce plc. and the Engineering and Physical Sciences Research Council. I have also greatly benefited from the 2017 TMS International Superalloys Scholarship.

I am particularly grateful for the assistance given by **Professor Angus Wilkinson**, **Dr. David Collins**, and **Dr. Kexue Li** who provided support and warm encouragement throughout regarding HR-EBSD and NanoSIMS analysis. I wish to thank the technical team at the University of Oxford for their assistance and outstanding performance; I am particularly grateful to **Jeffrey Fullerton**. I received

generous support from the Max-Planck-Institut für Eisenforschung, in particular **Dr. Christian Liebscher**. Without his guidance the STEM-EDS work would have not been possible.

I owe a very important debt to all my colleges who are part of Professor Reed's research group: **Koji Kageyama**, **Tony Tang**, **Sabin Sulzer**, **Heather Wilson**, **Daniel Barba**, **Dr. Enrique Alabort**, and **Dr. Fauzan Adziman**. Without their support it would not have been possible to conduct this research. I would like to extend my gratitude to my closest friends in Oxford **Josh Abbott**, **Cloé Ragot**, **Robert Shalloo**, **Alistair Inglis**, **Jay Patel**, **James Harris**, and **Kathleen Keown**. Thank you for the stimulating discussions, sleepless nights, and all the fun we have had in the last three years. Also I thank my friends in the **Lincoln College Boat Club** for the excellent comradeship.

Thank you to my family, my parents **György Németh** and **Iris Ludwig-Németh**, and my sister **Désirée Németh** for their constant and unwavering support, and teaching me the value of hard work. Most importantly, thank you **Johanna Beer** for your unconditional love and emotional comfort in my life.

Table of contents

1 Introduction **1**

1.1 The Importance of Environmentally-Assisted Cracking 1

1.2 Turbine Discs in Aeroengines 3

1.3 Research Aims and Thesis Structure 5

2 Literature Review **9**

2.1 Polycrystalline Nickel-Based Superalloys for Turbine Disc Applications 9

2.1.1 The Physical Metallurgy of Nickel-Based Superalloys 9

2.1.2 Processing Superalloys for Turbine Disc Applications 15

2.2 Deformation and Failure Mechanisms in Nickel-Based Superalloys . . . 20

2.2.1 High Temperature Deformation Mechanisms 20

2.2.2 High Temperature Crack Propagation 23

2.2.3 Crack Tip Damage Mechanisms 30

2.3 Metallurgical Control of Intergranular Growth in Nickel-Based Superalloys 42

2.3.1 Microstructural Factors 43

2.3.2 Compositional Factors 51

3 Novel Techniques to Assess Environmentally-Assisted Cracking **61**

3.1 Introduction 62

3.2 Experimental Procedure 66
3.2.1 Material 66
3.2.2 Electro-Thermal Mechanical Testing 68
3.2.3 Conventional Tensile Testing 70
3.2.4 Mirco-Mechanical Bend Testing 71
3.2.5 Analysis Methods 72
3.3 Experimental Results 73
3.3.1 Miniaturised Tensile Tests 73
3.3.2 Conventional Tensile Tests 75
3.3.3 Fractography 76
3.3.4 Micro-Mechanical Bend Tests 79
3.4 Discussion 82
3.4.1 Miniaturized ETMT Tensile Tests 82
3.4.2 Environmentally-Assisted Intergranular Failure 86
3.4.3 Site-Specific Micro-Cantilever Tests 88
3.5 Conclusions 90

4 Environmentally-Assisted Attack as a Mechanism of Embrittlement 91

4.1 Introduction 92
4.2 Experimental Procedure 95
4.2.1 Material 95
4.2.2 Assessment of the Tensile Ductility 96
4.2.3 Measurement of the Oxide Kinetics 97
4.2.4 Fractography and Damage Analysis 97
4.3 Results 99
4.3.1 Temperature-Dependence of the Tensile Ductility 99
4.3.2 On the Temperature-Dependence of the Tensile Strength 103

4.3.3 Characterisation of Environmentally-Assisted Failure 104
4.3.4 Measurement of the Oxidation Kinetics 111
4.4 Discussion 115
4.4.1 On the Mechanism of Intergranular Oxidation 115
4.4.2 On the Role of Slip-Assisted Grain Boundary Sliding 118
4.4.3 On the Influence of Heat Treatment on Embrittlement 121
4.5 Conclusions 123

5 The Influence of Nb/Ti Ratio on Environmentally-Assisted Failure 125
5.1 Introduction 126
5.2 Experimental Design, Procedure and Rationalisation 129
5.2.1 Material 129
5.2.2 Theoretical Modelling of the Yield Stress 133
5.2.3 Experimental Assessment of the Mechanical Properties 135
5.2.4 Fractography and Damage Analysis 137
5.3 Results 139
5.3.1 Characterisation of the Mechanical Properties 139
5.3.2 Characterisation of Environmentally-Assisted Failure 143
5.4 Discussion 152
5.4.1 On the Mechanism of Environmentally-Assisted Grain Boundary Embrittlement 152
5.4.2 On the Role of Grain Size Dependent Toughening 155
5.4.3 On the Relevance to Alloy Design 157
5.5 Summary and Conclusions 161

6 Conclusions and Future Work 163
6.1 Conclusions 163

6.2 Future Work 166

References **171**

Appendix A Stress-Strain Curves **191**

Appendix B Individual STEM-EDS Elemental Maps **197**

Chapter 1

Introduction

1.1 The Importance of Environmentally-Assisted Cracking

Polycrystalline Ni-based superalloys are used for rotating components in gas turbine applications such as jet propulsion and electricity generation. Current interest relates particularly to turbine discs as they are key components in aeroengines representing about 20% of the engines total weight and 10% of an engine's value upon entry into service [1]. The turbine disc is also one of the most critical components in the aeroengine as the failure of the disc can lead to the loss of the aircraft. Thus, their performance dictates the overall efficiency of the engine cycle. The outer rims of the turbine discs, onto which are attached the turbine blade aerofoils, experience temperatures in the regime of 700 to 800°C [2]. These locations are subject to not just complex thermal-mechanical cycles but also oxidative/corrosive gases which cause intergranular environmentally-assisted cracking. Attack is exacerbated by extended periods of exposure at the very highest stress levels; this is known as the 'dwell' condition. So-

called dwell fatigue crack propagation is one of the grand challenges in the physical metallurgy of Ni-based superalloys. This is because the precise mechanism(s) of environmental attack at the crack tip are not yet fully understood and indeed controversial, and influences of alloy chemistry as well as microstructure — alloy-to-alloy variation — needs clarification [3]. An overview of previously proposed damage mechanisms leading to environmentally-assisted crack propagation is shown in Figure 1.1.

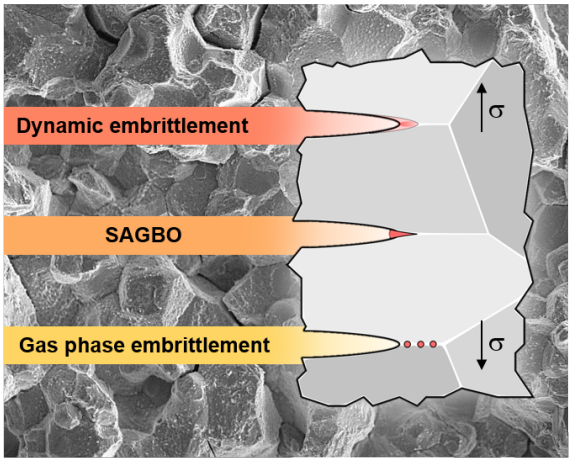


Fig. 1.1 Overview of proposed environmental damage mechanisms, namely dynamic embrittlement, stress assisted grain boundary oxidation (SAGBO) and gas phase embrittlement. Phenomenological factors which are required for environmentally-assisted crack propagation are (i) an oxidising environment, (ii) a susceptible material, and (iii) an applied tensile stress.

An appreciation of the importance of environmentally-assisted crack growth can be obtained by showcasing the consequences of an uncontained high pressure turbine disc failure. In 2006, during a high powered test ground run, the disc of the left engine of a Boeing 767-223 aeroplane failed as a result of intergranular environmentally-assisted cracking in a blade slot bottom [4]. The fragments of the turbine disc exited the engine and punctured both wing tank in addition to the left center tank, causing fire damage before lodging in the outboard side of the right wing engine. To prevent such an accident, significant effort is placed in the development of new generation damage tol-

erant polycrystalline Ni-based superalloys. Alloys with an increased damage tolerance enable the jet engine to operate safely at higher temperatures and therefore employ a thermodynamically more efficient engine cycle. An increase of the temperature capability of 30°C will result in an approximately 0.3% improvement in specific fuel consumption. For a large twin-engined aircraft flying from London to New York, this equates to a 700 kg reduction in fuel consumption, which translates into a reduction of $\approx$ 2.25 tonnes of CO_2 emissions per flight [5]. This represents a significant step towards the ACARE (Advisory Council for Aviation Research and Innovation in Europe) 'FlightPath 2050 Goals' of a 50% reduction in CO_2 emissions per passenger-kilometre [6].

1.2 Turbine Discs in Aeroengines

The design of an aeroengine brings together a multitude of different disciplines and technologies but the overall system performance is greatly dependent on the material's temperature capability in the compressor and turbine section [7].

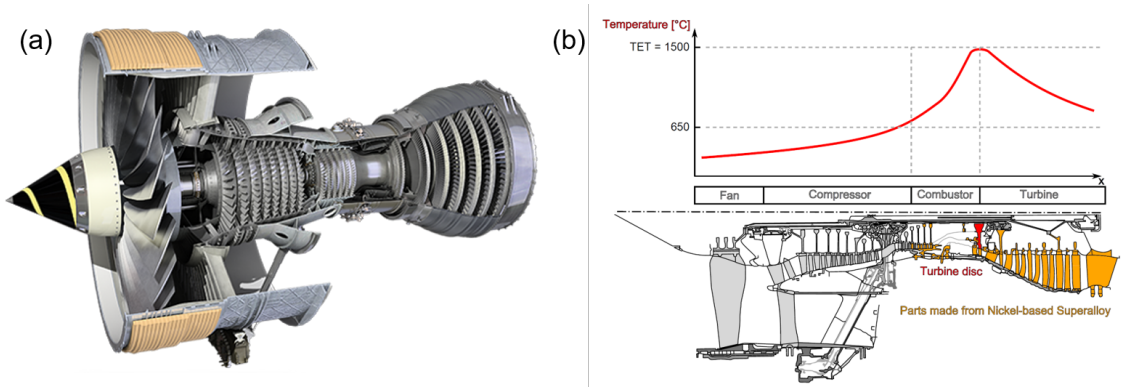


Fig. 1.2 (a) Rolls-Royce's Trent 800 found on the Boeing 777 delivering over 90,000 lb thrust [8]. (b) Illustration of material usage in the Trent 800 engine. Parts made from Ni-based superalloys in the combustor as well as the turbine sections and the turbine disc are highlighted. In addition, the temperature within the jet engine is shown schematically. Image redrawn from [1].

Figure 1.2 shows a turbofan Rolls-Royce Trent 800 jet engine together with an engine cross-section illustrating the extensive use of Ni-based superalloys in those sections and the temperature at different points within the engine. As the gas turbine temperatures increase — due to ongoing fuel efficiency demands and the need to reduce emissions — there is need for more advanced Ni-based superalloys, especially for the high pressure turbine disc where temperatures at the rim are approaching 800°C while being subject to high centrifugal stresses and loads imposed on the rim by the attached turbine blades. In addition, thermal stresses are induced in the bulk of the disc by temperature gradients during engine start and shut down. Figure 1.3 shows the stress and temperature distribution of a turbine disc component. Typically, the stress and temperature ranges between 500-1200 MPa and 300-800°C, respectively. The development of alloys and processes for turbine disc manufacture have concentrated on the trade-off between the material property requirements which are different at the rim compared to the bore of the disc. While the bore is subject to larger stresses at relatively low temperatures, the stresses at the rim are much lower but the temperature is much greater.

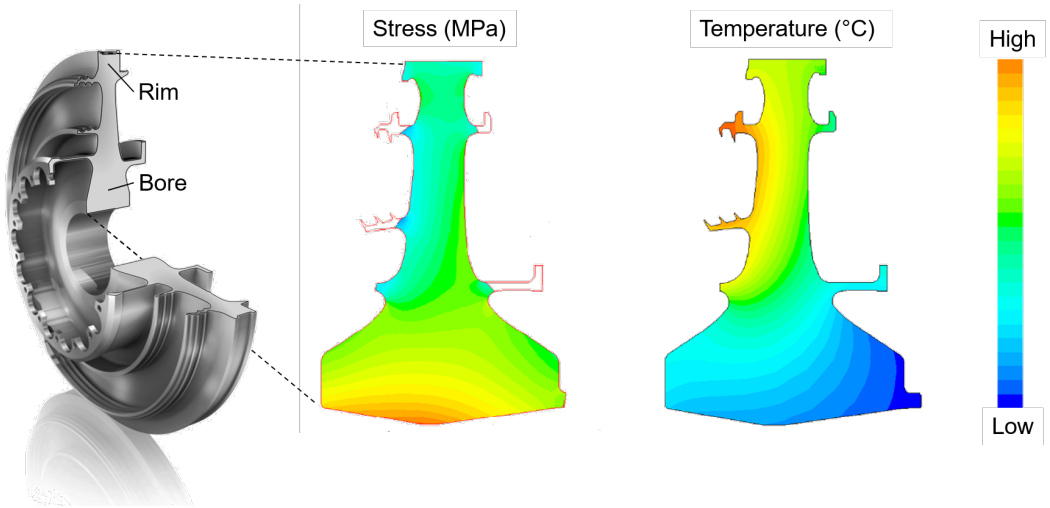


Fig. 1.3 Typical stress and temperature distribution in a turbine disc component. Turbine disc adapted from *www.sandvik.coromant.com/SiteCollectionImages/industries/aero/turbinedisc.jpg*.

The bore of the disc must be capable of withstanding an excursion to 122% of the maximum engine speed to protect the system in the event of overspeed [7]. Burst strength is essentially a direct function of the tensile strength, so a high tensile strength becomes a key design requirement. In addition, this region must also be resistant to crack propagation under low and high cycle fatigue conditions. Conversely, at the high temperatures and intermediate loads present at the rim of the disc thermally activated time-dependent degradation mechanisms such as environmentally-assisted crack growth under dwell conditions, creep deformation, and oxidation/corrosion are the major life limiting factors.

1.3 Research Aims and Thesis Structure

In this thesis, the properties of new-generation Ni-based superalloys for turbine disc applications are investigated to guide the development of a next generation damage tolerant turbine disc alloy. The alloy systems under study include alloy 720Li and RR1000, which are employed in current Rolls-Royce jet engines. Furthermore, novel prototype alloys which have been isolated using our so-called Alloys-by-Design approach are considered [9].

Chapter 2 begins with an overview of the physical metallurgy of Ni-based superalloys and outlines the material processing steps relevant for turbine disc applications. Next the deformation and failure mechanisms in the high temperature regime are reviewed. Particular focus is placed on the proposed mechanisms of environmental-attack at the crack tip. Finally, the known metallurgical factors controlling an alloy's susceptibility to environmentally-assisted cracking, namely alloy composition and microstructure are reviewed in detail, as understanding the composition-microstructure dependence of this property is the main focus of this thesis.

The presented research in Chapter 3 involves first the development of novel techniques to assess environmentally-assisted cracking. An electro-thermal mechanical testing system is introduced and employed which makes use of miniaturised test specimens, allowing for the assessment of mechanical property when only small quantities of material are available with significantly reduced test durations. It is demonstrated that electro-thermal-mechanical testing is able to capture the temperature and time-dependent effects that occur during environmentally-assisted cracking in a Ni-base superalloy. In addition, the effects of environmental-damage on the local mechanical properties in the region ahead of a γ-grain boundary are studied through micro-cantilever bend tests.

In Chapter 4, the temperature dependent loss of ductility in alloy 720Li and RR1000 is studied in detail and a relationship between tensile ductility and oxidation kinetics is established. The physical factors responsible for the ductility dip are established using energy-dispersive X-ray spectroscopy, nanoscale secondary ion mass spectrometry and the analysis of electron backscatter diffraction patterns. Embrittlement results from internal intergranular oxidation along the γ-grain boundaries, and, in particular, at incoherent interfaces of the primary γ'-precipitates with the matrix phase. These fail under local microstresses arising from the accumulation of dislocations during slip-assisted grain boundary sliding. This chapter has implications for the choice of heat treatment temperature for polycrystalline Ni-based superalloys.

In Chapter 5 the effect of Nb/Ti ratio on the strength, ductility and toughness of three prototype Ni-based superalloys is studied and rationalised. For these alloy variants, the yield strength is unaltered which allows the rationalisation of the factors influencing damage tolerance at 700°C. Primary intergranular cracks are investigated using energy-dispersive X-ray spectroscopy in a scanning transmission electron microscopy and the analysis of electron back-scatter diffraction patterns. Evidence is

presented to indicate that the tertiary γ'-precipitates are dissolving ahead of the crack consistent with the formation of oxides such as alumina and rutile. The presented results have implications for alloy design efforts; at any given strength level, both more and less damage tolerant variants of these alloys can be designed.

Finally, in Chapter 6 the key outcomes from this research are outlined. Suggestions for the future work regarding the design of a damage tolerant polycrystalline Ni-based superalloys are given.

Chapter 2

Literature Review

2.1 Polycrystalline Nickel-Based Superalloys for Turbine Disc Applications

2.1.1 The Physical Metallurgy of Nickel-Based Superalloys

In 1942 the first Ni-based superalloy Nimonic 80 was developed based on empirical findings from alloys within the Ni-Cr system. Nimonic 80 was used for uncooled turbine blades in the hot section of a gas turbine jet engine and had a 800°C turbine entry temperature (TET) capability [10]. Ni-based superalloys are still used for high temperature applications within jet engines for civil aeroplanes. Since the introduction of jet engines the TET has almost doubled from 800°C to approximately 1500°C [1, 11] and is estimated to reach 1700°C by 2030 due to ongoing fuel efficiency demands and the constant need to reduce emissions [12, 13]. Thus, increasing the TET is a major driving force for the continued development of new Ni-based superalloys. Associated with these high temperatures are material property requirements like a

high temperature strength, improved fatigue and creep life along with better corrosion resistance. Unsurprisingly, these high temperature materials have become increasingly complex in comparison to Nimonic 80 (Table 2.2) and are today one of the most chemically complex alloy systems, often containing up to eleven different alloying elements.

Alloy chemistry determines the equilibrium microstructure which is substantially compromised from a (i) Ni-base face centred cubic (fcc) austenitic matrix phase, γ-phase, and (ii) Ni_3Al, a fully coherent primitive cubic $L1_2$-type ordered strengthening precipitate named $\gamma^{'}$-phase. In addition, minor phases such as carbides, borides and topological closed packed (tcp) phases are often located at the grain boundaries (see Figure 2.1).

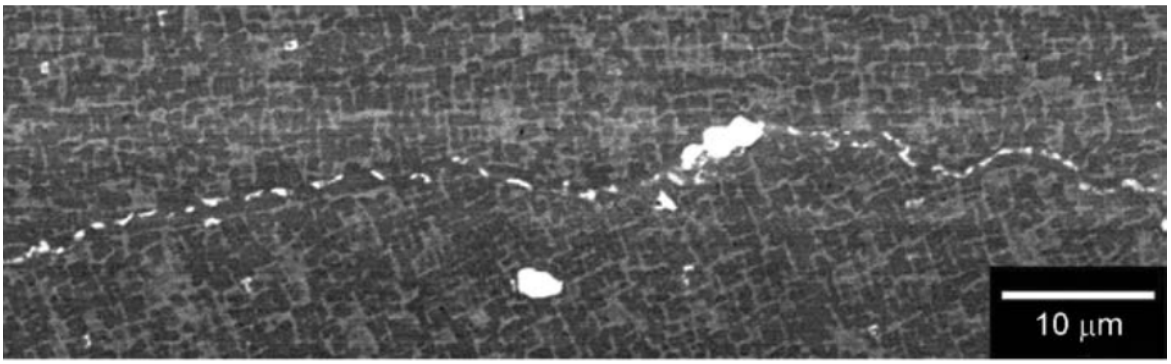


Fig. 2.1 $M_{23}C_6$ carbides at a γ-grain boundary in an experimental γ/γ'-phase strengthened Ni-base superalloy. Adapted from reference [14].

The austenitic γ-phase usually contains the following elements: Cr – in order to form a protective Cr_2O_3 oxide layer [15], Co – for an enhanced processing ability [16], Mo and W – for solid solution strengthening and creep resistance [17]. The partition tendency of each element is shown in Figure 2.2. The γ'-precipitate is an intermetallic compound and responsible for the excellent high temperature strength of Ni-based superalloys. Due to cross-slip of dislocations in the γ'-phase the yield stress increases with temperatures up to approximately 800°C [18]. Advanced polycrystalline Ni-based

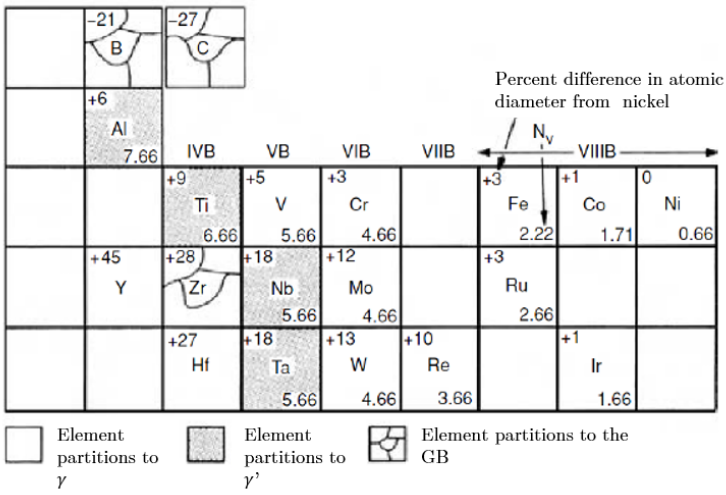


Fig. 2.2 Important alloying elements in Ni-based superalloys and their relative position in the periodic table of elements. Adapted from reference [20].

superalloys have a γ'-phase volume fraction between 40 and 60% [19].

The archetype of the γ'-precipitates is Ni_3Al which has a lattice parameter of $a_0^{\gamma'} = 0.3570$ nm [1]. The lattice parameter for pure fcc Ni is slightly smaller with $a_0^{\gamma} = 0.3517$ nm [1]. The phase boundary between the γ-matrix and the γ'-precipitate is therefore regarded to be fully coherent. This results in a low interface energy. The ideal orientation relationship between the γ-matrix and the γ'-precipitates is a cube-cube orientation. This orientation relationship is described by $\{100\}_\gamma/\{100\}_{\gamma'}$ with $\langle 010\rangle_\gamma/\langle 010\rangle_{\gamma'}$. The γ'-precipitates are reported to align along the $\langle 100\rangle_\gamma$ direction [1]. The lattice parameters, a_0^{γ} and $a_0^{\gamma'}$, are influenced by solute atoms in each phase. The substitution of atoms leads to an increase or decrease of the lattice parameters of several percent. While the Ni sites in Ni_3Al can be occupied by Co atoms, the Al corner sites can accommodate Ti, Ta and Nb [21]. This leads to (Ni, Co)$_3$(Al, Ti, Ta, Nb). It has been found that these elements increase the anti-phase boundary energy which leads to a higher overall tensile strength [11, 22, 23]. The misfit between the γ-matrix and the γ'-precipitate is a function of the lattice parameters a_0^{γ} and $a_0^{\gamma'}$ which

can be mathematically expressed as [1]:

$$\delta = 2 \cdot \frac{a_0^{\gamma'} - a_0^{\gamma}}{a_0^{\gamma'} + a_0^{\gamma}} \quad . \tag{2.1}$$

If the misfit is small, spherical precipitates are observed and the rate at which precipitates coarsen is slow. If the misfit is large, the growth of irregular octodendritic clover leaf shape precipitates is observed [24]. In superalloys which contain Nb – such as Inconel 706 and 718 – the meta-stable γ''-precipitate can occur [1].

At the grain boundaries of polycrystalline Ni-based superalloys the enrichment of elemental carbon and boron leads to carbide and boride formation. Common carbides are MC, $M_{23}C_6$ and M_6C; common borides are M_3B_2 and M_5B_3, where M represents a metal atom.

Table 2.1 Grain boundary phases in polycrystalline Ni-based superalloys. Adapted from reference [25]. The lattice parameter may vary due to changes in chemical composition.

Phase	Prototype	Pearson symbol	Structure symbol	Lattice parameter	Typical composition
MC	NaCl	cF8	B1	0.44 nm	TiC, TaC
$M_{23}C_6$	$Cr_{23}C_6$	cF116	$D8_4$	1.07 nm	$Cr_{21}Mo_2C_6$
M_6C	Fe_3W_3C	cF112	$E9_3$	1.11 nm	$(Mo, Cr)_6C$
M_3B_2	Si_3U_2	tP10	$D5_a$	a=0.6 nm c=0.32 nm	$(Mo, Cr)_3B_2$
M_5B_3	Cr_5B_3	tI32	$D8_1$	a=0.55 nm c=1.06 nm	$(Mo, Cr)_5B_3$

The MC carbide has a fcc NaCl-type structure with almost no orientation relationship to the γ-matrix [26]. It appears in three different morphologies: blocky, script and modular. Intra- and intergranular sites are equally preferred. The MC carbide can

decompose into the γ'-precipitate and $M_{23}C_6$ following a solid state transformation: $MC + \gamma \rightarrow M_{23}C_6 + \gamma'$. The $M_{23}C_6$ carbide directly nucleates at the grain boundary and has a cube orientation with the γ-matrix [26–28]. Therefore, the precipitation behaviour of $M_{23}C_6$ is dependent on the grain boundary character and energy [29]. High angle grain boundaries with a high interfacial energy are preferred nucleation sites [30]. The M radical is commonly Cr [27]. The MC carbide can also decay into the M_6C carbide: $MC + \gamma \rightarrow M_6C + \gamma'$ [31]. M_6C is observed to form as discrete particles within the γ-matrix as well as at the grain boundaries. Although M_6C carbides are more stable than $M_{23}C_6$ carbides, they are not common in polycrystalline Ni-based superalloys [26].

If boron is added to the composition borides such as M_3B_2 and M_5B_3 can be found at the grain boundaries. Both have a base centred tetragonal type structure where M is typically Mo and Cr. The morphology of the borides can be blocky to half-moon [20]. Carbides and borides play a role in strengthening the alloy by inhibiting the movement of dislocations, prohibiting grain boundary sliding and cavitation [32]. However, the role of grain boundary phases is controversial since they are intrinsically brittle and act as nucleation sites for cracks [33].

During service and after long-term high temperature exposure, unwanted TCP phases like the σ-, μ-, η- and laves-phases can form if sufficient amounts of Cr, W, Co and/or Mo are present in the alloy. The most common tcp-phase is the σ-phase. This phase consists of $(Cr, Mo)_x(Ni, Co)_y$ where x and y can vary between one and seven [20]. The σ-phase precipitates on the $\{111\}$-planes of the γ-grain and has a plate-like morphology. Tcp-phases exhibit a limited number of slip planes and are therefore brittle. Their presence is typically associated with a limited tensile ductility and a short stress rupture life.

Table 2.2 Chemistry (wt.%) of common commercial polycrystalline Ni-based superalloys for turbine disc applications.

Name	Cr	Co	W	Al	Ti	Ta	Nb	Mo	Fe	C	B	Zr
A286 [19]	15.0	0.0	0.0	0.2	2.0	0.0	0.0	1.3	55.2	0.04	0.005	0.000
AF115 [19]	10.7	15.0	5.9	3.8	3.9	0.0	1.7	2.8	0.0	0.050	0.020	0.050
Alloy 10 [1]	11.5	15.0	5.9	3.8	3.9	0.8	1.7	2.3	0.0	0.030	0.020	0.050
Astroloy [19]	15.0	15.0	0.0	4.4	3.5	0.0	0.0	5.3	0.0	0.060	0.030	0.060
EP741NP [34]	9.0	15.8	5.5	5.1	1.8	0.0	2.6	3.9	0.0	0.040	0.015	0.015
Inconel 100 [18]	12.4	18.4	0.0	4.9	4.3	0.0	0.0	3.2	0.0	0.070	0.020	0.070
Inconel 718 [35]	19.0	0.0	0.0	0.6	0.8	0.0	5.3	3.0	19.0	0.080	0.006	0.000
LSHR [36]	12.3	20.4	4.3	3.5	3.5	1.5	1.5	2.7	0.0	0.045	0.027	0.049
ME3 / René 104 [36]	12.8	20.7	2.0	3.4	3.7	2.3	0.9	3.8	0.0	0.050	0.025	0.050
MERL-76 [37]	12.4	18.6	0.0	5.1	4.3	0.0	1.4	3.3	0.0	0.030	0.030	0.060
N18 [38]	11.5	15.7	0.0	4.4	4.4	0.0	0.0	6.5	0.0	0.015	0.015	0.030
N19 / SMO43 [38]	12.2	13.3	3.0	2.9	3.6	0.0	1.5	4.6	0.0	0.015	0.010	0.050
Nimonic 80 [18]	20.0	0.0	0.0	1.0	2.5	0.0	0.0	0.0	0.0	0.000	0.000	0.000
NR3 [39]	14.7	11.8	0.0	3.7	5.5	0.0	0.0	3.3	0.0	0.024	0.013	0.052
René 88DT [40]	16.0	13.0	4.0	2.1	3.7	0.0	0.7	4.0	0.0	0.030	0.015	0.000
René 95 [18]	13.0	8.0	3.5	3.5	2.5	0.0	3.5	3.5	0.0	0.065	0.013	0.050
RR1000 [1]	15.0	18.0	0.0	3.0	3.6	2.0	1.1	5.0	0.0	0.027	0.015	0.060
Udimet 720 [37]	17.8	14.5	1.2	2.5	4.9	0.0	0.0	3.0	0.0	0.032	0.032	0.030
Udimet 720Li [41]	14.6	15.9	1.4	2.4	5.2	0.0	0.0	3.0	0.0	0.023	0.016	0.042
Waspaloy [42]	19.5	13.5	0.0	1.3	3.0	0.0	0.0	4.3	0.0	0.040	0.006	0.060

2.1.2 Processing Superalloys for Turbine Disc Applications

The conventional processing route for polycrystalline Ni-based superalloys is ingot metallurgy [1, 18]. The steps involved are shown in Figure 2.3. The process begins with vacuum induction melting, electro-slag refining and vacuum arc melting to produce the alloy composition. These steps are typically followed by annealing, drawing and forging in order to achieve near-final component shape and to homogenize the alloy composition. Alloys produced via this route, for example Udimet 720Li, are called cast and wrought Ni-based superalloys. The advantage of the cast and wrought manufacturing process are cost benefits.

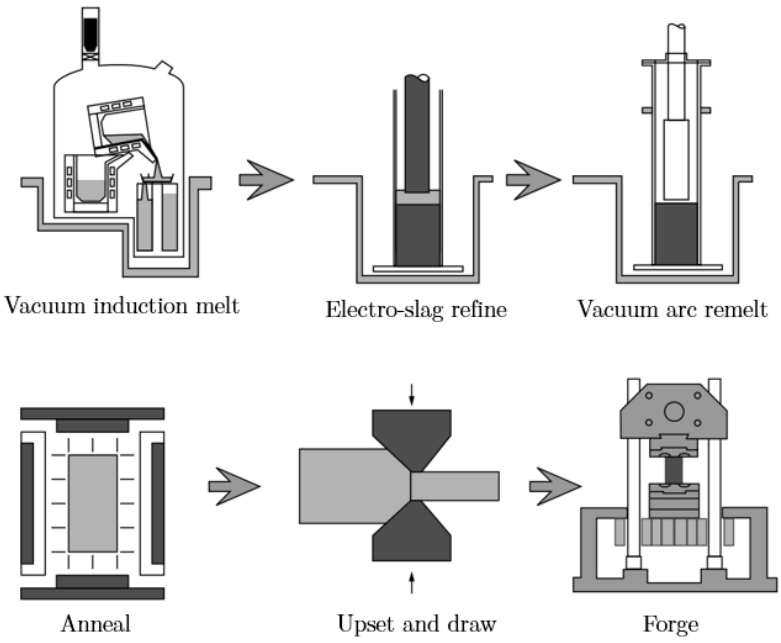


Fig. 2.3 Basic steps of ingot metallurgy for a cast and wrought Ni-based superalloy. Adapted from reference [1].

Advanced new generation Ni-based superalloys are produced via powder metallurgy. The process starts with vacuum induction melting and inert gas or vacuum atomization in order to remelt the alloy. This step is followed by atomisation and solidification of the alloy into a powder. This powder is then collected in steel cans

which are evacuated under vacuum and sealed. Hot isostatic pressing or extrusion consolidates the powder which is then hot deformed into a billet by extrusion or forging. Billet increments are forged into near final component shape (see Figure 2.4).

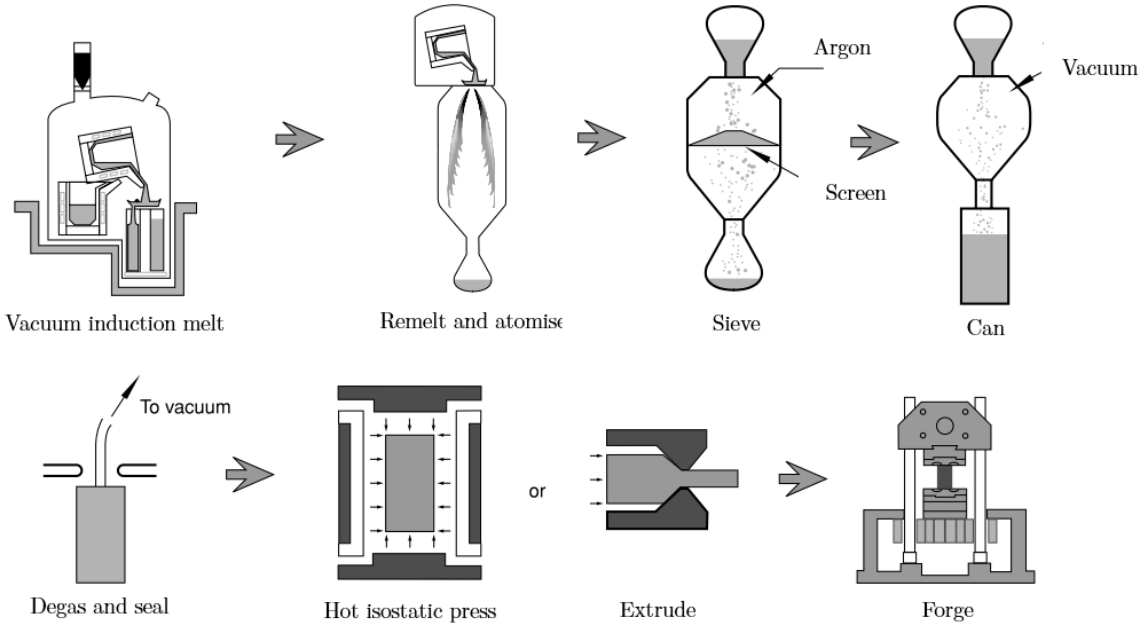


Fig. 2.4 Basic steps of powder metallurgy for an advanced Ni-based superalloy. Adapted from reference [1].

The γ-grain size and the γ'-precipitate size distribution is dependent on the heat treatment of the alloy after the last processing step. The γ'-phase can be present in the form of (i) primary incoherent γ'-particles (1-10 μm) which are located at the grain boundary triple points, (ii) secondary coherent γ'-particles (70-500 nm) within the γ-matrix and at the γ-grain boundaries and (iii) tertiary coherent γ'-particles (5-50 nm) within the γ-matrix. The γ'-precipitate size distribution can be bimodal (including secondary and tertiary γ'-particles) or a trimodal (including primary, secondary and tertiary γ'-particles). A schematic illustration of a trimodal γ'-phase size distribution is shown in Figure 2.5.

After forging, a non-uniform γ'-precipitae size distribution is present in the alloy

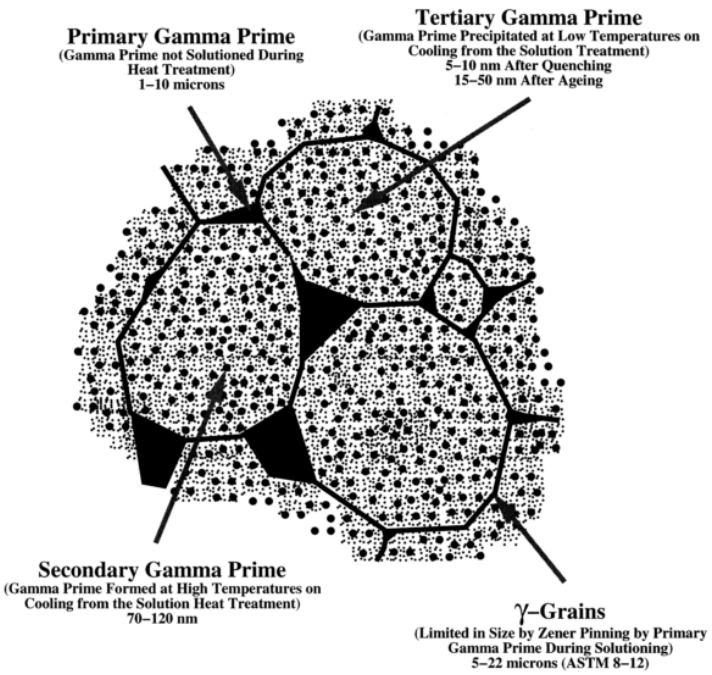


Fig. 2.5 Schematic illustration of a Ni-based superalloy microstructure with a trimodal γ'-precipitate size distribution. Adapted from reference [43].

[44]. The γ'-precipitate size distribution is optimised through a series of heat treatments which are illustrated in Figure 2.6. Studies performed on LSHR showed that the carbide and boride phase content in turbine disc alloys is also dependent on these heat treatments. It was found that the amount of minor phases diverge from the equilibrium conditions [45].

Figure 2.6 explains the three-stage heat treatment process which involves (i) a solution, (ii) a stabilization and (iii) an ageing heat treatment. The solution heat treatment can be performed either above the γ'-phase solvus temperature or below. Depending on this heat treatment, alloys are classified as sub- or super-solvus heat treated. The super-solvus solution heat treatment is typically conducted at 30°C above the γ'-phase solvus. During this first step the totality of γ'-phase is dissolved and γ-grain growth is promoted. At this stage MC carbides at the grain boundaries are desired to control grain growth and therefore grain size. If a sub-solvus solution

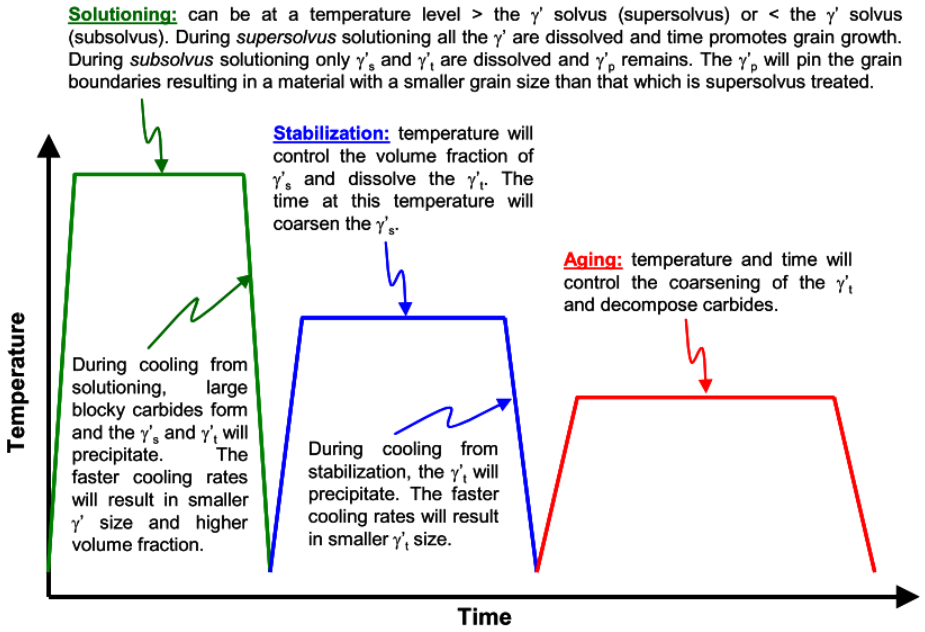


Fig. 2.6 Schematic illustration of typical heat treatment stages for polycrystalline Ni-based superalloy. Adapted from reference [46].

heat treatment is applied, secondary and tertiary γ'-precipitates dissolve while the primary γ'-precipiates, which are located at the grain boundaries, remain. If primary γ'-precipiates are present at the grain boundaries they can suppress grain growth. Upon cooling, secondary γ'-precipitates are formed from the supersaturated γ-matrix. The cooling rate controls the secondary γ'-precipitate size. A fast cooling rate results in relatively small secondary γ'-precipitates and a unimodal γ'-particle size distribution. A slow cooling rate results in a larger γ'-particles and a serrated grain boundary morphology due to interactions between the nucleating γ'-precipitates and the growing γ-grains [47]. For turbine disc components, cooling rates are desired to be around 0.5 - 1.5°C per second [11].

The stabilization heat treatment is applied to coarsen the secondary γ'-particles and to dissolve very fine γ'-particles. The temperature is below the γ'-phase solvus. During cooling from stabilization to room-temperature, the tertiary γ'-precipitates

will form out of solution. The ageing heat treatment is performed at temperatures too low to modify the primary and secondary γ'-size and is aimed at completing the precipitation of the γ'-phase, thus to form additional tertiary γ'-precipitates and to modify the tertiary γ'-size. Furthermore, the stabilisation heat treatment promotes the decomposition of MC to $M_{23}C_6$ carbides.

2.2 Deformation and Failure Mechanisms in Nickel-Based Superalloys

The main damage mechanism in high pressure turbine discs is low cycle and dwell fatigue. Due to its high strength, a polycrystalline Ni-based superalloy is more susceptible to crack growth [48]. First, the relevant deformation mechanisms for this work are briefly reviewed. Second, a background to environmentally-assisted crack propagation is given and the known relationships between low cycle fatigue and dwell fatigue crack growth to temperature, load frequency and the dwell time are explained. In addition, linear elastic models are discussed which describe fatigue and dwell fatigue crack growth using the cyclic stress intensity parameter ΔK. The physical mechanism leading to environmentally-assisted cracking is still subject to ongoing research. So far two main mechanism have been proposed which are introduced in the last Subsection.

2.2.1 High Temperature Deformation Mechanisms

Tensile Deformation

Plastic deformation in Ni-based superalloys in the mid-temperature regime at intermediate and fast deformation rates is governed by the interactions of dislocations with (i) alloying elements in the γ-matrix, (ii) γ-grain boundaries, and (iii) the coherent γ'-precipitates.

Additions of Co, Cr, Mo and W strengthen the γ-matrix. Atoms of a different size replace Ni within the crystal structure. The resulting internal strain fields inhibit dislocation movement, thus causeing a strengthening effect. In addition, solute additions of, for example, Co in the γ-matrix can lower the stacking fault energy by

changing the *ABC ABC ABC* sequence and making dislocation movement more difficult [49]. Below 750°C dislocations move on the $a/2\ \langle 1\bar{1}0\rangle\ \{111\}$ slip system where they dissociate into two shockley partial dislocations [1]:

$$a/2\ \langle 1\bar{1}0\rangle\ \{111\} \rightarrow a/6\ \langle 211\rangle\ \{\bar{1}11\} + a/6\ \langle 12\bar{1}\rangle\ \{\bar{1}11\} \tag{2.2}$$

Lowering the stacking fault energy has an important implication on the resistance to dislocation glide. As the stacking fault energy is reduced, the distance between the partial dislocations increases. In addition, in polycrystalline Ni-based superalloys grain boundaries impede dislocation movement. As a consequence, strengthening can be achieved through grain refinement.

The greatest proportion of strengthening in Ni-based superalloys comes from the Ni_3Al phase within the γ-matrix. Shearing of γ'-precipitates is hindered due to the fact that two superlattice partial dislocations are required to generate a dislocation in the ordered γ'-phase. During deformation, a superlattice partial dislocation in the γ-matrix enters the precipitate by forming a planar fault: a so-called antiphase boundary (APB). The order of the γ'-phase $L1_2$ crystal structure is overcome by forcing undesirable first neighbour bonds, a trailing superlattice partial dislocation is then able to restore the ordered $L1_2$ structure. Consequently, precipitate shearing only occurs when the shear stress is large enough to force the leading partial dislocation to cut the γ'-particle creating an ABP. The shearing of a γ'-precipitate can either be 'strongly' or 'weakly' coupled depending on the radius of the γ'-particle [1]. Both 'strongly' and 'weakly' refers to the attractive force that the leading dislocations apply on the trailing dislocation as they permeate through the γ'-precipitate. If the distance between the leading and the trailing dislocation is much greater than the γ'-precipitate radius the dislocations are 'weakly' coupled – this occurs when the superalloy is in

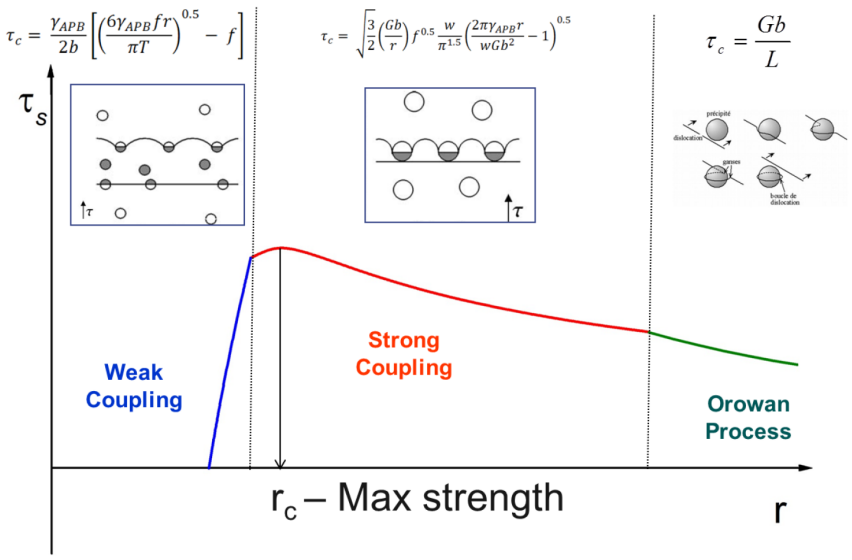


Fig. 2.7 An overview how dislocations can overcome the γ'-precipitate in Ni-based superalloys. Adapted from reference [11].

an under-aged condition. In an over-aged condition, the dislocations are 'strongly' coupled. Figure 2.7 provides an overview of the γ'-precipitate shearing mechanisms occurring; Orowan shearing is not observed in turbine disc alloys [50]. The maximum γ'-phase strengthening effect occurs at the point where dislocation shearing transitions from the weakly to strongly coupled pairs [51]. At this critical γ'-precipitate radius it is possible to approximate the strength of the precipitate to $1/2{\cdot}\gamma_{APB}\ f^{1/2}/b$ [23], where γ_{APB} is the anti-phase boundary energy, f is the volume fraction of the γ'-phase and b is the Burger's vector. From this approximation it is evident that strengthening in Ni-based superalloys is strongly dependant on the volume fraction of the precipitate phase as well as the fault energy in the phase.

Creep Deformation

In the mid and high temperature regime at sufficiently slow deformation rates thermally activated time-dependent creep mechanisms contribute to plastic deformation. In polycrystalline Ni-based superalloys the creep behaviour depends strongly upon the

metallurgical structure, mainly (i) the γ-grain size, the (ii) γ'-particle size distribution in addition to the (iii) concentrations of alloying elements in the γ-matrix. Dislocation movement within a γ-grain occurs though a climb-plus-glide mechanism. If a gliding dislocation is pinned, the climb can release it, allowing further glide. Dislocation climb occurs via lattice-diffusion. Alloying additions lead to strengthening effect when the atomic size misfit of solute and solvent is large [1]. The strengthening increases with the concentration of solute added. Mo and W are effective strengtheners.

Coble creep takes place along the grain boundaries. It describes the diffusion of vacancies along those interfaces leading to a net flow of material and a sliding of the grain boundaries under the applied stress. This effect is the most prominent form of creep damage in polycrystalline Ni-based superalloys resulting in creep cavitation at grain boundaries [1]. Coble creep is dependent on the grain size and becomes less influential as the grain size increases. If the grain size is large, creep life is also dependent on the γ'-phase volume fraction. The increase in number of γ'-precipitates reduces the creep rate because dislocation have to climb around obstacles. Modifying the precipitation of carbide and borides at grain boundaries can help improve the creep resistance of the polycrystalline alloys.

2.2.2 High Temperature Crack Propagation

Low Cycle Fatigue

In general fatigue crack growth can be separated into three stages, as illustrated in Figure 2.8: (1) Initial short crack propagation (2) stable cyclic crack growth and (3) rapid fracture of the remaining cross-section. The second region in Figure 2.8 is called the Paris-regime and represents stable transgranular crystallographic slip crack growth normal the the applied load. A power-law type liner elastic model links the

crack growth rate and the cyclic stress intensity range:

$$\frac{da}{dN}_{\text{cyclic}} = C(\Delta K)^n \quad , \tag{2.3}$$

where C and n are material dependent constants obtained from linear regression [52]. This simple model does not capture thermally activated and time dependent effects [53]. It is therefore only valid at room-temperature.

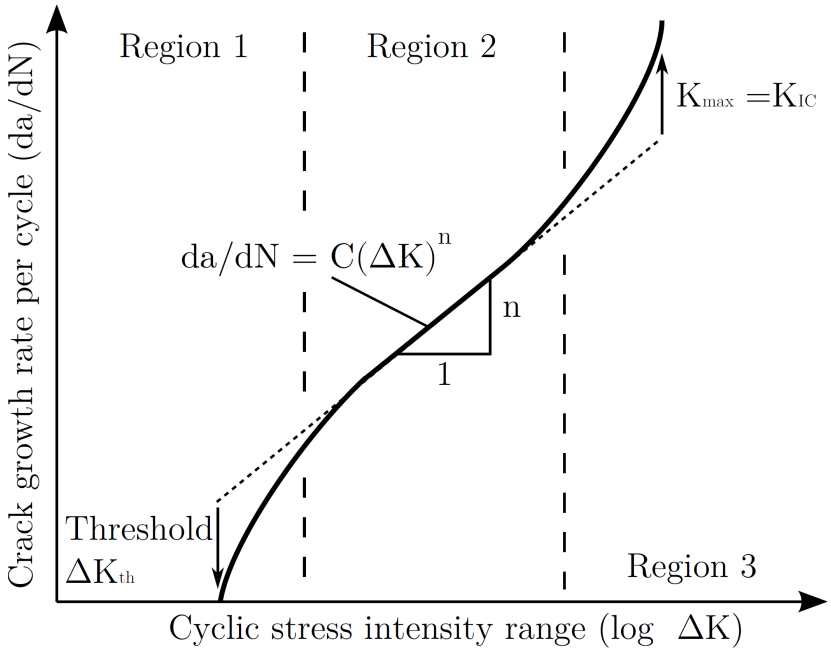


Fig. 2.8 Schematic illustration of the fatigue crack growth rate versus the cyclic stress intensity range showing three regions of primary crack growth mechanisms. Redrawn from [54].

Many early studies on Fe- and Ni-based superalloys demonstrated that temperature and load frequency affects the crack propagation rate in air [37, 55–58]. It was shown that a decreasing load frequency increases the crack propagation rate due to a change in the fracture mode from transgranular to intergranular (Figure 2.9 and Figure 2.10) [55]. This observation was confirmed *inter alia* by Floreen *et al.* [57].

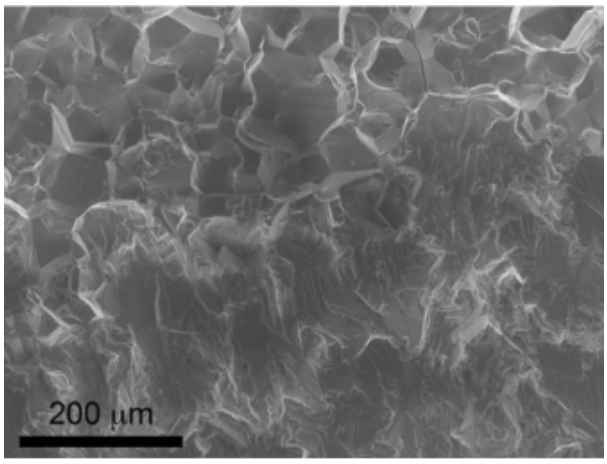


Fig. 2.9 Fracture surface in Allvac 718Plus showing a transition from transgranular to intergranular fracture due to an increase in test temperature. Adapted from reference [59].

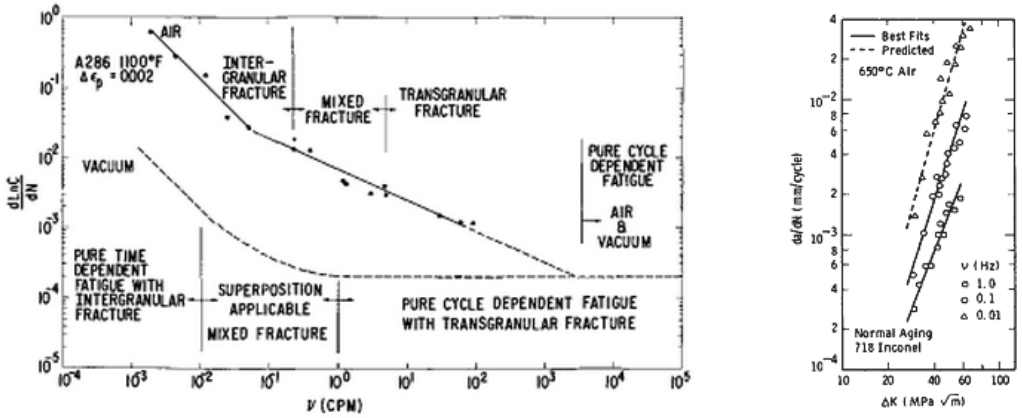


Fig. 2.10 Left: Effect of frequency using notched fatigue bars of A286 at 593°C in air and vacuum. Adapted from reference [55]. Right: Fatigue crack growth rate in Inconel 718 at 650°C at different loading conditions. Adapted from reference [57].

Above 400°C, at intermediate temperatures, fatigue life is not only dependent on the load frequency but also on the test temperature. The fatigue crack propagation rate of Inconel 718 and its relationship with temperature and load frequency (cycle period) is shown in Figure 2.11 [58].

The examples presented illustrate the general belief that at intermediate temperatures, low cycle fatigue crack propagation rate is increased due to time-dependent

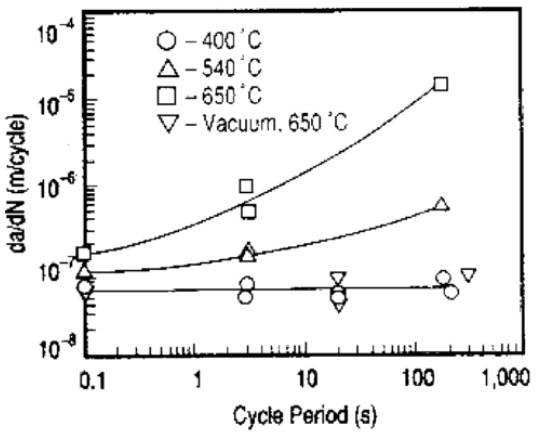


Fig. 2.11 Fatigue crack propagation rate in Inconel 718 at a constant ΔK. Adapted from reference [58].

environmentally-assisted processes. Figure 2.12 shows the fatigue life of Inconel 706 at temperatures between room-temperature and 900°C [60]. A dip in fatigue life can be observed at 700°C in air when compared to vacuum tests.

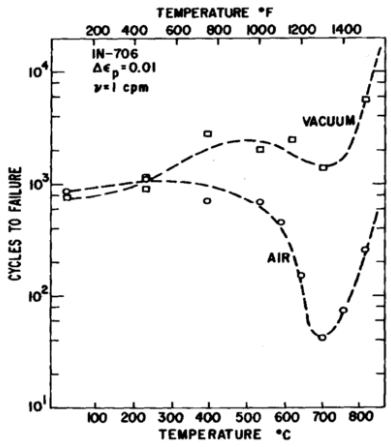


Fig. 2.12 Effect of an oxygen environment on the fatigue life on IN706 as a function of temperature. Adapted from reference [60].

The mode of fracture during low cycle fatigue in air therefore changes between transgranular and intergranular, depending upon load frequency and temperature as shown in Figure 2.13. The influence of temperature and environment during low cycle fatigue is still present in advanced polycrystalline Ni-based superalloys such as LSHR

[61].

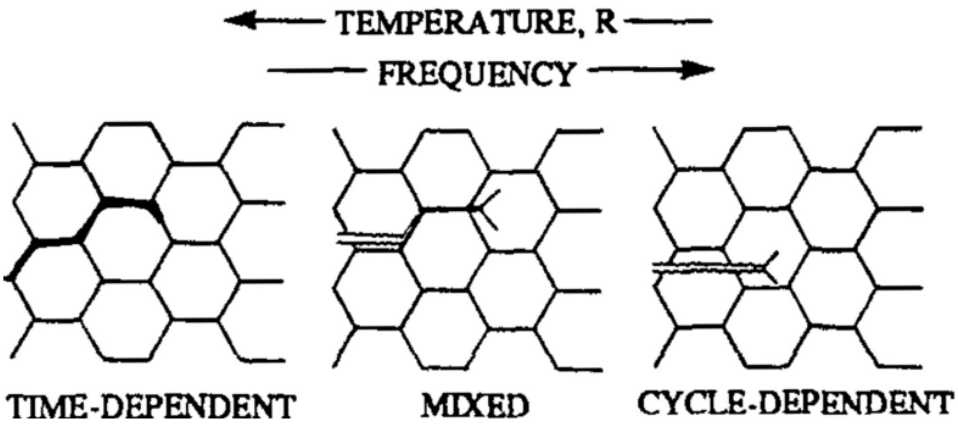


Fig. 2.13 Schematic of fatigue crack growth mechanisms for time-dependent, mixed and cycle-dependent crack growth regimes in air environment. Adapted from reference [62].

In order to account for the demonstrated temperature dependence, the following Arrhenius-type cycle-dependent crack growth model was developed:

$$\frac{da}{dN} = A \cdot \Delta K^m \exp\left\{ -\frac{Q}{RT} \right\} \quad , \tag{2.4}$$

where A and m are material constants at a given temperature, Q is the apparent activation energy for the rate controlling process, R is the universal gas constant, and T is the absolute temperature [63, 64]. This model was modified by Yoon *et al.* [65] to contain temperature independent material constants as follows:

$$\frac{da}{dN} = c_0 \Delta K^{m_0 + \frac{c_1}{RT}} \exp\left\{ -\frac{Q}{RT} \right\} \quad , \tag{2.5}$$

where c_0, m_0 and c_1 are temperature independent material constants. This model attempts to predict the crack growth rate as a function of temperature. Both models fail to capture the time-dependent nature of low-cycle fatigue crack growth at intermediate temperatures.

Dwell Fatigue

The rim of the turbine disc experiences periods at high stress levels and at the highest temperature during a typical flight cycle. These hold times are called the dwell condition. An ideal dwell fatigue cycle is shown in Figure 2.14.

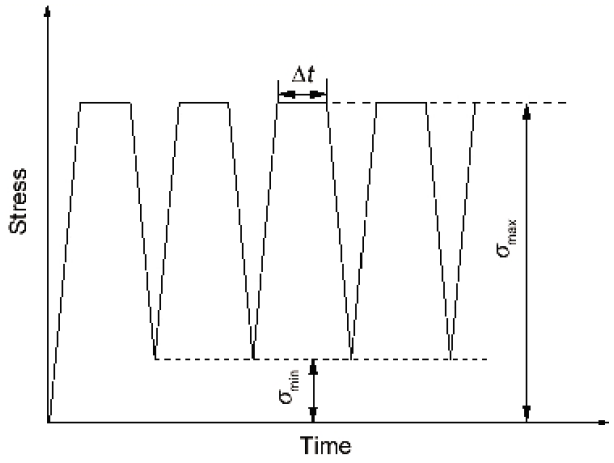


Fig. 2.14 Stress over time during during dwell fatigue testing.

The length Δt of the dwell period determines the additional time provided for time-dependent processes to operate. Multiple studies show that, at intermediate temperatures, fatigue crack propagation rates are increased if a hold time at maximum load and temperature is introduced [66–70]. Figure 2.15 shows an order of magnitude increase in crack propagation rate when a 20 second dwell was introduced at 650 and 725°C for a coarse grained variant of LSHR [61]. Similar observations were made for N18 [69]. Dwell fatigue crack growth models need to account for the hold-time component in addition to the cycle-dependent component. A linear super-position model was proposed

$$\frac{da}{dN}_{\text{dwell}} = \frac{da}{dN}_{\text{cycle}} + \frac{da}{dN}_{\text{time}} \quad , \tag{2.6}$$

where da/dN_{cycle} is the cycle-dependent component and da/dN_{time} is the time-dependent component of the crack growth rate [66]. This model describes dwell fatigue as the sum

of pure cycle-dependent and time-dependent effects. This model does not capture the fact that at intermediate temperatures, fatigue crack growth includes time-dependent processes. The time-dependent component was described by Saxena [71]:

$$\frac{da}{dN}_{\text{time}} = c_1 \Delta K^{n_1} + c_2 \Delta K^{n_2} \cdot \sqrt{\Delta t} \quad , \tag{2.7}$$

where n_1, n_2, c_1 and c_2 are constants obtained from crack growth data. The hold time is represented through Δt. For alloy 720Li, a model was proposed which includes the load ramp time t_{ramp} in addition to Δt:

$$\frac{da}{dN}_{\text{time}} = C \cdot \exp\left\{ -\frac{Q}{RT} \right\} \Delta K^m (t_{\text{ramp}} + \Delta t)^{1/2-\phi} \quad , \tag{2.8}$$

where C and ϕ are fitting parameters [72].

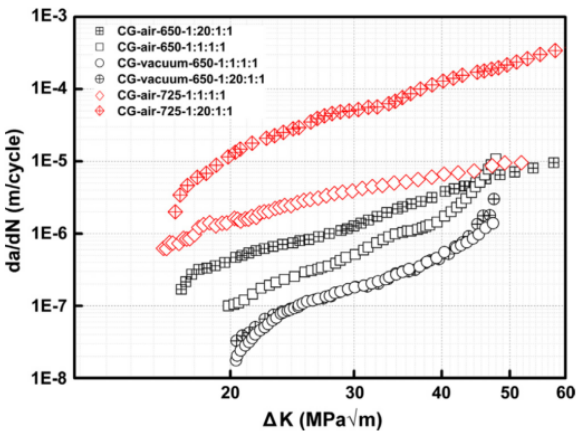


Fig. 2.15 Comparison of the low cycle and dwell fatigue crack growth rate in a coarse grain (CG) variant of LSHR tested at 650 and 725°C in air and vacuum. Adapted from reference [61].

The hold time during dwell fatigue promotes not only environmentally assisted time-dependent processes but also crack tip relaxation processes such as creep deformation. Stress relaxation has been found to be affected by an overload at the beginning

of each dwell period [73]. An overload may provide a greater driving force for stress relaxation and consequently a reduced dwell fatigue crack growth rate was observed.

2.2.3 Crack Tip Damage Mechanisms

It is generally believed that oxygen is the damaging species in laboratory air. Independent studies from the late 90's performed by Molins *et al.* [74] and Pineau *et al.* [75] proved the existence of a transition oxygen partial pressure. The transition is marked by a sharp increase in the fatigue crack growth rate and a change in fracture mode from transgranular to intergranular failure (Figure 2.16).

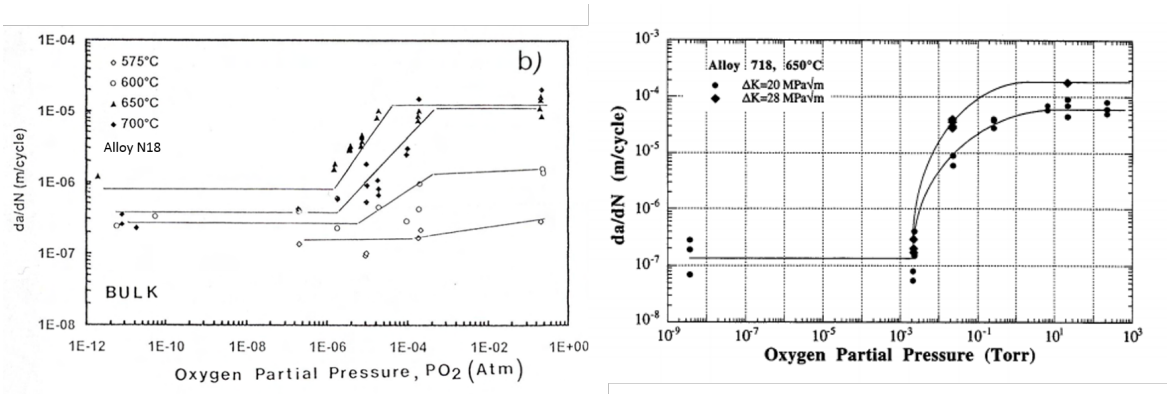


Fig. 2.16 Left: Fatigue crack growth rate in N18 as a function of the oxygen partial pressure for a range of temperatures. Adapted from reference [74]. Right: Fatigue crack growth rate in N18 as a function of the oxygen partial pressure at 650°C and a constant ΔK in Inconel 718. Adapted from reference [75].

In both cases the cycles to failure were a function of oxygen partial pressure as well as temperature. This dependence was also shown more recently to be valid for dwell fatigue in alloy N18 [69]. The transition oxygen partial pressure $p(O_2)_{\text{crit}}$ is around 10^{-3} mbar at 650°C [74]. However, the actual partial pressure at the crack tip might be smaller due to the oxidation of the fracture surface behind the crack front [76]. These studies led to the prevalent opinion that elemental oxygen penetration and/or a subsequent reaction at the grain boundary is responsible for intergranular

crack propagation in polycrystalline Ni-based superalloys at elevated temperatures. The presence of oxygen at the crack tip induces a damage zone at the crack tip. The nature of this damage zone is still subject to current research. Currently two damage mechanisms are proposed in the literature: Dynamic embrittlement and stress accelerated grain boundary oxidation (SAGBO).

Dynamic Embrittlement

Dynamic embrittlement generally describes time-dependent intergranular cracking due to stress driven diffusion of an embrittling element into the grain boundary ahead of the crack tip (Figure 2.17) [77].

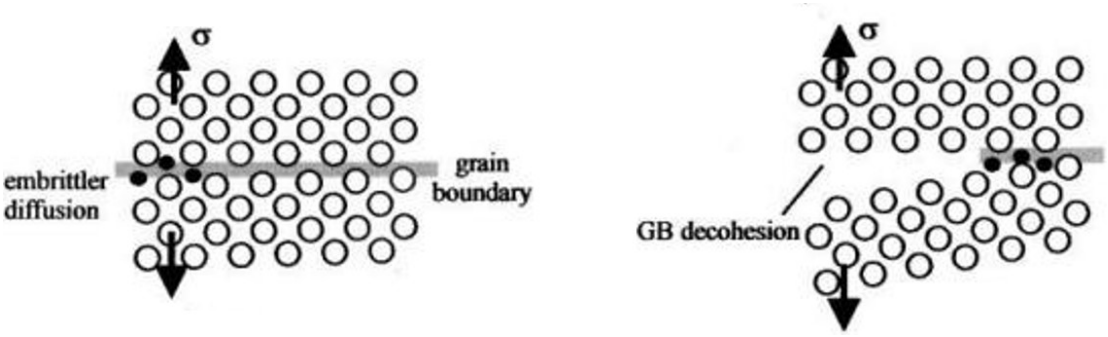


Fig. 2.17 Schematic representation of dynamic embrittlement. Adapted from reference [77].

The embrittling element lowers the cohesive strength of the grain boundary and the crack propagates intergranular. This damage zone is typically on a nanometre scale [77]. A prominent example of dynamic embrittlement is the case of hydrogen embrittlement in steels [78]. However, the theory of dynamic embrittlement cannot be transferred to environmentally-assisted cracking without modification. Stress rupture tests performed on hydrogen annealed (carbon removed) commercially pure nickel did not fail intergranularly at high temperatures [79]. This key result suggests that elemental oxygen does not embrittle pure nickel. Nevertheless, elemental oxygen em-

brittlement on an atomic level at the core of a crack tip was assumed by Pfaendtner and McMahon [76, 80]. In addition, the acceleration of grain boundary sliding and cavitation due to a lower grain boundary surface energy as a result to elemental oxygen had been proposed by Hayes *et al.* [81] in the past.

Woodford [82] conculed that elemental oxygen at the grain boundary has to react; a subsequent oxidation reaction is required. Three distinct oxidation reactions have been suggested at the grain boundary ahead of the crack tip to date. First, oxidation of intergranular sulphides causing dynamic sulphur embrittlement [83]. Second, oxidation of elemental carbon causing carbon dioxide gas bubbles and cavities [84, 85]. Third, oxidation of precipitates and impurities forming oxides along the grain boundary [86]. All three processes require the stress driven diffusion of elemental oxygen into the grain boundary. Post-failure oxidation of the grain boundary will always occur after the intergranular crack has propagated. Sulphur embrittlement can be ruled out, since dynamic sulphur embrittlement leads to clean intergranular fracture surfaces with no signs of reaction products [82]. This does not correspond with overall observations where oxidation products have been found at the fracture surface (Figure 2.18). Therefore intergranular gas bubble formation or oxidation of grain boundary features ahead of the crack tip are proposed to be the reason for gas phase embrittlement.

Theses mechanisms lead to grain boundary immobilisation, which reduces the local ability to accommodate stress through grain boundary sliding and migration. Consequently, stresses built up during loading lead to grain boundary decohesion [82]. Other authors point out that the increase in the specific volume during oxidation of carbides might cause localised plastic deformation which nucleates microcracks at the grain boundary [87]. It should be noted that in highly alloyed Ni-based superalloys elemental carbon within the grain boundary forms various carbides and is therefore unavailable for gas bubble formation.

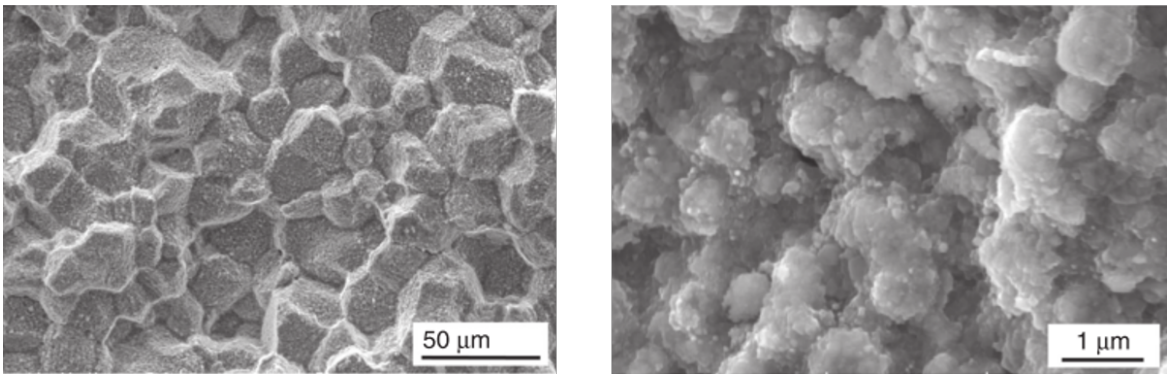


Fig. 2.18 SEM fractography after 1 hour dwell fatigue at 700°C in air in an advanced Ni-based superalloy. Adapted from reference [70].

In the following the term 'gas phase embrittlement' in conformity with as Woodford [82] is used, rather than 'dynamic embrittlement'. While dynamic embrittlement typically occurs on a nano scale, gas phase embrittlement is dominated by oxygen diffusion processes well beyond the crack tip [82].

The diffusion coefficent of oxygen in pure Nickel was reported to be between 10^{-5} and 10^{-4} m^2s^{-1} between 850 and 1400°C [88]. This is in contrast to early internal oxidation experiments on dilute Ni-Be alloys which estimated the diffusivity of oxygen in nickel to be $4.27{\cdot}10^{-16}$ m^2s^{-1} at 650°C and $1.14{\cdot}10^{-11}$ m^2s^{-1} at 1000°C [89, 90]. Values for the diffusivity of oxygen along the grain boundary are very limited in the literature. The rate of diffusion along the grain boundary is higher than for bulk matrix diffusion [91]. The grain boundary diffusivity in nickel has been estimated to be on the order of $2.5{\cdot}10^{-12}$ m^2s^{-1} at 650 deg C [92]. This is in the order of magnitude reported by Bricknell and Woodford [84] for nickel and Pedron and Pineau [91] for Inconel 718 (Summarised by Lu *et al.* in Figure 2.19). If the diffusion is stress-assisted, the rate will increase due to the applied load. Furthermore, the diffusivity is likely to be affected by the overall alloy composition.

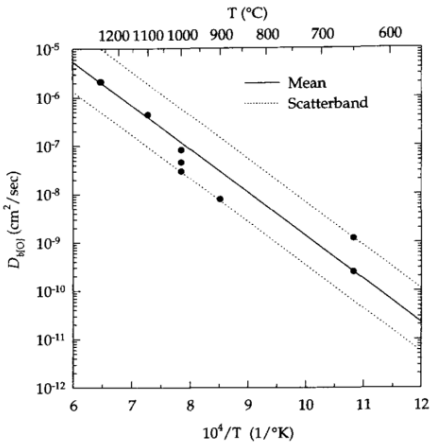


Fig. 2.19 Reported values for oxygen diffusion along the grain boundary. Adopted from reference [93].

The theory of gas phase embrittlement is heavily based on observations made during static embrittlement experiments where greater oxygen-induced damage distances are achieved [82]. For example tensile tests performed in air and vacuum exposed (200 h at 1000°C) Ni270 showed a reduction in tensile ductility at intermediate temperatures (Figure 2.20) [94].

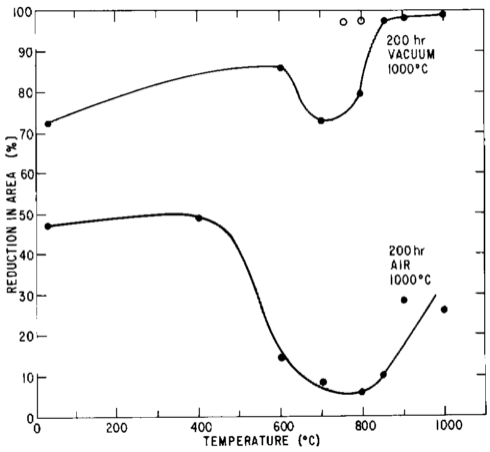


Fig. 2.20 Effect of 200 h air exposure at 1000°C on Ni270 as a function of temperature on the tensile ductility [94].

A comparable degradation of the tensile ductility was shown after air exposure at 1000°C for Inconel 903A [95] and at intermediate temperatures for commercially

pure nickel [96, 97]. The temperature dependent degradation of tensile ductility is in agreement with observations made during low cycle fatigue tests on Inconel 706 [60] (Figure 2.12) and on Inconel 718 [98]. This loss of ductility in the intermediate temperature regime was shown to be due to intergranular embrittlement which occurred far in advance of the observed internal oxidation [99]. A study on Ni270 observed intergranular cracking after exposure in a Ni−NiO pack. This Ni−NiO pack was considered to produce an oxygen partial pressure too low to allow stable NiO oxide formation along the grain boundaries [94]. At temperatures above 800 to 900°C the ductility is usually restored [60, 94, 95, 98]. Woodford interprets this transition from *ductile-to-brittle-to-ductile* with increasing temperature as evidence of gas phase embrittlement [82]. The argument is centred around grain boundary mobility. While at temperatures where intergranular fracture occurs the grain boundary is immobile due to gas phase embrittlement, at high enough temperatures the grain boundary gains enough thermal energy to break away from gas bubble or oxide induced grain boundary pinning. Another supporting observation is the absence of dynamic recrystallisation during quasi-static testing of Inconel 903A in the intermediate temperature regime [94].

Static loading of notched Inconel 718 bars at 650°C demonstrated that susceptibility to intergranular cracking is dependent on the orientation of the grain boundaries [100]. Kane *et al.* [101] shows that low angle grain boundaries and Σ3 grain boundaries are more resistant to cracking than random high angle grain boundaries in Inconel 718 at 650°C in air. The dependence on the grain boundary structure was also confirmed for Inconel 718 [102] and Allvac 718Plus [103]. It was concluded that a low free grain boundary volume results in a low grain boundary diffusivity for elemental oxygen. These observations were regarded as evidence that diffusion processes along the grain boundary are responsible for time-dependent crack growth. Preferential grain

boundary embrittlement would also explain the observation of transgranular cracked lingaments on the fracture surface [59, 102, 104]. Since the cracking rate would vary form grain boundary to grain boundary, crack fingers would extend into the uncracked material [80]. A recent study performed on Allvac 718Plus confirmed oxidation of grain boundary carbides and γ''-precipitates by means of fractography [105].

A study performed on fatigue pre-cracked Inconel 783 specimens at temperatures up to 650°C showed intergranular cracking along localized patches of grain boundaries during an incubation period before steady crack growth was achieved. After much discussion this was found to be consistent with the dynamic embrittlement mechanism. [80, 106, 107].

Stress Accelerated Grain Boundary Oxidation

Stress accelerated grain boundary oxidation (SAGBO) describes the time-dependent formation and subsequent brittle failure of wedge-shaped bulk oxide intrusions at the crack tip and at the grain boundary ahead (Figure 2.21) [108]. The propagated crack is subject to oxidation again and the process is repeated. The damage zone is assumed to be on a micron scale [109]. The role of stress, which is expected to become tensile at the tip of the oxide intrusion [110], is to assist the accommodation of the volumetric expansion that accompanies the oxide formation [80]. Enhanced oxygen diffusion along the grain boundary causes the grain boundary region to oxidise faster.

At first, NiO plus FeO and their spinels ($NiCr_2O_4$ and/or $Ni(FeCr)_2O_4$) are formed under atmospheric pressure. Once the oxygen partial pressure drops due to the oxidation of Ni and Fe, a continuous layer of Cr_2O_3 is formed and so-called crack tip passivation occurs. This limits further oxidation damage. The incubation time for passivation increases with increasing oxygen partial pressure but is also dependent on

the degree of Cr matrix depletion alongside the grain boundary paths [108]. During time-dependent crack propagation, the NiO and FeO crack before a sufficient Cr_2O_3 layer is formed. This has been observed post-failure on the fracture surface of Inconel 718 (Figure 2.21).

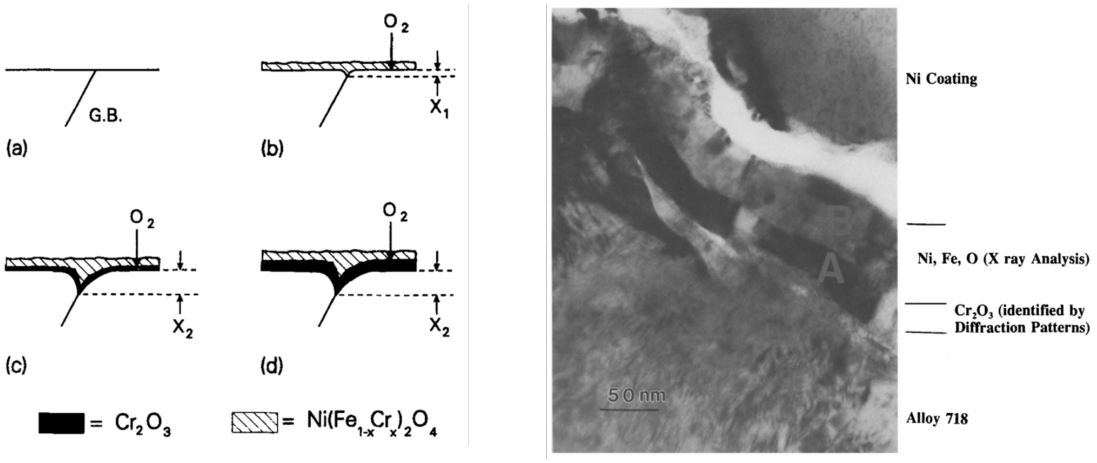


Fig. 2.21 Left: Suggested two-stage grain boundary oxidation mechanism. Adapted from reference [108] and [111]. Right: TEM and microanalysis of oxide types on the fracture surface of Inconel 718. Adopted from reference [108].

This oxide structure is consistent with the thermodynamics of the oxygen partial pressure gradient ahead of the crack tip and has been observed post-failure on fracture surfaces (Figure 2.21 and Table 2.3) [108].

Table 2.3 Oxide formation free energy and the dissociation pressure at 727°C for the elements introduced in this section. Adapted from reference [113]

Element	Oxide formation	Free energy	Oxidation dissociation pressure
Ni	NiO	-149 kJ/mole	-16 $\log_{10}$ bar
Co	CoO	-166 kJ/mole	-18 $\log_{10}$ bar
Cr	Cr_2O_3	-877 kJ/mole	-31 $\log_{10}$ bar
Ti	Ti_2O_3	-1295 kJ/mole	-44 $\log_{10}$ bar
Al	Al_2O_3	-1425 kJ/mole	-48 $\log_{10}$ bar

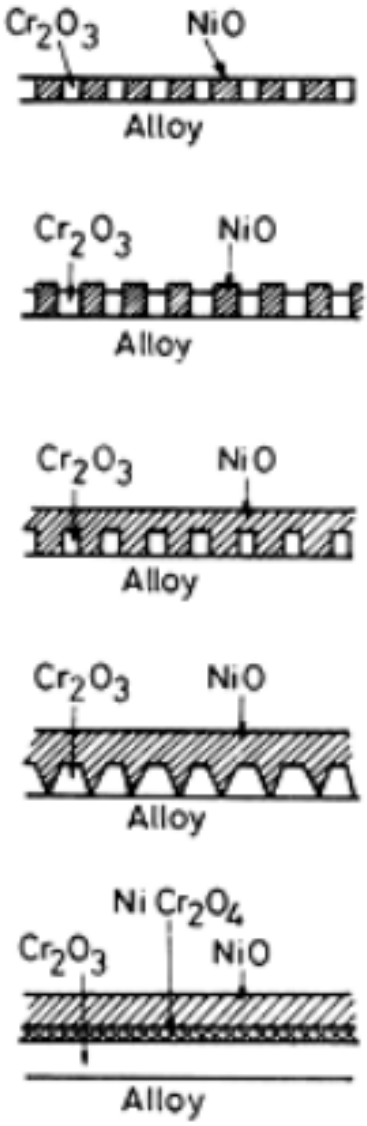


Fig. 2.22 Schematic diagram of the oxidation process of a binary Ni-Cr alloy. Adapted from reference [112].

At first, Ni- and Cr-rich oxide formation is taking place simultaneously [112]. Due to faster kinetics, NiO dominates during the initial stages of oxidation (Figure 2.22). After the initial stage, Cr_2O_3 particles are growing within the NiO layer. The rate of nickel oxide formation drops due to a change in the oxygen partial pressure and Cr_2O_3 establishes a layer underneath the NiO. If the Cr_2O_3 reaches a critical thickness, further oxygen diffusion into the alloy is prohibited. This is called passivation [114].

Environmentally-assisted crack growth is challenging to study due to the reported size of the oxides at the crack tip. Kitagutchi *et al.* [28, 115] studied the tip of cracks of a interrupted crack propagation tests at 650°C using scanning transmission electron microscopy equipped with energy-dispersive X-ray spectrometry in an advanced polycrystalline Ni-based superalloy (Figure 2.23). The crack tips were found to be filled with oxides. Co and Ni-rich oxides were found in the middle of the crack tip and a Cr-rich oxide layer at each side of the crack. Additional STEM-EDS line scans were performed across the oxide and showed the segregation of Ti and Al in the studied region. It was concluded that the crack tip oxide formation follows the oxygen partial pressure gradient along the oxide tip ahead of the crack tip (Table 2.3) [28, 110, 115].

Viskari *et al.* [104, 116, 117] made similar observations on Inconel 718 and Allvac 718Plus. The intergranular crack tip oxides were found to be layered with a Ni-rich oxide in the middle of the crack and a Cr-rich oxide at each side of the crack. Atom probe tomography at a crack tip in Allvac 718Plus showed local regions of NiO. The Ni-rich layer was found Co-enriched in the outer part and Fe-enriched in the inner part (Figure 2.24). The subsequent Cr-rich layer showed variations with a pronounced presence of Al and Nb. This suggests the oxidation of the γ'-phase. The overall oxide layering was again found to be consistent with thermodynamic predictions. The presence of oxygen was found to be confined to the observed oxides. The grain boundary ahead of the crack tip was not reported to be oxygen enriched. Testing performed in a controlled

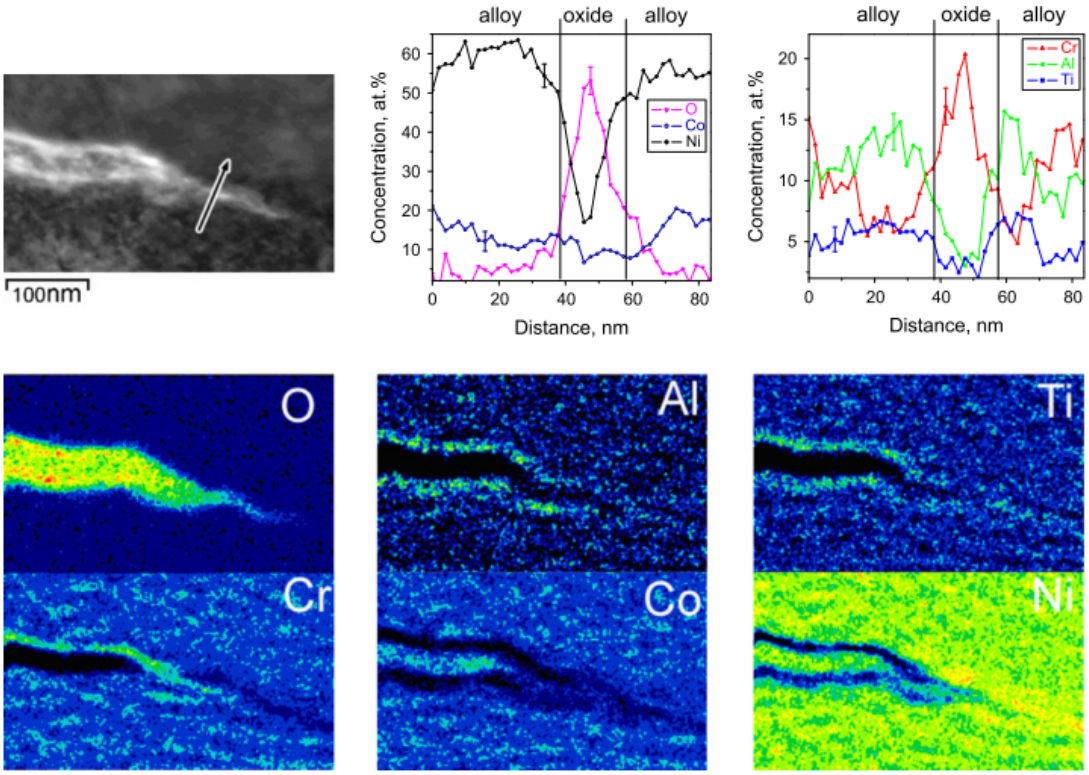


Fig. 2.23 A bright field STEM image, EDX maps and linescans obtained at an intergranular crack tip of an advanced Ni-based superalloy. The relative concentration in the EDX maps increases from low to high in the sequence: black, blue, green, yellow, orange and red. Adapted from reference [115].

^{18}O environment and SIMS also showed that the presence of oxygen was limited to the crack tip oxides [117]. Based on these observations, Viskari concluded that SAGBO is the time-dependent crack growth controlling mechanism in air for Inconel 718 and Allvac 718Plus at intermediate temperatures [104].

Li *et al.* [70] performed dwell fatigue crack growth tests in air to study the effects of microstructure on RR1000. STEM-EDS at a crack tip showed Co and Ni oxides in the middle and a thin Cr oxide layer towards the metal matrix. It was suggested that the crack propagation mechanism during high temperature dwell fatigue involves oxide formation ahead of the crack tip grain boundaries and their subsequent fracture.

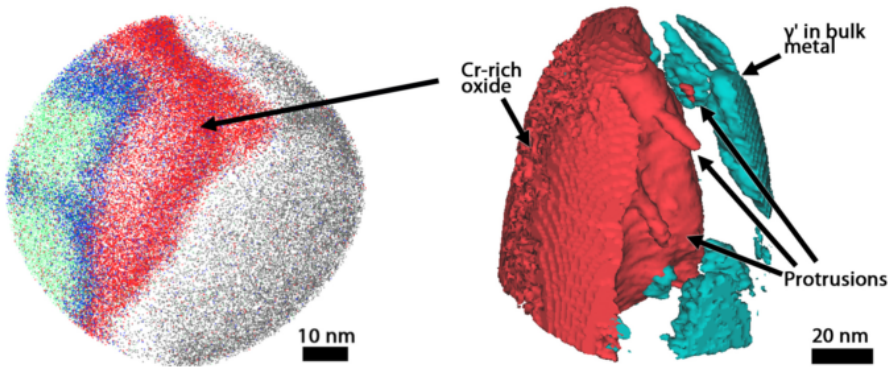


Fig. 2.24 Left: Cross-section of a APT reconstruction showing the NiO (green), Fe enriched (blue) and Cr-rich oxides and also the Cr in the unoxidised metal. Right: APT reconstruction by iso-surfaces showing oxygen-rich protrusions into the matrix. The γ' precipitates in the metal are also shown. Adapted from reference [117].

Andrieu *et al.* [108] demonstrated the feasibility of a damage mechanism based on crack tip oxide failure experimentally using fatigue tests at 650°C in Inconel 718. Three different loading conditions were applied: continuous cycling, 600s dwell at minimum load and 600s dwell at minimum load overlaid with 1 Hz cycle. The 600 seconds dwell was considered to be the transition time for crack tip passivation and thus spinels should have stopped forming. By applying a small load 1 Hz cycle the spinels at the crack tip would break up and the crack growth would be accelerated. The crack growth rate did in fact accelerate. This outcome can indeed be explained by the proposed mechanism of a two-step oxidation model for time-dependent crack growth in air [108, 118]. The failure of crack tip oxides is favoured by its low fracture toughness of ≈ 2 MPa$\sqrt{m}$ at 700°C [119]. The preferantial cracking of NiO and the interface between the nickel oxide and the chromium oxide was also reported in Inconel 718 [116].

Andrieu *et al.* [120] also noted that NiO at the crack tip could lead to the injection of vacancies into the grain boundary. The following migration and accumulation of these vacancies could act as nucleation sites for pores and micro-cracks.

2.3 Metallurgical Control of Intergranular Growth in Nickel-Based Superalloys

Intergranular crack growth in Ni-based superalloys at intermediate temperatures can be controlled through metallurgical modifications in both microstructure and composition. Figure 2.25 demonstrates that microstructural changes through different solution heat treatments can significantly improve crack growth resistance in variants of Alloy 10. Moreover, different crack propagation rates can also be attributed to changes in alloy composition.

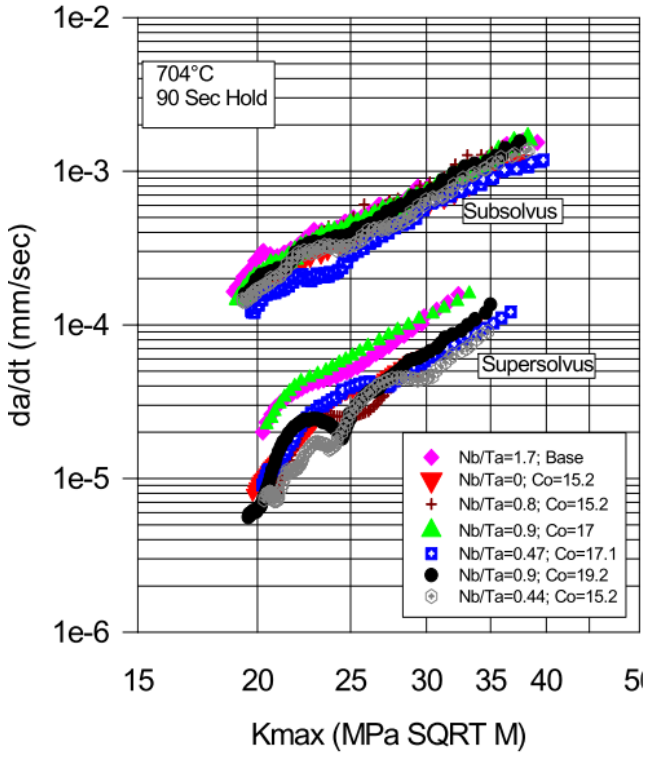


Fig. 2.25 Dwell fatigue crack growth resistance for two microstructural variants – resulting from a subsolvus versus a supersolvus heat treatment – of various chemistry modification based on Alloy 10. Adapted from reference [121].

The first subsection will summarise the microstructural features that influence the crack growth resistance at intermediate temperatures. This includes the γ-grain size,

the γ'-precipitate size distribution and the grain boundary character. Modifications of the alloy microstructure influences the tensile ductility and the ability to relax stresses in front of the crack tip. Crack tip relaxation reduces the driving force for crack propagation and stress assisted diffusion processes. The grain boundary structure directly affects the diffusion and crack path.

Alloy composition influences crack growth through elements which partition to the γ-matrix, the γ'-precipitates and elements which segregate at the grain boundary and/or form grain boundary phases. Alloy chemistry could have an impact on the type and rate of oxide formation at the crack tip. This is shown in the second subsection.

2.3.1 Microstructural Factors

Grain Size

Time-dependent crack growth rates are reported to have a strong dependence on the γ-grain size. Figure 2.26 shows a difference of two orders of magnitude in the time-dependent crack growth rate in Udimet 720 at 650°C in air which was attributed to changes in average grain size [122]. A similar dependence on the grain size was also observed in Astroloy [123], René 95 [58], Udimet 720Li [41, 124], RR1000 [41], Alloy 10 [121] and LSHR [61].

Crack growth tests in Inconel 718 at temperatures between 538 and 650°C identified the same grain size dependence as a result of a so-called necklace microstructure where large grains are surrounded by small grains [125, 126]. These results were confirmed by Osinkolu *et al.* [127]. Improvements in the time-dependent crack growth rate are often attributed to reduced oxidation effects due to the decrease of grain boundary area [41, 123, 127], an increase stress relaxation through grain boundary sliding and

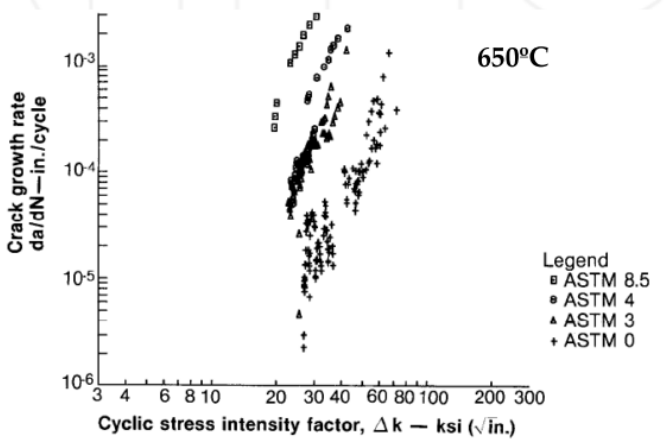


Fig. 2.26 Fatigue crack growth rate as function of grain size in Udimet 720 at 650°C. Adapted from reference [122].

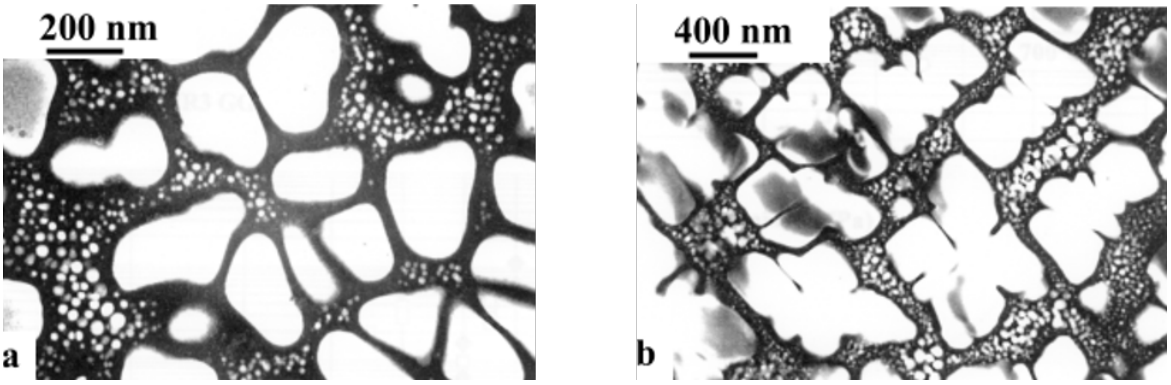


Fig. 2.27 Effects of the heat treatments on the NR3 microstructure: (a) subsolvus heat treatment (b) supersolvus heat treatment. Adapted from reference [39].

enhanced matrix creep deformation [38, 61] which increases the plastic zone size and the crack tip opening distance [128]. Since a coarse grain microstructure is achieved through a supersolvus heat treatment, the grain size is not independent of the γ'-size distribution. Figure 2.27 shows a supersolvus and a subsolvus microstructure, and the relating γ-grain size and γ'-particle size distribution in NR3.

Therefore it has been suggested that the observed improvements in crack growth rate in high γ'-phase volume fraction superalloys are because of changes in the γ'-particle size distribution and not due to changes in grain size [58]. This objection is supported by a study performed on Inconel 718; both the fine and coarse grained

microstructure exhibited similar crack growth rates at 540°C [58]. However, this result could have been influenced by the relatively low test temperature. Everitt *et al.* [41] also concluded that grain size alone cannot account for differences in crack propagation rates across the alloys Udimet 720Li and RR1000. This contradicts Pang *et al.* [124], who concluded for Udimet 720Li that the overall high temperature fatigue performance is governed far more by the γ-grain size than by the γ'-precipitate sizes distribution. This conclusion was based on the fact that a large grain variant of Udimet 720Li demonstrated a significantly improved fatigue life compared to a large intragranular γ'-precipitate variant of Udimet 720Li [124].

γ'-Particle Size Distribution

Differences in the solution heat treatment and the subsequent cooling rate have been shown to influence the crack growth rate substantially (see Figure 2.28).

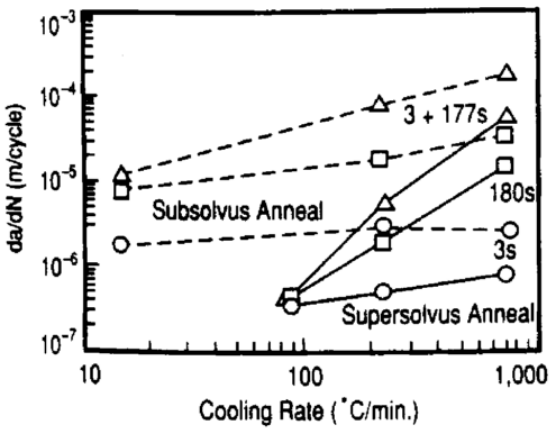


Fig. 2.28 The effect of different cooling rates on crack growth rate in both subsolvus and supersolvus heat treated René 95 at 650°C with $\Delta K = 30$ MPa$\sqrt{m}$. Adapted from reference [58].

During the supersolvus heat treatment the primary γ'-particles at the grain boundary are dissolved,and secondary plus tertiary γ'-precipitates form upon cooling and

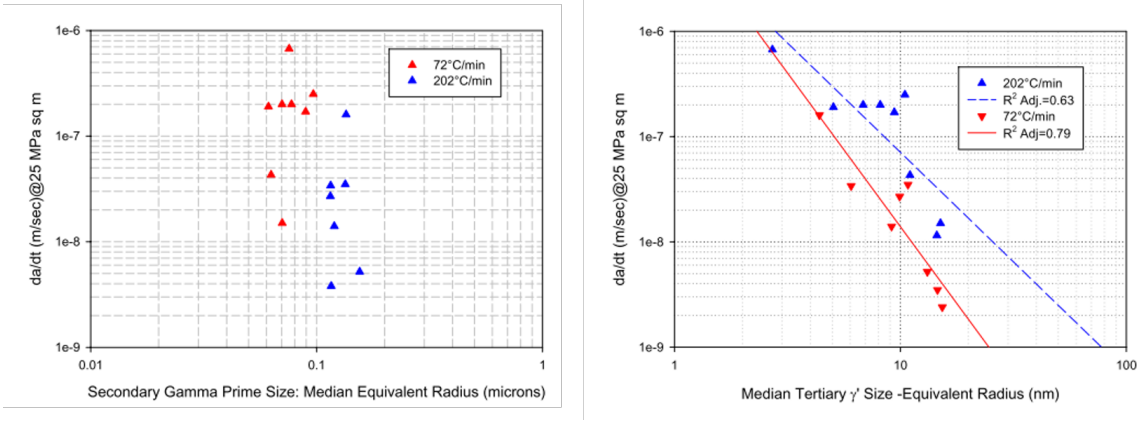


Fig. 2.29 Left: Weak relationship between the secondary γ' precipitate sizes and da/dt. Right: Relationship between the tertiary γ' precipitate sizes and da/dt. Adapted from reference [129].

subsequent ageing heat treatment [43]. Telesman *et al.* [121] performed dwell fatigue tests at 704°C on variations of Alloy 10 and highlighted that the secondary and tertiary γ'-size have a strong effect on the measured crack growth rates. A larger mean size of the precipitates was linked to a better resistance to hold time crack growth in air. A second extensive study on the effect of the secondary and tertiary γ' precipitates size distribution was performed on nineteen different microstructures of LSHR by Telesman *et al.* [129]. The different microstructures were achieved by systematically controlling the supersolvus cooling rate and by applying different single- and double-step ageing anneals. The crack growth resistance at 704°C varied by more than two orders of magnitude. The mean size of tertiary γ' precipitates was found to have the greatest impact. This can be seen in Figure 2.29. Figure 2.29 shows that the size distribution of secondary γ'-particles plays a minor role. Stress relaxation tests showed that the increase in tertiary γ'-precipiate size results in a faster stress relaxation. Dwell fatigue tests performed on variations of RR1000 at 700°C also showed a strong dependence on the size distribution of the tertiary γ'-precipitates [70]. Rapid near-tip stress relaxation induced by tertiary γ'-particles dissolution was reported to be beneficial for RR1000 and Udimet 720Li [130, 131].

These result correspond to the fact that the slowest crack growth rates were observed by Molins *et al.* [74] when the oxygen was introduced at points during a hold time where stress relaxation was assumed to have already taken place. The size distribution of the tertiary γ'-precipitates affects the intrinsic ductility of the material as well as the degree of homogeneity of plastic deformation at the crack-tip [111]. Fast crack tip relaxation leads to a decrease of the crack driving force [129], crack tip blunting and influences the stress assisted diffusion of oxygen along the grain boundaries [108, 129]. This is in agreement with the fact that the hold time crack growth rate is also affected by an overload at the beginning of the dwell period [73]. It is assumed that the overload provides a greater driving force for stress relaxation. Crack tip relaxation is assumed to be dominated by dislocation creep within the bulk of the grains, while contributions from grain boundary sliding was considered to be little or non existing [44, 111, 129].

While there is no direct evidence suggesting that time-dependent crack growth rates depend on the mean size of secondary γ'-particles, there is evidence suggesting that slow cooling rates after a supersolvus heat treatment lead to preferential growth of secondary γ'-precipitates at grain boundaries which lowers the crack growth rates [47, 54, 58, 70, 131–133]. Detailed metallographic analysis on Udimet 720Li showed that the formation and growth γ'-precipitates at the grain boundary cause grain boundary serration [134]. The precipitation of secondary γ'-particles is preferential at random high angle grain boundaries and the serration is increased at grain boundaries with small coincidence due to their relatively high mobility. The amplitude of the serrations is therefore dependent on the misorientation between the to adjoining grains [133]. The introduction of serrated grain boundaries in Inconel 792 was reported to significantly improve the resistance to crack growth at 704°C [47]. Danflou *et al.* [133] studied the crack propagation along serrated grain boundaries in Astroloy at 750°C. The

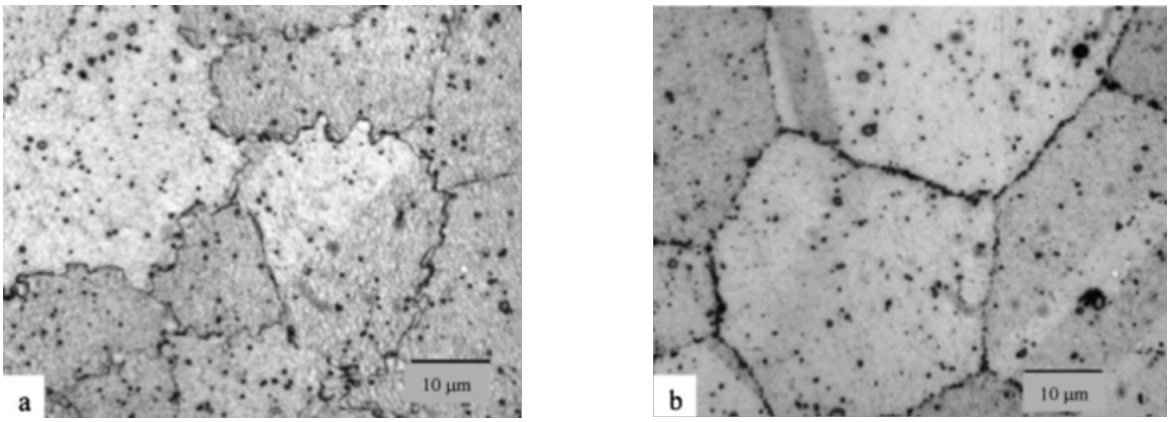


Fig. 2.30 Difference in magnitude of grain boundary serration due to (a) furnace cooled and (b) air cooled. Adapted from reference [121].

material showed a three to five times slower crack propagation rate than Astroloy without serrated grain boundaries. The change in the crack growth rate was solely attributed to the grain boundary morphology since tensile tests at 750°C showed no significant difference in yield stress between the microstructures. This is in agreement with previous findings on Inconel 792 (Figure 2.31) [47].

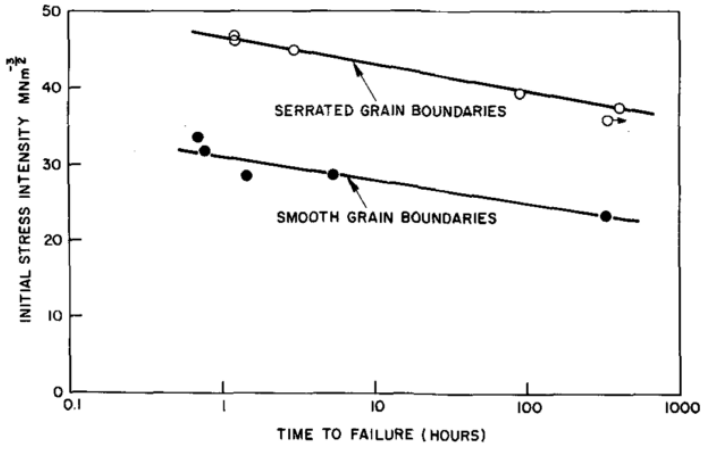


Fig. 2.31 Time to failure at 704°C versus initial stress intensity for Inconel 792 with smooth and serrated grain boundaries. Adapted from reference [47].

Effects associated with serrated grain boundaries could be enhanced crack tip shielding effects [61]; the hindering of boundary sliding due to geometrical reason [133] and longer diffusion and crack propagation paths [135]. In addition, it has been

reported that γ'-precipitates at the grain boundary lead to a local Cr enrichment which accelerates crack tip passivation [58]. This enrichment has been confirmed using atom probe tomography on a Nb-Mo bearing Ni-based superalloy [136]. However, low cycle fatigue tests at 400°C performed on Cr-free René 95 still showed lower crack propagation rates when serrated grain boundaries where introduced through a supersolvus heat treatment [58].

Rice *et al.* [137] performed creep rupture and dwell fatigue tests on Alloy 10 with a serrated grain boundary morphology. While fatigue life was increased, the authors argue that improvements can be mainly attributed to a decrease in the yield stress due to a different γ'-precipitate size distribution. A study performed on NR6 concluded that tertiary γ'-precipitate dissolution in addition to grain boundary serration is the reason for reduced time-dependent crack growth rates [135]. The metastable γ''-precipitates are reported to act as a sink for oxygen if present at the grain boundary [81].

Grain Boundary Structure

In addition to the discussed dependence on the grain boundary morphology, the geometrical structure of the grain boundary has been observed to influence intergranular crack growth resistance.

In Inconel 718, several steps of cold rolling followed by a heat treatment produced a microstructure with an increased fraction of special Σ1-29 grain boundaries. Four-point bending tests performed at 550°C showed a reduced susceptibility of the alloy to environmentally-assisted cracking [102]. The same study showed that grain boundaries with a random character cracked much faster than symmetrical Σ5 tilt grain boundaries (Figure 2.32).

The resistance to intergranular fracture therefore varies locally. This is consistent with work performed on the same alloy which showed that low angle grain boundaries and Σ3 grain boundaries are more resistant to cracking than random high angle grain boundaries in at 650°C [101].

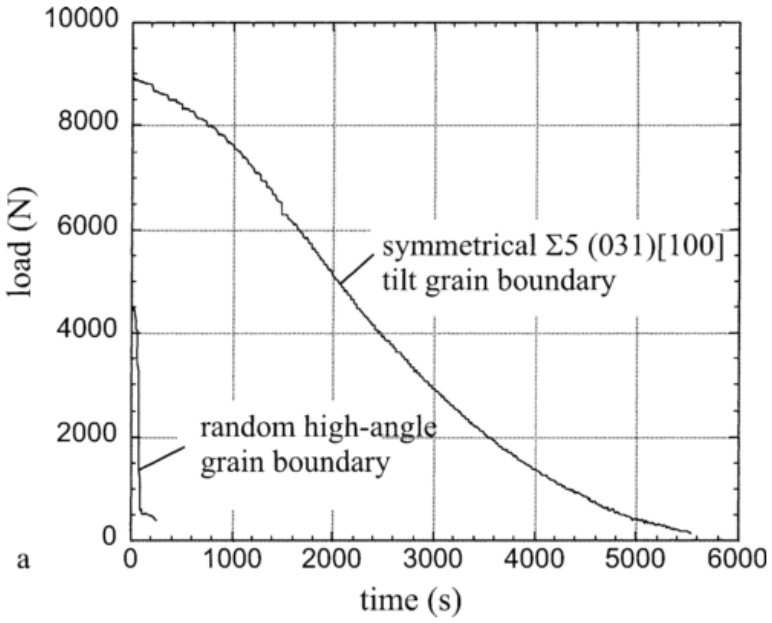


Fig. 2.32 Load-relaxation curves due to cracking of bicrystals with a symmetrical Σ5 grain boundary and a random high-angle boundary at 650°C in oxygen. Adopted from reference [102].

Unocic *et al.* [103] observed an inherent resistance to oxygen embrittlement at 704°C in Allvac 718 Plus for Σ3 and low-angle grain boundaries. It was concluded that by increasing the fraction of special grain boundaries, the susceptibility to intergranular crack propagation can be diminished.

Reasons for the observed damage tolerance is that special grain boundaries, like coherent Σ3 boundaries, have a low concentration of crystalline defects and vacancies which hinders stress-driven grain boundary diffusion and grain boundary sliding at elevated temperatures [77, 138].

2.3.2 Compositional Factors

γ-Matrix Strengtheners

Without Cr additions, Ni-based superalloys are very susceptible to envrironmentally-assisted cracking. A Cr free variant of René 95 exhibited a fatigue life three orders of magnitude less than the standard variant [58]. In Figure 2.33, the time-dependent crack growth rates at 540°C in Inconel 718 variants with different ratios of Cr and Fe are shown. Clearly the chromium content influences long-term fatigue and sustained-load lifetimes [58].

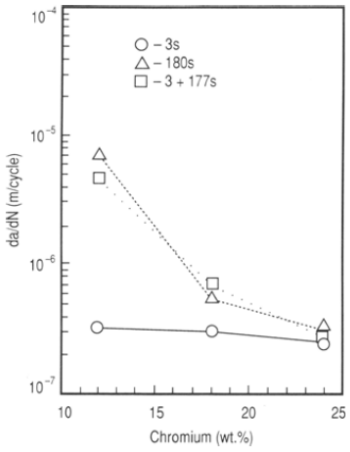


Fig. 2.33 The effect of Cr on the fatigue crack growth rate in Inconel 718 at 540°C with a constant ΔK measured under different fatigue cycles. Adopted from reference [58].

Molins *et al.* [74] studied binary Ni-Cr alloys with 5, 20 and 30 wt-% Cr as well as Inconel 718 and N18. The transition oxygen partial pressure (Figure 2.34) was found to be a function of the alloy Cr content.

The transition pressure increased relative to the Cr content; for the Ni-30Cr alloy, no transition could be determined. It is important to note that in highly-alloyed Ni-based superalloys the Cr content within the γ-grain is dependent on the other alloying elements [139]. Al and Ti, for example, raise the Cr content in the γ-matrix

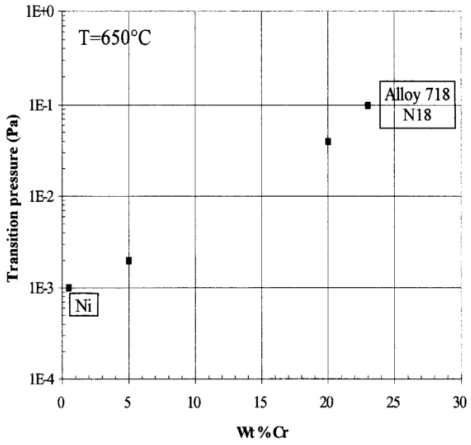


Fig. 2.34 Variation of the transition pressure with the chromium content. Adapted from reference [74].

by removing Ni from the γ-grain to form the γ'-phase. The increase in total Cr also enriches the grain boundaries with Cr [58]. This is believed to provide a better resistance to environmentally-assisted cracking due to the formation of a stable Cr-rich oxide scale at the crack tip. As a result, the oxygen partial pressure decreases and the depth of penetration of oxygen or the size of the wedge shaped oxide decreases [130]. The presence of Cr also suppresses gas forming oxygen-carbon reactions since the Cr_2O_3 reaction is thermodynamically favoured [85].

At high Cr contents, the brittle σ-phase [48, 140], as well as $M_{23}C_6$ carbides and M_3B_2 borides [141], are forming along the grain boundaries. Cr-rich grain boundary precipitates cause a local Cr depleted zone where the material is potentially more susceptible to environmentally induced damage (Figure 2.35).

In addition, the Cr distribution between the γ-matrix and grain boundary precipitates will influence the diffusion of Cr towards the oxidation front [142]. The negative effect of the σ-phase was shown in a study performed on three variants of Alloy 10 with different Cr levels. Needle- and plate-like grain boundary precipitates, presumably the σ-phase, formed and lead to brittle failure in the medium and high chromium alloy

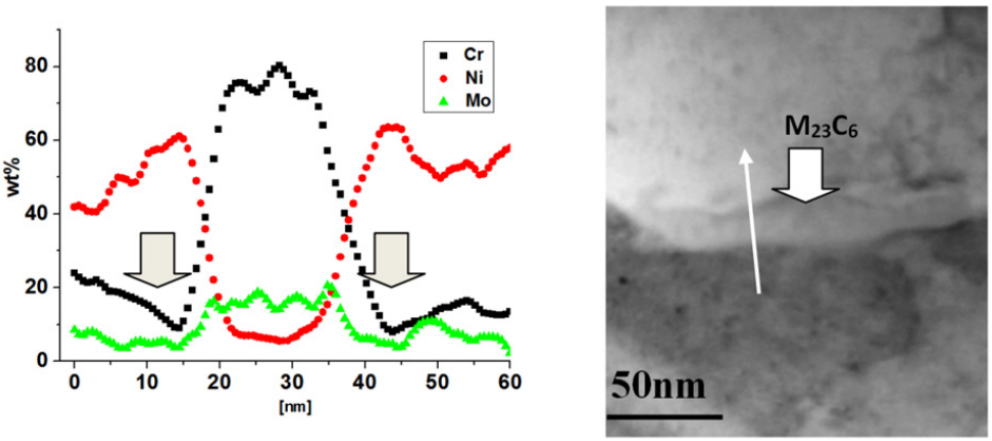


Fig. 2.35 Left: STEM EDX line scan results across $M_{23}C_6$ in a Ni-superalloy revealed a Cr depletion. Right: STEM bright field image of the $M_{23}C_6$. Adopted from reference [28].

[137]. Heavy σ-phase grain boundary decoration in RR1000 leads to an increase in crack growth rate at 725°C [130]. If Cr from the matrix reacts with less-stable MC carbides $M_{23}C_6$ is formed [18, 41]. Mo in RR1000 is reported to have a beneficial effect since it substitutes for Cr in the formation of $(Cr,Mo)_{23}C_6$. The formation therefore causes less Cr depletion at the grain boundary. The excessive formation of $M_{23}C_6$ can be controlled through Hf [140] and Ta additions [67]. Both elements form MC carbides (HfC and TaC) which are relatively stable. In addition, the diffusion of Ta and Hf is slow. Therefore the rate of $M_{23}C_6$ formation is decelerated due to the slow primary carbide decomposition rate [67]. For example, Hf additions in Udimet 720 improved fatigue crack growth rates at 650°C [143]. Figure 2.36 shows the effect of Hf additions in variants of RR1000 [140].

γ'-Precipitate Strengtheners

Al and Ti are the two main elements which lead to the γ'-phase formation – Ni_3(Al, Ti) – in Ni-based superalloys. The volume fraction of γ'-phase can therefore be varied by changing the Al and Ti content in the alloy. The effect of the γ'-phase volume

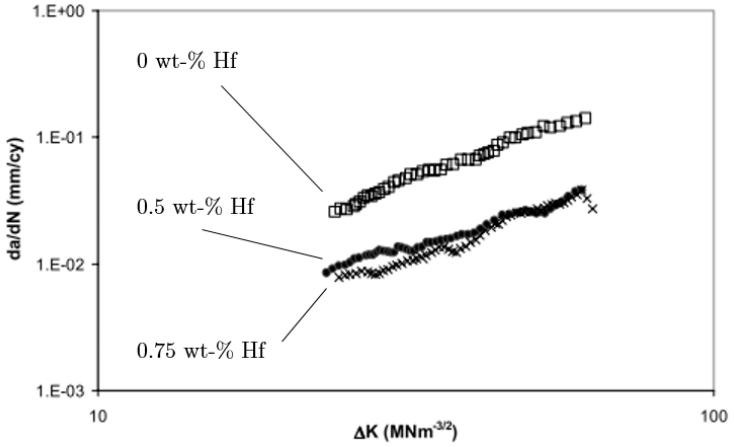


Fig. 2.36 Influence of Hf content on hold time crack growth in RR1000 at 725°C. Adapted from reference [140].

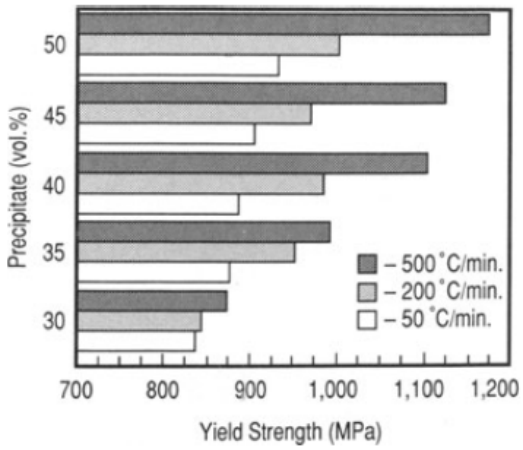


Fig. 2.37 Effect of cooling rate on the 650°C yield stress versus the γ' volume fraction. Adapted from reference [58].

fraction on the fatigue crack growth rate at 650°C in air was studied using a series of superalloys with a fixed-base composition and varied Al and Ti levels [58]. In this study Al and Ti levels were varied to form γ'-phase volume fractions between 30 and 50%. The ratio between the two elements was maintained constant at 1:2. Subsequent to a supersolvus heat treatment, three different cooling rates were applied. Figure 2.37 shows the change in yield strength at 650°C as a function of volume fraction and cooling rate.

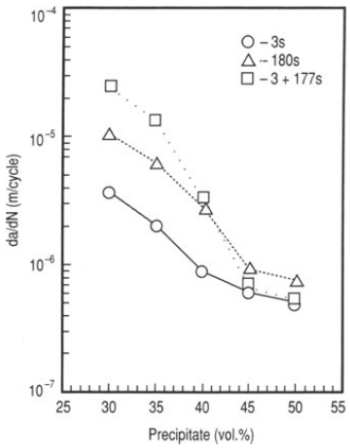


Fig. 2.38 Fatigue crack growth rate as a function of the volume fraction of γ' precipitate for alloys cooled at 50°C/min at a constant ΔK at 650°C measured under different fatigue cycles. Adapted from reference [58].

The measured crack growth rate as a function of γ'-phase volume fraction for alloys cooled at 50°C/min can be seen in Figure 2.38.

Chang *et al.* [58] argued that high γ'-phase volume fractions are beneficial. This was attributed to larger and denser secondary precipitates within the γ-grains and follow the grain boundaries. However, changes in yield stress, overall alloy composition and microstructure were not rationalised in this publication and this result is therefore controversial.

Miller *et al.* [144] suggested that the oxidation of Ti from the Ni_3(Al,Ti) precipitate may contribute to environmentally-assisted cracking. This would explain why intergranular cracking was observed along the incoherent interfaces between the γ'-precipitates and the γ-matrix [145, 146]. Ta increases the stability of γ'-phase and substitutes for Ti. Thus Ta additions could reduce the formation of Ti-rich oxides prior to the Ni_3(Al, Ti) oxidation [67]. Huron *et al.* [147] showed the positive effect of Ta on hold time fatigue crack growth rates at around 700°C (Figure 2.39). As mentioned above, Ta is also a grain boundary modifier, and forms TaC and potentially influences the formation of Cr-rich $M_{23}C_6$ carbides.

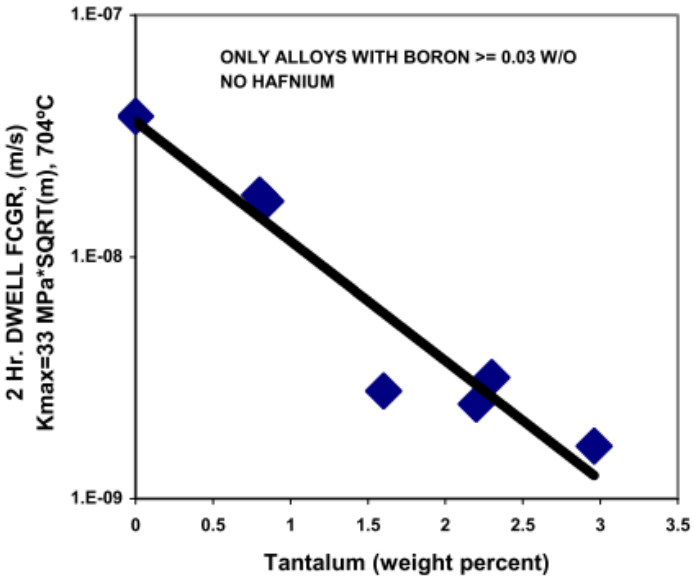


Fig. 2.39 Influence of tantalum content on hold time crack growth at 704°C. Adapted from reference [147].

Some alloys, such as Inconel 718 and 706, form the metastable γ''-precipitate – Ni_3Nb – instead of the γ'-phase. The effect of the Nb-containing γ''-precipitate on environmenatlly-assisted cracking has been studied extensively by Gao, Wei and Miller [35, 144, 148–153] in the past years. Their studies suggested that the Nb content plays an important role in environmentally-enhanced crack growth. It was proposed that Nb is the cause for increased crack growth rates in air due to the brittle failure of Nb_2O_5 oxide films which form at the grain boundaries. These oxide films were assumed not only to be the result γ''-precipitate oxidation but also due to environmental interactions with primary NbC and secondary Nb-rich carbides along the grain boundaries. Wei *et al.* [153] studied three different alloys with 0, 2.5 and 5 wt-% Nb. The base-line composition was similar to Inconel 100. This study showed that the presence of niobium increases the time-dependent crack growth rate in air; while the 0 and 2.5 wt.-% niobium containing alloys had comparable crack growth rates, the alloy containing 5 wt.-% showed an increase. This is shown in Figure 2.40.

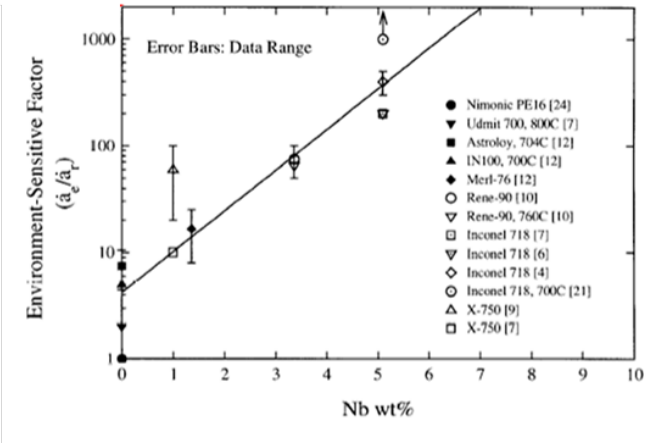


Fig. 2.40 Influence of Nb content on hold time crack growth. Adapted from reference [150].

In a study performed by Telesman *et al.* [121] four variants of Alloy 10 with different Nb to Ta ratios at three Co levels were investigated. All alloys were tested with a subsolvus as well as a supersolvus microstructure. Figure 2.25 shows that the variation in heat treatment has a significant difference in the hold time crack growth rates. The changes in crack growth rate due to compositional changes were regarded as insignificant [121]. However, a change due to composition can be observed mainly in the supersolvus microstructure. An increase in Ta can be attributed to lower crack growth rates. While these compositional effects were not highlighted in the study, they are in agreement with the study which focused on the effect of Ta [147].

Grain Boundary Elements

In polycrystalline Ni-based superalloys, additions of carbon lead to carbide formation along grain boundaries. Carbides along the grain boundary suppress grain boundary sliding and therefore counteract local stress relaxation during creep conditions [53, 67]. In addition, carbides can oxidise readily [154, 155] and it is still unclear whether preferential carbide oxidation is a fundamental factor on the crack tip damage mechanism during oxidation assisted cracking. Alternatively, oxygen could form CO bubbles with

the carbon from grain boundary carbides. As mentioned above, chromium-rich $M_{23}C_6$ carbides are assumed to cause rapid grain boundary oxidation. Nevertheless, there is evidence suggesting that discrete $M_{23}C_6$ particles along grain boundaries are beneficial [156]. Huron *et al.* [147] also showed that the presence of carbides reduces creep and hold time crack growth rates [147]. The effect of carbon on environmentally-assisted cracking is connected with the bulk chemistry and very controversial. While there is evidence suggesting that the presence of specific types of carbides (NbC, TaC, HfC and $Cr_{23}C_6$) have an influence on the time-dependent crack growth rate, the effect of carbide distribution was not shown to be influential. For example, Telesman *et al.* [129] did not observe a relationship between the $M_{23}C_6$ carbide distribution and crack growth resistance in LSHR.

Additions of boron lead to an enrichment of the grain boundary and can lead to the formation of borides at the grain boundary. The effect of boron is generally assumed to be beneficial regarding the overall mechanical properties and time-dependent environmentally-assisted cracking. It has been shown that boron can increase grain boundary interfacial strength [141, 157, 158], decrease grain boundary diffusivity [141, 158] and can modify morphology of carbides and γ' precipitates at the grain boundary [141**?**]. It is generally assumed that the strengthening role of boron is not related to the formation of borides (M_3B_2) [141]. Boron additions above the solubility limit of the grain boundary does not cause further improvement.
Huron *et al.* [147] perfomed a study on variants of the following 12Cr-18Co-4Mo-2Nb-4Al-4Ti-0.030Zr base composition. Boron levels were varied between 0.01 and 0.04 wt-%. In addition, carbon, Mg and Hf levels were modified. In this study, the lowest dwell fatigue crack growth rate was achieved by the combination of high boron and high hafnium content [147]. In Inconel 706, boron and magnesium were found to

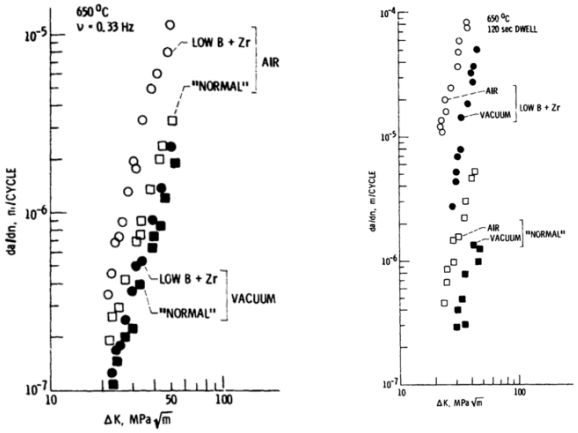


Fig. 2.41 Influence of boron content on fatigue and dwell fatigue crack growth in Waspaloy. Adapted from reference [162].

improve resistance to oxygen-induced intergranular cracking [161]. The effect of grain boundary chemistry on crack propagation rates was studied in a Waspaloy with normal and reduced levels of boron and zirconium. Figure 2.41 show an increase in crack growth rate in the Waspaloy with reduced boron and zirconium content [162]. These observations are in accordance with observations made by Garosshen *et al.* [141].

Boron can completely suppress intergranular failure in air (Figure 2.42). Constant strain rate tensile tests at 600°C were performed on regular Inconel 706 specimen and boronized Inconel 706 specimen by Roesler and Mueller [163]. The regular specimen fractured early and fractography revealed an intergranular failure mode. The boronized test pieces had a significantly higher fracture strain and fractured transgranular in the 150 μm surface region. This study confirms the positive effect of boron on oxidation-assisted cracking and demonstrates that boron can protect the grain boundary form oxygen-induces damage along the grain boundary. This is confirmed by tensile tests on a directionally solidified Ni-based superalloy at 870°C where fracture mode was reported to change from intergranular to transgranular with an increase in boron content [158]. These results indicate that boron strengthens the grain boundary by increasing grain boundary cohesion and is able to inhibit or reduce

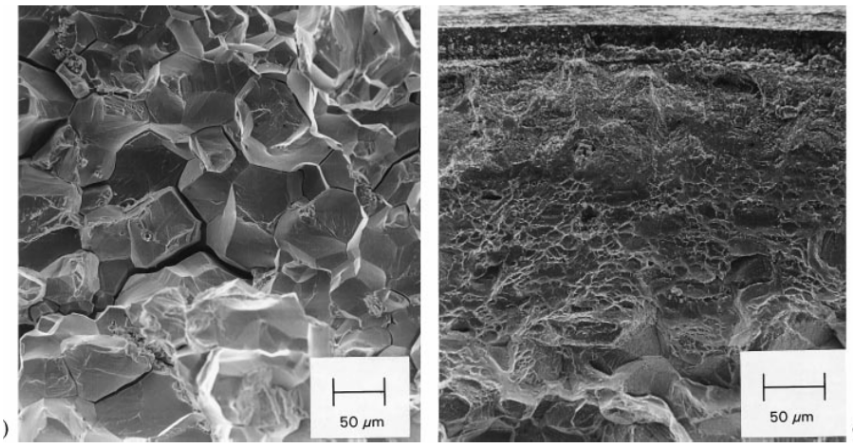


Fig. 2.42 SEM micrographs of the fracture surface after constant strain rate testing. (a) Brittle, intergranular fracture of unmodified Inconel 706. (b) Transition zone of the boronized sample. Adapted from reference [163].

the intergranular oxygen penetration by occupying grain boundary sites. This is in agreement with a study performed by Xiao *et al.* at 650°C on Inconel 718 [164].

Chapter 3

Novel Techniques to Assess Environmentally-Assisted Cracking

Summary A number of drawbacks are associated with conventional mechanical testing methodologies for Ni-based superalloys: (i) a substantial amount of material is needed, which exacerbates cost, (ii) thus for alloy development purposes – when the quantity of material is often limited – it may not be possible to do the necessary range of tests required to assess fully the properties, (iii) it does not always provide sufficient insight into the mechanisms occurring locally, especially on the length-scales of the grains. In this chapter, an electro-thermal-mechanical testing system is introduced and employed. Miniature test specimens of small cross-section of 1×1 mm^2 are used; this allows for rapid mechanical property assessment from small quantities of material. It is demonstrated that time-dependent damage mechanisms in a superalloy can be studied. Micro-cantilever bend tests are conducted at both a virgin grain boundary and at an oxidized secondary crack-tip, thus providing insight into the mechanisms of fracture. These novel methods for mechanical assessment allow the susceptibility of a Ni-based superalloy to environmentally-assisted cracking to be assessed.

3.1 Introduction

Environmentally-assisted crack propagation in polycrystalline Ni-based superalloys is a complicated phenomenon. The fracture mechanisms and electrochemical processes which cause damage span a wide range of length scales, from the electronic-scale right up to the mesoscopic or beyond. It has been established that oxygen is the main damaging species in air which weakens an intergranular crack tip [82]. As turbine entry temperatures continue to rise, damage from environmentally assisted cracking is becoming increasing prevalent; particularly for Ni-based superalloys in their polycrystalline form where environmentally-assisted fatigue crack propagation is becoming life limiting.

Two mechanisms for the time-dependent oxygen-assisted crack propagation processes of importance have been emphasized in the literature: stress accelerated grain boundary oxidation (SAGBO) [74, 108, 115] and dynamic embrittlement [76, 77, 101]). The SAGBO theory emphasises the formation and subsequent brittle failure of a wedge-shaped bulk oxide intrusion at the crack tip. Due to an enhanced diffusion rate along the grain boundary, the crack tip oxide grows into and along it rather rapidly. The imposed tensile stress is assumed to accelerate the oxide formation by accommodating a volumetric expansion during oxide formation [165]. Dynamic embrittlement on the other hand emphasizes the stress-driven diffusion of elemental oxygen along the grain boundary. This second theory emphasizes that intergranular cracking occurs from a reduction in the local cohesive strength followed by decohesion of metallic bonds [166]. In addition, the formation of intergranular oxidation products at the γ-grain boundary ahead of the crack tip, pinning the γ-grain boundary, has been proposed [82].

At present, the susceptibility of an alloy to time-dependent environmentally-assisted

intergranular cracking is typically assessed through the use of low-cycle and dwell-fatigue tests [167]. Application of these tests has been successful in determining the transition from transgranular to intergranular crack propagation to be dependent on the oxygen partial pressure [69, 108, 148], temperature [41, 69, 168], frequency and dwell time [41, 69, 169], alloy composition [41, 147, 164] and microstructure [70, 121, 129]. The effect of oxygen partial pressure and test temperature can be seen in Figure 3.1. However, the complexity of the testing combined with the substantial time and material requirements is somewhat limiting. In addition, it is difficult to isolate controlling factors since both cycle and time-dependent effects, such as stress relaxation and redistribution, are occurring simultaneously at the crack tip during dwell fatigue loading. Alternatively, for a given alloy a first approximation of susceptibility to environmentally-assisted degradation has been recently gained using uniform slow strain-rate tensile tests at elevated temperatures [36, 170]. Gabb *et al.* [36] demonstrated that the inelastic failure strain of slow strain-rate tensile tests can be correlated to the dwell fatigue crack propagation rate. If an alloy has limited elongation during uniform tensile deformation this can be related to a poor resistance to fracture under other loading conditions, such as dwell fatigue – provided comparable rates of deformation are applied.

Although dwell fatigue testing – or slow strain-rate testing – can provide a measure of an alloy's susceptibility to environmental cracking, it can be the case that little insight into the mechanism of cracking can be gained from it without further work. In principle, techniques can be used to examine crack-tip regions of fatigue specimens. Possible methods include transmission electron microscopy coupled with energy dispersive X-ray (EDX) spectroscopy, nano-SIMS and atom probe tomography all of which have been applied to an extent to study this problem [59, 70, 117]. These studies have revealed that often the environmental degradation is occurring

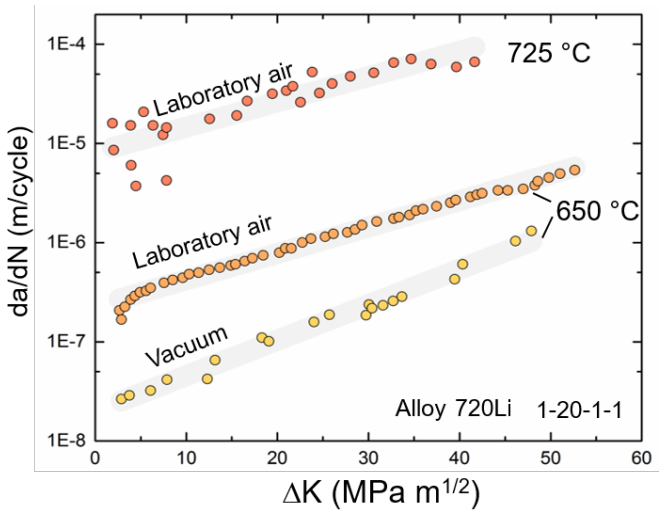


Fig. 3.1 Dwell fatigue crack propagation rates in alloy 720Li in air and in vacuum at 650 and 725°C. 1-20-1-1 indicates a trapezoidal waveform with a 1 second ramp up, 20 s dwell time at maximum load, 1 s ramp down and 1 second at minimum load. Redrawn from [3].

very locally at the sub-micron scale. However, up until now the effect of environmental damage on the local mechanical properties in the region ahead of the crack tip has not been studied. The use of micro-mechanical testing techniques can now be applied to assess mechanical behaviour at the sub-micron scale. Such experiments have been performed elsewhere to understand the failure of oxidized grain boundaries in alloy 600 [171]. These types of test allow site-specific measurements at a sub-micron length scale, and indeed may play a critical role in developing a better understanding of crack mechanisms.

In this chapter, tensile tests are performed between room-temperature and 1000°C in order to study environmentally-assisted cracking in the high strength Ni-based superalloy 720Li. An electro-thermal mechanical testing machine is employed, allowing for the use of miniaturized tensile test specimens. This experimental technique allows for the rapid assessment of mechanical properties using limited amounts of material. In addition, a limited number of conventional slow strain-rate tensile tests were performed for comparison. It is shown that the use of varied strain-rates and atmospheres, both

oxidizing and inert, can be used to capture the transition from time independent to time dependent failure. The mode of fracture is further investigated using advanced high resolution experimental techniques including site specific micro-cantilever bend tests.

In summary, the present chapter addresses the following two questions:

(1) Are miniaturized slow strain-rate tensile tests capable of capturing the temperature and time-dependent effects that occur during environmentally-assisted cracking in a Ni-based superalloy?

(2) Is it possible to perform site-specific micro-mechanical bend tests in order to assess crack propagation within an environmentally induced damage zone at a crack tip?

3.2 Experimental Procedure

3.2.1 Material

The material used in this chapter is alloy 720Li, a cast and wrought Ni-based alloy used for high pressure disk rotors. The nominal composition is given in Table 3.1.

Table 3.1 Nominal composition of alloy 720Li in wt-% (Ni-base).

Alloy	Ni	Cr	Co	W	Mo	Al	Ti	Ta	C	B	Zr
720Li	bal	16.0	15.0	1.25	3.0	2.5	5.0	0.0	0.015	0.015	0.035

Alloy 720Li has a temperature capability of around 700°C [134] and was supplied by Rolls-Royce plc. in the form of a test ring taken from a turbine disc forging. The following sub-solvus heat treatment was applied: a solution heat treatment at 1095°C for 4 hours followed by an oil quench and a subsequent ageing heat treatment at 760°C for 16 hours. Figure 3.2 (a) shows the as-received microstructure of alloy 720Li prior to testing. This region was investigated using EBSD in order to calculate the γ-grain and primary incoherent γ'-precipitate size distribution, see Figure 3.2 (b). A Gaussian non-linear curve fit was applied in order to distinguish the average γ-grain size, $d_\gamma \approx 8 \pm 3\,\mu$m, and the average intergranular primary γ'-precipitate size, $d_{\gamma'} \approx 4 \pm 0.5\,\mu$m. The size of these intergranular primary γ'-precipitates can be determined using EBSD because their incoherency results in a crystal orientation which differs from the adjoining γ-grains. The measured average γ-grain and primary γ'-precipitate size is in close agreement with previous microstructural assessment of Alloy 720Li [127, 172–174]. The mean diameter of the intergranular secondary γ'-precipitates which are shown in Figure 3.2 (c) was found to be $\approx 100\,$nm

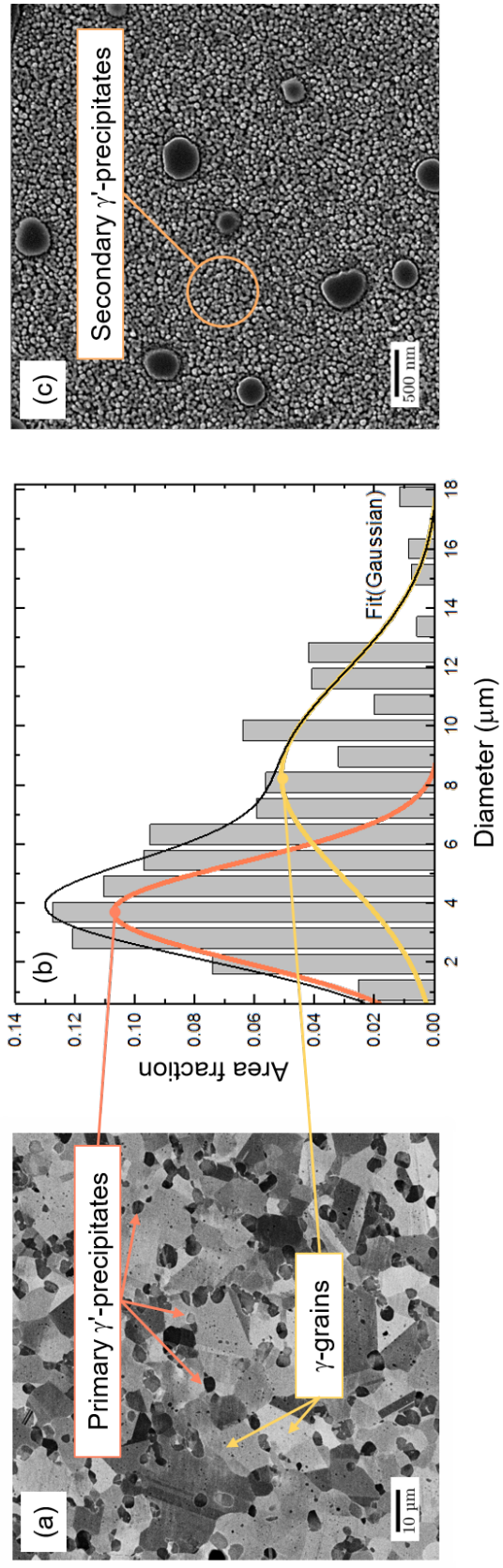


Fig. 3.2 (a) Backscattered electron image of the microstructure of alloy 720Li consisting of γ-grains and incoherent intergranular γ'-precipitates used in this study. (b) Measured size distribution using EBSD including two Gaussian type fits to determine the γ-grain and incoherent intergranular primary γ'-precipitate size distribution and the overall cumulative fit. A total number of 2443 grains were measured. (c) SEM image of a γ-grain after electro-chemical etching in 10% phosphoric acid showing smaller coherent intragranular primary and secondary γ'-precipitate.

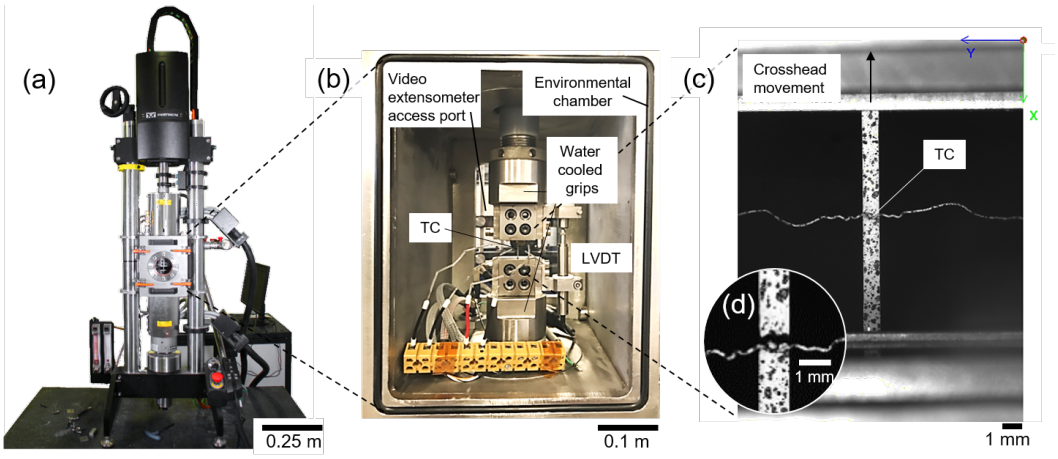


Fig. 3.3 (a) Overview of high stiffness load frame which acts as the mechanical platform for the ETMT system. (b) Inside of the environmental test chamber including a test piece within the ETMT gripping arrangement. First (c) and last frame (d) captured by the DIC camera which is employed to calculate strain during crosshead extension. Deformation and failure occurs in the center of the test piece where temperature is localised.

3.2.2 Electro-Thermal Mechanical Testing

Tensile testing using miniaturised test pieces was conducted on a Instron electro-thermal mechanical testing (ETMT) machine. The ETMT system was initially developed by NPL [175–177] and is now manufactured by Instron under licence. The basic ETMT system is shown in Figure 3.3 and comprises of the following parts:

(1) An environmental chamber with electric lead-throughs and water cooled sample grips mounted to a high stiffness load frame.

(2) A computer controlled direct resistance sample heating which utilises a 400 A, 8 V direct current power supply with thermocouple feedback.

(3) A 5 kN load cell and displacement transducer with a sub-micrometre resolution and 7 mm range together with a computer controlled motor displacement control.

More detailed information related to the developement of the ETMT equipment can be found elsewhere [177]. Tensile testing was conducted between room temperature and

1000°C on this Instron ETMT machine. Miniaturised specimens of cross-section 1×1 mm^2 and a gauge length of 14 mm were used; the full sample length was 40 mm. The specimens were produced using wire-based electrical discharge machining (EDM), with surfaces subsequently ground to 1200 grit finish using silicon carbide grinding paper to maintain a consistent surface finish and to remove the recast layer resulting from the EDM process. Figure 3.4 shows a typical ETMT tensile test piece used throughout this thesis. Temperature measurement during testing was achieved by spot-welding a K-type thermocouple to the central portion of the specimen gauge. Slow strain-rate tests were performed in laboratory air with an initial slow strain-rate close to $1{\cdot}10^{-4}\,s^{-1}$. These were conducted at room temperature, 400, 500, 600 and between 700 and 1000°C in steps of 50°C. Consistent with the design of the ETMT machine, specimens were heated using electrical resistance by passing a direct current through the specimen. Tests were performed at a constant extension rate using a linear variable displacement transformer (LVDT). This approach will be further discussed in Section 3.4.1. The engineering strain was used as a measure of the ductility; engineering strain is defined as:

$$\varepsilon = [(L_f - L_0)/L_0] \quad , \tag{3.1}$$

where the gauge length extension $L_0 - L_f$ was monitored using digital image correlation (DIC) following a thermal paint pattern in the central 5 mm of the specimen (see Figure 3.3 (c) and (d)). An Imetrum DIC package was used for this purpose operating at 1 Hz which was connected to the Instron load cell for accurate engineering stress-strain measurements in real time with a strain resolution of 20 microstrain. For a nominal gauge length of 5 mm this leads to a resolution of 0.1 μm.

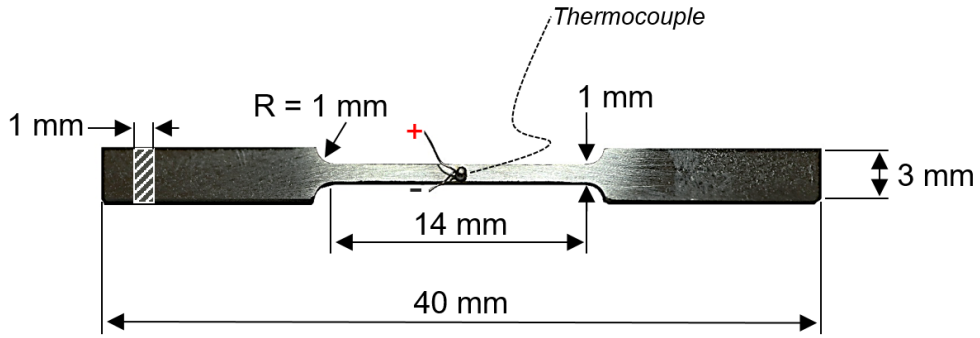


Fig. 3.4 Miniaturised specimens with a cross-section of 1×1 mm^2 and a gauge length of 14 mm. Spot-welded K-type thermocouple for temperature control in the center of the gauge length.

Further testing was carried out at 750°C using a variation of initial strain-rates – close to $1{\cdot}10^{-2}$, $1{\cdot}10^{-3}$, $1{\cdot}10^{-5}$ and $1{\cdot}10^{-6}$ s^{-1} – in laboratory air to assess the rate dependency. Slow strain-rate tensile testing was also conducted in argon at 800°C. This was achieved by evacuating the environmental chamber to $\approx 5{\cdot}10^{-2}$ mbar vacuum and then backfilling the with inert argon gas.

3.2.3 Conventional Tensile Testing

A 200 kN Instron 8862 servo electric system was used to test conventional threaded round tensile specimens with a gauge diameter of 4 mm and a gauge length of 24 mm (Figure 3.5 (a)). Tensile tests were conducted in laboratory air with an initial slow strain-rate close to $1{\cdot}10^{-4}$ s^{-1} per ASTM E8M and E21 [178, 179] at the following specific temperatures: room temperature, 500, 700 and 900°C. A constant cross head extension rate was used after soaking the specimen for 30 minutes at the test temperature. The temperature was monitored at all times using a K-type thermocouple inside the furnace close to the test piece as shown in Figure 3.5 (b). The engineering strain was used as a measure of the tensile ductility; engineering strain is defined by

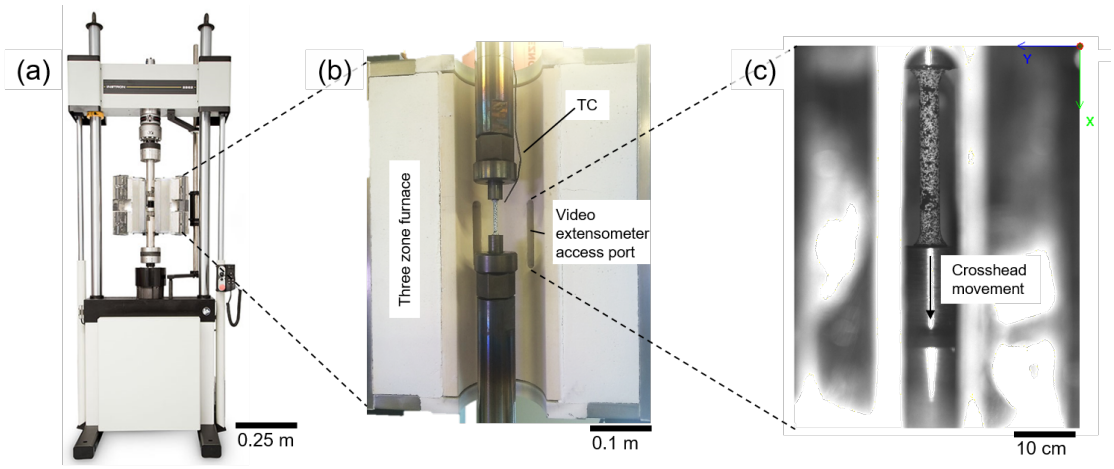


Fig. 3.5 (a) Overview of Instron 8862 servo electric platform. (b) View into the three zone furnace used in this study. (c) DIC camera view.

Equation 3.1. The gauge length extension was monitored using digital image correlation following a random thermal paint pattern along the gauge length of the sample using the same DIC set-up used for the ETMT, see Figure 3.5 (c).

3.2.4 Mirco-Mechanical Bend Testing

Micro-cantilever bend tests were performed on the as-received alloy 720Li and also on the ETMT specimens failed at 800°C in air using slow strain-rate testing. Micro-cantilevers were prepared using focused ion beam (FIB) milling using the method described in [171]. Cantilevers with a triangular cross section were prepared using a FIB 200-TEM instrument, the cantilever was 3 μm wide by 14 μm long. For the as-received alloy, micro-cantilevers where prepared such that a grain boundary was located in at the base of the cantilever where bending stresses are highest. For the failed ETMT specimen micro-cantilevers were prepared at secondary cracks which propagated from the fracture surfaces of the failed specimen. This secondary crack was located in the base of the cantilever. To reveal these secondary cracks the sides of the failed ETMT specimen were ground back using silicon carbide paper followed

by three polishing steps, finishing with a 1 μm diamond polish. A final three minute active oxide polishing step using colloidal silica was applied.

Site specific micro-mechanical tests were performed at room-temperature using a G200 Agilent Nano Indenter system with a diamond Berkovich tip. Prior to testing, the micro-cantilevers were scanned using the diamond Berkovich tip in contact mode. This produces a topographical map of the sample and allows an accurate alignment of the Berkovich tip with the free end of the micro-cantilever. Micro-cantilevers were displaced at a constant rate of 5 nm/s.

3.2.5 Analysis Methods

The microstructure of alloy 720Li before and after testing was primarily characterized through secondary and backscatter electron imaging mode on a JEOL 6500F FEG scanning electron microscope (SEM). Observation of the fracture surfaces following mechanical testing was carried with a three dimensional optical metrology on an Alicona optical microscope. Fractography was supported by secondary electron imaging and high resolution energy-dispersive X-ray spectroscopy using a Zeiss Merlin SEM equipped with an Oxford instruments Xmax 150 detector.

3.3 Experimental Results

3.3.1 Miniaturised Tensile Tests

The stress-strain behaviour was measured using slow strain-rate tests, with an initial strain-rate close to $1{\cdot}10^{-4}$ s^{-1}, in laboratory air between room temperature and 1000°C (see Figure 2). The observed deformation behaviour of alloy 720Li is in good agreement with previous studies performed on this material [173, 174]. Between room temperature and 700°C the 0.2 proof stress was found to change by approximately 100 MPa. Beyond 700°C a substantial drop in 0.2 proof stress is observed. Between room temperature and 700°C measurement of the ultimate tensile strength (UTS) was possible, at 750°C and beyond it was not possible to attain a measurement of the UTS due to the absence of work hardening.

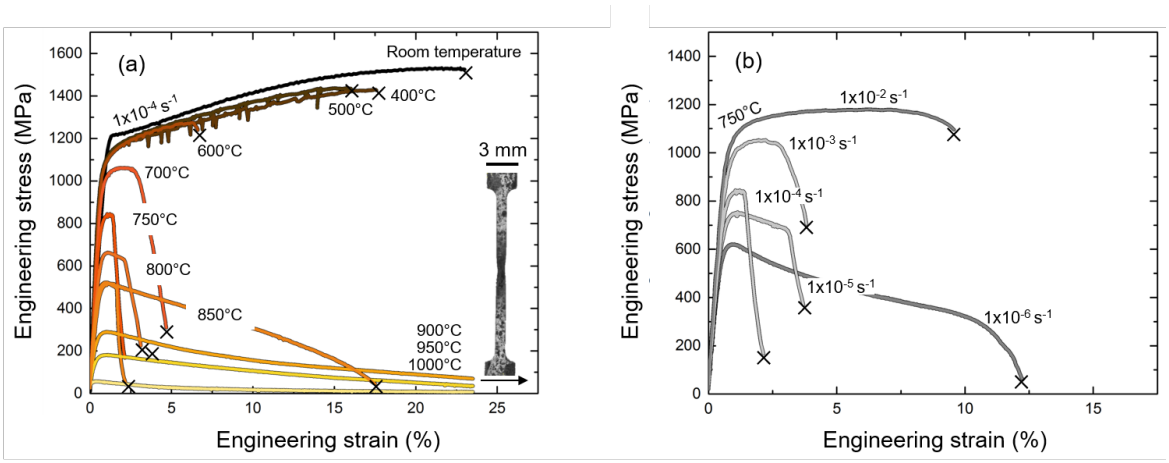


Fig. 3.6 (a) Representative stress-strain curves for alloy 720Li between room temperature and 1000°C at an initial strain-rate close to $1{\cdot}10^{-4}$ s^{-1}. Between 900 and 1000°C tests were stopped after 24% engineering strain due to the pronounced development of a neck. Corresponding individual stress-strain curves are shown in the Appendix A. (b) Representative stress-strain curves for alloy 720Li at 750°C at an initial strain-rate between $1{\cdot}10^{-2}$ and $1{\cdot}10^{-6}$ s^{-1}.

The percentage elongation was used as a measure of the ductility; Percent elon-

gation is defined by Equation 3.1 as $\%EL = [(L_f\text{-}L_0)/L_0]\cdot 100$, where L_0 is the initial gauge length and L_f is the gauge length of the gauge section at fracture [180]. Percent elongation is therefore defined as engineering strain. Between room temperature and 500°C no significant loss of ductility is observed. The ductility drops significantly between 600 and 850°C, reaching a minimum at 750°C. Above 850°C the ductility of the material is fully restored. The observed loss and regain of percent elongation will be addressed hereon with the term ductility dip. The temperature dependence of the tensile ductility summarized Figure 3.6 (a). A critical temperature regime where tensile ductility is limited by quasi-brittle failure can be identified.

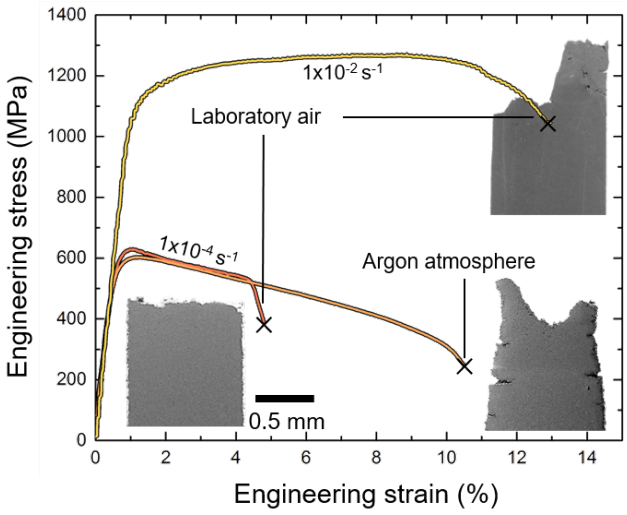


Fig. 3.7 Representative stress-strain curves for alloy 720Li tested at 800°C in laboratory air using a slow and a fast strain-rate and when tested in an argon environment. SEM images of the samples after failure demonstrate the failure mode. Corresponding individual stress-strain curves are shown in the Appendix A.

The strain-rate dependency of alloy 720Li at 750°C is shown in Figure 3.6 (b). As the strain-rate decreases the 0.2% proof stress was found to decrease, a variation of ≈ 500 MPa was observed between the fastest and slowest strain-rates. In comparison to the intermediate initial strain-rates ($1\cdot10^{-3}$ to $1\cdot10^{-5}$ s^{-1}) the percentage elongation increased when a fast initial strain-rate ($1\cdot10^{-2}$ s^{-1}) and a very slow ($1\cdot10^{-6}$ s^{-1}) was

applied. A critical strain-rate regime at 750°C where tensile ductility is limited by quasi-brittle failure can be identified.

Conducting slow strain rate tests in an inert argon gas atmosphere resulted in a substantial change in percent elongation to failure. In laboratory air at 800°C percentage elongation to failure was only 3.8 ± 1.6%. When the atmosphere was changed to argon the percentage elongation to failure was 13.4 ± 0.2 %, see Figure 3.7. While there is a clear effect of environment on the percent elongation, the 0.2% proof stress was found to be unaffected. Tests performed at 800°C using a fast initial strain-rate close to $1{\cdot}10^{-2}$ s^{-1} also showed a significant increase in percent elongation. This effect of deformation rate and environment at 800°C is shown in Figure 3.7.

3.3.2 Conventional Tensile Tests

The stress-strain behaviour measured using conventional tensile test pieces, with an initial strain-rate close to $1{\cdot}10^{-4}$ s^{-1}, in laboratory air at room temperature, 500, 700 and 900°C is summarised in Figure 3.8.

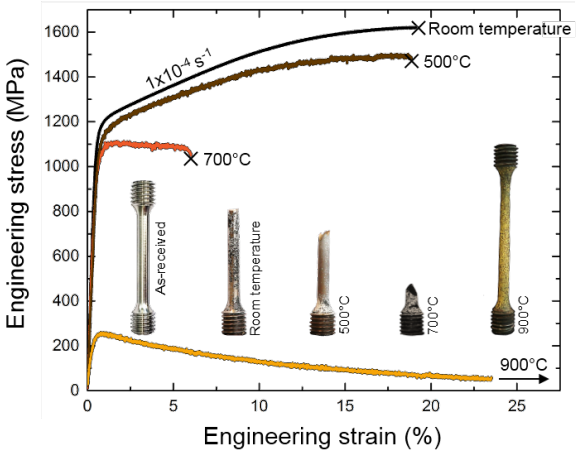


Fig. 3.8 Representative stress-strain curves for alloy 720Li tested at room temperature, 500, 700 and 900°C in laboratory air using a slow initial strain-rate close to $1{\cdot}10^{-4}$ s^{-1}. Images of the samples after failure demonstrate the regain of tensile ductility at 900°C.

Percent elongation remained unchanged, around 19%, at room temperature and 500°C. At 700°C tensile ductility is significantly reduced to 6.1%. At 900°C the ductility of the material is restored and the tensile test was stopped after an percent elongation of 24% was reached.

3.3.3 Fractography

Scanning electron microscopy (SEM) was used to examine the cross section perpendicular to the fracture surface of failed ETMT specimens. Depending on the test conditions either quasi-brittle or ductile failure was observed; examples of the cross-section for both modes of failure are shown in Figure 3.7. Quasi-brittle failure occurred during slow strain-rate testing at temperatures between 600 and 850°C in laboratory air. Necking of the sample was not observed during quasi-brittle failure. This is in contrast to the ductile cup-and-cone type failure shown in Figure 3.7. Ductile failure was observed during slow strain-rate tests in air below 600 and above 850°C. In addition, quasi-brittle failure was observed at 750°C when an initial strain-rate of $1{\cdot}10^{-3}$, $1{\cdot}10^{-4}$ and $1{\cdot}10^{-5}$ s^{-1} was applied.

Fractographic analysis of the fracture surface performed at lower magnifications using optical metrology shows surface initiated environmental damage. Figure 3.9 shows the fracture surfaces of specimens tested in air using the slow strain-rate at 600, 700, 750, 800 and 850°C. An increase in environmental damage can be observed on the fracture surfaces with increasing temperature. In the regions of the fracture surface where environmental-damage was observed failure was found to be intergranular. Regions without signs of environmental damage failed in a transgranular fashion; dimples and micro voids were observed in these regions. SEM observations showing a intergranular fracture surface is demonstrated in Figure 3.10. The transition from

intergranular to transgranular cracking at 600 and 700°C was found to be abrupt. At 800°C the entire fracture surface of the ETMT specimen showed environmental damage, thus only failure due to intergranular cracking was observed. This observation is supported by the flat fracture surface perpendicular to the load axis in the environmentally damaged regions and the presence of a shear lip where transgranular failure occurred. At 850°C test pieces failed either due to intergranular cracking or due to transgranular tearing thus marking a brittle-to-ductile transition temperature if a slow strain-rate of $1{\cdot}10^{-4}$ s^{-1} is applied.

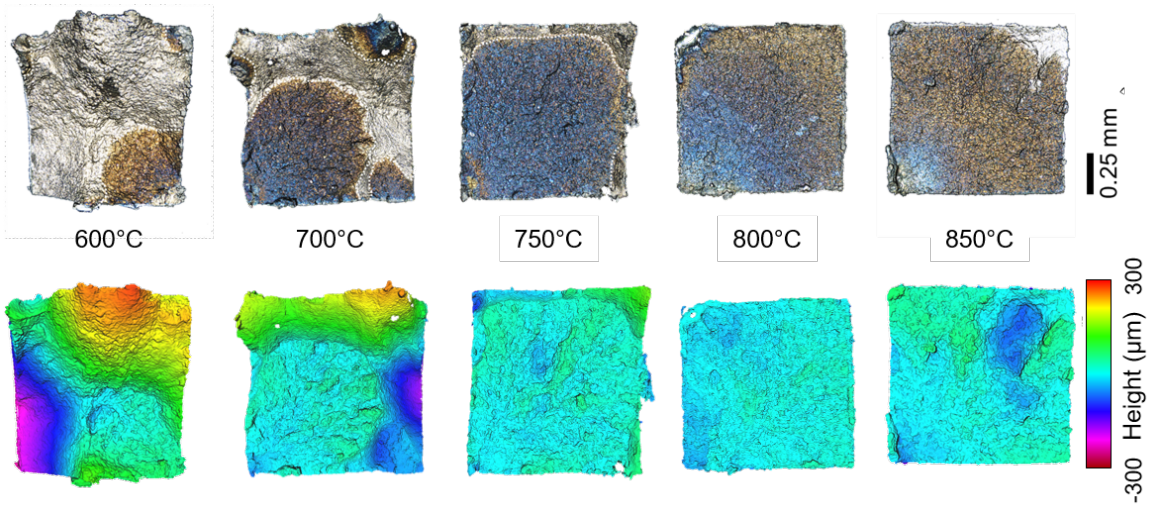


Fig. 3.9 Optical microscopy images showing representative fracture surfaces of specimens failed between 600 and 850°C. Surface initiated environmental damage can be seen and distinguished from undamaged regions on the fracture surface. The environmental damage on the fracture surface increases with temperature.

As shown in Figure 3.10 (a) multiple secondary cracks branch off the primary crack which led to failure. In order to investigate these secondary cracks that initiated during slow strain-rate testing at 800°C, samples were prepared using the procedure describe in the previous section. Secondary cracks were consistently found at incoherent primary γ'-interfaces and are therefore the preferred sites for crack initiation. The secondary crack path was found to be purely intergranular. Figure 3.10 (b)-(e) sug-

gests that the primary γ'-precipitates play a key role in environmentally assisted-crack propagation in alloy 720Li.

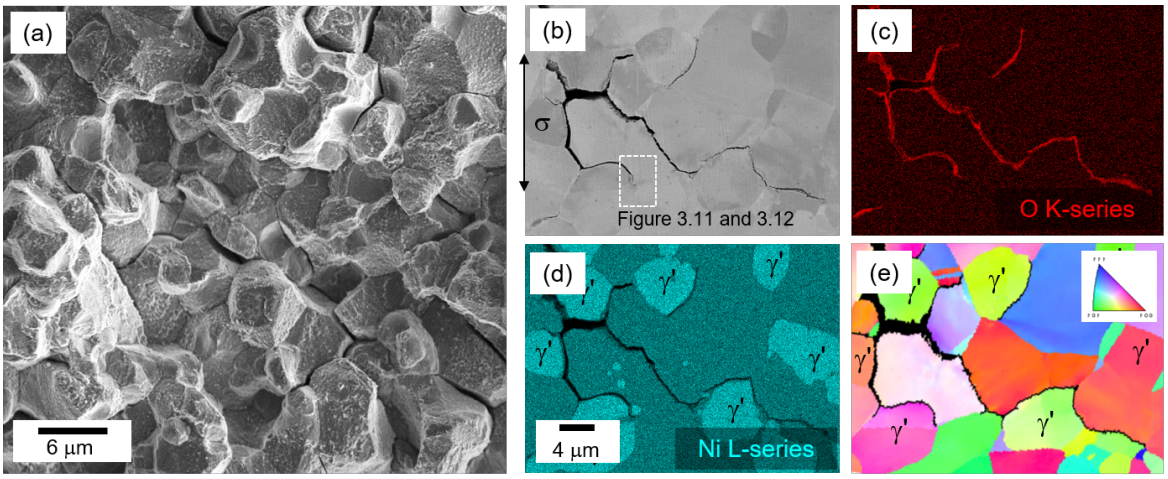


Fig. 3.10 (a) Secondary electron image of a intergranular fracture surface at 800°C. Grain contours can be clearly identified. (b) Interganular secondary cracks close to the fracture surface at 800°C. Cracks which propagated primarily along high angle g-grain boundaries and incoherent primary γ'-interfaces are filled with oxidation products. These observations were confirmed using EDX mapping (c), (d) and EBSD (e).

Energy dispersive x-ray mapping showed that the cracked grain boundaries are decorated with oxides. Sub-micron sized oxides were found at the secondary crack tips. While limitations such as (i) additional signals from the bulk of the specimen, (ii) the surface topography at the crack tip and (iii) the overlap of the oxygen K-series with the chromium L-series have to be considered, the oxide intrusions were found to be layered. A nickel enriched region was found in the middle of the oxide intrusion (see Figure 3.12 (c)). Along the γ-grain boundary a chromium enrichment was detected, whilst primary γ'-interfaces had slight increases in titanium and aluminium.

3.3.4 Micro-Mechanical Bend Tests

The local mechanical properties at the oxidized crack tip shown in Figure 3.10 (b) was investigated using micro-cantilever bend tests at room temperature. Loading of the cantilever was achieved using a nanoindenter. A micro-cantilever was prepared with the shown bulk oxide intrusion shown in Figure 3.11 (a) close to the fixed end of the cantilever. Upon loading a fracture event was observed after the onset of plasticity, Figure 3.11 (b). A second displacement of the bend micro-cantilever confirmed that the crack has arrested. The fracture event observed in the stress-displacement curve can be associated with the fracture of the bulk oxide ahead of the crack tip. The failed crack tip oxide is shown in Figure 3.12 together with images of the oxide intrusion before failure.

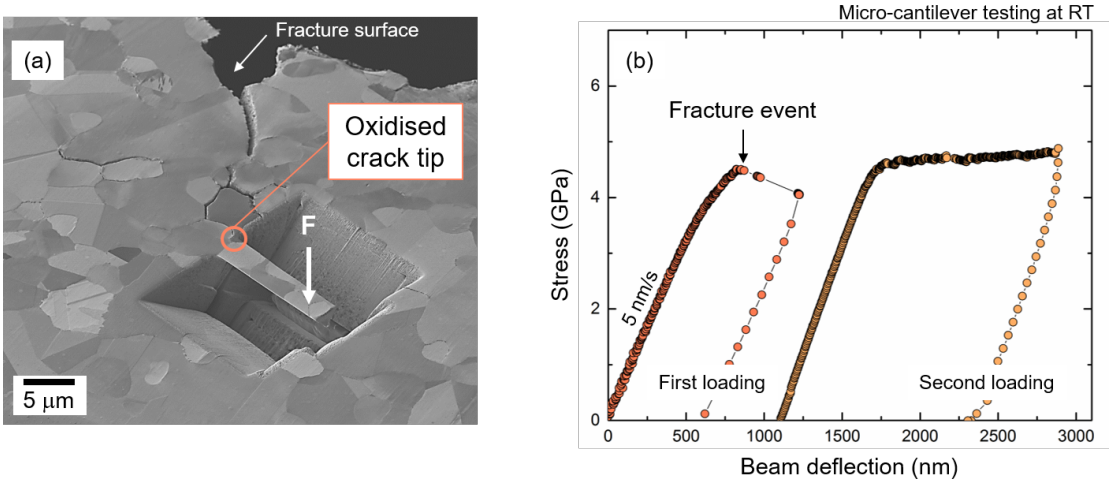


Fig. 3.11 (a) Microcantilever close to the fracture surface containing an environmentally-damaged grain boundary close to the fix end. (b) Stress-displacement curve of the micro-cantilever containing environmental damage close to the fixed end.

The crack propagated under the applied tensile stress from the crack tip through the nickel-rich inner layer of the crack tip oxide. The oxide/metal interface (aluminum, titanium and chromium-rich oxides) was not observed to crack. In addition, slip lines are observed on the surface close the oxide indicating a degree of plastic de-

formation within the grains at room temperature. For comparative purposes a second cantilever was prepared at a grain boundary in the virgin alloy 720Li i.e. there was no environmental damage. The micro-cantilever contained a random high angle γ-grain boundary close to the fixed end, see Figure 3.13 (a).

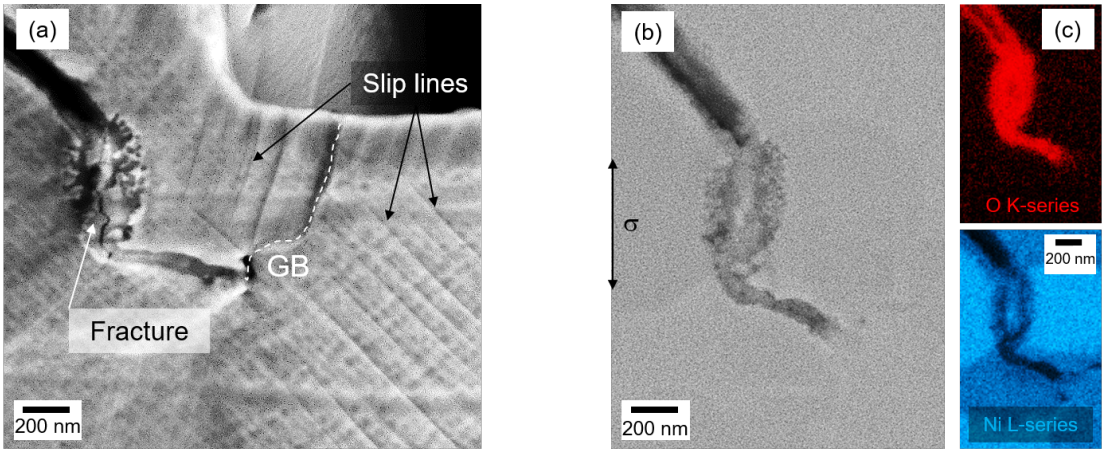


Fig. 3.12 (a) Secondary electron image after the micro-cantilever bend test. A crack is observed to grow though the inner layer of the crack tip oxide. (b) Energy selective backscatter electron image and (c) high resolution EDX map of the environmentally-induced damage zone at and ahead of a secondary crack tip in alloy 720Li prior to testing.

The stress-displacement curve is shown in Figure 3.13 (b). No fracture events were observed and the micro-cantilever deformed plastically. Differences in flow stress are attributed to anisotropic behavior of the individual γ-grains close to the fixed end. In the undamaged micro-cantilever the reductions in stress are attributed to individual slip events, which are being activated. Slip lines were visible on the surface and the micro-cantilever was bent after unloading.

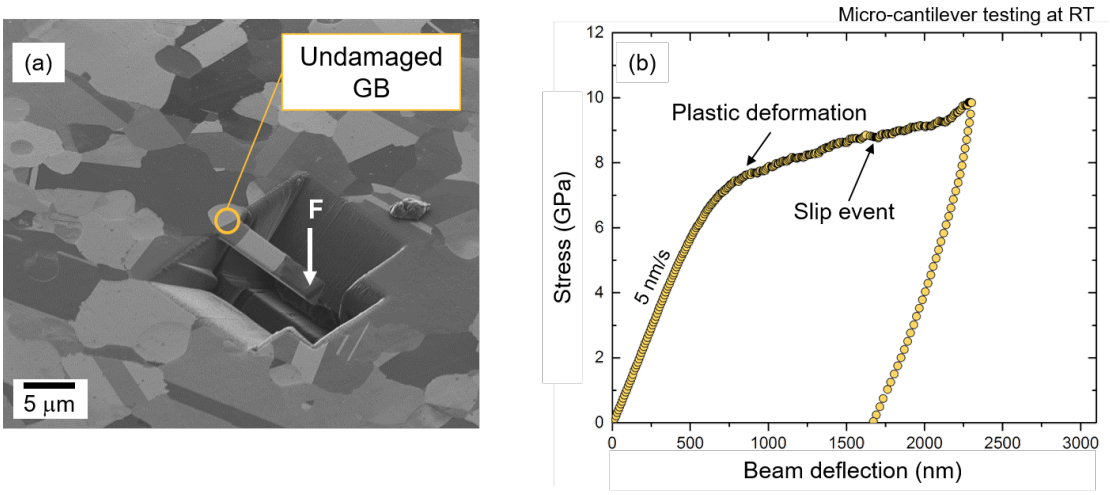


Fig. 3.13 (a) Microcantilever in the as-received alloy 720Li containing an undamaged grain boundary close to the fix end. (b) Stress-displacement curve of the micro-cantilever.

3.4 Discussion

3.4.1 Miniaturized ETMT Tensile Tests

The 0.2% proof stress data obtained from ETMT tests for alloy 720Li was found to be close to the results presented in this work from conventional tensile testing and published data from conventional tensile tests which were performed per ASTM E8M and E21 [134, 173, 181]. A comparison is shown in Figure 3.14.

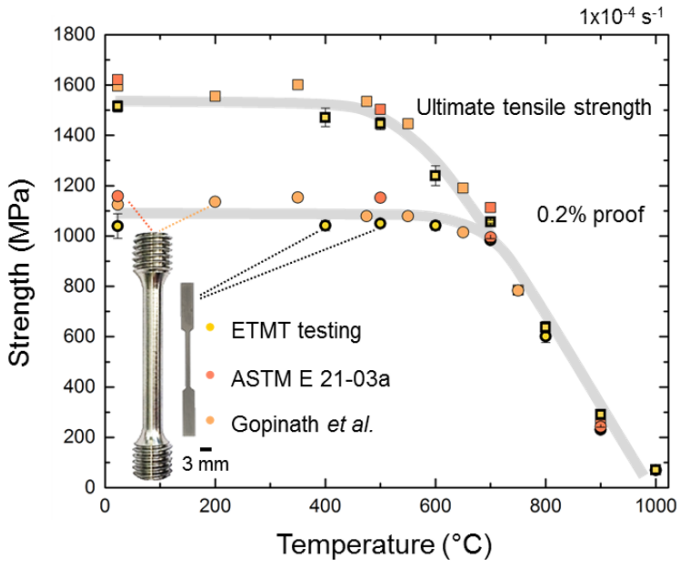


Fig. 3.14 Temperature dependent strength of alloy 720Li at an initial strain-rate of $1{\cdot}10^{-4}$ s^{-1}. The ETMT yield stress and ultimate tensile strength is compared against data from conventional tensile tests from this work and data available in literature from Gopinath *et al.* [173].

Small variations in the 0.2% proof stress can be attributed to differences due to the processing and heat treatment history. Differences for example in the cooling rate from the solution heat treatment are known to affect the properties of alloy 720Li significantly [43]. Therefore, it is demonstrated that miniaturized ETMT tests are able to rapidly assess the flow behavior of a superalloy; this is particularly useful for alloy development purposes. Moreover, at room temperature the total percent elongation is

in good agreement with data reported already in the literature [173, 174]. However, the average measured total percent elongation to failure at high temperatures was found to be relatively small compared to the results from conventional tensile tests (see Figure 3.15) and to the results presented by Gabb *et al.* [36] who used conventionally sized tensile specimens for slow strain-rate tests at comparable conditions.

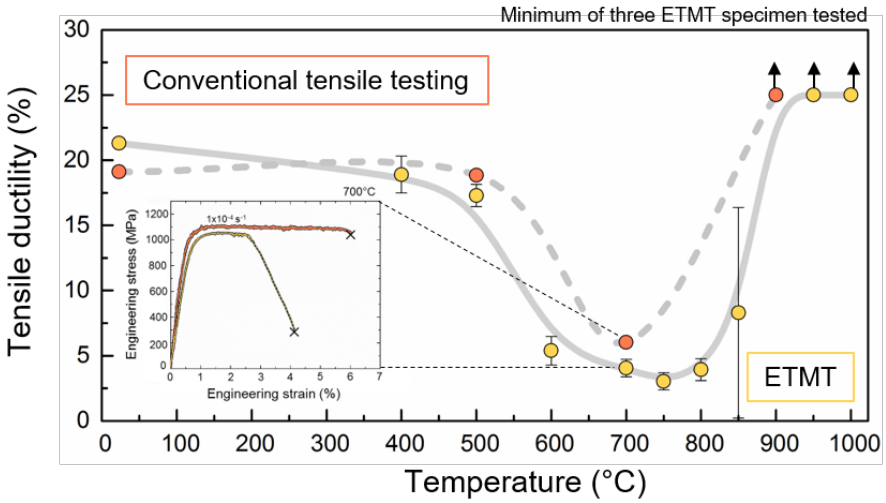


Fig. 3.15 Temperature dependent ductility of alloy 720Li at an initial strain-rate of $1{\cdot}10^{-4}$ s^{-1}. Results obtained from conventional tensile tests are compared to ETMT tests.

The following is important to acknowledge. When miniaturized tensile tests are performed at high temperatures, two effects on the percent elongation have to be considered: (1) the parabolic temperature distribution along the specimen gauge length and (2) the increased surface-to-volume ratio relative to conventional specimen.

The heating current induces a parabolic temperature distribution along the specimen because of the water-cooled gripping arrangement. This temperature distribution was characterized using non-invasive infra-red thermal imaging thermography using a reference K-type thermocouple. Temperature measurements close to the gripping arrangement are considered to be inaccurate due to large changes in the specimen emissivity. The measured temperature distribution is shown in Figure 3.16. At the

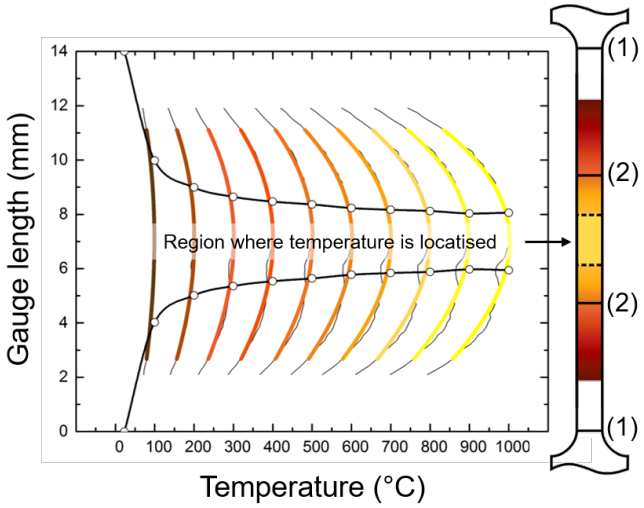


Fig. 3.16 Temperature distribution along the miniaturized ETMT specimen at test temperatures between 100 and 1000°C. (1) Grip separation of the LVDT and (2) point of displacement monitored using digital image correlation.

center of the sample a region develops where temperature is localized (T= ± 5°C). The size of this region is a function of the applied current and within the temperature range investigated it varies between 2.4 mm at 700°C and 2.2 mm at 900°C. This is in good agreement with previous findings [177].

The majority of plastic deformation during a tensile test will occur in the region where temperature is localized. This is assumed to have an effect comparable to a smooth notch because the strength is reduced in this part of the specimen at high temperatures [182]. Since the possibility of limited amounts of plastic deformation outside the specimen center cannot be excluded, an the extension of the central 5 mm of the test piece was monitored using digital image correlation. This is in accordance with the Instron recommended default value for ETMT tensile testing [183]. A 5 mm nominal gauge length was also employed by previous studies using an ETMT system [184] and is consistent though out this thesis. Figure 3.17 shows the strain-rate measured using DIC in the central 5 mm of the specimen at 750°C.

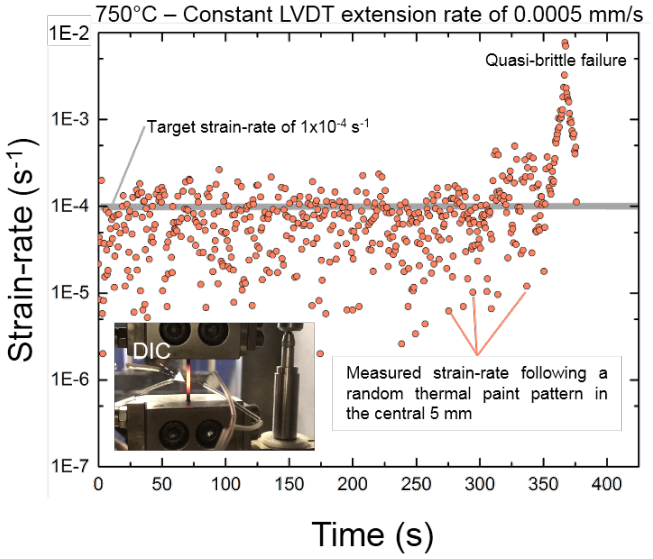


Fig. 3.17 Strain-rate measured using DIC in the central 5 mm of the specimen over time at 750°C. A slow constant cross head displacement of 0.0005 mm/s using the LVDT was used.

The measured percent elongation is dependent on the gauge length if the cross-section is constant [180], consistent with:

$$\%\mathrm{EL} = \frac{\mathrm{L_f} - \mathrm{L_0}}{\mathrm{L_0}} \cdot 100 = \left(\frac{\alpha}{\mathrm{L_0}} + \mathrm{EU}\right) \cdot 100 \quad , \tag{3.2}$$

where α is the local necking extension and EU is the uniform elongation. This indicates that percent elongation is a function of the specimen gauge length [180]. Thus, percent elongation obtained at high temperature cannot be directly compared to room-temperature.

At high temperatures during neck formation, deformation is assumed to be limited to the specimen center where temperature is localized. Since there is only a limited amount of uniform elongation, elongation during necking can account for most of the percent elongation (see Equation 3.2). This is in agreement with the results presented at 800°C in argon atmosphere and above 850°C in laboratory air (Figure 2 and 3). In addition, the size of the localized temperature region is dependent on the test

temperature (Figure 12). This leads to an increase in localized necking extension with increasing test temperature which additionally makes a comparison of percent elongation difficult. In addition, extensive necking at high test temperatures can lead to a further increase in temperature due to the reduced cross-section in combination with the heating current. Therefore, due the effect of necking extension ductile ETMT tensile tests were stopped after 24% engineering strain.

When ETMT tensile tests were performed at 600, 700, 750 and 800°C in laboratory air, samples failed in a quasi-brittle manner without necking. Percent elongation is therefore determined by the uniform elongation in the middle ≈ 5 mm of the specimen. This means that results can be compared directly. The increased surface-to-volume ratio of the miniaturized specimen used in this study enhances surface dominated effects such as environmentally-assisted surface crack initiation and propagation. Proof of surface initiated environmentally-assisted crack growth is shown in Figure 3.9. This makes ETMT slow strain-rate tensile tests well-suited for the assessment of Ni-based superalloys and their susceptibility to quasi-brittle environmentally-assisted cracking.

3.4.2 Environmentally-Assisted Intergranular Failure

Miniaturized slow strain-rate tensile tests demonstrated that environmentally-assisted cracking occurs with-in a critical temperature and strain-rate regime, see Figure 3.6. Between 600 and 850°C the enviornmental damage becomes more pronounced with increasing temperature. This is the same temperature regime that parts of rim of turbine disks will experience in the future. While ductility was found to decrease between 600 and 850°C, at 900°C ductility recovers and environmentally-assisted cracking is not observed probably due to what is believed to be a change in the apparent damage mechanism. This dip in ductility is in agreement with conventional tensile tests over

a wide range of temperatures for example those performed on Waspaloy [185]. The observed temperature dependence of the ductility can be related to environmental damage during other forms of loading such as low-cycle and dwell fatigue in alloy 720Li [41] and P/M superalloys such as LSHR [61] and RR1000 [70]. In addition, the observed dip in ductility correlates well to early studies on IN706 where the low cycle fatigue life time was assessed in laboratory air and a maximum in crack propagation rate was found at around 700°C [186].

In an air environment, the fatigue crack growth rate in alloy 720Li has been reported to increase with increasing dwell time [187]. This correlates to the observed changes in ductility when tests at different strain-rates are compared (Figure 3.6 (b). This is in agreement with the general belief that environmentally-assisted crack propagation is a time-dependent process [118]. The observed strain-rate dependence suggests that there is a distinctive link between the apparent tensile deformation mechanisms and environmentally assisted fracture. Elemental oxygen, however, is not likely to interact with slip as specimens tested in an argon atmosphere showed no change in 0.2% proof stress compared to tests in laboratory air (Figure 3.6). Diffuse necking or serrated flow was also not observed in combination with quasi-brittle failure.

Fractographic analysis performed at a higher magnification showed that the observed environmental damage along the secondary cracks and at the crack tip is in agreement with damage features observed in low cycle and dwell fatigue tests [115]. The secondary cracks were found to be covered in oxidation products which is in agreement with the general consensus that oxygen is the damaging species in laboratory air [118, 169]. SEM imaging showed that environmentally-assisted cracking in alloy 720Li predominantly occurred along the incoherent primary γ'-interfaces and high angle γ-grain boundaries. The results presented support the hypothesis that environmentally assisted cracking is directly linked to the formation of oxides at the

crack tip. High resolution electron microscopy and EDX mapping revealed layered bulk crack tip oxide intrusions narrowing down into unattacked γ-grain boundaries. It is assumed that the inner nickel-rich oxide is NiO and the chromium, aluminum and titanium enriched metal/oxide interfaces are associated with Cr_2O_3, Al_2O_3 and TiO_2 respectively. These observations regarding the layered crack tip oxides are consistent with studies performed on various Ni-based superalloys during dwell fatigue loading tests [70, 115, 117, 188].

The mechanical testing technique used has been demonstrated to replicate the temperature and time-dependent effects that are typically observed during environmentally-assisted crack propagation; mainly an increased crack propagation rate in an oxidizing environment if temperature is increased or hold times are introduced. This has been recently demonstrated by Jiang *et al.* [61].

These finding have some important implications for the mechanism of embrittlement in polycrystalline superalloys, as discussed further in the next chapter.

3.4.3 Site-Specific Micro-Cantilever Tests

Observations made from the micro-cantilever tests have provided new insights into environmentally-assisted crack propagation. While micro-cantilevers without environmental damage showed no sign of failure, crack propagation at an exposed crack tip occurred after the onset of plasticity. This confirms that the fracture event is not an artefact from the sample preparation process.

Cracking of the oxide intrusion can be attributed to the local tensile stresses imposed by the micro-cantilever displacement. In addition, dislocation pile up at the oxide intrusion is likely to contribute to local increases in stress.

After unloading, the crack was observed to propagate through the nickel-rich region, presumably nickel oxide. This shows that the formation of bulk oxides at the crack tip and the growth into the undamaged grain boundary is critical during environmentally-assisted cracking. The metal/oxide interfaces were not observed to fail under the imposed stress. This highlights the importance of protective oxide layers which limit the extent of nickel oxide formation at the crack tip. Failure of the high angle grain boundary ahead of damaged crack tip was not observed.

This work highlights the unique ability of microscale cantilever bend experiments to elucidate the fracture behavior of individual microstructural features and to determine their contribution to the overall material strength. Further recent work has demonstrated how these tests can be performed at temperatures up to 770°C [189].

3.5 Conclusions

In this chapter, two mechanical testing techniques are presented which are suitable for testing the susceptibility of polycrystalline superalloys to environmentally-assisted intergranular cracking. The following conclusions can be drawn:

(1) It is confirmed that the strength and tensile ductility of Ni-based superalloys can be assessed rapidly over a wide range of test temperatures and strain-rates using miniaturized electro-thermal mechanical tensile tests.

(2) The mechanical properties obtained for alloy 720Li are in close agreement with results from conventional tensile test. However, care must be taken in the interpretation of percent elongation, due to challenges associated with the definition of the gauge length.

(3) The employed miniaturized tensile tests identified a critical temperature and strain-rate regime where intergranular failure occurs. These tests are therefore capable of capturing the temperature and time-dependent effects that occur during environmentally-assisted failure under other forms of loading such as low-cycle and dwell fatigue.

(4) Micro-cantilever bend tests are demonstrated to be a useful tool for the investigation of the micro-mechanisms of failure at an oxidized crack tip showing that the environmentally induced embrittlment effect is confined to a short range. The grain boundary ahead of the damage zone are not embrittled by the environment.

(5) The observations made reinforce the hypothesis that environmentally-assisted cracking is linked to the fracture of oxides which narrow down into the undamaged grain boundary.

Chapter 4

Environmentally-Assisted Attack as a Mechanism of Embrittlement

Summary In this chapter the temperature dependent loss of ductility in the high strength polycrystalline superalloy 720Li is studied in detail. Chapter 3 shows that tensile ductility is influenced profoundly by the environment, leading to a pronounced minimum at 750°C. Here a relationship between tensile ductility and oxidation kinetics is established. The physical factors responsible for the ductility dip are rationalised using energy-dispersive X-ray spectroscopy, nanoscale secondary ion mass spectrometry and the analysis of electron backscatter diffraction patterns. Embrittlement results from internal intergranular oxidation along the γ-grain boundaries, and in particular, at incoherent interfaces of the primary γ'-precipitates with the matrix phase. These fail under local microstresses arising from the accumulation of dislocations during slip-assisted grain boundary sliding. Above 850°C, ductility is restored because the accumulation of dislocations at grain boundaries is no longer prevalent.

4.1 Introduction

Polycrystalline γ/γ'-strengthened Ni-based superalloys are very strong, but their grain boundaries are a source of weakness at elevated temperature due to their interaction with gaseous environments containing oxygen. This problem is of particular concern when considering the application of these materials in the hot-section components needed for power generation and/or jet propulsion: these are subjected to oxidative and corrosive gas streams whilst under high stresses at temperatures in excess of 700°C. Operating temperatures are rising markedly – due to ongoing fuel efficiency demands and the need to reduce emissions – hence damage from so-called environmentally-assisted cracking is becoming increasing prevalent and is now the major limitation to the application of Ni-based superalloys at the higher temperatures [3]. The precise mechanism for this effect is contentious, necessitating systematic experimentation and associated characterisation at the appropriate length scale to elucidate the underlying physical and chemical factors at play.

Environmentally-assisted cracking has been proposed by some investigators to be influenced by dynamic embrittlement involving the migration of elemental oxygen ahead of the crack front [76, 100, 101, 190]; others propose that the phenomena is affected by stress-assisted grain boundary oxidation (SAGBO) [70, 110, 115, 117]. The distribution of oxygen at an intergranular crack tip has been characterised recently using techniques of high spatial resolution including transmission electron microscopy combined with energy dispersive X-ray spectroscopy (EDX) [70], nanoscale secondary ion mass spectrometry (NanoSIMS) [59], and atom probe tomography [117]. These studies revealed the formation of a layered oxide structure along the γ-grain boundaries ahead of the cracks thus supporting a damage mechanism similar to the SAGBO concept. In general, the layering was found to be in agreement with thermodynamics:

thermodynamically unstable oxides consisting of Ni, Fe and Co were found at the beginning and centre of the crack while more stable oxides consisting of Cr, Ti and Al were found closer to the interface of the oxide and metal [115, 117, 191]. The oxidation of secondary γ'-precipitates has been suggested to lead to the formation of Ni- and Al-rich oxides [117]. However, the proposed concepts so far fail to explain fully why a super-solvus heat treatment with only intragranular γ'-precipitates is observed to be more resistant to environmentally assisted cracking than a sub-solvus heat treatment where both intra- and intergranular γ'-precipitates are present [121].

In the literature, environmentally-assisted cracking is most usually recognised in the context of low-cycle fatigue and dwell-fatigue loading tests. However, the complexity of such testing combined with the substantial time and material requirements is somewhat problematic. Alternatively, Gabb *et al.* [36] demonstrated that inelastic failure strain of slow strain-rate tensile tests can be correlated to the dwell fatigue crack propagation rate. Here, these pioneering concepts are built upon. Sub-solvus heat treated superalloy 720Li is subjected to slow strain-rate tensile tests between room temperature and 1000°C. Miniature test pieces of enhanced surface/volume ratio are employed, in order to accelerate the embrittlement effect and thus facilitate its study. These miniaturised tensile tests have been shown to be capable of capturing the temperature and time-dependent effects that occur during environmentally-assisted failure [192]. In the past, a temperature dependent minimum in tensile ductility [185, 193] and maximum in fatigue crack propagation rate [60] was observed. This was reviewed by Woodford [82] who proposed that a mid-temperature embrittlement is not exclusively due to environmental interactions but is also linked to the grain boundary mobility. This hypothesis is not incompatible with more recent results which emphasise that the ability to reduce stresses at the crack tip by stress relaxation has an impact on an alloy's susceptibility to oxidation-assisted cracking [70, 129, 194].

In this study, quantitative data for the ductility of alloy 720Li are reported and the role of environmental attack is confirmed. Detailed characterisation of the crack tip processes is then carried out – notably with EDX, NanoSIMS and high resolution electron backscatter scatter diffraction (HR-EBSD) in an attempt to answer the following questions:

(1) What is the nature of the environmentally-assisted grain boundary attack leading to intergranular crack propagation?

(2) What is role of the deformation mechanism on the failure of the environmentally-induced damage zone?

(3) How can we rationalise the effect of heat treatment on an alloy's susceptibility to environmentally-assisted cracking?

4.2 Experimental Procedure

4.2.1 Material

The cast/wrought Ni-based superalloy alloy 720Li was primarily used. Detailed information regarding the microstructure can be found in the previous chapter. In addition, a super-solvus heat treatment at 1170°C was applied to the alloy 720Li. Unfortunately, due to the lack of grain boundary pinning after the dissolution of the primary γ'-precipitates abnormal grain growth occurred; the reason can be traced to the low content of grain boundary elements such as carbon and boron (Table 4.1). In addition, upon cooling at requisite rates, quench cracking was observed. As a result, alloy RR1000 processed by powder metallurgy was studied additionally in both sub- and super-solvus heat treated condition. Nominal compositions are given in Table 4.1 and Figure 4.1 displays micrographs of each alloy after electro-chemical etching in an aqueous solution of 10% phosphoric acid showing intergranular primary γ'-precipitates and intragranular secondary and tertiary γ'-precipitates. The materials were supplied by Rolls-Royce plc. in the form of fully heat treated forgings.

Table 4.1 Nominal composition of alloy 720Li and RR1000 in wt-% (Ni-base).

Alloy	Ni	Cr	Co	W	Mo	Al	Ti	Ta	Hf	C	B	Zr
720Li	bal	16.0	15.0	1.25	3.0	2.5	5.0	0.0	0.0	0.015	0.015	0.035
RR1000	bal	15.0	18.5	0.0	5.0	3.0	3.6	2.0	0.5	0.027	0.015	0.06

The sub-solvus heat treatment for RR1000 consisted of a solution heat treatment at 1120°C for 4 hours followed by an air quench and an ageing heat treatment at 760°C for 16 hours which resulted in a γ-grain size of $d_\gamma \approx 5 \pm 1$ μm and a primary γ'-precipitate size of $d_{\gamma'} \approx 3$ μm. The super-solvus heat treatment consisted of a

solution heat treatment at 1170°C for 1 hour followed by an fan air cool and an ageing heat treatment at 760°C for 16 hours. This super-solvus heat treatment was shown to increase the γ-grain size to $d_\gamma \approx 55 \pm 21$ μm. A full characterisation of the as-received microstructure of RR1000 can be found elsewhere [70, 130, 195, 196].

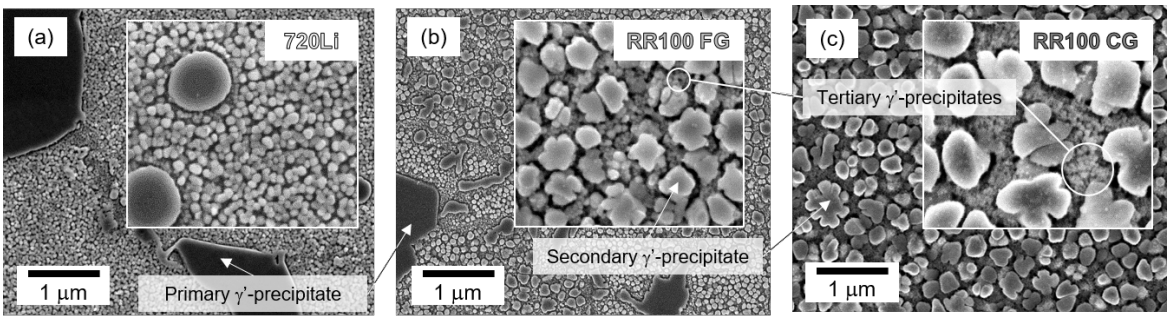


Fig. 4.1 SEM images of a γ-grain after electro-chemical etching in 10% phosphoric acid showing primary, secondary and tertiary γ'-precipitates in (a) alloy 720Li, (b) sub-solvus heat treated RR1000 and (c) super-solvus heat treated RR1000.

4.2.2 Assessment of the Tensile Ductility

Tensile testing was conducted between room-temperature and 1000°C on the 5 kN Instron ETMT machine introduced in Chapter 3. Miniaturised specimens of cross-section 1×1 mm^2 and a gauge length of 14 mm were used; the full sample length was 40 mm. The specimens were produced using wire-based electrical discharge machining (EDM), with surfaces subsequently ground to 1200 grit finish using silicon carbide grinding paper to maintain a consistent surface finish and to remove the re-cast layer resulting from the EDM process. Temperature measurement during testing was achieved by spot-welding a K-type thermocouple to the central portion of the specimen gauge. A minimum of three tests were performed at each condition.

Slow strain-rate tests were performed in laboratory air with an initial slow strain-rate close to $1{\cdot}10^{-4}\,\mathrm{s}^{-1}$. These were conducted at room temperature, 400, 500, 600 and between 700 and 1000°C in steps of 50°C. Consistent with the design of the ETMT

machine, specimens were heated using electrical resistance by passing a direct current through the specimen. Tests were performed at a constant extension rate using a linear variable displacement transformer (LVDT). The engineering strain was used as a measure of the ductility; engineering strain is defined as $\varepsilon = [(L_f - L_0)/L_0]$, where the gauge length extension $L_0 - L_f$ was monitored using digital image correlation following a thermal paint pattern in the central 5 mm of the specimen where the temperature and therefore deformation is uniform [192]. Further but more limited testing was carried out at 800°C using intermediate and fast initial strain-rates — close to $1{\cdot}10^{-3}$ and $1{\cdot}10^{-2}$ s^{-1} – in laboratory air.

4.2.3 Measurement of the Oxide Kinetics

Thermo-gravimetric analysis (TGA) was conducted on 10 × 10 × 1 mm test pieces between 700 and 1000°C using a Netsch Jupiter TGA rig. Prior to isothermal exposure, specimen surfaces were ground to a 1200 grit finish using silicon carbide grinding paper. In addition, all edges were chamfered. Specimens were exposed between 700 and 1000°C in 100°C steps to 50 ml/min laboratory air for a short exposure time of 10 minutes and for a longer exposure time of 50 hours. The heating and cooling was performed in a protective argon atmosphere.

4.2.4 Fractography and Damage Analysis

The microstructures both before and after testing was characterised with a JEOL 6500F FEG scanning electron microscope (SEM). Secondary/backscattered electron imaging and HR-EBSD analysis were used. Diffraction patterns were acquired with a TSL Digiview II detector - controlled with the OIM software - at the full resolution of 1000 x 1000 pixels to maximise the available angular resolution, and saved for

subsequent analysis. Using an in-house method to measure the lattice curvature, the distribution of geometrically necessary dislocations (GNDs) is estimated with the help of Dr. D.M. Collins. A description of this technique is described in Wilkinson *et al.* [197].

Observation of the fracture surfaces following mechanical testing was carried with three dimensional (3D) optical metrology using an Alicona optical microscope. Fractography was supported by secondary electron imaging and sub-micron resolution NanoSIMS using a Cameca NanoSIMS 50 system operated by Dr. K. Li, for details see [198]. The fracture surfaces were nickel plated prior to this to allow mechanical polishing. In addition, a Zeiss Merlin FEG SEM equipped with a in column energy selective backscattered (ESB) detector and an Oxford Instruments XMax 150mm^2 detector for obtaining EDX maps at a high spatial resolution was applied. Oxide scales were assessed using a Zeiss Auriga focussed ion beam (FIB) system.

In addition, annular bright-field (ABF) and high angle annular dark field (HAADF) images as well as STEM-EDS elemental maps were acquired with the help of Dr. C.H. Liebscher at the Max-Planck-Institut für Eisenforschung in a probe corrected FEI Titan Themis 60-300 microscope equipped with a ChemiSTEM Si-drift EDS-system operated at 300 kV. A probe semi-convergence angle of 17 mrad was used to form the electron probe. The semi-collection angles for ABF and HAADF imaging conditions were chosen to be 8-16 mrad and 17-73 mrad, respectively.

4.3 Results

4.3.1 Temperature-Dependence of the Tensile Ductility

Miniaturised slow strain-rate tensile tests were performed on alloy 720Li between room-temperature and 1000°C in laboratory air. Representative engineering stress-strain curves are shown in Chapter 3. Three temperature regimes are seen with markedly different tensile ductility. First at low temperatures below 500°C alloy 720Li remains ductile with a failure strain exceeding 15%. Second, a significant reduction in tensile ductility is observed at intermediate temperatures in the range 600 to 850°C, with a minimum failure strain of 3% at 750°C. Third, a high-temperature regime above 850°C where ductility is restored.

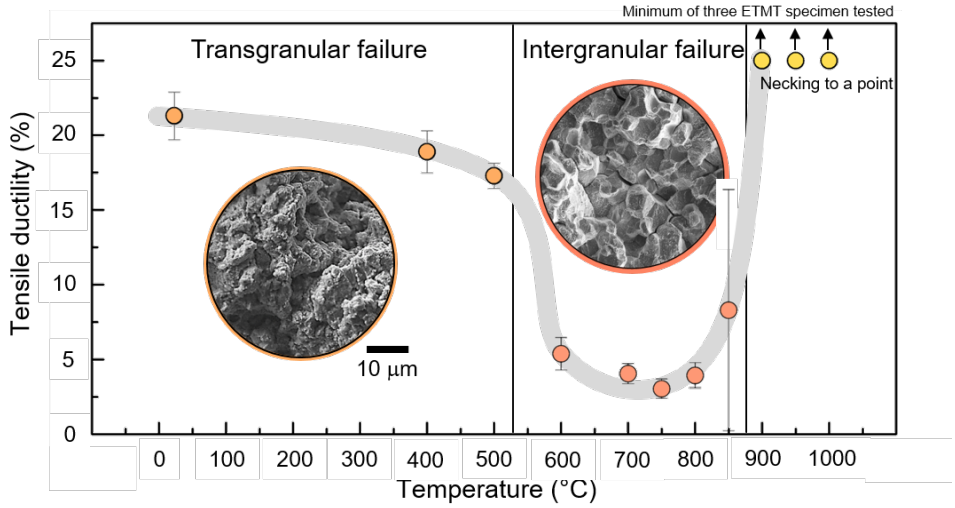


Fig. 4.2 Variation in tensile ductility with temperature for slow strain-rate tensile tests in laboratory air. Error bars represent the standard deviation of a minimum of three test repetitions. Representative types of failure below and above 500°C are illustrated. Above 850°C ductility is restored. Representative stress-strain curves for alloy 720Li between room temperature and 1000°C at an initial strain-rate close to $1{\cdot}10^{-4}$ s^{-1} are shown in Chapter 3.

Notably, fracture was not reached at tests performed at temperatures above 900°C.

The tests were stopped at 24% due to potential necking above or below the thermocouple, which would result in an increase in temperature in the vicinity of the reduced section as a result of the heating current [192]. The strain to failure obtained at each test temperature is summarised in Table 4.2. The dramatic loss in ductility in the mid-temperature regime is consistent with observations made on other superalloy systems [36, 170, 185, 193] and can be explained as follows. At 500°C a transition occurs between ductile transgranular and quasi-brittle intergranular failure. Therefore, intergranular crack propagation in this regime limits the tensile ductility. This is illustrated in Figure 4.2 where tensile ductility is plotted against temperature.

Table 4.2 Effect of test temperature on the mechanical properties of alloy 720Li when tested in laboratory air with an initial strain-rate of $1{\cdot}10^{-4}$ s^{-1}. Mean results and standard deviation (SD) of a minimum of three test repetitions are given. Corresponding individual stress-strain curves are shown in the Appendix A.

Temperature (°C)	YS (MPa)	UTS (MPa)	Tensile ductility (%)
23	1139 ± 49	1557 ± 22	24.6 ± 1.6
400	1061 ± 21	1472 ± 36	18.9 ± 1.4
500	1051 ± 15	1447 ± 24	17.3 ± 0.9
600	1042 ± 18	1240 ± 39	5.4 ± 1.1
700	978 ± 7	1057 ± 6	4.1 ± 0.7
750	814 ± 31	863 ± 32	3.0 ± 0.7
800	601 ± 25	637 ± 23	3.9 ± 0.8
850	524 ± 31	554 ± 30	8.3 ± 8.0
900	274± 11	291 ± 21	>24
950	188 ± 19	202 ± 21	>24
1000	69 ± 18	71 ± 19	>24

The effects of strain-rate was further assessed at 800°C. At both slow and inter-

mediate strain-rates, $1{\cdot}10^{-4}$ and $1{\cdot}10^{-3}$ s^{-1} respectively, quasi-brittle failure occurred with limited strain to failure. A significant increase in elongation was noted if a fast strain-rate of $1{\cdot}10^{-2}$ s^{-1} was applied. The clear effect of strain-rate on the tensile ductility of alloy 720Li is summarised in Table 4.3. These results suggest that the observed environmental embrittlement is thermally-activated and time dependent.

Table 4.3 Effect of variations in atmosphere and initial strain-rate on the mechanical properties of Alloy 720Li when tested in laboratory air at 800°C. Mean results and SD of a minimum of three test repetitions are given. Corresponding individual stress-strain curves are shown in the Appendix A.

Atmosphere	Strain-rate (s^{-1})	YS (MPa)	UTS (MPa)	Tensile ductility (%)
Laboratory air	$1{\cdot}10^{-4}$	601 ± 25	637 ± 23	3.9 ± 0.8
Laboratory air	$1{\cdot}10^{-3}$	751 ± 21	761 ± 28	2.8 ± 1.3
Laboratory air	$1{\cdot}10^{-2}$	1102 ± 49	1298 ± 22	12.4 ± 1.0

The effect of heat treatment was assessed at 700, 750 and 800°C. Figure 4.3 (b) compares the tensile ductility of sub-solvus heat treated alloy 720Li & RR1000 and super-solvus heat treated RR1000 using a slow initial strain-rate close to $1{\cdot}10^{-4}$ s^{-1} in laboratory air. Both sub-solvus heat treated superalloys, alloy 720Li and RR1000, failed with limited strain to failure and a minimum in tensile ductility at 750°C, with RR1000 performing better than alloy 720Li. The same trend has been reported for fatigue crack propagation [41]. If the two variants of RR1000 are compared an significant improvement in tensile ductility due to the super-solvus heat treatment is unambiguously observed. This is in agreement with the reported decrease in dwell fatigue crack propagation rate after applying a super-solvus heat treatment to the powder metallurgy Ni-superalloy, Alloy 10 [121].

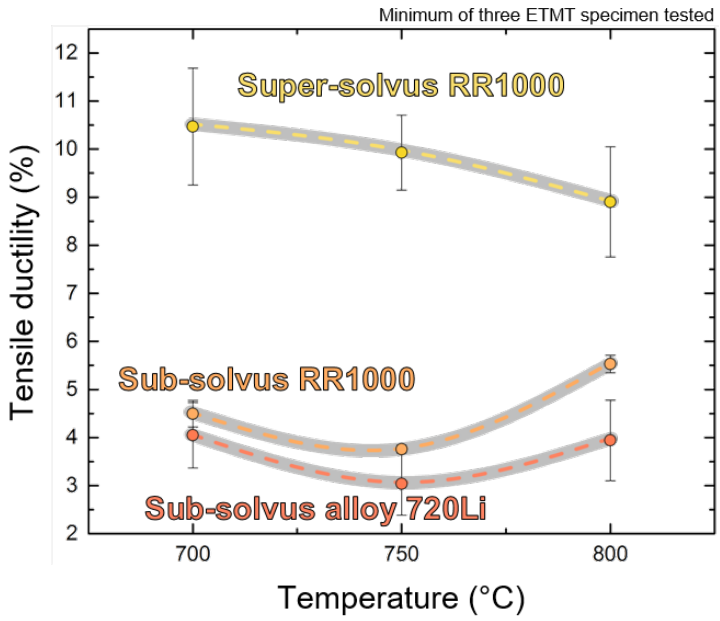


Fig. 4.3 Variation in tensile ductility between 700 and 800°C for slow strain-rate tensile tests performed on sub-solvus alloy 720Li, sub-solvus RR1000 and super-solvus RR1000. Error bars represent the standard deviation of a minimum of three test repetitions.

Table 4.4 Effect of heat treatment on the YS and UTS of RR1000 when tested in laboratory air between 700 and 800°C. Mean results and SD of a minimum of three test repetitions are given. Data for alloy 720Li is shown for comparison. Corresponding individual stress-strain curves are shown in the Appendix A.

Alloy	Temperature (°C)	YS (MPa)	UTS (MPa)	Tensile ductility (%)
RR1000 (sub)	700	986 ± 12	1052 ± 6	4.5 ± 0.3
	750	823 ± 24	878 ± 25	3.8 ± 0.1
	800	624 ± 24	647 ± 20	5.5 ± 0.2
RR1000 (super)	700	845 ± 3	1007 ± 17	10.5 ± 1.2
	750	813 ± 3	861 ± 10	9.9 ± 0.8
	800	733 ± 12	737 ± 14	8.9 ± 1.1
720Li (sub)	700	978 ± 7	1057 ± 6	4.1 ± 0.7
	750	814 ± 31	863 ± 32	3.0 ± 0.7
	800	601 ± 25	637 ± 23	3.9 ± 0.8

4.3.2 On the Temperature-Dependence of the Tensile Strength

The measured 0.2% proof stress (YS) and ultimate tensile strength (UTS) of alloy 720Li is summarised in Table 4.2. The strength of alloy 720Li was found to be temperature independent up to 600°C; a result that was in good agreement to those obtained by conventional tensile tests [192]. Above 700°C the strength is highly temperature dependent and decreases rapidly which suggests a change in the deformation mechanism. This is consistent with the data obtained for RR1000 (Table 4.4).

The temperature dependent nature of the YS between 700 and 850°C, where extensive environmental damage occurs, can be assessed using the following equation:

$$\sigma_y = C_1 \cdot \exp\left(\frac{Q}{RT}\right)\Bigg|_{\varepsilon,\dot{\varepsilon}} , \tag{4.1}$$

where Q is an activation energy for the dominant deformation mechanism, R is the universal gas constant, C_1 is a constant and T is the test temperature [199]. Applying this equation to our experimental results, a straight line was fitted to the plot of $\ln(\sigma_y)$ versus $1/T$ with an adjusted R^2 of 97.4%. The activation energy obtained from the slope of this line was calculated to be $Q \approx 40$ kJ mol^{-1} (see Figure 4.4).

The YS and UTS of alloy 720Li increases with strain-rate. A difference of ≈ 500 MPa was observed between the fastest and slowest strain-rate. These findings are summarised in Table 4.3.

The dependence of the YS on the applied strain-rate can be expressed through:

$$\sigma_y = C_2 \cdot (\dot{\varepsilon})^m \Big|_{\varepsilon,T} , \tag{4.2}$$

where C_2 is a constant and m describes the strain-rate sensitivity [200]. The strain-

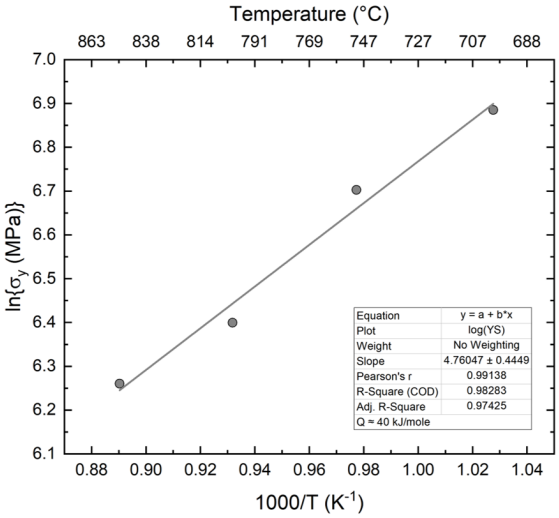


Fig. 4.4 Arrhenius plot of yield stress versus temperature from which an activation energy of ≈ 40 kJ mol^{-1} is deduced.

rate sensitivity m is the ratio of the incremental change in ln σ to the resultant change in ln $\dot{\varepsilon}$, at a given strain and temperature. For the change in flow stress upon the rise from slow to intermediate strain-rate at 800°C, where quasi-brittle failure is observed, a strain-rate sensitivity of $m \approx 0.17$ was calculated. This is close to the strain-rate sensitivity of ≈ 0.1 determined by Gopinath *et al.* [173] for alloy 720Li at 750°C for comparable deformation rates.

4.3.3 Characterisation of Environmentally-Assisted Failure

The ductility dip observed in alloy 720Li in the mid-temperature regime correlates to evidence of increased environmental damage on the fracture surfaces of the failed miniaturised tensile specimens. This increase with test temperature is illustrated in Figure 3.9. Environmental damage is evident across the whole fracture surface for specimens tested above 750°C. In general, the regions of the fracture surface that showed environmental damage failed perpendicular to the applied load in an inter-granular manner, see Figure 3.10. Regions without environmental damage failed at $\sim$

45° to the tensile axis; dimples and micro-voids were observed in these regions. The transition between regions that failed in a trans- and intergranular fashion is sharp. At 800 and 850°C the entire fracture surface showed signs of environmental damage, indicating failure in an purely intergranular manner. In contrast, when tested below 600°C or in an inert atmosphere, environmental damage was absent from the fracture surface and ductile failure occurred after uniform elongation.

Figure 3.10 (a) – presented in Chapter 3 –shows a secondary electron SEM image of the intergranular fracture surface at 800°C. Multiple secondary cracks branch off the primary crack which led to failure. In order to investigate these secondary cracks, sections through the failed test pieces were prepared metallographically. Secondary cracks were consistently found along high angle γ-grain boundaries and the incoherent primary γ'-interfaces. These microstructural features are therefore identified as preferred paths for crack propagation in alloy 720Li. EDX mapping showed that the cracked grain boundaries and the incoherent primary γ'-interfaces are decorated with oxidation products. Fatigue cracks under comparable testing conditions have also been found to initiate and propagate along these features in alloy 720Li [124] and N18 [69]. Therefore, the primary γ'-precipitates play a key role in environmentally assisted-crack propagation in alloy 720Li.

A backscattered electron image showing a representative environmental damage zone at an intergranular crack tip is shown in Figure 4.5 (a). A local EDX analysis revealed that this damaged zone contains oxides consisting of Ni, Co, Ti, Cr and Al (Figure 4.5 (b)). The elemental distribution shown in the EDX elemental maps correlate to the contrast seen in the SEM ESB backscattered electron image (a). In order to overcome the problems in EDX analysis posed by the overlap of the O K_α and Cr L_α peaks at 0.525 and 0.573 keV respectively, NanoSIMS analysis of the same area was employed. The selection in the NanoSIMS of the $^{16}O^-$, $^{58}Ni^{16}O^-$, $^{52}Cr^{16}O^-$

and $^{27}Al^{16}O^-$ at masses 16, 74, 68 and 43 amu allowed the distribution of O, Al, Ni and Cr to be studied at this location with a spatial resolution below 100 nm and with the local sensitivity at the ppm level. The NanoSIMS maps in Figure 4.5 (c) together with the EDX elemental maps show a layered structure of the oxide at and ahead of the crack tip comprising Ni- and Co-, Cr-, Ti- and Al-rich layers.

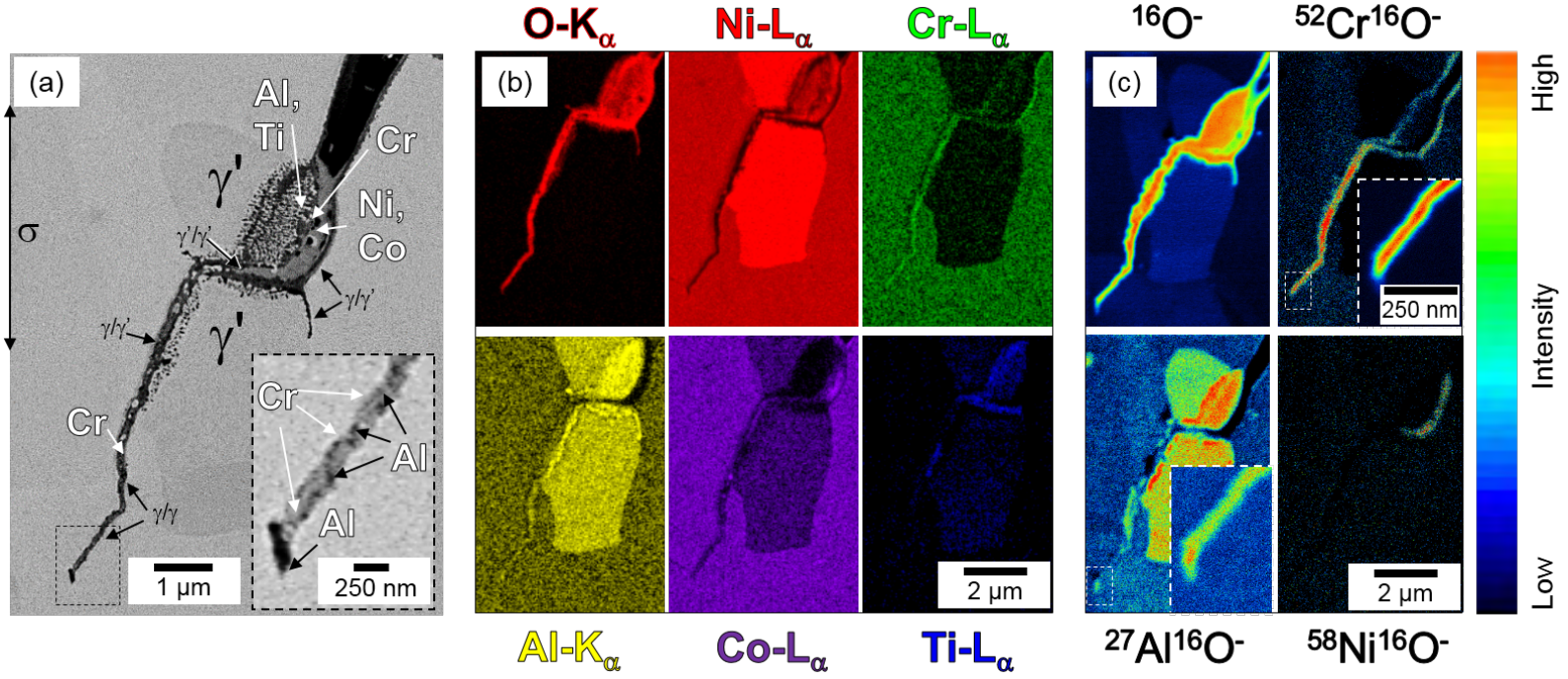


Fig. 4.5 (a) ESB image showing an environmentally-induced damage zone at and ahead of a secondary crack tip along a primary γ'-interface and a γ-grain boundary after slow strain-rate testing at 850°C. The Z-contrast suggests Al-rich oxide particles within a Cr-rich oxide layer. (b) Corresponding EDX maps showing the formation of Ni-, Co-, Cr-, Ti- and Al-rich oxidation products at and ahead of the crack tip. (c) Corresponding NanoSIMS $^{16}O^-$, $^{58}Ni^{16}O^-$, $^{52}Cr^{16}O^-$ and $^{27}Al^{16}O^-$ maps confirming the simultaneous occurrence of both Cr- and Al-rich oxides at the crack tip.

This oxide sequence is in agreement with their relative thermodynamic stability. The oxidation damage zone is observed to penetrate into the primary γ'-precipitates and the γ-grain boundaries. An external Ni- and Co-rich oxide is observed at the beginning of each oxide intrusion. This layer is porous and polycrystalline (Figure 4.5 (a)). Between this oxide and the γ-grain a thin Cr-rich layer was detected together with Al-rich features. Between the Ni- and Co-rich layer and the primary γ'-precipitates the Cr-rich layer is followed by an Ti- and Al-rich oxide growing into the primary γ'-precipitate. The tip oxide growing into the uncracked grain boundary is Al-rich. Within the spatial resolution and sensitivity limits of NanoSIMS elemental oxygen was not observed ahead of the oxide intrusion which is in general agreement with recent studies [70, 115, 117].

The environmental damage present at the primary γ'-precipitates was further studied using STEM-EDX. Z-contrast HAADF-STEM image shown in Figure 4.6 (a) illustrates the formation of a layered oxide penetrating the γ'-precipitate. From this image a Ni and Co-rich oxide layer followed by porosity can be identified. Al-rich oxide fingers are present at the furthest extend of the environmental damage zone. This is followed by a distinct Cr-rich oxide layer. Substantial amounts of Ti- and Al-rich oxides are present between the Al-rich oxide fingers, the Cr-rich oxide layer, and the Ni-, Co-rich bulk oxide (Figure 4.6 (b)).

HR-EBSD was used to calculate an estimate of the GND density distribution with a patch size of 50 nm at microstructure specific damage sites at 800 and 950°C. The technique used to calculate the GND density is described elsewhere [201]. Slow strain-rate tests were performed at these temperatures and terminated at 4% strain. At 800°C – in the mid-temperature regime – quasi-brittle failure was observed. At 950°C – in the high-temperature regime – alloy 720Li did not fail at 4% and the straining was interrupted. Figure 4.7 (a) and (b) illustrate the damage sites in these tests.

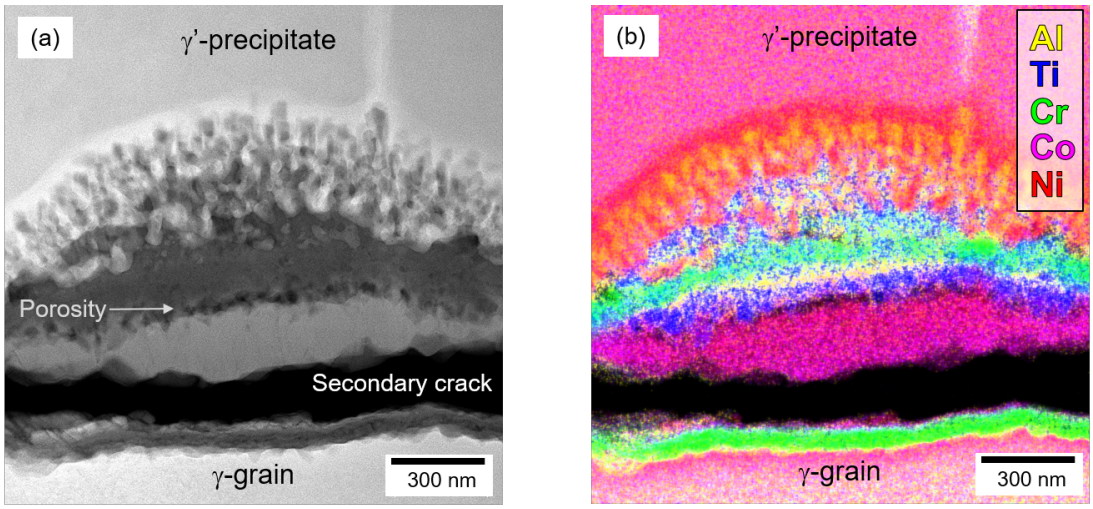


Fig. 4.6 (a) HAADF-STEM image of environmental damage at a cracked γ/γ'-interface close to the fracture surface of a slow strain-rate tensile test piece failed at 850°C. (b) Composite STEM-EDS elemental maps showing high X-ray count regions of Ni, Co, Cr, Ti and Al illustrating a layered oxide formation. Corresponding individual STEM-EDS elemental maps are shown in Appendix B.

While at 800°C failure occurs along the γ-grain boundaries and at γ'-precipitates, at 950°C intragranular ductile voiding and tearing is observed. At these damage sites, GND density distributions were calculated from the lattice curvatures obtained from HR-EBSD measurements, shown in Figure 4.7 (d) and (f). At 800°C, distinct grain boundary regions with an increase in GND density can be observed along the cracked and uncracked γ-grain boundaries and primary γ'-precipitates (Figure 4.7 (d)). At 950°C dislocations were not observed to accumulate at the grain boundaries. Moreover, the grain boundaries were observed to migrate due to dislocations aligning at 45° to the tensile loading axis. High GND density very low angle boundaries were also seen in this alignment and seemed to suggest some interactions with a γ-grain boundary, see Figure 4.7 (f).

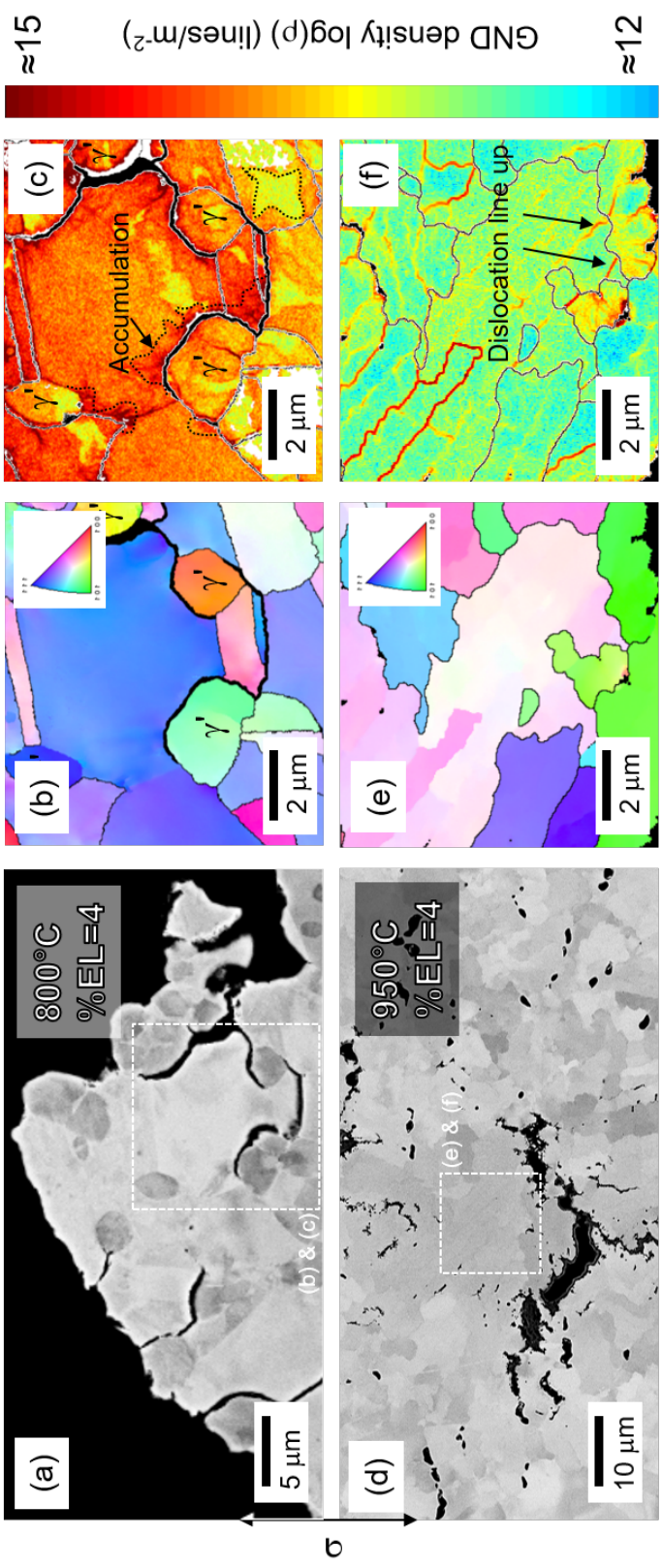


Fig. 4.7 (a) Back-scatter electron image perpendicular to the fracture surface at 800°C and (d) at 950°C after 4% strain. (b) and (e) shows EBSD maps at the damage sites. Corresponding maps of GND densities calculated from measured lattice curvatures obtained from EBSD data are shown in (c) and (f), respectively. The overlaid grain boundary positions have a misorientation exceeding 15°.

4.3.4 Measurement of the Oxidation Kinetics

Thermo-gravimetric analysis was performed on alloy 720Li between 700 and 1000°C for 50 hours and for 10 minutes in order to quantify the steady-state and pre-steady-state oxidation kinetics. Figure 4.8 (a) shows the specific mass gains during 50 hours exposure.

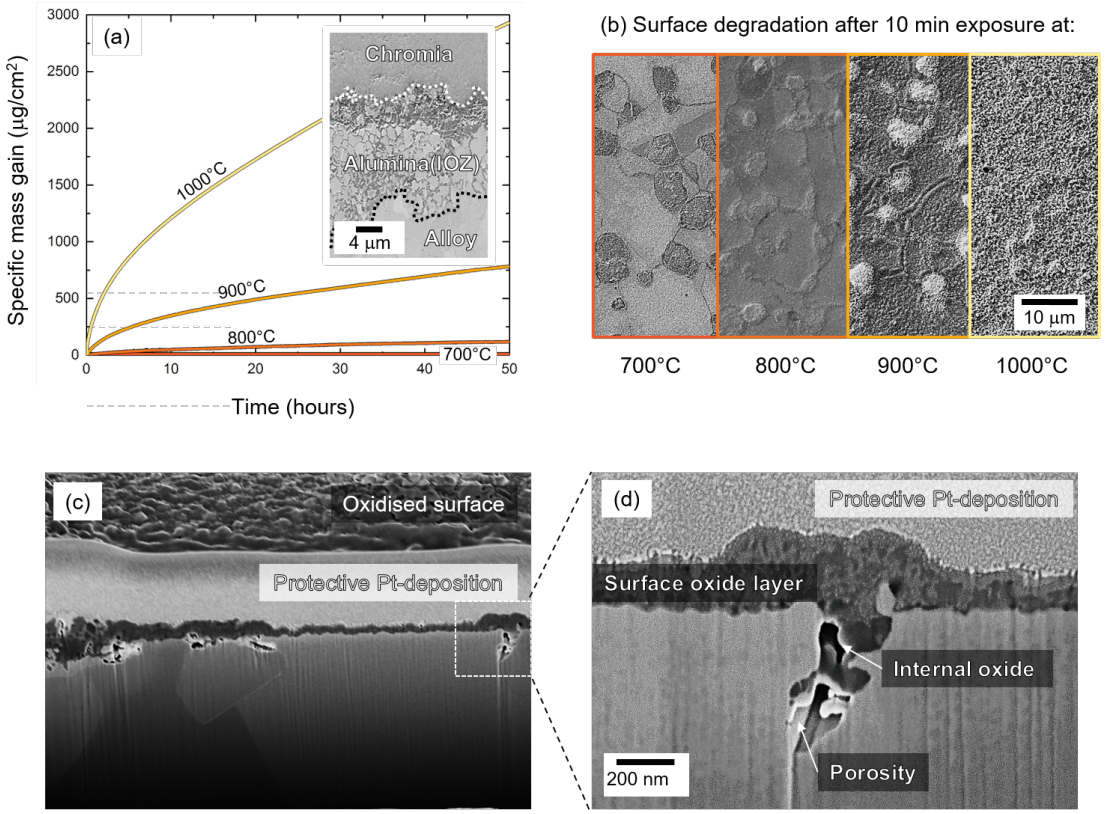


Fig. 4.8 (a) Specific mass gains during 50 hours exposure time between 700 and 1000°C. The typical oxide sequence after 50 hours at 800°C consisting of a chomia and internal alumina is shown. (b) Micrographs of oxygen attack on the sample surface after 10 minutes between 700 and 1000°C. The γ-grain boundaries and primary γ'-precipitates oxidise faster than the bulk of the γ-grains. (c) Focused ion beam cross section of γ-grain boundary damage after 10 minutes of exposure in laboratory air at 800°C. Beneath the protective Pt-layer an oxide layer and a grain boundary intrusion is visible.

The reaction kinetics were assessed through mass change measurements in the

following manner:

$$\left(\frac{m}{A}\right)^2 = k_p'' \cdot t \quad , \tag{4.3}$$

where A is the area over which the reaction occurs, m is the mass, k_p'' is the parabolic oxidation rate constant and t is time [202]. The oxidation kinetics were seen to increase with temperature and duration in a parabolic manner, see Figure 4.8 (a). This response replicates the kinetic response of typical chromia forming Ni-based superalloys such as RR1000 [203]. A cross-sections perpendicular to the oxidised surface at 800°C shows the sequence of oxide layers after 50 hours: a dense top layer, presumably Cr_2O_3, and sub-surface internal oxidation zone, presumably Al_2O_3. This is illustrated in Figure 4.8 (a). The protective chromia surface layer was confirmed by calculating the activation energy for oxide formation using the average parabolic rate constants, k_p'', shown in Table 4.5 using the following equation:

$$k_p'' = C_3 \cdot \exp\left(\frac{\text{-}Q}{RT}\right) \quad , \tag{4.4}$$

where Q is the activation energy for oxide formation, R is the universal gas constant, C_3 is a constant and T is the test temperature.

Table 4.5 Average scaling rate constants k_p' and parabolic rate constants k_p'' for alloy 720Li between 600 and 1000°C.

Temperature (°C)	k_p' (cm^2s^{-1})	k_p'' ($mg^2cm^{-4}s^{-1}$)
700	$8.3 \cdot 10^{-14}$	$2.2 \cdot 10^{-9}$
800	$5.2 \cdot 10^{-13}$	$8.2 \cdot 10^{-8}$
900	$1.3 \cdot 10^{-12}$	$5.4 \cdot 10^{-7}$
1000	-	$4.7 \cdot 10^{-5}$

A linear fit with an adjusted R^2 of 94.6% was used to calculated the activation

energy from the Arrhenius plot resulting in $Q \approx 325$ kJ mole^{-1}. This indeed confirms the formation of a protective Cr-layer [203].

After 10 minutes of exposure in laboratory air the formation of a thin surface oxide layer is observed at the metal/gas interface at all test temperatures. Figure 4.8 (b) illustrates the oxide formed on the surfaces between 700 and 1000°C. The thickness of these oxide layers were assessed using FIB cross-sections and were found to increase linearly with increasing temperature. An example cross-section at 800°C is shown in Figure 4.8. The relationship between the oxide thickness on top of γ-grains and exposure time at a given temperature can be expressed as:

$$x^2 = 2k_p' \cdot t \quad , \tag{4.5}$$

where k_p' is the scaling constant and t is time [202]. The deduced scaling rate constants k_p' are given in Table 4.5. A linear fit with an adjusted R^2 of 98.5% was used to calculated the activation energy from the Arrhenius plot resulting in $Q \approx 120$ kJ mole^{-1}. This is unambiguously smaller than the activation energy necessary for chromia formation ($Q \approx 325$ kJ mole^{-1}). Therefore, a $(Ni_{1-x}Co_x)O$ is assumed to form on the free surface in the early stages of transient oxidation over the temperature range investigated. Below 900°C the majority of the oxidation damage was observed to be limited to γ-grain boundaries and the primary γ'-precipitates (Figure 4.8 (b)). No evidence of environmental damage was observed for special $\Sigma 3$ grain boundaries. The cross-section shown in Figure 4.8 (c) shows the enhanced environmental damage at a γ-grain boundary. Porosity and an oxide intrusion can be seen. As exposure temperature is increased the bulk of the γ-grains become equally susceptible to oxidation damage relative to the γ-grain boundaries and primary γ'-precipitates. This is evident at temperatures above 900°C where the surface of γ-grains showed a comparable

amount of environmental damage compared to the grain boundaries and the primary γ'-precipitates. At 1000°C γ-grain boundaries and the primary γ'-precipitates could not be distinguished on the sample surface.

4.4 Discussion

The results presented above demonstrate conclusively that alloy 720Li is prone to intergranular embrittlement in air at 600 to 850°C. But these findings require rationalisation so that the physical mechanisms and chemical reactions causing this effect can be better understood. Moreover, the ramifications particularly for the optimisation of heat treatment of high strength superalloys need to be elucidated.

4.4.1 On the Mechanism of Intergranular Oxidation

Of critical importance is the observation of an internal oxidation zone which has been shown to penetrate the γ-grain boundaries and primary γ'-interfaces. By making use of bend testing of a microcantilever in Chapter 3, this environmental damage zone has been shown to be brittle; this explains the decrease of tensile ductility above 500°C. It is also consistent with the reported increase in dwell fatigue crack propagation rate above 500°C which has been reported for many alloys including 720Li [204]. Also relevant is the acceleration in oxidation kinetics with increasing temperature; this rationalises the decrease in ductility with temperature up to 750°C. Nonetheless, it is the precise details of the internal oxidation process which are of prime concern; as different oxidation reactions are occurring and it is to be expected that not all of these are equally damaging.

Consider the oxidation reactions which might be expected to occur – on the basis of established oxidation behaviour of Ni-based superalloys on plane, polished surfaces – at a notch being subjected to an oxidative environment, see Figure 4.9. In the first instance we imagine that the crack is progressing along a γ grain boundary. It is well

established that NiO and CoO oxides are likely to form quickly in an outward fashion, at a rate controlled by the migration of Ni^{2+} and Co^{2+} ions through the oxide [1]. On this basis, $(Ni_{1-x}Co_x)O$ is expected to fill the cracked notch rather than extending it, but with porosity remaining in the substrate below it which is consistent with the evidence of Figure 4.8 (c). Consistent with the very lowest equilibrium partial pressures of oxygen, Al_2O_3 is expected to arise with the deepest penetration, growing inwards at a rate controlled by O^{2-} migration inwards. A region of Cr_2O_3 is expected above the Al_2O_3. A three layer oxide structure has been proposed in the literature to occur at the crack tip [115], see Figure 4.9 (a). There is also the possibility of a spinel layer $NiCr_2O_4$ existing between NiO and Cr_2O_3. In addition, TiO_2 can precipitate alongside of Cr_2O_3 and Al_2O_3. In contrast to oxidation on plane polished surfaces mass transport of ion species by volume diffusion is not required at a crack tip. Note that – unlike the case of oxidation on a plane, polished surface – matrix/oxide interfaces are aligned parallel to the direction of oxide growth and are thus available as short-circuit diffusion paths resulting in the oxide growth into the grain boundary.

What is found in practice at a crack tip in this study is broadly consistent with the above simplified picture but differs from it in some important respects. For instance, the order of the reaction products is consistent with an Al-rich oxide (presumably Al_2O_3) at the furthest extent and Ni- and Co-rich oxides – $(Ni_{1-x}Co_x)O$ and/or spinel – closer to the crack tip, with Cr-rich oxides (Cr_2O_3) lying in-between. The elemental maps in Figure 4.5 (b) suggest the internal formation of an Ti-rich oxide (presumably TiO_2) particles alongside of the alumina. This is consistent with [205] and has been confirmed using STEM-EDX (see Figure 4.6). Additionally, the contentious damage zone extension during the process of crack propagation requires that alumina dissolves within the chromia at the γ-grain boundary, and evidence exists that this is indeed

occurring, see Figure 4.5. Here, it was shown that the γ-grain boundary ahead of the crack tip consists of what seems to be Al-rich oxides embedded in a Cr-rich oxide. These observations are based on the elemental contrast of the energy selective backscatter (ESB) detector. This is illustrated for steady-state crack extension in Figure 4.9 (b). But importantly, the γ-grain boundaries and the primary γ'-interfaces are found to oxidise at markedly different rates, see Figure 4.9 (c). This finding has some important implications for the optimisation of the heat treatment of polycrystalline superalloys for resisting oxidation-assisted cracking, as discussed further in Section 4.3.

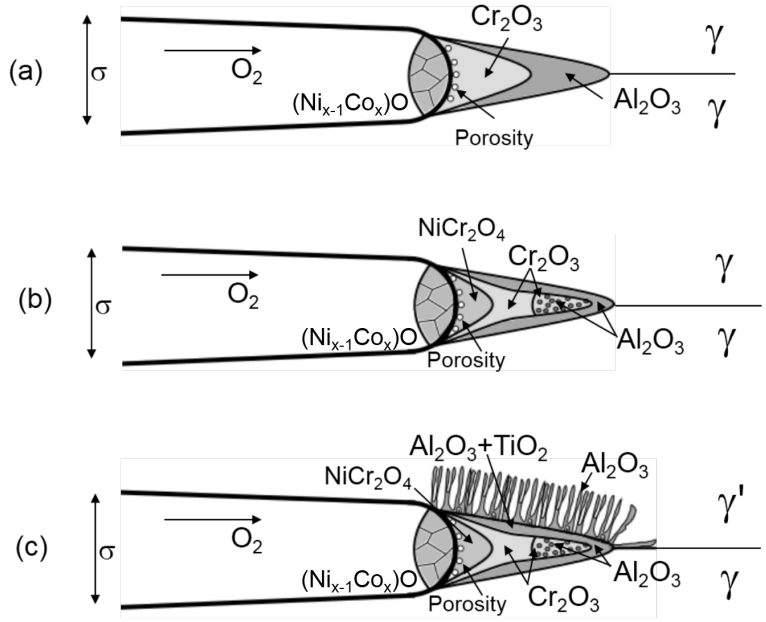


Fig. 4.9 (a) Schematic diagram of the oxidation morphology of a layered crack tip oxide in the thermodynamic sequence of NiO, Cr_2O_3 and Al_2O_3. (b) and (c) Schematic diagram of the oxidation morphology observed in alloy 720Li at a γ-grain boundary and at a primary γ'-interface. An external NiO layer is formed at the intergranular crack with an inner layer Ni,Cr_2O_4. Oxygen diffusion results in the formation of Cr_2O_3 subscale, Al_2O_3 is dissolved within this subscale before a continuous Al_2O_3 layer is formed. The primary γ'-interface shows internal Al_2O_3 formation.

4.4.2 On the Role of Slip-Assisted Grain Boundary Sliding

Intergranular oxidation attack explains the decrease in ductility between 600 and 750°C due to the increase in oxidation kinetics with increasing temperature. However, this fails to explain the increase in ductility above 750°C. Here we postulate that slip-assisted grain boundary sliding contributes to the net deformation and plays a crucial role in the quasi-brittle failure of the environmentally-damaged grain boundaries in the mid-temperature regime. This concept is consistent with the ideas proposed by Woodford [82]. Stress concentrations at a sliding grain boundary will lead to quasi-brittle failure of the intergranular oxides at and ahead of the crack tip. Above 750°C the rapid decrease in yield stress goes hand in hand with an increase in tensile ductility. This is due to an increase in grain boundary mobility but also changes in the γ'-precipitates morphology and distribution resulting from γ'-phase dissolution. In addition to diffusion processes along grain boundaries, the thermal activation of multiple slip systems and cross-slip in the γ'-precipitate is believed to result in softening of the γ'-phase strengthened microstructure.

The author believes that with increasing temperature and decreasing stress slip-assisted grain boundary sliding is contributing to the overall strain. The activation energy for the deformation process providing the temperature dependence of the flow stress between 700 and 850°C can be calculated to be $Q \approx 40$ kJ mol^{-1}, see Equation 4.1 and Figure 4.4. This is lower then the activation energy necessary for nickel-self diffusion (≈ 300 kJ mol^{-1} [206]) in the γ-matrix or the activation energy necessary to unpin Kear-Wilsdorf locks ($\approx$ 300-600 kJ mol^{-1} [207]). The deduced activation energy is in the range of values reported for grain boundary self-diffusion in nickel ($\approx$ 20 - 70 kJ mol^{-1} [206, 208]). This is indicative of a contribution from a thermally-activated deformation process involving diffusion along the grain boundaries. The

author suggests that grain boundary self diffusion is linked to grain boundary sliding in the studied temperature and strain-rate regime. This supports the results obtained by Carter *et al.* [209] who demonstrated the occurrence of grain boundary sliding in René-104 at 700°C and at stresses between 900 and 1100 MPa. Similarly, Soula *et al.* [210] and Thibault *et al.* [135] concluded that grain boundary sliding contributed to the creep strain at temperatures in NR6 between 700 and 850°C under an applied stress of 700 MPa.

Nevertheless, it is important to acknowledge that several independent deformation processes will be thermally activated and will therefore contribute to the overall deformation in the mid-temperature regime when a slow deformation rate is applied. In addition to the onset of diffusion processes along grain boundaries, changes in the intragranular mode of deformation will contribute to the drop in yield stress and accommodate a sliding grain boundary. At low temperatures, deformation is governed by diffusionless shearing of γ'-precipitates by $a/2$ $\langle 110 \rangle$ dislocation pairs leading to planar and heterogeneous deformation on localized slip bands. As temperature is increased sufficient thermal activation results in multiple active slip systems. As a result dislocations can disperse out of the planar bands through cross-slip and climb causing more homogeneous intragranular deformation. Under those conditions $a/3$ $\langle 112 \rangle$ and/or $a/6$ $\langle 112 \rangle$ type dislocations shear the γ'-precipitates [1]. In addtion, γ'-precipitates can be by-passed by matrix dislocations. This is supported by the absence of strain hardening above 700°C (see Figure 3.6) and the rate dependence of the flow stress which suggests a diffusion-controlled dislocation process which does not produce the hardening resulting from the increase in dislocation density with strain. It is proposed that intragranular diffusion assisted deformation in the grain boundary regions accommodates grains displacing relative to each other and controls the grain boundary sliding rate explaining the observed strain-rate sensitivity of the flow stress of m

≈ 0.17. Intergranular deformation proceeding through cross-slip was shown in TEM observations where tangles of dislocations were observed in addition to the presence of stacking faults within secondary γ'-particles during the deformation of alloy 720Li at 750°C and $1 \cdot 10^{-5}\ s^{-1}$ [173]. Grain boundary sliding accommodated by deformation in the grain boundary regions would explain localised stress and strain concentrations which fracture environmentally-damaged grain boundaries.

At temperatures above the age heat treatment of alloy 720Li – 760°C – changes in the γ'-precipitate volume fraction and size distribution will also contribute to the drop in yield stress and the gain in ductility. The γ'-phase volume fraction can be estimated with Thermo-Calc using the Thermotech TTNi8 thermodynamic database to drop from 45% at 760°C to 42% at 850°C to 33% at 1000°C. Tertiary and small secondary γ'-precipitates are then expected to coarsen and dissolve first reducing the strength of the alloy significantly [212] while reducing the amount of γ'-phase in the vicinity of the grain boundary available for oxidation. The change in microstructure due to the onset of the γ'-phase dissolution and the increase in ductility correlate well. In addition, Soula *et al.* [210] observed a decrease of the grain boundary sliding contribution with increasing temperature through creep test on NR6 performed at 700, 750 and 800°C under an applied stress of 700 MPa. This was linked to the dissolution of tertiary γ'-precipitates in a subsequent study [135].

In support of these postulates, distinct regions with an increase in GND density can be observed neighbouring the cracked and uncracked γ-grain boundaries and primary γ'-precipitates in Figure 4.7 (d) when HR-EBSD is applied. It seems probable that slip and slip accommodated grain boundary sliding in the mid-temperature regime leads to dislocation tangles and pileups which produce local stress concentrations at the grain boundaries which fracture intergranular oxides. In contrast, at 950°C the ability to relieve local stresses at the grain boundary increases which leads to the observed

recovery in tensile ductility. The coarsening and dissolution of the small population of the γ'-phase as well as grain boundary migration to relieve stresses are regarded to be a key effect. The absence of grain boundary regions with an increase in GND density as well as local migration of the grain boundary can be observed in Figure 4.7 (f).

The observed three temperature regimes with regards to the tensile ductility are illustrated in Figure 4.10.

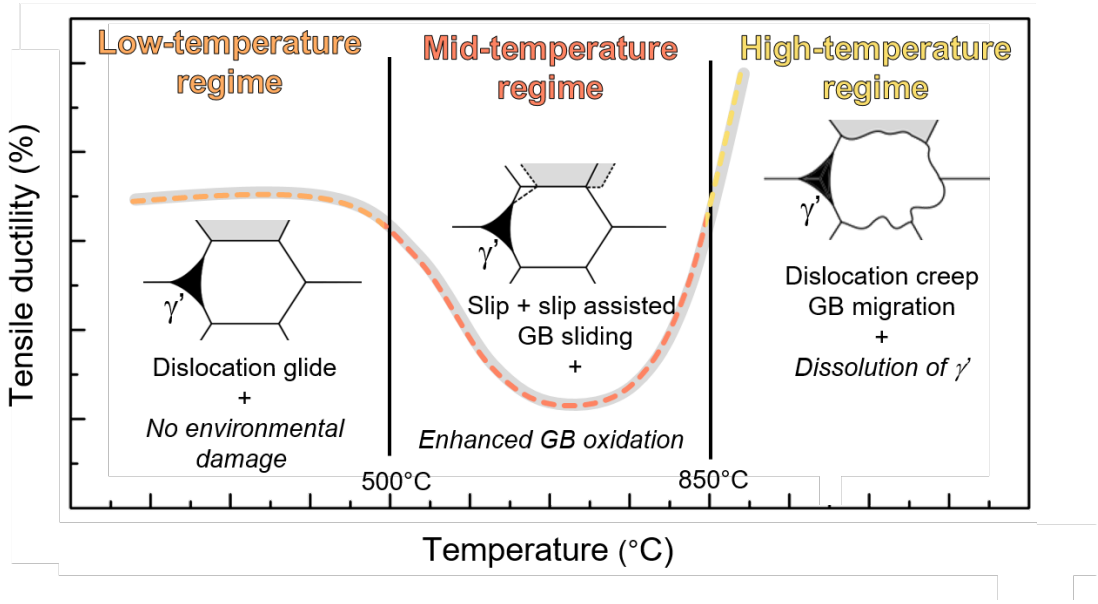


Fig. 4.10 Schematic illustration of the interplay between environmental damage and apparent deformation mechanism responsible for the observed temperature dependent ductility in Alloy 720Li.

4.4.3 On the Influence of Heat Treatment on Embrittlement

This work confirms that sub-solvus alloys such as 720Li are susceptible to environmentally-assisted cracking at operation-relevant temperatures. The microstructure conferred by the sub-solvus heat treatment exacerbates oxidation-assisted cracking mainly due to two reasons. First, the primary γ'-precipitates, $Ni_3(Al,Ti)$, act as nucleation sites for external NiO and internal TiO_2 and Al_2O_3 formation, see Figure 4.9 (c). Second,

the relatively small γ-grain size of the alloy promotes the onset of slip-assisted grain boundary sliding and the accumulation of dislocations at the grain boundaries in the mid-temperature regime.

Consequently, a super-solvus heat treatment will modify the microstructure, dissolving primary γ'-precipitates and allowing γ-grain growth. The identified relationship of tensile ductility to microstructure indicates that such changes will lead to an improvement in tensile ductility in the mid-temperature regime, prohibiting the onset of intergranular oxidation-assisted cracking. However, the resulting loss in alloy strength due to the increase in γ-grain size and the absence of primary γ'-precipitates can be counteracted by means of composition [213]. Creep properties will be improved due to the increase in γ-grain size. This is confirmed when alloy RR1000 was tested in both sub- and super-solvus heat treated condition in the mid-temperature regime. The increase in tensile ductility after a super-solvus heat treatment can be rationalised in the following way. First, the super-solvus heat treatment increases the γ-grain size. Therefore, slip-assisted grain-boundary sliding is not dominating in the studied temperature regime. Second, primary γ'-precipitates are dissolved. Both changes lower the magnitude of stress build up at the γ-grain boundaries and delays the accumulation of dislocations at the grain boundaries. In addition, the overall grain boundary content is reduced. This explains why the details of the heat treatment used for polycrystalline superalloys – and the associated changes in microstructure – influence the time-dependent crack growth behaviour of turbine disc alloys regardless of the chemical composition as demonstrated by [121]. A correlation between the macroscopic tensile strength and ductility is not observed, see Table 4.4.

4.5 Conclusions

The following specific conclusions can be drawn from this chapter:

(1) The temperature dependence of the tensile ductility is characterised by three distinct regimes. Below 600°C, the oxidising environment does not affect the ductility which then exceeds 15%; failure is transgranular as a result of homogeneous dislocation slip. But between 600 and 850°C, ductility is reduced substantially with a pronounced minimum found at 750°C of a few percent; intergranular quasi-brittle failure is then observed. Above 850°C, tensile ductility is recovered and it exceeds 25%.

(2) In the embrittled regime, the oxidation damage occurs preferentially at incoherent primary γ'-precipitates and at high angle γ-grain boundaries. Growth of internal oxide intrusions at these interfaces is the cause of the limited tensile ductility and the quasi-brittle failure. The oxide intrusions contain different phases present in an order consistent with thermodynamics and the expected gradient in equilibrium partial pressure of oxygen. Thus $(Ni_{(1-x)}Co_x)O$ is followed by spinel and closer to the crack tip Cr_2O_3, TiO_2 and finally Al_2O_3. Evidence is shown indicating alumina dissolution within the chromia layer during steady-state crack propagation. The amount of oxidation damage increases with temperature and time, thus explaining the rather more ductile behaviour at high deformation rates.

(3) The mechanism of embrittlement involves the accumulation of dislocations in the vicinity of the grain boundaries. The resulting local stresses fracture the crack-tip oxides, causing intergranular crack propagation. As the temperature is increased, grain boundaries migrate thus delaying stress build up. This explains

the regained ductility above 750°C. Above 900°C grain boundaries are fully mobile and intergranular fracture does not occur.

(4) This work has implications for the choice of heat treatment temperature for polycrystalline Ni-based superalloys. A sub-solvus heat treatment exacerbates oxidation-assisted cracking. First, the concomitant – relatively small – grain size promotes slip assisted grain boundary sliding. Second, the primary γ'-precipitates act as nucleation sites for oxide formation, in particular Ni, Ti, and Al-rich ones. Conversely, a super-solvus heat treatment dissolves primary γ'-precipitates and increases the γ-grain size in a favourable fashion, thus reducing the susceptibility to oxidation-assisted cracking.

Chapter 5

The Influence of Nb/Ti Ratio on Environmentally-Assisted Failure

Summary The effect of Nb/Ti ratio on the strength, ductility and toughness of three prototype Ni-based superalloys is studied and rationalised. Nb and Ti are γ'-forming elements and the work presented in Chapter 4 highlighted the role of γ'-precipitates with regards to grain boundary embrittlement. Whilst the properties at room temperature are insensitive to alloying, at 700°C the tensile ductility and fracture toughness are impaired – being worse for the lowest Nb/Ti ratio examined – by internal oxidation along the grain boundaries and newly formed sub-grain boundaries. For these alloys, the yield strength is unaltered with increasing Nb/Ti ratio due to an increase in grain size and this situation has allowed the rationalisation of the factors influencing damage tolerance at 700°C. Primary intergranular cracks have been investigated using energy-dispersive X-ray spectroscopy in a scanning transmission electron microscopy and the analysis if electron back-scatter diffraction patterns. Any possible detrimental effect of Nb on the observed crack tip damage due to Nb-rich oxide formation is not observed. Instead, evidence is presented to indicate that the

tertiary γ'-precipitates are dissolving ahead of the crack consistent with the formation of oxides such as alumina and rutile. Our results have implications for alloy design efforts; for any given strength level, both more and less damage tolerant variants of these alloys can be designed.

5.1 Introduction

As shown previously, brittleness due to surface-initiated intergranular attack by oxygen is the major limitation to the application of polycrystalline Ni-based superalloys, particularly in the mid-temperature regime of 600 to 800°C [214]. Hence crack initiation and/or growth can be accelerated under either static or fatigue loading situations, and therefore this phenomenon is of significant importance for high temperature applications [18]. Alloying has been found to play a role in alleviating this effect, presumably because the chemical reactions during oxidation which are promoted are then altered in subtle ways [215]. However, these are not fully understood since the mechanism responsible for intergranular crack propagation is yet to be established. Whilst this is the case, it seems unlikely that the chemistry of these alloys has yet been optimised with regards to this.

The work presented in the previous chapters has emphasised the formation of a layered oxide structure consisting of different oxide phases growing ahead of an intergranular crack. This suggests that an oxidation reaction is occurring and that it is not oxygen in its elemental form which is embrittling [117, 191, 216]. Thermodynamically less stable oxides consisting of Ni and Co are found at the beginning and centre of the crack while more stable oxides consisting of Ti and Al were found closer to the interface of the oxide and metal [117]. In particular, superalloys containing Nb are considered more susceptible to environmentally-assisted cracking due to the formation

of Nb-rich oxides such as NbO_2 and Nb_2O_5 at the grain boundary ahead of the crack tip [150, 153]. But any interpretation is made very much more complex by the interaction of chemistry, microstructure, processing and the details of the grain boundary reactions which can arise [70].

In addition, damage tolerance arising from microstructure-dependent crack tip shielding and relaxation has to be considered [194]. There are two points which are of overarching importance if progress is to be made towards improved understanding of this effect and hence its alleviation. First, there is a need for systematic experimentation involving the control of the important compositional and microstructural variables such that the effects of others can be isolated, identified and confirmed. Second, there is a need to better understand the chemical processes occurring at the grain boundaries at the most appropriate lengthscale and with techniques which are capable of providing the most revealing information. Scanning transmission electron microscopy/energy dispersive spectroscopy (STEM-EDS) and high resolution electron backscatter diffraction (HR-EBSD) are particularly well suited in this regard, and these are used in the present work.

In this study, three model powder metallurgy (PM) Ni-based superalloys are studied of varying Nb/Ti ratio. Nb partitions to the γ'-phase and in particular the Al site; it also increases the anti-phase boundary (APB) energy and thus is known to promote strength [217]. Ti behaves similarly. Both are strong oxide formers, but their thermodynamic potentials for doing so differ and therefore one might reasonably expect the Nb/Ti ratio to influence the damage tolerance displayed by these alloys in oxidative environments. Both, slow strain-rate tests and single edge notch tension tests at 700°C were performed, to elucidate the role of Nb and Ti on the strength, ductility and toughness displayed in this system. Miniature testpieces of enhanced surface/volume ratio are employed, in order to accelerate the embrittlement effect and

thus facilitate its study [192].

5.2 Experimental Design, Procedure and Rationalisation

5.2.1 Material

Three polycrystalline prototype Ni-based superalloys with Nb/Ti-ratios of 0, 0.1 and 0.4 were studied. Their nominal compositions are shown in Table 5.1. All three alloys were designed with a fixed baseline chemistry and increasing Nb levels with Nb being substituted for Ti on a 1:1 basis, using the Alloys-by-Design of approach [11, 218] and deliberately resulting in the same γ'-precipitate volume fraction. Each ABD-alloy was manufactured by ATI Powder Metals using a lab-scale version of a commercial powder metallurgy process. Powders for each alloy composition were compacted using Hot Isostatic Pressing (HIP) which involved the application of 100 MPa at 1107°C. These HIP compacts were isothermally forged at 1100°C at 0.2 min^{-1} and then given a super-solvus heat treatment conducted at 1170°C for 2 hours followed by a controlled quench of 1°Cs^{-1} to 1050°C. Finally, an ageing heat treatment at 850°C was performed for 4 hours (see Figure 5.1).

Thermodynamic calculations using Thermocalc [219] were performed to estimate the volume fraction of the γ-phase and γ'-phases resulting from the final ageing heat treatment at 850°C (see Table 5.1). Only major phases of interest were included from the thermodynamic database: γ, γ' and MC phases, all other phases were suspended. The results are summarised in Table 5.1. The γ'-solvus temperatures were estimated to be 1157, 1156 and 1154°C for ABD-2, ABD-4 and ABD-6 respectively.

The microstructure of each alloy was assessed using SEM and EBSD characterisation. Differences in the grain size were observed (Figure 5.2 (a)) and quantified though a Gaussian curve fitted to the grain size distribution obtained from EBSD analysis,

see Figure 5.2 (b). An increase in grain size is observed with increasing the Nb/Ti ratio. The mean grain size of each alloy was determined to be $d_{\mathrm{ABD-2}} = 18.5 \pm 1.5$ μm, $d_{\mathrm{ABD-4}} = 24 \pm 2.5$ μm and $d_{\mathrm{ABD-6}} = 45 \pm 9.7$ μm respectively using a grain misorientation threshold of 15°.

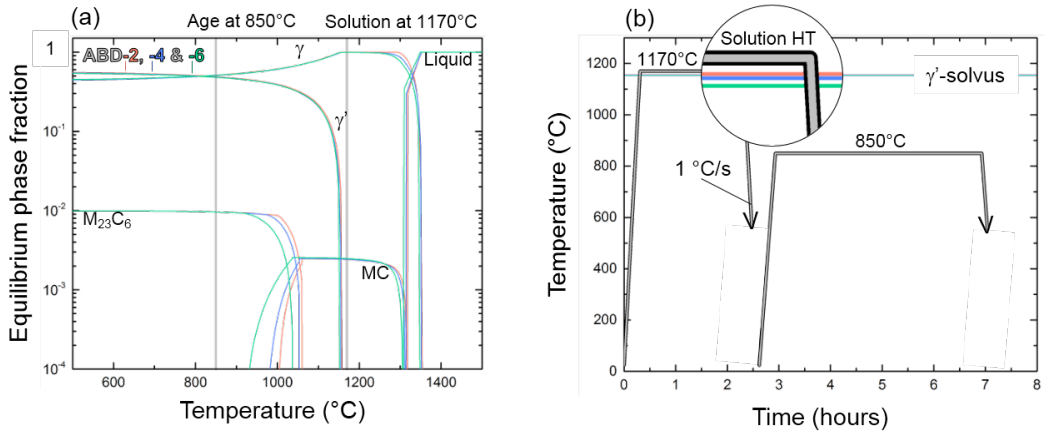


Fig. 5.1 (a) Predictions of equilibrium phase fraction versus temperature using Thermo-Calc with TTNI8 database. (b) Schematic illustration of the heat treatment cycle employed for each ABD alloy.

The grain boundaries of each ABD alloy were found to be serrated and decorated with $M_{23}C_6$ (see Figure 5.2 (c)) in addition to intragranular MC. Micrographs of each alloy composition after electro-chemical etching in an aqueous solution of 10% phosphoric acid show the intergranular secondary and tertiary γ'-precipitates (see Figure 5.3). These images were post-processed using ImageJ software [220] to obtain the mean diameter. Unlike grain size which was found to be composition dependent, the size of both secondary and tertiary γ'-precipitates were found to be alloy composition independent. The secondary γ'-precipitates were found to be on average 230 nm while the tertiary γ'-precipitates had an average diameter of 40 nm. Primary γ'-precipitates were not observed as a result of the supersolvus heat treatment. A composition independent γ'-size distribution was also demonstrated by Collins *et al.* [221] in his work utilising the same prototype ABD alloys.

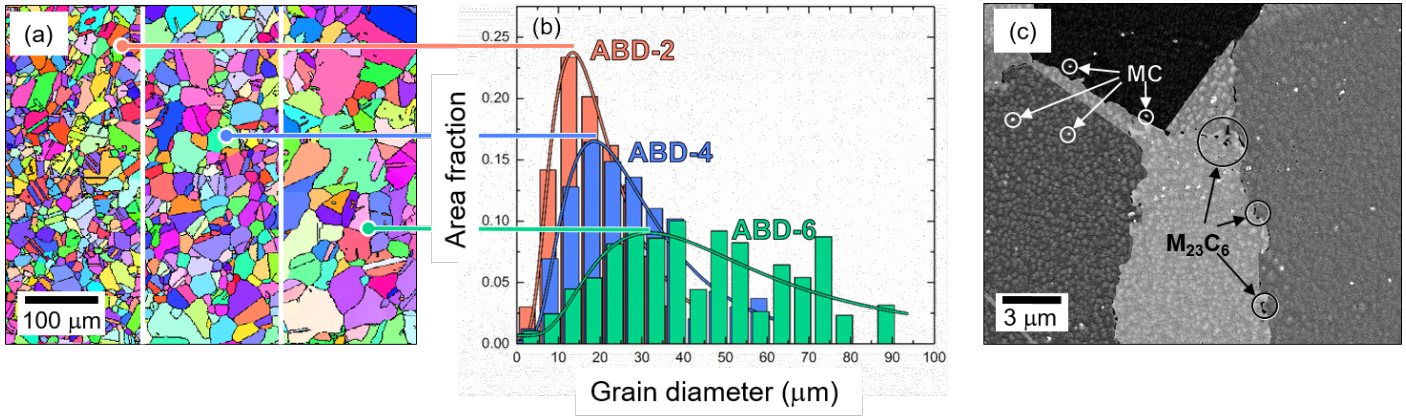


Fig. 5.2 (a) Inverse pole figure maps of each ABD alloy taken from within a 0.45 x 0.45 mm region which used to study the grain size distribution using EBSD analysis. (b) Measured grain size distribution and Gaussian fit for each ABD alloy using EBSD analysis. (c) Backscattered electron image showing the microstructure of the ABD alloys after the heat treatment cycle. The image was taken on ABD-6. The grain boundaries were found to be serrated and decorated with $M_{23}C_6$. MC-type carbides were found to be intragranular.

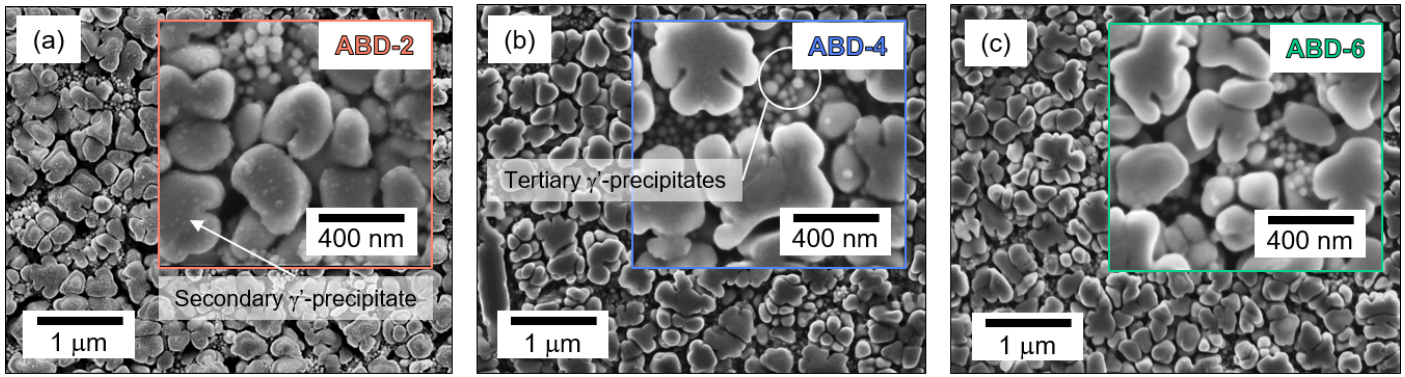


Fig. 5.3 SEM images of (a) ABD-2, (b) ABD-4 and (c) ABD-6 after electro-chemical etching in an aqueous 10 % phosphoric acid solution showing coherent intragranular secondary and tertiary γ'-precipitates.

Table 5.1 Composition of each ABD alloy and the corresponding individual phases in at.%. Phase compositions were calculated with Thermo-Calc using the Thermotech TTNi8 thermodynamic database.

Alloy	Phase fraction (mol.%)		Ni	Cr	Co	W	Al	Ti	Ta	Nb	C	B
			(at.%)									
ABD-2	Bulk nominal	-	48.5	18.9	18.5	1.0	7.9	4.3	0.7	0.0	0.13	0.05
	γ-phase	51.1	36.4	33.7	25.7	1.1	2.6	0.3	0.0	0.0	0.01	0.16
	γ'-phase	48.7	63.0	3.0	10.5	0.7	13.7	8.1	1.1	0.0	0.00	0.00
	MC-phase	0.24	0.0	0.1	0.0	1.8	0.0	42.7	7.0	0.0	47.40	0.00
ABD-4	Bulk nominal	-	48.5	18.6	18.6	0.9	7.9	4.0	0.6	0.4	0.14	0.10
	γ-phase	52.0	36.7	33.4	25.7	1.1	2.6	0.2	0.0	0.0	0.01	0.15
	γ'-phase	47.8	63.3	2.8	10.2	0.6	13.9	7.2	1.1	0.8	0.00	0.00
	MC-phase	0.25	0.0	0.0	0.0	0.1	0.0	21.7	1.4	27.5	48.27	0.00
ABD-6	Bulk nominal	-	48.1	18.9	18.8	0.9	8.1	2.9	0.6	1.2	0.12	0.11
	γ-phase	52.3	36.6	33.4	25.9	1.1	2.5	0.2	0.0	0.1	0.01	0.15
	γ'-phase	47.5	63.7	2.6	9.8	0.6	14.1	5.7	1.2	2.3	0.00	0.00
	MC-phase	0.26	0.0	0.0	0.0	0.0	0.0	12.5	0.8	37.8	47.75	0.00

5.2.2 Theoretical Modelling of the Yield Stress

The detailed interpretation which emerges in the rest of the chapter relies upon an assessment of the relative contributions to the strengthening of the alloys. Increments to the the yield stress will arise from three strengthening mechanisms: (1) Hall-Petch strengthening, (2) solid solution strengthening within the γ-matrix and (3) precipitation hardening due to resistance to shearing of the secondary and tertiary γ'-precipitates. Orowan by-passing of the γ'-precipitates can be neglected due to the absence of large primary γ'-precipitates in these alloys. The Hall-Petch effect gives:

$$\sigma_d = \frac{k_y}{\sqrt{d_\gamma}} \quad , \tag{5.1}$$

where k_y is the Hall-Petch coefficient and d_γ is the mean grain size. In this work $k_y = 501$ MPa$\mu m^{-1/2}$ was used, based on work performed on Nimonic 105 with a comparable γ'-phase volume fraction of $f_{\gamma'} = 47\%$ [222]. The strengthening effect due to changes in the γ-matrix chemistry, σ_{ss}, was determined using the method of Gypen & Deruyttere [223] using the following equation:

$$\sigma_{\text{ss}} = (1 - f_{\gamma'})\left(\sum_i k_i^n c_i\right)^{1/n} \quad , \tag{5.2}$$

where c_i is the concentration of solute i, and k_i is the strengthening constant for solute i. The value of n, a constant, is taken to be 2/3 [17]. A further increase in the yield stress results from solute atoms acting as frictional obstacles for dislocation slip. The strengthening constants in Ni, k_i, have been estimated by Mishima *et al.* [224]. The calculated chemical composition of the γ-matrix is summarised in Table 5.1 for each ABD alloy. The final precipitation shearing stress was estimated using a model proposed by Galindo-Nava [213] which allows one to calculate the γ'-precipitation

hardening contributions using an estimate mean radius for the secondary and tertiary γ'-precipitate size, r_s and r_t:

$$\sigma_p = M\frac{\gamma_{APB}}{2b}\left(w_s\frac{l_s}{\Lambda_s + 2r_s} + w_t\frac{l_t}{\Lambda_t + 2r_t}\right) \quad , \tag{5.3}$$

where M is the Taylor orientation factor, γ_{APB} is the anti-phase boundary energy of the γ'-phase, b is the magnitude of the Burgers vector, w_s and w_t are the particle number fractions of secondary and tertiary γ'-precipitates, l_s and l_t are the average segment lengths of the leading dislocation acting in the cutting of a secondary and tertiary γ'-precipitate, Λ_s and Λ_t are the average effective lengths of the leading dislocations driving the secondary and tertiary γ'-precipitate cutting. Values for the Taylor orientation factor and the Burgers vector are taken to be 3 and 0.248 nm respectively. The anti-phase boundary energy of the γ'-phase at 0K were obtained from theoretical predictions employing DFT and are as follows: $\gamma_{\mathrm{APB}}^{\mathrm{ABD}-2} = 0.344$, $\gamma_{\mathrm{APB}}^{\mathrm{ABD}-4} = 0.349$, $\gamma_{\mathrm{APB}}^{\mathrm{ABD}-6}$ $= 0.36$ Jm^{-2} [11]. These values were fitted to the following polynomial function to capture the effect of temperature at 700°C as proposed by Galindo-Nava *et al.* [213]: $\gamma_{\mathrm{APB}} = \gamma_{\mathrm{APB}}^{0K} - (7\cdot10^{-6}\,T - 3\cdot10^{-8}\,T^2)$. The γ'-precipitate shearing stress is controlled by strong-pair coupling since both r_s and r_t are greater than the particle radius when the maximum strength is defined by $r_m = \mu b^2/2\gamma_{\mathrm{APB}}$, with $\mu = E/(2(1+v))$ and $v = 0.32$. The following analytical expressions were used to capture the effect of temperature $\mu = 87.3 - 9\cdot10^{-4}\,T - 1.9\cdot10^{-5}\,T^2$ [213]. The length of the leading dislocation cutting the precipitates is expressed as $l = 2(r^2 - (r - r_m)^2)^{(1/2)}$ and the effective length of the leading dislocation driving γ'-precipitate cutting is given by $\Lambda = \max\{\lambda, \mathrm{L} - \mathrm{l}\}$. λ is the Friedel sampling length which is defined by $\lambda = (2T_{ten}/r\cdot\gamma_{\mathrm{APB}})$, where T_{ten} is the dislocation line tension and given by $0.5\cdot\mu b^2$ and L is the mean particle spacing $L = (2\pi/3f_{\gamma'})^{1/2}\cdot r$.

5.2.3 Experimental Assessment of the Mechanical Properties

As described in chapter 3, tensile testing was conducted at a slow strain-rate of $1{\cdot}10^{-4}$ s^{-1} at room temperature and at 700°C using a 5 kN Instron electro-thermal mechanical testing (ETMT) machine. Detailed information relating to the design and operation of the ETMT equipment can be found elsewhere [177]. Miniaturised specimens of cross-section 1×1 mm^2 and a gauge length of 14 mm were used; the full sample length was 40 mm. Great care was taken with preparation of specimens. These were produced using wire-based electrical discharge machining (EDM), with surfaces subsequently ground to 1200 grit to maintain a consistent surface finish and to remove the recast layer resulting from the EDM process. Consistent with the design of the ETMT machine, specimens were heated using electrical resistance by passing a direct current through the specimen. Temperature measurement during testing was achieved by spot-welding a K-type thermocouple to the central portion of the specimen gauge. A minimum of three tests were performed at each condition, at a constant extension rate consistent with a linear variable displacement transformer (LVDT). The engineering strain was used as a measure of the ductility; engineering strain is defined as: $\varepsilon = [(L_f - L_0)/L_0]$, where the gauge length extension $L_0 - L_f$ was monitored using digital image correlation measurements of a thermal paint pattern applied in the central 5 mm of the specimen where the temperature and therefore deformation is uniform [192]; a detailed description is given in Chapter 3.

To quantify the conditional fracture toughness at 700°C in air, additional ETMT testing was carried out using single edge notch tension specimens. The specimens described above were modified by machining a circular notch on one side to a depth of 150 μm. From this notch a low cycle fatigue crack was grown at room temperature under load control using an R-ratio of 0.1 and a 2 Hz sinusoidal cycling waveform. A

maximum stress level of 95 % of σ_y was applied. Hereafter the pre-fatigue cracked test pieces were subjected to a constant extension rate of $5{\cdot}10^{-4}$ mm s^{-1} at 700 °C causing the environmentally-assisted growth of the crack. Upon crack growth, tests were interrupted by unloading and simultaneously reducing the temperature to ambient with a cooling rate close to 100°Cs^{-1}.

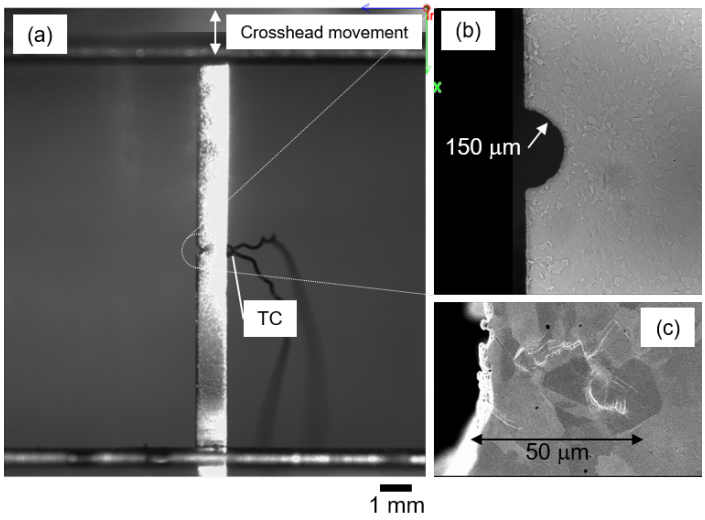


Fig. 5.4 (a) Overview of the ETMT single edge notched tension specimen. (b) Optical micrograph of the 150 μm circular notch in ABD-4 before testing. (c) SEM image of a 50 μm low cycle fatigue pre-crack in ABD-4.

The conditional fracture toughness, K_q, was calculated with conditional load P_q obtained from the load displacement curve and the measured initial crack length, a, according to the following equation:

$$K_q = \frac{P_q}{A}\sqrt{\pi a} \cdot Y \quad , \tag{5.4}$$

where P_q is the maximum load that the specimen could withstand before quasi-brittle crack propagation occurred, and A is the specimen cross-section area. The term Y is

a geometry factor, taken from [225] and is given by:

$$Y = 1.12 - 0.23\left(\frac{a}{w}\right) + 10.6\left(\frac{a}{w}\right)^2 - 21.7\left(\frac{a}{w}\right)^3 + 30.4\left(\frac{a}{w}\right)^4 \quad , \tag{5.5}$$

where w is the specimen width. The determined conditional fracture toughness, K_q, has to be regarded as a geometry-dependent material parameter, due to the amount of crack tip constraint arising due to the miniaturised ETMT tests.

5.2.4 Fractography and Damage Analysis

The microstructure of each alloy both before and after testing was characterised with a Zeiss Merlin scanning electron microscope (SEM). Secondary/backscattered electron imaging and HR-EBSD analysis were used. Diffraction patterns were acquired with a Bruker Quantax EBSD system – at a 800 x 600 pixels^2 resolution to provide suitable angular resolution, and saved for subsequent analysis. Using an in-house method to measure the lattice curvature, the distribution of geometrically necessary dislocations (GNDs) was estimated with the help of Dr. D.M. Collins following Wilkinson *et al.* [201]. Fractography was supported by a Zeiss Merlin FEG SEM equipped with an in-column energy selective backscattered (ESB) detector and an Oxford Instruments XMax 150mm^2 detector for obtaining SEM-EDX elemental maps. Samples for transmission electron microscopy (TEM) were prepared together with Dr. V. Kuksenko by focussed ion beam thinning in a Zeiss Auriga dual beam system. Annular bright-field (ABF) and high angle annular dark field (HAADF) images as well as STEM-EDS elemental maps were acquired with the help of Dr. C.H. Liebscher at the Max-Planck-Institut für Eisenforschung in a probe corrected FEI Titan Themis 60-300 microscope equipped with a ChemiSTEM Si-drift EDS-system operated at 300 kV. A probe semi-convergence angle of 17 mrad was used to form the electron probe. The semi-collection

angles for ABF and HAADF imaging conditions were chosen to be 8-16 mrad and 17-73 mrad, respectively.

5.3 Results

5.3.1 Characterisation of the Mechanical Properties

Engineering stress-strain curves are shown in Figure 5.5 at both ambient temperature and 700°C at a strain-rate of $1{\cdot}10^{-4}$ s^{-1}. At room-temperature the alloys showed no significant variation in yield stress, at 935 ± 10 MPa, and ultimate tensile stress (UTS), at 1460 ± 0 MPa; moreover, the tensile ductility showed no dependence on the Nb/Ti ratio and was determined to be 26.7 ± 0.1%. At 700°C all three alloys showed the same 0.2% proof stress of 792 ± 3 MPa but significantly the tensile ductility now varied appreciably. The UTS increased with increasing ductility due to the increased amount of work hardening as a function of sample elongation.

Table 5.2 The mechanical properties of each ABD alloy when tested in laboratory air with an initial strain-rate of $1{\cdot}10^{-4}$ s^{-1}. Mean results and standard deviation (SD) of a minimum of three test repetitions are given. Corresponding individual stress-strain curves are shown in the Appendix A.

Alloy	Temperature (°C)	YS (MPa)	UTS (MPa)	Tensile ductility (%)
ABD-2, 4, 6	23	935 ± 10	1460 ± 0	26.7 ± 0.1
ABD-2	700	794 ± 8	911 ± 12	4.2 ± 1
ABD-4	700	795 ± 10	942 ± 13	5.4 ± 0.6
ABD-6	700	788 ± 14	979 ± 5	7.8 ± 1.1

For tests at 700°C, ABD-2 showed the least ductility at 4.2 ± 1% whilst ABD-4 showed an increase in ductility to 5.4 ± 0.6%. The highest tensile ductility was observed for ABD-6 at 7.8 ± 1.1%. This is illustrated in Figure 5.5 (b) together with SEM images of cross-sections through failed specimens. The tensile properties obtained for each alloy are summarised in Table 5.2.

Thus, tensile ductility in the mid-temperature regime increased as a function of the Nb/Ti ratio (see Figure 5.6 (a)) despite the alloys all having the same yield stress. The observed loss in ductility in the mid-temperature regime is consistent with recent observations made on other superalloy systems [36, 170, 193, 216] and can be explained by the occurrence of intergranular quasi-brittle failure. Crack propagation along the grain boundaries at 700°C also explains the relatively low conditional fracture toughness (see Figure 5.6 (b)). Just like the tensile ductility, toughness increased with increasing Nb/Ti ratio.

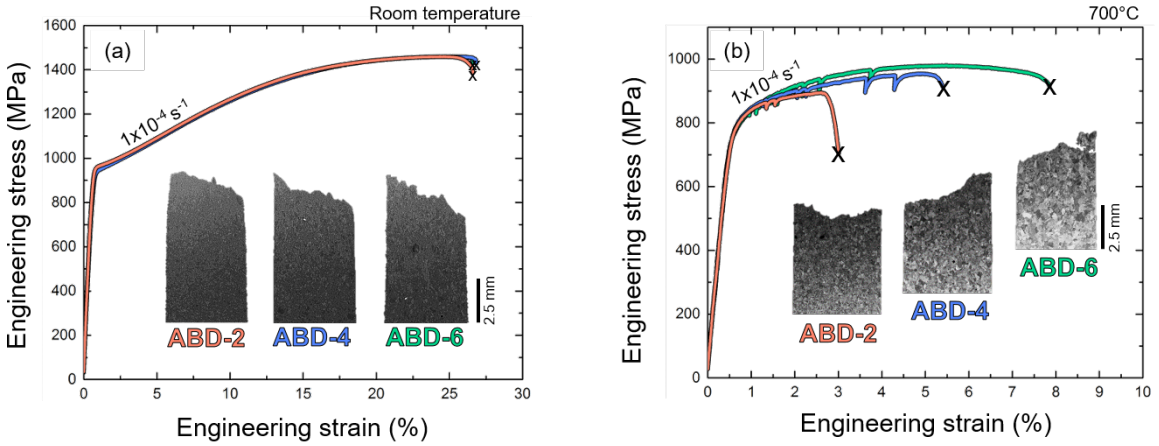


Fig. 5.5 (a) Representative stress-strain curves for ABD alloys at room temperature using an initial strain-rate close to $1{\cdot}10^{-4}$ s^{-1}. At room temperature all three ABD alloys experience the same 0.2% proof stress and tensile ductility. (b) Representative stress-strain curve for each ABD alloy at 700°C and an initial strain-rate close to $1 \cdot 10^{-4}$ s^{-1} showing differences in tensile ductility. Cross-sections of the failed specimens are shown. Individual stress-strain curves are shown in the Appendix A.

ABD-2 exhibited the lowest conditional fracture toughness with 19.7 ± 0.5 MPa$\sqrt{\text{m}}$ followed by 21.8 ± 1.2 and 24.6 ± 0.4 MPa$\sqrt{\text{m}}$ for ABD-4 and 6 respectively. This is summarised in Table 5.3 together with the maximum applied load P_{max} and the estimate pre-crack length, a, from which the conditional fracture toughness K_q was calculated using Equation 5.4. The pre-crack and sample geometry were maintained between the tests so that comparisons between alloys are valid.

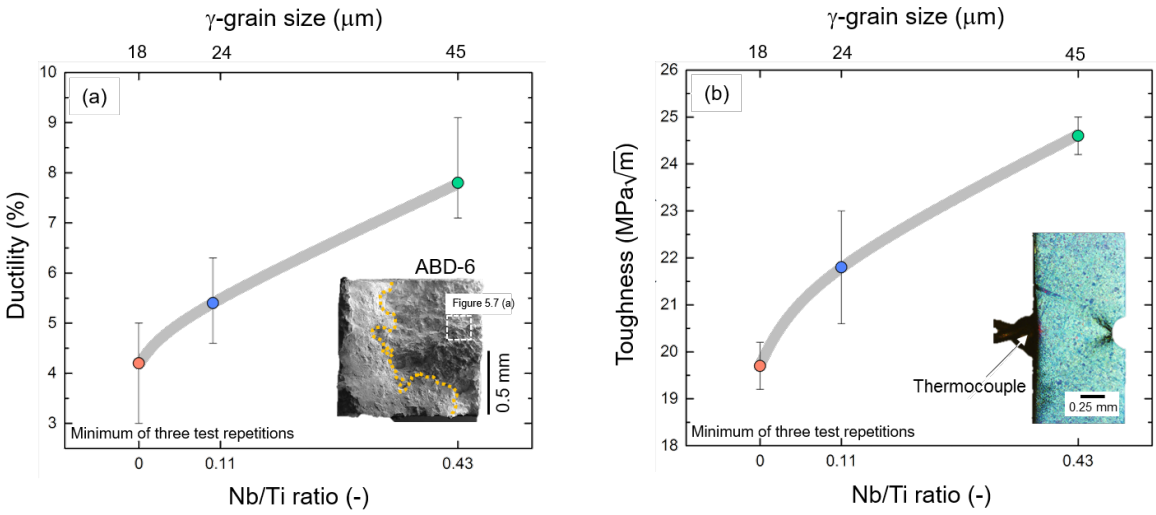


Fig. 5.6 (a) Variation in tensile ductility at 700°C for slow strain-rate tensile tests performed on ABD alloys. Error bars represent the standard deviation of a minimum of three test repetitions. A SEM image of the fracture surface of ABD-2 shows the surface initiated intergranular quasi-brittle failure. (b) Variation in conditional fracture toughness, K_q, for each ABD alloy at 700°C. K_q has been calculated from the maximal applied force when pronounced crack growth occurred; error bars represent the standard deviation of a minimum of three test repetitions. A miniaturised single edge notched tension specimen is show. The thermocouple is attached opposite of the notch location.

Table 5.3 Conditional fracture toughness calculated from the maximum obtained load and the measured initial crack length for each ABD alloy. Mean results and SD of a minimum of three test repetitions are given.

Alloy	K_q (MPa$\sqrt{\text{m}}$)	P_{max} (N)	a_0 (μm)
ABD-2	19.7 ± 0.5	543 ± 38	213 ± 13
ABD-4	21.8 ± 1.2	621 ± 35	207 ± 5
ABD-6	24.6 ± 0.4	663 ± 21	220 ± 0

The yield stress obtained at 700°C is constant regardless of the apparent changes in Ti/Nb ratio and grain size. To rationalise this, the yield stress was theoretically assessed for each alloy composition including the three dominant strengthening contributions, as described in Subsection 5.2.2: (1) Hall-Petch strengthening (σ_d), (2) solid solution strengthening within the γ-matrix (σ_{ss}) and (3) resistance to shearing of the

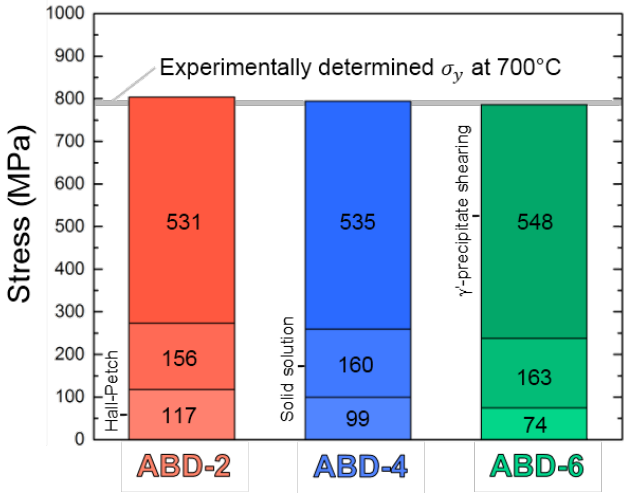


Fig. 5.7 Model estimation of the individual contributions to the yield strength at 700°C and the experimentally determined yield stress for the ABD alloys.

secondary and tertiary γ'-precipitates (σ_p) The estimated strengthening contributions for each alloy are summarised in Table 5.4.

Table 5.4 Yield stress prediction and the respective individual strengthening contributions for each ABD alloy at 700°C.

Alloy	Yield stress prediction (MPa)	σ_d (MPa)	σ_{ss} (MPa)	σ_p (MPa)
ABD-2	804	117	156	531
ABD-4	795	99	160	535
ABD-6	786	74	163	548

The yield strength modelling predictions are in good agreement with the experimental results. Figure 5.7 shows the yield stress prediction at 700°C and compares it against the experimental results.

By comparing individual strength contributions, one can see that γ'-precipitate shearing resistance provides the majority of the strength in the mid-temperature regime whilst Hall-Petch strengthening is the lowest component of the overall yield stress. The predicted strength loss with increasing grain size for ABD-6, a stress de-

crease of 43 MPa, is counteracted by the increase in the γ'-precipitate shearing stress and γ-solid solution strengthening resulting in a stress increase of 24 MPa. The APB energy of the γ'-phase increases with increasing Nb additions thereby increasing its resistance to cutting. The results thus far confirm that for alloy of an equivalent strength there can be substantial difference in ductility and toughness, resulting from changes in phase chemistry and alloy microstructure, in particular grain size.

5.3.2 Characterisation of Environmentally-Assisted Failure

The loss in tensile ductility at 700°C is associated with an increase in the ease of intergranular crack propagation. Intergranular regions on the fracture surface failed perpendicular to the applied load and showed signs of environmental damage. Regions without environmental damage failed at 45° to the tensile axis. Figure 5.8 (a) shows a representative secondary electron SEM image of the intergranular fracture surface at 700°C in ABD-2. The fracture surfaces observed for each alloy showed similar characteristics. Secondary cracks branch off the primary crack which led to failure. Secondary cracks were consistently found along high angle grain boundaries which act as preferred paths for crack propagation (Figure 5.8 (b), and (e)). Moreover, SEM-EDS mapping showed that the cracked grain boundaries are decorated with oxidation products, see Figure 5.8 (c). It is suggested that secondary cracks did not propagate at the time of failure. This could have otherwise lead to subsequent oxidation and have altered the damage ahead of the crack tip.

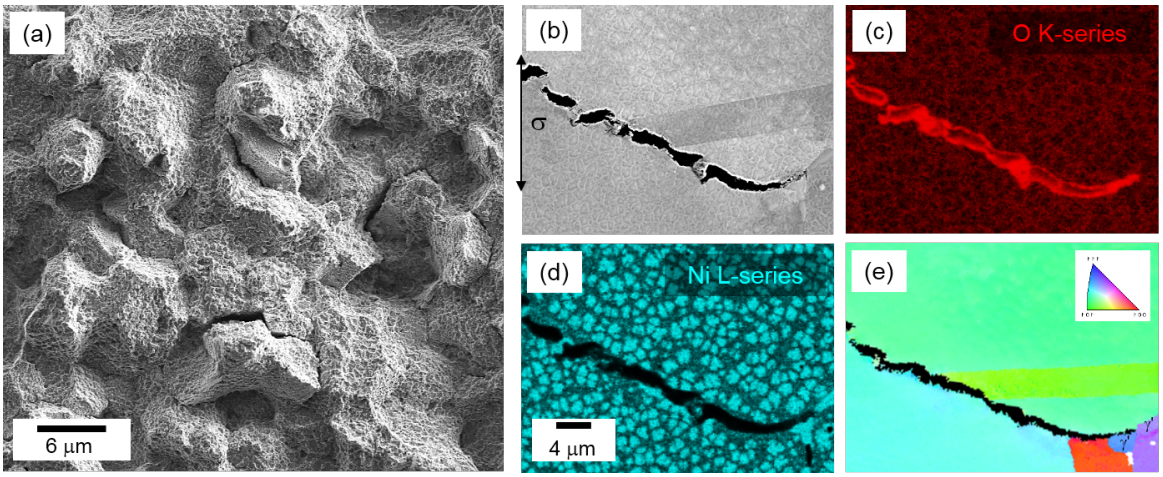


Fig. 5.8 (a) Example SEM image of an intergranular fracture surface following failure at 700°C in ABD-2. Grain contours can be clearly identified. (b) Interganular secondary cracks close to the fracture surface at 700°C in ABD-2. Cracks which propagated primarily along high angle grain boundaries and incoherent primary γ'-interfaces are filled with oxidation products. These observations were confirmed using EDX mapping (c), (d) and EBSD inverse pole figure map with respect to the loading direction (e).

Primary cracks from interrupted miniaturised single edge notched crack growth tests in alloy ABD-2 and 6 were chosen for further characterisation using high resolution characterisation techniques such as EBSD analysis to provide an estimate of the GND density distribution and STEM-EDS mapping for elemental distribution. All characterisation was performed along the crack growth direction normal to the crack face in the centre of the testpiece (see Figure 5.9 (a)). Figure 5.9 (b) and (c) shows two EBSD inverse pole figure maps with respect to the loading direction on sections through interrupted primary cracks in ABD-2 and 6, respectively. A transition from transgranular to intergranular cracking can be observed after the first $\approx$ 50 μm. The transgranular crack growing from the notch is a result of the room temperature fatigue pre-cracking. The fine grained alloy ABD-2 shows a straight fracture path. In contrast, the crack in the coarse grained ABD-6 is more tortuous and the opening displacement is reduced. HR-EBSD has been used to calculate an estimate of the GND density distribution with a step size of 450 nm in a 200 x 175 μm area

within the wake of each crack. In ABD-2 this area showed a low overall GND density. This can be observed in Figure 5.9 (d) and highlights the quasi-brittle nature of the intergranular crack propagation. Regions neighbouring the intergranular crack show higher GND densities. In addition, there is evidence of a GND storage at the grain boundaries and at triple junctions indicating some amount of deformation at or near the grain boundaries. Figure 5.9 (e) shows that in ABD-6 the GND storage near grain boundaries is less localised suggesting that intragranular deformation is more pronounced. A high GND density is revealed in a bridging grain which is surrounded by the intergranular crack. Figure 5.9 (f) and (g) shows a magnified EBSD and GND map of the intergranular crack tip in ABD-6. The GND density distribution here was calculated with a 100 nm step size showing the accumulation of damage at locations where the grain boundary is serrated and directly ahead of the crack tip. At the tip, the crack is deflected around a smaller grain. In addition, damage accumulation and cracking of a particle, presumably TiN, can be seen within the plastic zone ahead of the crack tip.

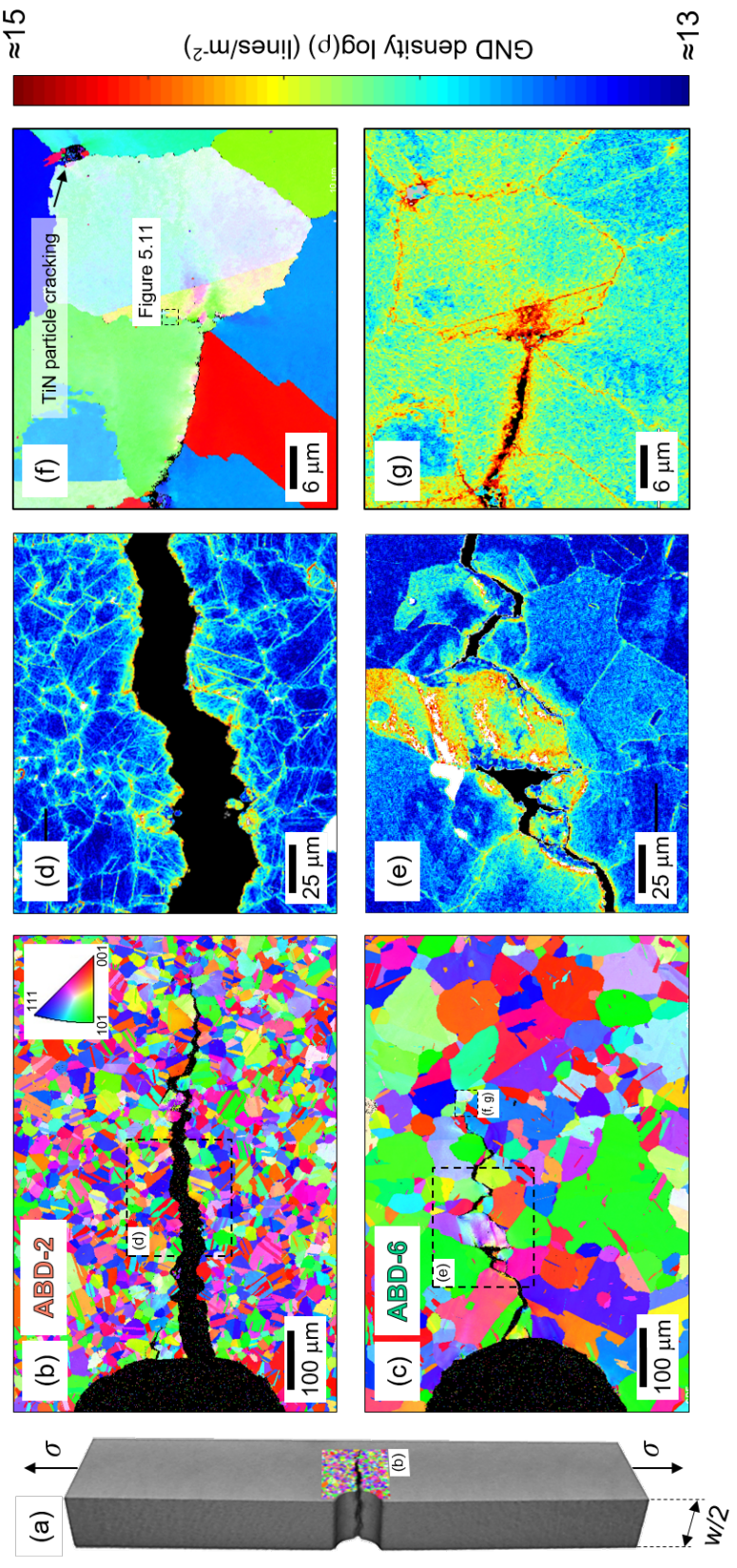


Fig. 5.9 (a) Overview of a interrupted crack growth sample indicating sectioning plane through the center with w being the original sample thickness of 1 mm. (b) and (c) show inverse pole figure maps with respect to the loading direction on sections normal to the crack face in ABD-2 and 6. Corresponding maps of GND densities calculated from measured lattice curvatures obtained from EBSD maps in the crack wakes are shown in (d) and (e), respectively. (f) Inverse pole figure map with respect to the loading direction of a representative intergranular primary crack tip in ABD-6; (g) shows the corresponding GND density map.

To study the nature of the environmental attack leading to the observed intergranular failure, TEM samples were extracted containing a primary crack tip as demonstrated in Figure 5.10.

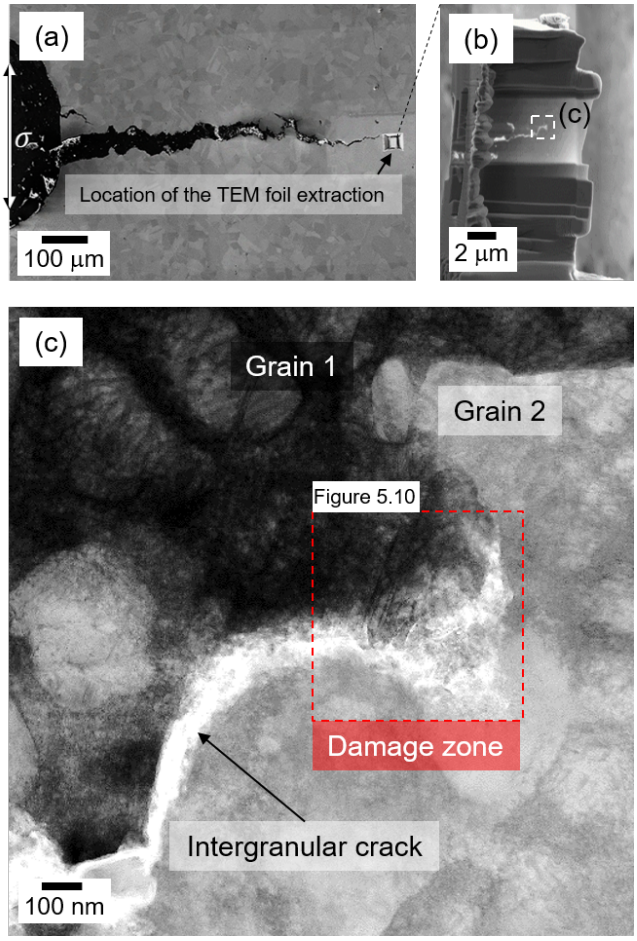


Fig. 5.10 (a) SEM image of a cross section though the middle plane of a interrupted miniaturised single edge notched tensile test in ABD-2. The location of the TEM sample containing the primary crack tip is highlighted. (b) SEM image of the TEM sample imaged at 7 kV. (c) Overview ABF-SEM image showing the intergranular nature of the primary crack in ABD-2.

The Z-contrast HAADF-STEM images shown in Figure 5.11 (a) and 5.12 (a) illustrates an environmentally-damaged zone ahead of the crack tip. The size of this was found to be independent of alloy composition at a total length of $\approx$ 770 nm and a width of $\approx$ 130 nm narrowing down into the undamaged grain boundary ahead – while

intergranular environmental damage is most pronounced the environmental damage can be observed to penetrate the grains (see Figure 5.11 (b) and 5.12 (b)). No significant differences in the damage morphology was observed as a function of Nb/Ti ratio. Figure 5.11 (c) and 5.12 (c) show composite STEM-EDS elemental maps. The overlap of O-K_α and Cr-L_α X-rays was not found to influence the qualitatively-obtained elemental distributions which show the relative elemental distribution integrated over the specimen thickness. More details of the surrounding microstructure such as the tertiary γ'-precipitates are clearly visible in specimen ABD-2 compared to ABD-6. This effect is related to an increased sample thickness of ABD-6. From these images a Co and Cr-rich region can be identified mainly in the middle of the damage zone at the γ-interfaces. Regions which are Ni and Cr-rich are present close to the damage zone at the γ'-interfaces. There is evidence suggesting the formation of a distinct Cr-rich oxide layer present in both alloys. In addition, O is observed to penetrate secondary γ'-precipitates. Internal oxides where found to be Ti and Al-rich. Nb and Ta were found to accumulate in the γ'-precipitates but were not observed to concentrate in the O-rich regions. Close to the undamaged grain boundary in ABD-6 a Ti and Nb-rich particle, presumable a laves phase, is shown in Figure 5.12 (c). This particle did not exhibit enhanced oxidation damage.

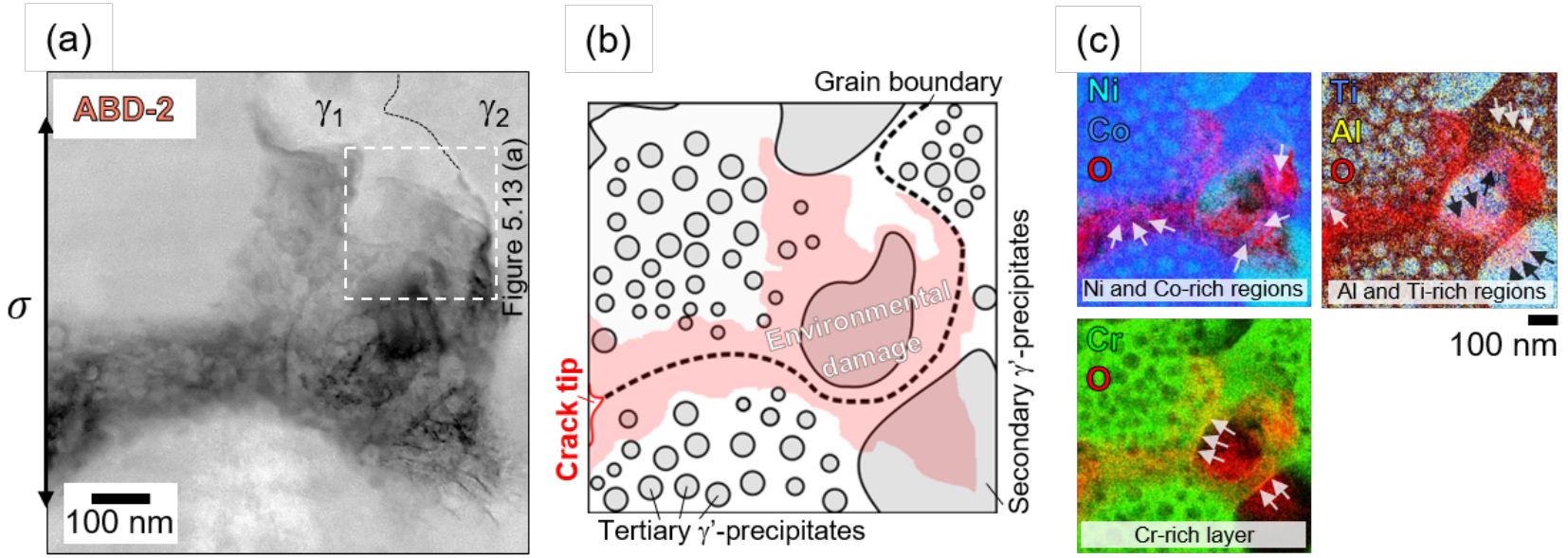


Fig. 5.11 HAADF-STEM image of an environmental damage zone ahead of a crack tip in (a) ABD-2, (b) show a corresponding schematic illustration highlighting the environmental damage zone ahead of the crack tip. Composite STEM-EDS elemental maps of O with Ni and Co, Al and Ti as well as Cr are illustrated in (c). The brightest pixels indicate the highest count areas and dark or black areas indicate little or no X-ray counts. The arrows indicate high X-ray count areas. Corresponding individual STEM-EDS elemental maps are shown in Appendix B.

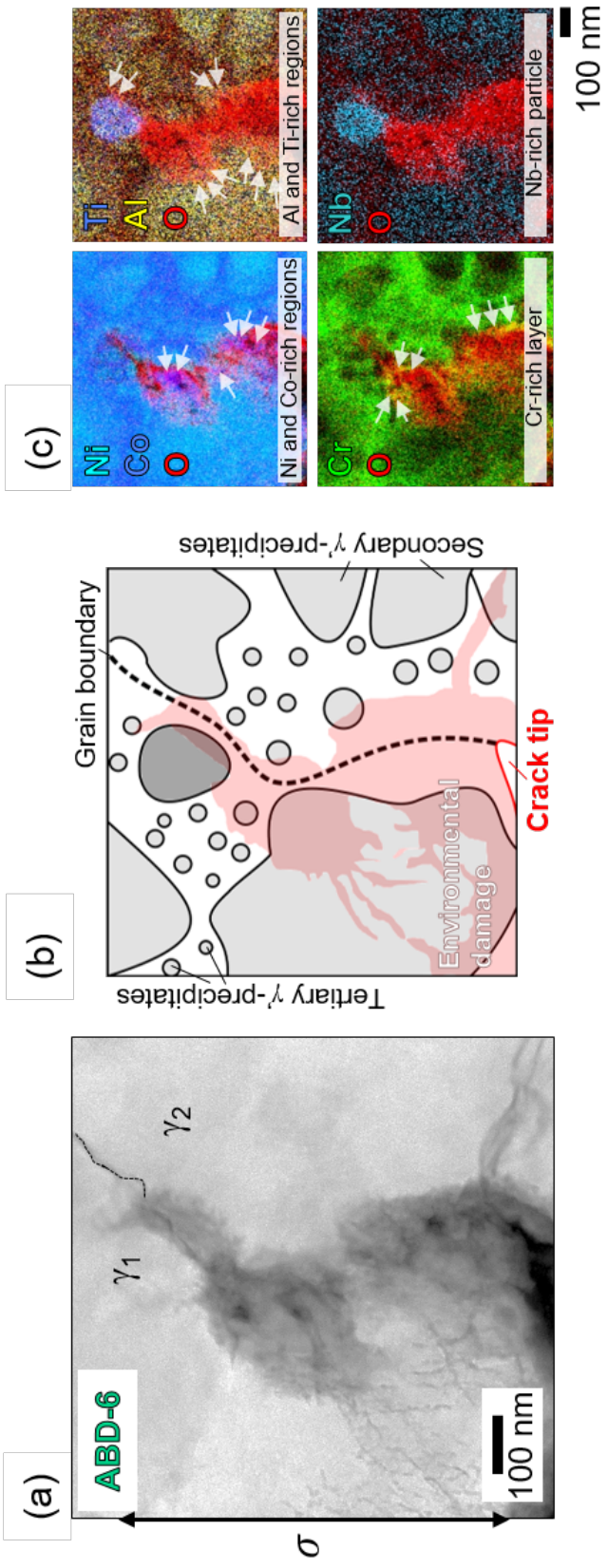


Fig. 5.12 HAADF-STEM image of an environmental damage zone ahead of a crack tip in (a) ABD-6, (b) show a corresponding schematic illustration highlighting the environmental damage zone ahead of the crack tip. Composite STEM-EDS elemental maps of O with Ni and Co, Al and Ti as well as Cr are illustrated in (c). The brightest pixels indicate the highest count areas and dark or black areas indicate little or no X-ray counts. The arrows indicate high X-ray count areas. Corresponding individual STEM-EDS elemental maps are shown in Appendix B.

A Ni-rich single phase tertiary γ'-precipitate free zone is observed in ABD-2 ahead of the environmental damage zone closest to the undamaged grain boundary (Figure 5.13 (a)). Figure 5.13 (b) shows individual STEM-EDS elemental maps and Figure 5.13 (c) demonstrates the results of a linescan taken across the sub-boundary of the Ni-rich single phase γ'-phase depleted zone. Striking is the observation that oxygen seems to penetrate a sub-boundary along the Ni-rich region and not the grain boundary. At this sub-boundary an enrichment in Ti and Al is observed. Ni, Co and Cr are depleted in this location.

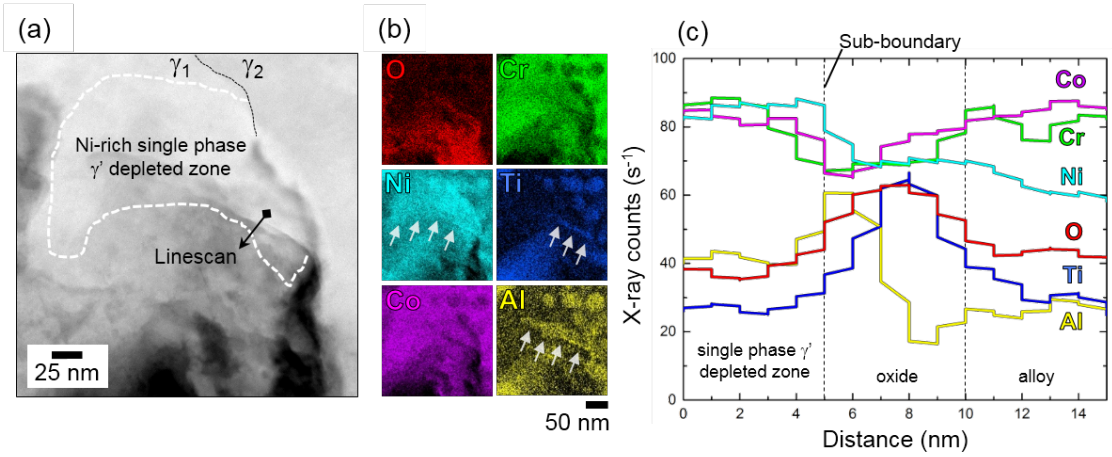


Fig. 5.13 (a) High angle annular dark field STEM image obtained in ABD-2 at the region closest to the undamaged grain boundary shown in Figure 5.11 (a). Corresponding individual STEM-EDS elemental maps are shown in (b) and Appendix B. (c) Linescan obtained across the sub-boundary of the single phase γ'-precipitate depleted zone. A fast Fourier transform filter method was applied to the line profiles.

5.4 Discussion

The results presented above demonstrate conclusively a relationship between the Nb/Ti ratio and the alloys susceptibility to environmentally-assisted cracking at 700°C. Nonetheless, a number of unresolved issues emerge and these are now considered in this section of the chapter.

5.4.1 On the Mechanism of Environmentally-Assisted Grain Boundary Embrittlement

The nature of the mechanism of embrittlement in these alloy systems has been the subject of intense interest; one significant issue is the challenge associated with the choice of the most appropriate analytical tool for the characterisation of damage. Here, STEM-EDS in the TEM has been employed on carefully prepared crack tips; this combination has been particularly insightful. An environmentally-damaged zone penetrating the grain boundary ahead of primary crack tips has been confirmed; within this the formation of a tertiary γ'-precipitate free-zone is formed which complements the commonly-emphasised oxide formation close to the crack tip, which is also observed here. It is this combination of damage which is responsible for intergranular crack propagation which in turn leads to the observed low tensile ductility and low conditional fracture toughness at 700°C (Figure 5.6). But which of these is the more important in controlling the loss of ductility?

Particularly pertinent is the observation that the size and order of the reaction products in the environmentally-damaged zone ahead of the crack tip is independent of the Nb/Ti ratio, see Figure 5.11. The appearance is broadly consistent with

the sequence expected from the relative thermodynamic stability of the individual oxidation products, as seen in Figure 5.11 (c) and 5.12 (c), as reported elsewhere [115, 117, 191, 192, 216]. Thus, an Al-rich oxide (Al_2O_3) alongside a Ti-rich oxide (TiO_2) are found closest to the undamaged grain boundary, resulting from the oxidation of these reactive elements which are found in the γ'-precipitates, Ni_3(Al,Ti). Therefore, these oxides are associated with extension of the environmentally-damaged zone. This is supported by the observation of a tertiary γ'-phase depleted zone which is present ahead of the advancing internal oxide as shown in Figure 5.13 (a) and (b). Unlike during the formation of a surface oxide layer, oxygen is readily available at the furthest extent of the oxide intrusion. Because the metal/oxide interfaces are aligned parallel to the direction of oxide growth they act as short-circuits for oxygen diffusion, see Figure 5.14. Thus, the damage zone extension during steady-state crack propagation is limited by the dissolution of tertiary γ'-precipitates and the migration of Al and Ti cations to the oxide/metal interface ahead of the oxide intrusion. For the simple case of Ni_3Al precipitates the rate controlling reaction is $\gamma' \rightarrow \gamma + Al_2O_3$. The compositional gradient produced by the depleted zone is assumed to act as an additional driving force for the metal ion diffusion.

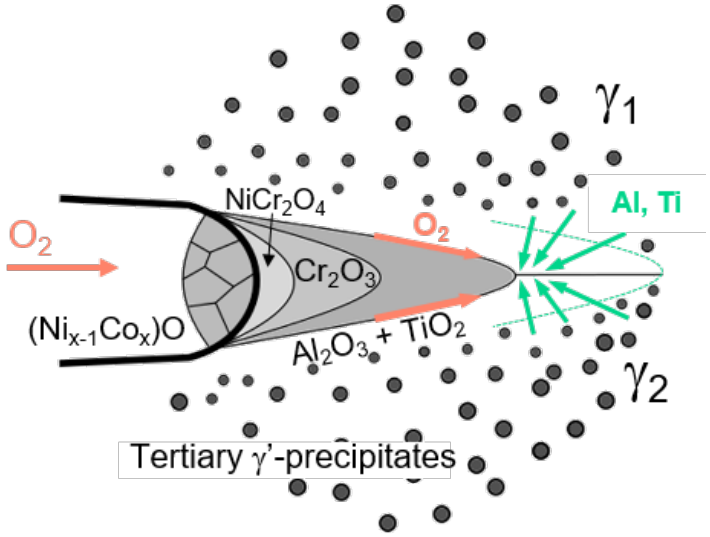


Fig. 5.14 Schematic diagram of the grain boundary embrittling crack tip oxide in the thermodynamic sequence of $(Ni_{x-1}Co_x)O$, NiCr2O4, Cr_2O_3 and Al_2O_3 + TiO_2 adapted by [216]. Oxygen diffusion along the metal/oxide interfaces and the dissolution of tertiary γ'-precipitates results in the formation of Al_2O_3 and TiO_2 at the undamaged grain boundary.

It is important to note that the formation of discrete Nb-rich oxides ahead of interrupted primary cracks has not been observed here. Thus it would appear that any influence of Nb cannot be attributed to its oxidation. This finding is in contrast to the work of Miller & Wei *et al.* [144, 150, 152, 153] who have studied a number of Nb-containing alloys including IN718. They have suggested that even small additions of Nb increase the susceptibility to environmental-assisted creep crack growth due to the formation of Nb-rich oxides ahead of the crack tip, including NbO_2 and Nb_2O_5. The results presented here indicate that small additions of Nb – up to 2.1 wt-% – are however not detrimental and indeed are advantageoous. While the formation of Nb-rich oxides is more favoured by thermodynamic equilibrium than TiO_2, Nb is not as abundant as Ti in for example alloy ABD-6 (see Table 5.1) and is believed to stay in solution. Thus, it seems likely that the threshold for Nb to have any negative effect

is associated with the formation of γ''-precipitates, Ni_3Nb, at the grain boundary. Our findings are in agreement with Telesman *et al.* [121] who showed that hold time crack growth resistance was insensitive to small changes in the Nb content in Alloy 10.

The above suggests that it is the loss of tertiary γ'-precipitates which is detrimental to the localised mechanical properties. This would explain why the tip of the oxide intrusion in ABD-2 does not follow the prior grain boundary (see Figure 5.13 (b)). It nucleates along what is believed to be a newly formed sub-boundary of the single phase tertiary γ'-precipitate depleted zone. It is likely that this interface is formed due to local deformation-induced recrystallisation as suggested by Wlodek *et al.* [226]. The formation of the γ'-phase free zone will be dictated by the tertiary γ'-size and its dissolution kinetics; this is discussed further in Section 5.4.3.

5.4.2 On the Role of Grain Size Dependent Toughening

Of significance here is the observed increase in grain size with increasing Nb/Ti ratio and its influence on improving the tensile ductility and the conditional fracture toughness. Putting aside for now the issue of why the grain size is influenced by Nb/Ti ratio – this is discussed in the following section – what are the implications of this effect?

While a coarser-grained microstructure resulting from a supersolvus heat treatment has been demonstrated to be beneficial – for example by comparing the behavior of any given alloy to sub-solvus and super-solvus processing [41, 61, 70, 121, 124] – so far, grain size has not been varied independently of the γ'-precipitate size distribution. This gives rise to the question whether grain size independently improves environmentally-assisted crack growth resistance. The yield stress as well as the mean diameter of the secondary and tertiary γ'-precipitates is approximately constant in the

present study, so this makes this analysis possible. The HR-EBSD technique has been used for this purpose in order to characterize the deformation in the crack wakes and also the intergranular crack tips. Both the finer grained ABD-2 and coarser grained ABD-6 have been studied, in order to deduce any influence of (i) crack bridging as well as (ii) the grain boundary sliding resistance. While the first mechanism will aid resistance to crack propagation along the environmentally-induced damage zone along an embrittled γ-boundary, an increase in sliding resistance will retard the build-up of a critical strain ahead of the crack tip.

An influence of crack bridging has indeed been observed in the present work, for example in coarser-grained ABD-6, see Figure 5.9 (e), which exhibits significant evidence of this effect in the crack wake. Plastic deformation is also confirmed in GND density maps of this alloy. By way of comparison, grain bridging is not readily apparent in the finer-grained ABD-2, see Figure 5.9 (d). Bridging grains in the wake of the crack are well known to increase the toughness substantially, by reducing the stress intensity at the crack tip. This finding also explains the *post-mortem* observation present in the literature of unbroken ligaments on the fracture surfaces of testpieces subjected to mid-temperature dwell fatigue [3, 59, 227, 228]. The resulting decrease in crack propagation driving force will contribute towards the observed increase in toughness and ductility as a function of grain size.

As demonstrated in Chapter 4, it is emphasised that the observed failure mechanism is closely related to the underlying deformation process. At 700°C plasticity is believed to occur through several independent processes including slip-assisted grain boundary sliding mechanism – due to the absence of stress-relieving mechanisms this leads to intergranular fracture and the observed ductility minimum [216]. The temperature corresponding to the ductility minimum increases with an increased grain size [229] which explains the observed grain size dependency of the tensile ductility

in these alloys, see Figure 5.5 (b). In the finer grained alloy ABD-2, an increase of GND density at the grain boundaries and grain boundary triple junctions suggests more grain boundary deformation compared to the coarser grained ABD-6, see Figure 5.9 (d). The increase in grain size as well as the grain boundary serrations inhibit intergranular failure by retarding the formation of local microstresses arising from grain boundary deformation. The observed effects of grain size on ductility and toughness agree with predictions based on a critical crack tip strain fracture model proposed by Floreen & Kane [230] where stress intensity at the crack tip, K, is proportional to $(\sigma_y \cdot d)^{1/2}$. A material with a higher resistance to intergranular failure is characterized by a lower strain at the crack tip due to a higher constraint to grain boundary sliding [46].

5.4.3 On the Relevance to Alloy Design

This work demonstrates that at 700°C – despite a high strength of fixed value – it is possible to design both more (high Nb/Ti) or less (low Nb/Ti) damage-tolerant alloy variants. For optimum resistance to environmentally-assisted cracking, one should aim for a high yield stress and coarse grain size, in as much as the two can be varied independently of one another. As shown here, resistance to γ'-precipitation shearing accounts for the majority of the strength at 700°C, see Table 5.4. So what relevance do Ti and Nb play in the present case?

Both Ti and Nb partition strongly to the γ'-phase, Ni_3(Al, Ti, Nb), thus influencing the fraction of γ'-precipitates and the ease of their shearing *via* changes in the APB energy [11]. This is in agreement with the reported experimental results. To achieve a high tensile strength the γ'-phase volume fraction the APB energy has to maximised as suggested by Crudden *et al.* [11]. This was done for the alloys designed and studied

in this work and can be described by the expression $M_{\text{strength}} = \bar{M} \cdot 1/2\ \gamma_{\text{APB}} f^{1/2}/b$, where $\bar{M}$ is the Taylor factor, f is the volume fraction of the γ'-phase, γ_{APB} is the anti-phase boundary energy and b is the Burgers vector. For damage tolerance, it is important to account for the reduction of the Hall-Petch contribution due to a coarse supersolvus microstructure which can be described by $\sigma_{\text{HP}} = k_y(D_{\text{sub}}^{-1/2}\text{-}D_{\text{super}}^{-1/2})$, where k_y is the Hall-Petch coefficient; D_{sub} and D_{super} denotes the grain size resulting from a sub-solvus or super-solvus heat treatment. This impact of this is illustrated in Figure 5.15 (a) where strength and ductility for a variety of polycrystalline Ni-based superalloys are plotted. The trade-off between strength and tensile ductility can therefore be described by $M^*_{\text{strength}} = \bar{M} \cdot 1/2\ \gamma_{\text{APB}} f^{1/2}/b$ - σ_{HP} where a grain size dependent strength reduction is counteracted by a degree of composition-dependent strengthening.

In addition to grain size, the observed dissolution of the tertiary γ'-precipitates during the extension of the environmental damage zone during continuous crack propagation suggests that both size and composition of the tertiary γ'-precipitates influence the susceptibility to embrittlement. Thus an increase in the mean diameter would result in slower dissolution. This is in agreement with Telesman *et al.* [129] and Li *et al.* [70] who have shown that an increase in tertiary γ'-precipitate size is beneficial during dwell fatigue loading. They concluded that the benefit comes form faster stress relaxation at the crack tip during hold times reducing the crack tip driving force. However, this does not explain a benefit during continuous cracking if no hold times are applied. The composition of the tertiary γ'-precipitates is important since the rate of dissolution and the availability of oxidising elements at the furthest end of the damage zone will be composition-dependent. Collins *et al.* [221] demonstrated that the Nb present in ABD-6 slows down the formation and dissolution kinetics of the γ'-phase compared to ABD-2. This is in agreement which the results presented here.

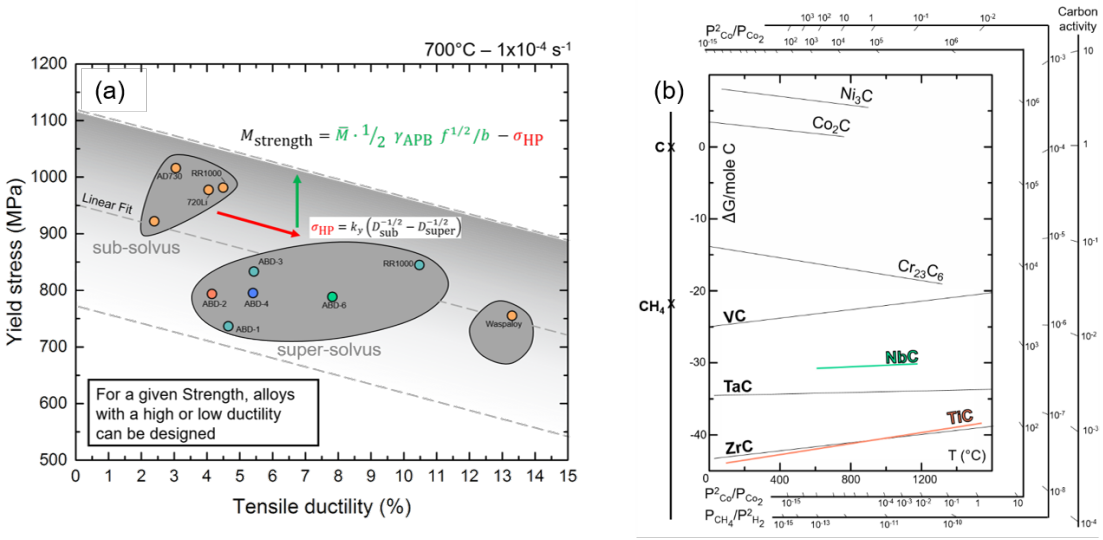


Fig. 5.15 (a) Yield stress and tensile ductility obtained from miniaturised ETMT tensile tests at 700°C using a strain-rate of $1{\cdot}10^{-4}$ s^{-1} for various Ni-based superalloys illustrating that for a given strength alloys with a low and a high tensile ductility can be designed. It is shown that the loss in strength due to Hall-Petch has to be counteracted via an increase in precipitation strengthening and γ'-phase volume fraction. (b) Ellingham diagram for carbides which commonly form in Ni-based superalloys. Adapted from S.R. Shatynski [231].

A last point relates to the reason why the Nb/Ti ratio alters the grain size in this system. It seems likely that this is due to the MC carbide composition, the temperature-dependence of the stability of this phase during forging/subsequent heat treatment and its influence on recrystallisation and grain growth. A number of studies have observed the effect of MC carbide composition on the grain size during the processing of polycrystalline Ni-based superalloys and specifically the pinning of grain boundaries by them [232, 233]. A change in the MC carbide composition from Ti to Nb-rich MC carbides is apparent in the thermodynamic predictions of Table 5.1. The difference in carbide stability at 1170°C is also seen in the carbide Ellingham diagram of Figure 5.15 (b). Ti is known to stabilise MC and hence retard its coarsening and dissolution [234]. This is likely to suppress grain growth at lower Nb/Ti ratio in for example alloy ABD-2. But accounting for the influence of alloy composition on grain size development during processing is a issue which should be the topic of future work.

5.5 Summary and Conclusions

In this chapter, three high strength Ni-based superalloys of varying Nb/Ti ratio have been studied. The following specific conclusions can be drawn:

(1) Differences in the Nb/Ti ratio did not alter the yield stress of these alloys either at ambient conditions – at which it is ∼935 MPa – or at 700°C where it is reduced to ∼792 MPa. This occurs despite an influence of the increasing Nb/Ti ratio which coarsens the grain size from 18 to 45 μm; the mean diameter of both secondary and tertiary γ'-precipitates is independent of Nb/Ti ratio at 200 and 40 nm respectively.

(2) The above implies that any loss in Hall-Petch strengthening due to the increase in grain size as the Nb/Ti ratio increases is offset by an increase in γ-matrix solid solution hardening and/or an increased resistance to γ'-precipitate shearing. Analysis via theoretical modelling has been used to rationalise the increments in strengthening due to these effects.

(3) In contrast, the tensile ductility at 700°C is influenced substantially by the Nb/Ti ratio due to an effect on the susceptibility to quasi-brittle intergranular cracking. Tensile ductility is no longer alloy independent and is approximately doubled from 4.2 for the smallest Nb/Ti ratio examined (zero) to 7.8 % for the largest (0.43). Consistent with this, the elevated temperature conditional fracture toughness calculated from interrupted single edge notched tests increases from 19.7 to 24.6 MPa$\sqrt{\text{m}}$.

(4) Characterisation of interrupted primary crack tips revealed sub-micron sized oxide intrusions which penetrate the grain boundaries. The size of the intrusions is found to be independent of the Nb/Ti ratio. However, the oxide intrusions con-

tain different phases present in an order consistent with thermodynamics. The internal oxidation of reactive elements found in γ'-precipitates, Al_2O_3 and TiO_2, are responsible for extending the environmental damage zone during steady-state crack propagation. Not observed are Nb-rich oxides such as NbO_2.

(5) Whilst all alloys investigated failed at 700°C in a quasi-brittle fashion due to environmentally-assisted cracking, a coarse grain size increases both the tensile ductility and the fracture toughness. Crack bridging and an increased resistance to grain boundary sliding play roles in this. In addition, evidence is presented which confirms that the tertiary γ'-precipitate size and composition affect the susceptibility to environmentally-assisted cracking, since the dissolution of the tertiary γ'-precipitates ahead of the crack is required to form Al_2O_3 and TiO_2 at undamaged grain boundaries.

(6) The present study has implications for the design of damage-tolerant high-strength Ni-based superalloys. At any given strength level, our results demonstrate clearly that more or less damage tolerant variants can be designed by subtle changes in alloy composition; for optimum resistance to environmentally-assisted cracking one should aim for a high yield stress and coarse grain size, in as much as the two can be varied independent of one another. The balance of the elements Nb and Ti needs to be chosen carefully in this regard.

Chapter 6

Conclusions and Future Work

6.1 Conclusions

The work presented studies intergranular environmentally-assisted cracking in high strength Ni-based superalloys for high pressure turbine discs through a combination of systematic experimentation coupled with multi-scale characterisation techniques.

First, a novel electro-thermal-mechanical testing (ETMT) system is introduced and employed which addresses a number of drawbacks associated with conventional mechanical testing methodologies for Ni-based superalloy. Miniature test pieces with a small cross-section of 1×1 mm^2 and an increased surface-to-volume ratio were used to enhance surface dominated effects such as environmentally-assisted surface crack initiation and propagation. The high strength polycrystalline superalloy 720Li was used for this purpose. It is demonstrated that these tests are capable of capturing the temperature and time-dependent effects that occur during environmentally-assisted cracking, while allowing for the rapid assessment of the alloy strength. Alloy strength was validated *via* a comparison between meso-scale ETMT tests and macro-scale me-

chanical data from conventional test pieces. The embrittlement was found to be both time and rate dependent. Using scanning electron microscopy, it is shown that the incoherent γ/γ'-precipitate interface are most susceptible to environmental damage. Further, it is possible to perform site-specific micro-mechanical bend tests in the vicinity of the environmentally-induced crack tip damage zone. These confirmed that long-range embrittlement of the grain boundary is not present, thus providing insight into the mechanisms of fracture. From this work, it is concluded that an alloys susceptibility to environmentally-assisted cracking can be rapidly assessed using slow strain-rate electro-thermal mechanical tensile testing.

Second, the observed quasi-brittle failure between 600 and 850°C in alloy 720Li is studied in detail and rationalised using energy-dispersive X-ray spectroscopy, nanoscale secondary ion mass spectrometry and the analysis of electron backscatter diffraction patterns. Embrittlement occurs due to (i) slip-assisted grain boundary sliding which causes the formation of local microstresses arising from grain boundary deformation and (ii) preferential nucleation and growth of internal oxide intrusions at incoherent primary γ'-precipitates and at high angle γ-grain boundaries. These oxide intrusions contain different phases present in an order consistent with thermodynamics and the expected gradient in equilibrium partial pressure of oxygen. The sliding grain boundary fractures the crack-tip oxides, causing intergranular crack propagation. Above 850°C, ductility is restored as the accumulation of dislocations at grain boundaries is no longer prevalent because grain boundaries become mobile. From these observations implications for the choice of heat treatment temperature for polycrystalline Ni-based superalloys have been derived and verified using alloy RR1000. A sub-solvus heat treatment exacerbates oxidation-assisted cracking. The concomitant – relatively small – grain size promotes grain boundary sliding and the primary γ'-precipitates act as nucleation sites for oxide formation, in particular ones from γ'-phase forming

elements. A super-solvus heat treatment therefore dissolves primary γ'-precipitates and increases the γ-grain size in a favourable fashion, thus reducing the susceptibility to environmentally-assisted cracking.

Third, the effect of γ'-phase forming elements, particularly Nb and Ti, on the strength, ductility and toughness of three prototype Ni-based superalloys is studied and rationalised. Whilst the properties at room temperature are insensitive to alloying, at 700°C the tensile ductility and fracture toughness are impaired – being worse for the lowest Nb/Ti ratio examined – by internal oxidation along the grain boundaries and newly formed sub-grain boundaries. While increasing the Nb/Ti ratio increased resistance to γ'-precipitate shearing, a loss in Hall-Petch strengthening is observed due to an increase in grain size. This results in an Nb/Ti ratio independent yield strength and subsequently allows the isolation of the factors influencing damage tolerance at 700°C. Using energy-dispersive X-ray spectroscopy in a scanning transmission electron microscopy, the internal oxidation of reactive elements found in γ'-precipitates, Al_2O_3 and TiO_2, are responsible for extending the environmental damage zone during steady-state crack propagation. Evidence is presented suggesting that the dissolution of the tertiary γ'-precipitates ahead of the damage zone is rate controlling. Any possible detrimental effect of Nb on the observed interrupted crack tip damage due to Nb-rich oxide formation is not observed. The analysis of electron back-scatter diffraction patterns shows that a coarse grain size increases both the tensile ductility and the fracture toughness. Crack bridging and an increased resistance to grain boundary sliding is responsible. These results have important implications for alloy design efforts; at any given strength level, both more and less damage tolerant variants of super-solvus heat-treated Ni-based superalloys can be designed. For optimum resistance to environmentally-assisted cracking, one should aim for a high yield strength and coarse grain size, in as much as the two can be varied independently of one another. The

balance of the γ'-phase forming elements needs to be chosen carefully in this regard.

Overall this work on environmentally-assisted fracture of high strength Ni-based superalloys has provided beneficial insights into important challenges associated with (i) the develop of novel experimental techniques which allow the rapid assessment of an alloy's susceptibility to environmentally-assisted crack growth, (ii) the physical mechanism of environmentally-assisted grain boundary embrittlement and (iii) the design of damage tolerant nickel-superalloy variants for high pressure turbine discs.

6.2 Future Work

The presented research is focused on the metallurgical control of environmentally-assisted crack propagation in Ni-based superalloys which has yielded an improved understanding of the embrittlement mechanism and the composition-microstructure-property relationships. Three main topics for further work arise from this study:

(1) The development of new testing methodologies for *in-situ* heat treatment and mechanical testing.

(2) A study of the influence of γ-matrix composition on environmentally-assisted failure.

(3) The application of *Alloys-By-Design* to damage tolerant polycrystalline Ni-based superalloys.

In the first category, Chapter 3 describes the use of miniature electro-thermal mechanical test (ETMT) specimen in a fully heat treated condition. Preliminary results shown in Figure 6.1 suggest that the ETMT system is capable to perform well defined heat treatments on test pieces manufactured from as-received material prior to testing.

The combination of an *in-situ* heat treatment followed by mechanical testing allows for the rapid assessment of microstructure-property relationships at elevated temperatures. An example is given in Figure 6.1 (a) and (b). A change in microstructure can be observed in the center of the test piece after a five minute supersolvus heat treatment. In addition, well defined cooling rates can be achieved (see Figure 6.1 (c)). The cooling rate is of particular importance since the precipitation of secondary and tertiary grain boundary γ'-precipitates has been shown to be of critical importance to an alloys resistance to environmentally-assisted failure. A future study is proposed, which builds upon these preliminary results and makes use of the ETMT set-up to rapidly determine the microstructure-property relationship during the development of next generation polycrystalline Ni-based superalloys and the optimisation of current alloys.

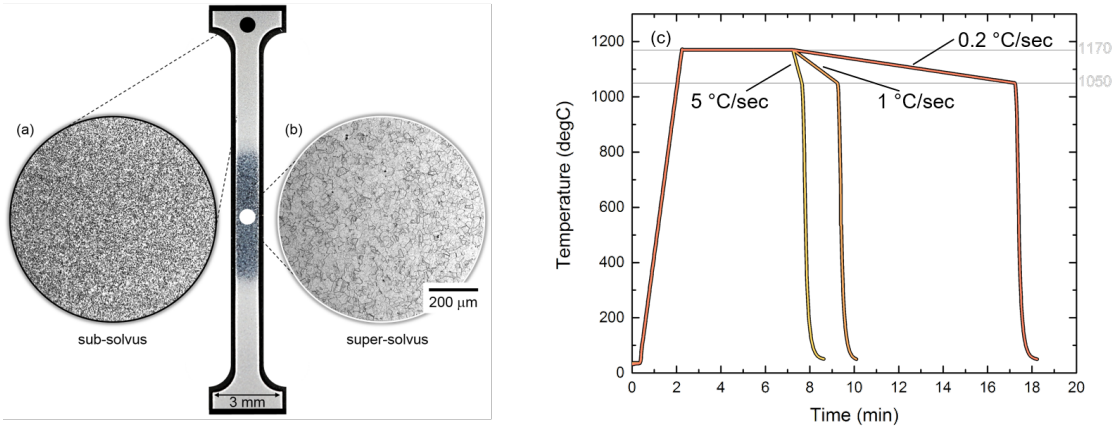


Fig. 6.1 (a) Optical micrograph demonstrating the use of the ETMT system to locally optimise the microstructure of a polycrystalline γ/γ'-strengthened Ni-based superalloy. (b) Measured temperature in the center of the test specimen as a function of time. Three different cooling rates are shown.

With respect to the second point above, preliminary work was performed to isolate the influence of Cr/W ratio on the tensile ductility at 700°C. Initial results suggest that while the oxidation resistance of chromia-forming alloys increases with increasing

Cr/W ratio, the resistance to environmentally-assisted crack growth was found to be Cr/W ratio independent (see Figure 6.2 (a) and (b)). This can be explained by the absence of a hold time. Future work is proposed to gain an increased understanding of the link between an alloys ability to form a surface chromia scale during long-term exposure and the growth of a protective Cr-rich oxide at the crack tip during environmentally-assisted crack growth. Of critical importance will be the assessment of the envriomental degradation at the right length scale. STEM-EDS has been shown to be well suited throughout this thesis.

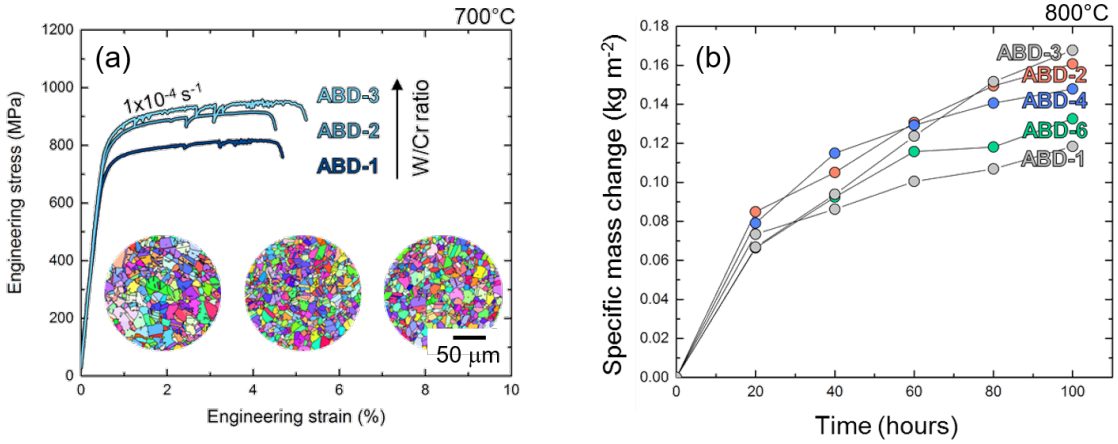


Fig. 6.2 (a) Representative stress-strain curves for ABD-1, -2 and -3 at 700°C using an initial strain-rate close to 1x10^{-4} s^{-1} showing a composition independent tensile ductility. (b) Specific mass gains during 100 h exposure time at 800°C for ABD-1, -2 and -3 in addition to the alloys introduced in Chapter 5. An increase in Cr/W ratio is found to decrease the chromia oxidation kinetics. In addition, the Cr/Ti ratio was observed to play a critical role.

With regards to the last point raised, the knowledge acquired in this work can be incorporated into the Alloys-by-Design approach [235] with the aim of aiding the future development of a damage tolerant high strength Ni-based superalloy. Figure 6.3 demonstrates that the dependence of strength on the APB energy and the γ'-phase volume fraction. Both γ'-phase composition and volume fraction are believed to influence an alloy's susceptibility to environmentally-assisted grain boundary embrittlement sig-

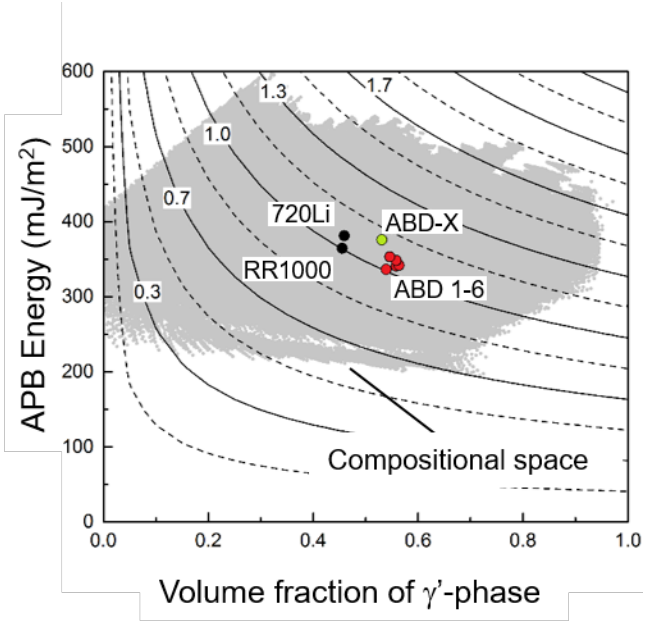


Fig. 6.3 APB energy versus γ'-phase volume fraction together with contours for predicted yield strength at 650°C normalised for RR1000.

nificantly. This can be incorporated into the Alloys-by-Design approach as a so-called merit index. In addition to these alloy composition dependent factors, the microstructure of a novel high-strength superalloy, can be further optimised for resistance to environmentally-assisted cracking through a tailored supersolvus heat treatment. For example, Figure 6.4 demonstrates how differential scanning calorimetry can be used to obtain the γ'-precipitate dissolution temperature for a novel prototype alloy ABD-X (Figure 4 (a)). Figure 4 (b) summarises the effect of changes in solution temperature, super-solvuscooling rate and age heat treatment. Testing of these microstructures where γ'-precipitate size distribution is varied, while keeping composition and grain size constant, will enable further understanding of the key factors controlling grain boundary embrittlement.

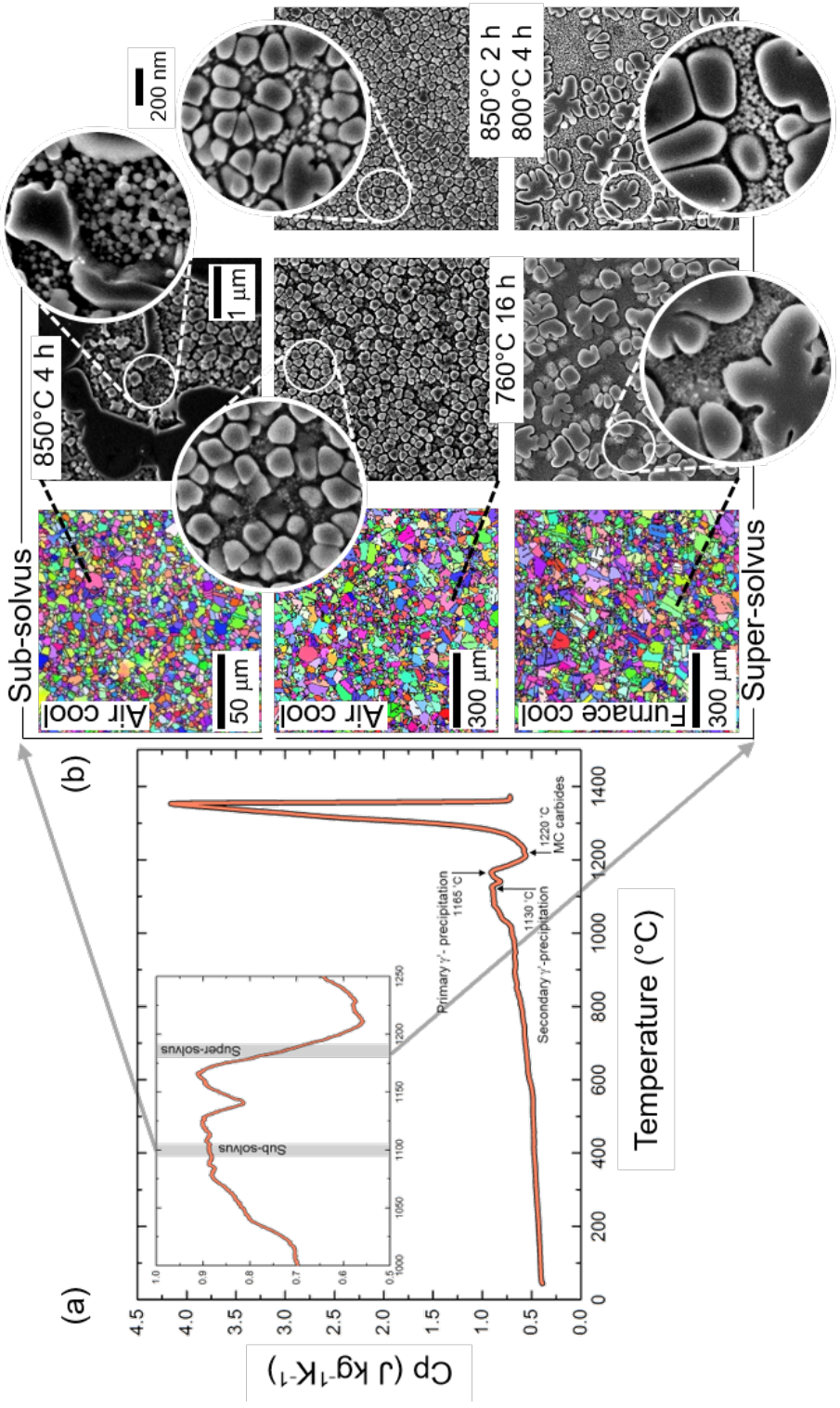


Fig. 6.4 (a) DSC trace of as-forged ADB-X. (b) Inverse pole figure maps and SEM images after electro-chemical etching in an aqueous 10% phosphoric acid solution of each ABD-X condition assessed in the heat treatment study.

References

[1] R. C. Reed, The Superalloys, Cambridge University Press, Cambridge, 2006. doi:10.1017/CBO9780511541285.

[2] A. K. Misra, L. A. Greenbauer-Seng, Aerospace Propulsion and Power Materials and Structures Research at NASA Glenn Research Center., J. Aerosp. Eng. 26 (2) (2013) 459–490. doi:10.1061/(ASCE)AS.1943-5525.0000325.

[3] R. Jiang, P. A. S. Reed, Critical Assessment 21: oxygen-assisted fatigue crack propagation in turbine disc superalloys, Mater. Sci. Technol. 32 (2016) 401–406. doi:10.1080/02670836.2016.1148227.

[4] Aircraft Accident Boeing 767-223 ER N330AA Los Angeles International Airport, Tech. rep. (2006).
URL http://aviation-safety.net/database/record.php?id=20060602-0

[5] University of Portsmouth, Impact Case: Improved Creep-Fatigue-Oxidation Resistance in Gas Turbine Disc Materials, Tech. rep. (2014). doi:10.1016/S0142-1123.

[6] S. Kallas, M. Geoghegan-Quinn, Flightpath 2050 Europe's Vision for Aviation, Tech. rep., European commission (2011). doi:10.2777/50266.

[7] M. Winstone, J. Brooks, Advanced high temperature materials: Aeroengine fatigue, Ciência e Tecnol. dos Mater. 20 (1/2) (2008) 15–24.

[8] Rolls-Royce Ltd, The Jet Engine, 5th Edition, Wiley-Blackwell, 2015.

[9] R. C. Reed, A. Mottura, D. J. Crudden, Alloys-by-design: Towards Optimization of Compositions of Nickel-Based Superalloys, in: Superalloys 2016 13th Int. Symp., 2016.

[10] D. Mukherji, J. Rösler, P. Strunz, R. Gilles, G. Schumacher, S. Piegert, Beyond Ni-based superalloys: Development of CoRe-based alloys for gas turbine applications at very high temperatures, Int. J. Mater. Res. 102 (9) (2011) 1125–1132. doi:10.3139/146.110563.

[11] D. J. Crudden, A. Mottura, N. Warnken, B. Raeisinia, R. C. Reed, Modelling of the influence of alloy composition on flow stress in high-strength nickel-based superalloys, Acta Mater. 75 (2014) 356–370. doi:10.1016/j.actamat.2014.04.075.

[12] S. Miller, Advanced materials mean advanced engines, Interdiscip. Sci. Rev. 21 (2) (1996) 117–129. doi:10.1179/isr.1996.21.2.117.

[13] M. Dareck, C. Edelstenn, T. Ender, Flightpath 2050 Europes Vision for Aviation, Tech. rep., High Level Group on Aviation Research (2011). doi:10.2777/50266.

[14] Q. Chen, N. Jones, D. Knowles, The microstructures of base/modified RR2072 SX superalloys and their effects on creep properties at elevated temperatures, Acta Mater. 50 (5) (2002) 1095–1112. doi:10.1016/S1359-6454(01)00410-4.

[15] C. S. Giggins, F. S. Pettit, Oxidation of Ni-Cr alloys between 800 and 1200C, Trans. Metall. Soc. AIME 245 (1969) 2495–2507.

[16] R. N. Jarrett, J. K. Tien, Effects of Cobalt on Structure, Microchemistry and Properties of a Wrought Nickel-Base Superalloy, Metall. Trans. A 13 (6) (1982) 1021–1032. doi:10.1007/BF02643399.

[17] H. A. Roth, C. L. Davis, R. C. Thomson, Modeling solid solution strengthening in nickel alloys, Metall. Mater. Trans. A 28 (6) (1997) 1329–1335. doi:10.1007/s11661-997-0268-2.

[18] T. M. Pollock, S. Tin, Nickel-Based Superalloys for Advanced Turbine Engines: Chemistry, Microstructure and Properties, J. Propuls. Power 22 (2006) 361–374. doi:10.2514/1.18239.

[19] D. Furrer, H. Fecht, Ni-based superalloys for turbine discs, JOM 51 (1) (1999) 14–17. doi:10.1007/s11837-999-0005-y.

[20] C. T. Sims, W. C. Hagel, The Superalloys, John Wiley and Sons Inc, 1972.

[21] S. Ochial, Y. Oya, T. Suzuki, Alloying behaviour of Ni3Al, Ni3Ga, Ni3Si and Ni3Ge, Acta Metall. 32 (2) (1984) 289–298. doi:10.1016/0001-6160(84)90057-9.

[22] N. Baluc, H. P. Karnthaler, M. J. Mills, TEM observation of the fourfold dissociation of superlattice dislocations and the determination of the fault energies in Ni3(Al, Ta), Philos. Mag. A 64 (1) (1991) 137–150. doi:10.1080/01418619108206131.

[23] B. Reppich, Some new aspects concerning particle hardening mechanisms in γ' precipitating Ni-base alloys—I. Theoretical concept, Acta Metall. 30 (1) (1982) 87–94. doi:10.1016/0001-6160(82)90048-7.

[24] R. Ricks, A. Porter, R. Ecob, The growth of γ' precipitates in nickel-base superalloys, Acta Metall. 31 (1) (1983) 43–53. doi:10.1016/0001-6160(83)90062-7.

[25] P. Villars, L. D. Calvert, Pearson's handbook of crystallographic data for intermetallic phases, Cryst. Res. Technol. 22 (11) (1987) 1436–1436. doi:10.1002/crat.2170221117.

[26] G. P. Sabol, R. Stickler, Microstructure of Nickel-Based Superalloys, Phys. status solidi 35 (1) (1969) 11–52. doi:10.1002/pssb.19690350102.

[27] B. J. Piearcey, R. W. Smashey, The carbide phases in Mar-M200, Trans. Metall. Soc. AIME 239 (1967) 451.

[28] H. Kitaguchi, Microstructure-Property Relationship in Advanced Ni-Based Superalloys, Metall. - Adv. Mater. Process.doi:10.5772/52011.

[29] G. Lvov, V. I. Levit, M. J. Kaufman, Mechanism of primary MC carbide decomposition in Ni-base superalloys, Metall. Mater. Trans. A 35 (6) (2004) 1669–1679. doi:10.1007/s11661-004-0076-x.

[30] R. Hu, G. Bai, J. Li, J. Zhang, T. Zhang, H. Fu, Precipitation behavior of grain boundary M23C6 and its effect on tensile properties of Ni–Cr–W based superalloy, Mater. Sci. Eng. A 548 (2012) 83–88. doi:10.1016/j.msea.2012.03.092.

[31] H. Collins, Relative Stability of Carbide and Intermetallic Phases in Nickel-Base Superalloys, in: Int. Symp. Struct. Stab. Superalloys, TMS, 1968, pp. 171–198. doi:10.7449/1968/Superalloys_1968_171_198.

[32] C. T. Sims, N. S. Stoloff, W. C. Hagel, Superalloys II, Wiley, New York, 1987.

[33] D. Raabe, M. Herbig, S. Sandlöbes, Y. Li, D. Tytko, M. Kuzmina, D. Ponge, P. P. Choi, Grain boundary segregation engineering in metallic alloys: A pathway to the design of interfaces, Curr. Opin. Solid State Mater. Sci. 18 (2014) 253–261. doi:10.1016/j.cossms.2014.06.002.

[34] J. Radavich, D. Furrer, T. Carneiro, J. Lemsky, The Microstructure and Mechanical Properties of EP741NP Powder Metallurgy Disc Material, in: Superalloys 2008 (Eleventh Int. Symp., TMS, 2008, pp. 63–72. doi:10.7449/2008/Superalloys_2008_63_72.

[35] C. Miller, G. Simmons, R. Wei, Mechanism for oxygen enhanced crack growth in inconel 718, Scr. Mater. 44 (2001) 2405–2410. doi:10.1016/S1359-6462(01)00933-2.

[36] T. P. Gabb, J. Telesman, A. Banik, E. McDevitt, Use of Slow Strain Rate Tensile Testing to Assess the Ability of Several Superalloys to Resist Environmentally-Assisted Intergranular Cracking, in: 8th Int. Symp. Superalloy 718 Deriv., John Wiley & Sons, Inc., Hoboken, NJ, USA, 2014, pp. 697–712. doi:10.1002/9781119016854.ch54.

[37] K. R. Bain, R. M. Pelloux, Effect of Environment on Creep Crack Growth in PM/HIP Rene-95, Metall. Trans. A 15 (2) (1984) 381–388. doi:10.1007/BF02645123.

[38] D. Locq, P. Caron, On Some Advanced Nickel-Based Superalloys for Disk Applications, J. AerospaceLab 3 (2011) 1–9.

[39] D. Locq, P. Caron, S. Raujol, F. Pettinari-Sturmel, A. Coujou, N. Clement, On the Role of Tertiary Gamma Prime Precipitates in the Creep Behaviour at 700C of a PM Disk Superalloy, in: Superalloys 2004 (Tenth Int. Symp., TMS, 2004, pp. 179–187. doi:10.7449/2004/Superalloys_2004_179_187.

[40] S. Wlodek, M. Kelly, D. A. Alden, The Structure of Rene' 88DT, in: Superalloys 1996 (Eighth Int. Symp., TMS, 1996, pp. 129–136. doi:10.7449/1996/Superalloys_1996_129_136.

[41] S. Everitt, M. Starink, P. Reed, Temperature and Dwell Dependence of Fatigue Crack Propagation in Various Heat Treated Turbine Disc Alloys, in: Superalloys 2008 (Eleventh Int. Symp., TMS, 2008, pp. 741–750. doi:10.7449/2008/Superalloys_2008_741_750.

[42] X. Liu, B. Kang, K.-M. Chang, The effect of hold-time on fatigue crack growth behaviors of WASPALOY alloy at elevated temperature, Mater. Sci. Eng. A 340 (1-2) (2003) 8–14. doi:10.1016/S0921-5093(02)00074-6.

[43] M. Jackson, R. Reed, Heat treatment of UDIMET 720Li: the effect of microstructure on properties, Mater. Sci. Eng. A 259 (1) (1999) 85–97. doi:10.1016/S0921-5093(98)00867-3.

[44] M. Durand-Charre, The Microstructure of Superalloys, Gordon & Breach Science, Amsterdam, 1997.

[45] T. P. Gabb, D. R. Miller, Formation of Minor Phases in a Nickel-Based Disk Superalloy, Tech. Rep. 217604 (2012).

[46] K. Maciejewski, H. Ghonem, Influence of continuum precipitates on intergranular fatigue crack growth of a P/M nickel-based superalloy, Mater. Sci. Eng. A 560 (2013) 439–449. doi:10.1016/j.msea.2012.09.088.

[47] J. M. Larson, S. Floreen, Metallurgical factors affecting the crack growth resistance of a superalloy, Metall. Trans. A 8 (1) (1977) 51–55. doi:10.1007/BF02677263.

[48] A. Saxena, K. Findley, Dwell-time fatigue crack growth in Ni-base superalloys, Tech. rep., University of Dayton, Research Institute Air Force Research Laboratory (2003).

[49] L. M. Nerodenko, E. V. Dabizha, Effect of stacking-fault energy on the parameters of high-temperature creep of nickel-cobalt alloys, Strength Mater. 14 (10) (1982) 1331–1337. doi:10.1007/BF00770129.

[50] R. W. Kozar, A. Suzuki, W. W. Milligan, J. J. Schirra, M. F. Savage, T. M. Pollock, Strengthening mechanisms in polycrystalline multimodal nickel-base superalloys, Metall. Mater. Trans. A Phys. Metall. Mater. Sci. 40 (7) (2009) 1588–1603. doi:10.1007/s11661-009-9858-5.

[51] E. C. Guo, F. J. Ma, The Strengthening Effect of Niobium on Ni-Cr-Ti Type Wrought Superalloy, in: Superalloys 1980, John Wiley & Sons, Inc., Hoboken, NJ, USA, 1980, pp. 431–438. doi:10.7449/1980/superalloys_1980_431_438.

[52] P. Paris, F. Erdogan, A Critical Analysis of Crack Propagation Laws, J. Basic Eng. 85 (4) (1963) 528. doi:10.1115/1.3656900.

[53] K. O. Findley, J. L. Evans, A. Saxena, A critical assessment of fatigue crack nucleation and growth models for Ni- and Ni,Fe-based superalloys, Int. Mater. Rev. 56 (1) (2011) 49–71. doi:10.1179/095066010X12777205875796.

[54] A. F. Liu, Mechanics and Mechanisms of Fracture : An Introduction, ASM International, 2005. doi:10.1361/memf2005p169.

[55] H. Solomon, L. Coffin, Effects of Frequency and Environment on Fatigue Crack Growth in A286 at 1100F, in: Fatigue Elev. Temp., Vol. 520, ASTM International, 100 Barr Harbor Drive, PO Box C700, West Conshohocken, PA 19428-2959, 1973, pp. 112–112–11. doi:10.1520/STP38833S.

[56] S. Floreen, The creep fracture of wrought nickel-base alloys by a fracture mechanics approach, Metall. Trans. A 6 (9) (1975) 1741–1749. doi:10.1007/BF02642302.

[57] S. Floreen, R. H. Kane, Effects of environment on high-temperature fatigue crack growth in a superalloy, Metall. Trans. A 10 (11) (1979) 1745–1751. doi:10.1007/BF02811710.

[58] K. M. Chang, M. F. Henry, M. G. Benz, Metallurgical control of fatigue crack propagation in superalloys, JOM 42 (12) (1990) 29–35. doi:10.1007/BF03220467.

[59] M. Hörnqvist, L. Viskari, K. L. Moore, K. Stiller, High-temperature crack growth in a Ni-base superalloy during sustained load, Mater. Sci. Eng. A 609 (2014) 131–140. doi:10.1016/j.msea.2014.04.102.

[60] D. A. Woodford, H. D. Solomon, L. F. Coffin, Mechanical behavior of materials, in: 2nd Internatioal Conf. Mech. Behav. Mater., 1976, pp. 983–897.

[61] R. Jiang, S. Everitt, M. Lewandowski, N. Gao, P. Reed, Grain size effects in a Ni-based turbine disc alloy in the time and cycle dependent crack growth regimes, Int. J. Fatigue 62 (2014) 217–227. doi:10.1016/j.ijfatigue.2013.07.014.

[62] H. Ghonem, D. Zheng, Depth of intergranular oxygen diffusion during environment-dependent fatigue crack growth in alloy 718, Mater. Sci. Eng. A 150 (2) (1992) 151–160. doi:10.1016/0921-5093(92)90107-C.

[63] T. Yokobori, A. T. Yokobori, A. Kamei, Dislocation dynamics theory for fatigue crack growth, Int. J. Fract. 11 (5) (1975) 781–788. doi:10.1007/BF00012896.

[64] N. Y. Tang, P. Niessen, A. Plumtree, Enhanced Fatigue Crack Growth Rate At Elevated Temperatures, Zeitschrift fuer Met. 82 (1991) 721–726.

[65] K. B. Yoon, T. G. Park, A. Saxena, Elevated temperatrue fatigue crack growth model for DS-GTD-111, Int. J. Strength, Fractrue Complex. 4 (2006) 35–40.

[66] R. P. Wei, Z. Huang, Influence of dwell time on fatigue crack growth in nickel-base superalloys, Mater. Sci. Eng. A 336 (1-2) (2002) 209–214. doi:10.1016/S0921-5093(01)01957-8.

[67] M. J. Starink, P. A. S. Reed, Thermal activation of fatigue crack growth: Analysing the mechanisms of fatigue crack propagation in superalloys, Mater. Sci. Eng. A 491 (1-2) (2008) 279–289. doi:10.1016/j.msea.2008.02.016.

[68] M. Hörnqvist, L. Viskari, Reduced Dwell-Fatigue Resistance in a Ni-Base Superalloy After Short-Term Thermal Exposure, Metall. Mater. Trans. A 45 (2014) 2699–2703. doi:10.1007/s11661-014-2291-4.

[69] R. Jiang, S. Everitt, N. Gao, K. Soady, J. Brooks, P. Reed, Influence of oxidation on fatigue crack initiation and propagation in turbine disc alloy N18, Int. J. Fatigue 75 (2015) 89–99. doi:10.1016/j.ijfatigue.2015.02.007.

[70] H. Li, J. Sun, M. Hardy, H. Evans, S. Williams, T. Doel, P. Bowen, Effects of microstructure on high temperature dwell fatigue crack growth in a coarse grain PM nickel based superalloy, Acta Mater. 90 (2015) 355–369. doi:10.1016/j.actamat.2015.02.023.

[71] A. Saxena, Thermal and environmental effects in fatigue-research design interface, in: Am. Soc. Mech. Eng., 1983, pp. 131–151.

[72] Tong, Byrne, Effects of frequency on fatigue crack growth at elevated temperature, Fatigue Fract. Eng. Mater. Struct. 22 (3) (1999) 185–193. doi:10.1046/j.1460-2695.1999.00160.x.

[73] J. Telesman, T. P. Gabb, P. T. Kantzos, Effect of Overloads on Time Dependent FCG in a Nickel-Based Superalloy, in: EMAS Fatigue 2002, 2002, pp. 2877–2886.

[74] R. Molins, G. Hochstetter, J. Chassaigne, E. Andrieu, Oxidation effects on the fatigue crack growth behaviour of alloy 718 at high temperature, Acta Mater. 45 (2) (1997) 663–674. doi:10.1016/S1359-6454(96)00192-9.

[75] A. Pineau, Fatigue and Creep-Fatigue Behavior of Ni-Base Superalloys: Microstructural and Environmental Effects, Kluwer Publishers, Holland, 1996.

[76] J. Pfaendtner, C. McMahon Jr, Oxygen-induced intergranular cracking of a Ni-base alloy at elevated temperatures—an example of dynamic embrittlement, Acta Mater. 49 (16) (2001) 3369–3377. doi:10.1016/S1359-6454(01)00005-2.

[77] U. Krupp, Dynamic Embrittlement — Time–dependent Quasi–brittle Intergranular Fracture at High Temperatures, Int. Mater. Rev. 50 (2) (2005) 83–97. doi:10.1179/174328005X14320.

[78] H. K. Birnbaum, P. Sofronis, Hydrogen-enhanced localized plasticity—a mechanism for hydrogen-related fracture, Mater. Sci. Eng. A 176 (1) (1994) 191–202. doi:http://dx.doi.org/10.1016/0921-5093(94)90975-X.

[79] R. H. Bricknell, D. A. Woodford, Prevention and reversal of oxygen embrittlement in nickel, Met. Sci. 18 (5) (1984) 265–272. doi:10.1179/030634584790420087.

[80] C. J. McMahon, Comments on "Identification of SAGBO-induced damage zone ahead of crack tip to characterize sustained loading crack growth in alloy 783", Scr. Mater. 54 (2) (2006) 305–311. doi:10.1016/j.scriptamat.2005.09.030.

[81] R. W. Hayes, D. F. Smith, E. A. Wanner, J. C. Earthman, Effect of environment on the rupture behavior of alloys 909 and 718, Mater. Sci. Eng. A 177 (1) (1994) 43–53. doi:10.1016/0921-5093(94)90476-6.

[82] D. A. Woodford, Gas phase embrittlement and time dependent cracking of nickel based superalloys, Energy Mater. 1 (1) (2006) 59–79. doi:10.1179/174892306X99679.

[83] R. H. Bricknell, R. A. Mulford, D. A. Woodford, The role of sulfur in the air embrittlement of nickel and its alloys, Metall. Trans. A 13 (7) (1982) 1223–1232. doi:10.1007/BF02645505.

[84] R. H. Bricknell, D. A. Woodford, The mechanism of cavity formation during high temperature oxidation of nickel, Acta Metall. 30 (1982) 257–264. doi:10.1016/0001-6160(82)90064-5.

[85] B. F. Dyson, An analysis of carbon/oxygen gas bubble formation in some nickel alloys, Acta Metall. 30 (8) (1982) 1639–1646. doi:10.1016/0001-6160(82)90185-7.

[86] D. A. Woodford, R. H. Bricknell, Grain Boundary Penetration of Oxygen in Nickel and the Effect of Boron Additions, Metall. Mater. Trans. A 12 (8) (1981) 1467–1475. doi:10.1007/BF02643692.

[87] T. Connolley, P. A. S. Reed, M. J. Starink, Short crack initiation and growth at 600 deg C in notched specimens of Inconel 718, Mater. Sci. Eng. A 340 (1-2) (2003) 139–154. doi:10.1016/S0921-5093(02)00169-7.

[88] J.-W. Park, C. J. Altstetter, The diffusion and solubility of oxygen in solid nickel, Metall. Trans. A 18 (1) (1987) 43–50. doi:10.1007/BF02646220.

[89] G. J. Lloyd, J. W. Martin, The Diffusivity of Oxygen in Nickel Determined by Internal Oxidation of Dilute Ni-Be Alloys, Met. Sci. J. 7 (1) (1973) 75–75. doi:10.1179/030634573790445325.

[90] G. J. Lloyd, J. W. Martin, The Diffusivity of Oxygen in Nickel Determined by Internal Oxidation of Dilute Ni–Be Alloys, Met. Sci. J. 6 (1) (1972) 7–11. doi:10.1179/030634572790446208.

[91] J. P. Pédron, A. Pineau, Influence de l'oxydation sur la propagation des fissures à haute température dans l'alliage Inconel 718, Les mémoires Sci. la Rev. métallurgie 80 (1983) 665.

[92] J. Hwang, R. Balluffi, On a possible temperature dependence of the activation energy for grain boundary diffusion in metals, Scr. Metall. 12 (8) (1978) 709–714. doi:10.1016/0036-9748(78)90313-7.

[93] H.-M. Lu, T. Delph, D. Dwyer, M. Gao, R. Wei, Environmentally-enhanced cavity growth in nickel and nickel-based alloys, Acta Mater. 44 (8) (1996) 3259–3266. doi:10.1016/1359-6454(95)00405-X.

[94] R. H. Bricknell, D. A. Woodford, The embrittlement of nickel following high temperature air exposure, Metall. Mater. Trans. A Phys. Metall. Mater. Sci. 12 (3) (1981) 425–433.

[95] R. H. Bricknell, D. A. Woodford, Grain boundary embrittlement of the Iron-base superalloy IN903A, Metall. Trans. A 12 (1981) 1673–1680. doi:10.1007/BF02643573.

[96] P. Hancock, R. Fletcher, The Oxidation of Nickel in the Temperature Range 700-1100C, Metallurgie 6 (1966) 1–9.

[97] D. Douglass, The effect of oxidation on the mechanical behavior of nickel at 600°C, Mater. Sci. Eng. 3 (5) (1969) 255–263. doi:10.1016/0025-5416(69)90010-X.

[98] K. Sadananda, P. Shahinian, Crack Growth Under Creep and Fatigue Condition, in: Creep-Fatigue Environ. Interact. TMS-AIME, 1979, pp. 86–111.

[99] D. A. Woodford, R. H. Bricknell, Air embrittlement of a cobalt-base superalloy, Metall. Trans. A 12 (11) (1981) 1945–1949. doi:10.1007/BF02643807.

[100] U. Krupp, W. Kane, C. Laird, C. McMahon, Brittle intergranular fracture of a Ni-base superalloy at high temperatures by dynamic embrittlement, Mater. Sci. Eng. A 387-389 (2004) 409–413. doi:10.1016/j.msea.2004.05.053.

[101] W. M. Kane, C. McMahon, Part II. Effects of grain-boundary structure on the path of cracking in polycrystals, Mater. Sci. Eng. A 507 (1-2) (2009) 61–65. doi:10.1016/j.msea.2008.07.015.

[102] U. Krupp, W. M. Kane, X. Liu, O. Dueber, C. Laird, C. J. McMahon, The effect of grain-boundary-engineering-type processing on oxygen-induced cracking of IN718, Mater. Sci. Eng. A 349 (2003) 213–217. doi:10.1016/S0921-5093(02)00753-0.

[103] K. A. Unocic, R. W. Hayes, M. J. Mills, G. S. Daehn, Microstructural features leading to enhanced resistance to grain boundary creep cracking in ALLVAC 718Plus, Metall. Mater. Trans. A Phys. Metall. Mater. Sci. 41 (2) (2010) 409–420. doi:10.1007/s11661-009-0099-4.

[104] L. Viskari, Y. Cao, M. Norell, G. Sjöberg, K. Stiller, Grain boundary microstructure and fatigue crack growth in Allvac 718Plus superalloy, Mater. Sci. Eng. A 528 (6) (2011) 2570–2580. doi:10.1016/j.msea.2010.11.080.

[105] R. Hayes, Oxygen Embrittlement and Time-Dependent Grain-Boundary Cracking of ALLVAC 718PLUS, Metall. Mater. Trans. A 39 (11) (2008) 2596–2606. doi:10.1007/s11661-008-9564-8.

[106] L. Ma, K. M. Chang, Identification of SAGBO-induced damage zone ahead of crack tip to characterize sustained loading crack growth in alloy 783, Scr. Mater. 54 (2006) 305–311. doi:10.1016/j.scriptamat.2005.09.030.

[107] L. Ma, X. Liu, K.-M. Chang, Reply to comment on "Identification of SAGBO-induced damage zone ahead of crack tip to characterize sustained loading crack growth in alloy 783", Scr. Mater. 54 (2) (2006) 305–311. doi:10.1016/j.scriptamat.2005.09.030.

[108] E. Andrieu, R. Molins, H. Ghonem, A. Pineau, Intergranular crack tip oxidation mechanism in a nickel-based superalloy, Mater. Sci. Eng. A 154 (1) (1992) 21–28. doi:10.1016/0921-5093(92)90358-8.

[109] D. Smith, E. Clatworthy, D. Tipton, W. Mankins, Improving the Notch-Rupture Strength of Low-Expansion Superalloys, in: Superalloys 1980 (Fourth Int. Symp., TMS, 1980, pp. 521–530. doi:10.7449/1980/Superalloys_1980_521_530.

[110] H. Evans, H. Li, P. Bowen, A mechanism for stress-aided grain boundary oxidation ahead of cracks, Scr. Mater. 69 (2) (2013) 179–182. doi:10.1016/j.scriptamat.2013.03.026.

[111] H. Ghonem, T. Nicholas, A. Pineau, ELEVATED TEMPERATURE FATIGUE CRACK GROWTH IN ALLOY 718 - PART II: EFFECTS OF ENVIRONMENTAL AND MATERIAL VARIABLES, Fatigue Fract. Eng. Mater. Struct. 16 (6) (1993) 577–590. doi:10.1111/j.1460-2695.1993.tb00103.x.

[112] G. C. Wood, F. H. Stott, Oxidation of alloys, Mater. Sci. Technol. 3 (7) (1987) 519–530. doi:10.1080/02670836.1987.11782263.

[113] G. V. Samsonov, The Oxide Handbook, Springer US, Boston, MA, 1982. doi:10.1007/978-1-4757-1613-9.

[114] L. L. SHREIR, Corrosion, Nature 236 (5345) (1972) 283–283. doi:10.1038/236283a0.

[115] H. Kitaguchi, H. Li, H. Evans, R. Ding, I. Jones, G. Baxter, P. Bowen, Oxidation ahead of a crack tip in an advanced Ni-based superalloy, Acta Mater. 61 (2013) 1968–1981. doi:10.1016/j.actamat.2012.12.017.

[116] L. Viskari, S. Johansson, K. Stiller, Oxygen influenced intergranular crack propagation: analysing microstructure and chemistry in the crack tip region, Mater. High Temp. 28 (4) (2011) 336–341. doi:10.3184/096034011X13189599518971.

[117] L. Viskari, M. Hörnqvist, K. Moore, Y. Cao, K. Stiller, Intergranular crack tip oxidation in a Ni-base superalloy, Acta Mater. 61 (2013) 3630–3639. doi:10.1016/j.actamat.2013.02.050.

[118] A. Pineau, S. D. Antolovich, High temperature fatigue of nickel-base superalloys – A review with special emphasis on deformation modes and oxidation, Eng. Fail. Anal. 16 (8) (2009) 2668–2697. doi:10.1016/j.engfailanal.2009.01.010.

[119] H. E. Evans, Stress effects in high temperature oxidation of metals, Int. Mater. Rev. 40 (1) (1995) 1–40. doi:10.1179/095066095790151124.

[120] E. Andrieu, B. Pieraggi, A. F. Gourgues, Role of metal-oxide interfacial reactions on the interactions between oxidation and deformation, Scr. Mater. 39 (4-5) (1998) 597–601. doi:10.1016/S1359-6462(98)00202-4.

[121] J. Telesman, P. Kantzos, J. Gayda, P. Bonacuse, A. Prescenzi, Microstructural Variables Controlling Time-Dependent Crack Growth in a P/M Superalloy, in: Superalloys 2004 (Tenth Int. Symp., TMS, 2004, pp. 215–224. doi:10.7449/2004/Superalloys_2004_215_224.

[122] K. Bain, M. Gambone, J. Hyzak, M. Thomas, Development of Damage Tolerant Microstructures in Udimet 720, in: Superalloys 1988 (Sixth Int. Symp., TMS, 1988, pp. 13–22. doi:10.7449/1988/Superalloys_1988_13_22.

[123] J. Gayda, R. V. Miner, The effect of microstructure on 650 °C fatigue crack growth in P/M astroloy, Metall. Trans. A 14 (11) (1983) 2301–2308. doi:10.1007/BF02663305.

[124] H. T. Pang, P. A. S. Reed, Microstructure effects on high temperature fatigue crack initiation and short crack growth in turbine disc nickel-base superalloy Udimet 720Li, Mater. Sci. Eng. A 448 (2007) 67–79. doi:10.1016/j.msea.2006.11.016.

[125] L. A. James, The effect of grain size upon the fatigue-crack propagation behavior of alloy 718 under hold-time cycling at elevated temperature, Eng. Fract. Mech. 25 (3) (1986) 305–314. doi:10.1016/0013-7944(86)90127-X.

[126] L. A. James, W. Mifflin, Fatigue Crack Propagation in Alloy 718: A Review, in: Superalloys 1989 TMS, 1989, pp. 489–515.

[127] G. Osinkolu, G. Onofrio, M. Marchionni, Fatigue crack growth in polycrystalline IN 718 superalloy, Mater. Sci. Eng. A 356 (1-2) (2003) 425–433. doi:10.1016/S0921-5093(03)00156-4.

[128] T. Yokobori, A Critical Evaluation of Mathematical Equations for Fatigue Crack Growth, in: Fatigue Mech., ASTM International, 100 Barr Harbor Drive, PO Box C700, West Conshohocken, PA 19428-2959, 1979, pp. 683–683–24. doi:10.1520/STP35910S.

[129] J. Telesman, T. Gabb, A. Garg, P. Bonacuse, J. Gayda, Effect of Microstructure on Time Dependent Fatigue Crack Growth Behavior in a P/M Turbine Disk Alloy, in: Superalloys 2008 (Eleventh Int. Symp., TMS, 2008, pp. 807–816. doi:10.7449/2008/Superalloys_2008_807_816.

[130] D. M. Knowles, D. W. Hunt, The influence of microstructure and environment on the crack growth behavior of powder metallurgy nickel superalloy RR1000, Metall. Mater. Trans. A 33 (10) (2002) 3165–3172. doi:10.1007/s11661-002-0302-3.

[131] N. J. Hide, M. B. Henderson, P. A. S. Reed, Effects of grain and precipitate size variation on creep-fatigue behaviour of Udimet 720Li in both air and vacuum, in: Superalloys 2000 TMS, 2000, pp. 495–503. doi:10.7449/2000/Superalloys_2000_495_503.
URL http://eprints.soton.ac.uk/43046/

[132] A. K. Koul, R. Thamburaj, Serrated grain boundary formation potential of Ni-based superalloys and its implications, Metall. Trans. A 16 (1) (1985) 17–26. doi:10.1007/BF02656707.

[133] H. Danflou, M. Marty, A. Walder, Formation of Serrated Grain Boundaries and Their Effect on the Mechanical Properties in a P/M Nickel Base Superalloy, in: Superalloys 1992 (Seventh Int. Symp., TMS, 1992, pp. 63–72. doi:10.7449/1992/Superalloys_1992_63_72.

[134] D. Furrer, H.-J. Fecht, Microstructure and Mechanical Property Development in Superalloy U720LI, in: Superalloys 2000 (Ninth Int. Symp., TMS, 2000, pp. 415–424. doi:10.7449/2000/Superalloys_2000_415_424.

[135] K. Thibault, D. Locq, P. Caron, D. Boivin, Y. Renollet, Y. Bréchet, Influence of microstructure on local intra- and intergranular deformations during creep of a nickel-based superalloy at 700C, Mater. Sci. Eng. A 588 (2013) 14–21. doi:10.1016/j.msea.2013.09.015.

[136] D. Blavette, A. Bostel, J. M. Sarrau, Atom-probe microanalysis of a nickel-base superalloy, Metall. Trans. A 16 (10) (1985) 1703–1711. doi:10.1007/BF02670358.

[137] D. Rice, P. Kantzos, B. Hann, J. Neumann, R. Helmink, P/M Alloy 10: A 700C Capable Nickel-Based Superalloy for Turbine Disk Applications, in: Superalloys 2008 TMS, 2008, pp. 139–147. doi:10.7449/2008/Superalloys_2008_139_147.

[138] M. Detrois, J. Rotella, R. C. Goetz, S. Tin, Grain boundary engineering of powder processed Ni-base superalloy RR1000: Influence of the deformation parameters, Mater. Sci. Eng. A 627 (2015) 95–105. doi:10.1016/j.msea.2014.12.112.

[139] T. J. Garosshen, Influence of alloy chemistry on carbide precipitation in a nickel base superalloy, Metall. Trans. A 17 (11) (1986) 2075–2077. doi:10.1007/BF02645004.

[140] M. Hardy, B. Zirbel, G. Shen, R. Shenkar, Developing Damage Tolerance and Creep Resistance in a High Strength Nickel Alloy for Disc Applications, in: Superalloys 2004 (Tenth Int. Symp., TMS, 2004, pp. 83–90. doi:10.7449/2004/Superalloys_2004_83_90.

[141] T. J. Garosshen, T. D. Tillman, G. P. McCarthy, Effects of B, C, and Zr on the structure and properties of a P/M nickel base superalloy, Metall. Trans. A 18 (1) (1987) 69–77. doi:10.1007/BF02646223.

[142] P. Berthod, Influence of Chromium Carbides on the High Temperature Oxidation Behavior and on Chromium Diffusion in Nickel-Base Alloys, Oxid. Met. 68 (1-2) (2007) 77–96. doi:10.1007/s11085-007-9062-1.

[143] S. K. Jain, B. A. Ewing, C. A. Yin, The development of improved performance PM Udimet 720 turbine disks, Superalloys 2000 TMS (2000) 785–794doi:10.7449/2000/Superalloys_2000_785_794.

[144] C. F. Miller, G. W. Simmons, R. P. Wei, Evidence for internal oxidation during oxygen enhanced crack growth in P/M Ni-based superalloys, Scr. Mater. 48 (2003) 103–108. doi:10.1016/S1359-6462(02)00355-X.

[145] R. P. Wei, Oxygen Enhanced Crack Growth in Nickel-Based P/M Superalloys, in: M. &. M. S. The Minerals (Ed.), Adv. Technol. Superalloy Affordabil., 2000, pp. 103–112.

[146] Z. Huang, C. Iwashita, I. Chou, R. P. Wei, Environmentally assisted, sustained-load crack growth in powder metallurgy nickel-based superalloys, Metall. Mater. Trans. A 33 (6) (2002) 1681–1687. doi:10.1007/s11661-002-0177-3.

[147] E. Huron, K. Bain, D. Mourer, J. Schirra, P. Reynolds, E. Montero, The Influence of Grain Boundary Elements on Properties and Microstructures of P/M Nickel Base Superalloys, in: Superalloys 2004 (Tenth Int. Symp., TMS, 2004, pp. 73–81. doi:10.7449/2004/Superalloys_2004_73_81.

[148] P. Valerio, M. Gao, R. Wei, Environmental enhancement of creep crack growth in inconel 718 by oxygen and water vapor, Scr. Metall. Mater. 30 (10) (1994) 1269–1274. doi:10.1016/0956-716X(94)90257-7.

[149] M. Gao, R. P. Wei, Grain boundary precipitation and niobium segregation in inconel 718, Scr. Metall. Mater. 32 (7) (1995) 987–990. doi:10.1016/0956-716X(95)98937-Z.
URL http://linkinghub.elsevier.com/retrieve/pii/0956716X9598937Z

[150] M. Gao, D. Dwyer, R. Wei, Niobium enrichment and environmental enhancement of creep crack growth in nickel-base superalloys, Scr. Metall. Mater. 32 (1995) 1169–1174. doi:10.1016/0956-716X(95)00120-K.

[151] M. Gao, R. P. Wei, Grain Boundary Niobium Carbides In Inconle 718, Scr. Mater. 6462 (97) (1997) 1843–1849.

[152] C. F. Miller, G. W. Simmons, R. P. Wei, High temperature oxidation of Nb, NbC and Ni3Nb and oxygen enhanced crack growth, Scr. Mater. 42 (2000) 227–232. doi:10.1016/S1359-6462(99)00336-X.

[153] R. P. Wei, C. F. Miller, Z. Huang, G. W. Simmons, D. G. Harlow, Oxygen enhanced crack growth in nickel-based superalloys and materials damage prognosis, Eng. Fract. Mech. 76 (2009) 715–727. doi:10.1016/j.engfracmech.2008.09.003.

[154] S. Shimada, F. Yunazar, S. Otani, Oxidation of Hafnium Carbide and Titanium Carbide Single Crystals with the Formation of Carbon at High Temperatures and Low Oxygen Pressures, J. Am. Ceram. Soc. 83 (4) (2004) 721–728. doi:10.1111/j.1151-2916.2000.tb01265.x.

[155] S. Shimada, Interfacial reaction on oxidation of carbides with formation of carbon, Solid State Ionics 141–142 (2001) 99–104. doi:http://dx.doi.org/10.1016/S0167-2738(01)00727-5.

[156] R. T. Holt, W. Wallace, Impurities and trace elements in nickel-base superalloys, Int. Mater. Rev. 21 (1976) 1–24. doi:10.1179/095066076790136762.

[157] L. Xiao, D. Chen, M. Chaturvedi, Effect of Boron Concentration on Fatigue Crack Propagation Resistance and Low Cycle Fatigue Properties of INCONEL 718, in: Superalloys 2004 (Tenth Int. Symp., TMS, 2004, pp. 275–281. doi:10.7449/2004/Superalloys_2004_275_281.

[158] B. C. Yan, J. Zhang, L. H. Lou, Effect of boron additions on the microstructure and transverse properties of a directionally solidified superalloy, Mater. Sci. Eng. A 474 (1-2) (2008) 39–47. doi:10.1016/j.msea.2007.05.082.

[159] R. F. Decker, J. W. Freeman, The Mechanism of Beneficial Effects of Boron and Zirconium on Creep Properties of a Complex Heat Resistant Alloy, Trans. Metall. Soc. AIME 218 (1961) 277–285.

[160] Sandvik Turbine Disk image.
URL www.sandvik.coromant.com/SiteCollectionImages/industries/aero/turbine{_}disc.jpg

[161] M. Nazmy, M. Staubli, C. Noseda, Effect of Compositional Modifications on the Mechanical Behavior of IN706, in: Superalloys 718, 625, 706 Var. Deriv., TMS, 1997, pp. 419–424. doi:10.7449/1997/Superalloys_1997_419_424.

[162] J. Gayda, T. P. Gabb, R. V. Miner, Fatigue crack propagation of Nickel-base superalloys at 650C, Tech. rep., National Aeronautics and Space Administration, Lewis Research Center (1985).

[163] J. Rösler, S. Müller, Protection of Ni-base superalloys against stress accelerated grain boundary oxidation (SAGBO) by grain boundary chemistry modification, Scr. Mater. 40 (2) (1998) 257–263. doi:10.1016/S1359-6462(98)00375-3.

[164] L. Xiao, D. Chen, M. Chaturvedi, Effect of boron on fatigue crack growth behavior in superalloy IN 718 at RT and 650°C, Mater. Sci. Eng. A 428 (1-2) (2006) 1–11. doi:10.1016/j.msea.2005.08.206.

[165] S. Guruswamy, S. M. Park, J. P. Hirth, R. A. Rapp, Internal oxidation of Ag-in alloys: Stress relief and the influence of imposed strain, Oxid. Met. 26 (1-2) (1986) 77–100. doi:10.1007/BF00664274.

[166] U. Krupp, P. E.-G. Wagenhuber, W. M. Kane, C. J. McMahon, Improving resistance to dynamic embrittlement and intergranular oxidation of nickel based superalloys by grain boundary engineering type processing, Mater. Sci. Technol. 21 (11) (2005) 1247–1254. doi:10.1179/174328405X63935.

[167] J. Saarimäki, J. J. Moverare, M. H. Colliander, Time- and cycle-dependent crack propagation in Haynes 282, Mater. Sci. Eng. A 658 (2016) 463–471. doi:10.1016/j.msea.2016.01.111.

[168] M. Bache, J. Jones, G. Drew, M. Hardy, N. Fox, Environment and time dependent effects on the fatigue response of an advanced nickel based superalloy, Int. J. Fatigue 31 (11-12) (2009) 1719–1723. doi:10.1016/j.ijfatigue.2009.02.039.

[169] J. J. Moverare, G. Leijon, F. Palmert, Environmental aspects on LCF-life of Ni-base superalloys during long term operation, Värmeforsk Service AB, Stockholm, 2011.
URL http://swepub.kb.se/bib/swepub:oai:DiVA.org:liu-77946?tab2=abs{&}language=en

[170] M. Calmunger, G. Chai, S. Johansson, J. Moverare, Deformation behaviour in advanced heat resistant materials during slow strain rate testing at elevated temperature, Theor. Appl. Mech. Lett. 4 (2014) 0410041 – 0410046. doi:10.1063/2.1404104.

[171] H. Dugdale, D. E. J. Armstrong, E. Tarleton, S. G. Roberts, S. Lozano-Perez, How oxidized grain boundaries fail, Acta Mater. 61 (13) (2013) 4707–4713. doi:10.1016/j.actamat.2013.05.012.

[172] S. Chiozzi, V. Dattoma, R. Nobile, Mechanical Behaviour of Udimet 720Li Superalloy, in: Exp. Anal. Nano Eng. Mater. Struct., Springer Netherlands, Dordrecht, 2007, pp. 463–464. doi:10.1007/978-1-4020-6239-1_230.

[173] K. Gopinath, A. Gogia, S. Kamat, R. Balamuralikrishnan, U. Ramamurty, Tensile Properties of Ni-Based Superalloy 720Li: Temperature and Strain Rate Effects, Metall. Mater. Trans. A 39 (10) (2008) 2340–2350. doi:10.1007/s11661-008-9585-3.

[174] K. Gopinath, A. Gogia, S. Kamat, U. Ramamurty, Dynamic strain ageing in Ni-base superalloy 720Li, Acta Mater. 57 (4) (2009) 1243–1253. doi:10.1016/j.actamat.2008.11.005.

[175] B. Roebuck, Uniaxial testing of particulate MMC, Mater. Des. 15 (1) (1994) 15–25. doi:10.1016/0261-3069(94)90056-6.

[176] B. Roebuck, D. Cox, R. Reed, The temperature dependence of γ' volume fraction in a Ni-based single crystal superalloy from resistivity measurements, Scr. Mater. 44 (6) (2001) 917–921. doi:10.1016/S1359-6462(00)00662-X.

[177] B. Roebuck, D. Cox, R. Reed, An Innovative Device for the Mechanical Testing of Miniature Specimens of Superalloys, in: Superalloys 2004 (Tenth Int. Symp., TMS, 2004, pp. 523–528. doi:10.7449/2004/Superalloys_2004_523_528.

[178] ASTM E 8M-04: Standard Test Methods for Tension Testing of Metallic Materials, in: Annu. B. ASTM Stand., ASTM International, West Conshohocken, PA, 2005, pp. 86–109.

[179] ASTM E 21-03a: Standard Test Methods for Elevate Temperature Tension Tests of Metallic Materials, in: Annu. B. ASTM Stand., ASTM International, West Conshohocken, PA, 2005, pp. 150–157.

[180] J. R. Davis, Tensile Testing, second edi Edition, ASM International, Ohio, 2004.

[181] C. Branco, F. Santos, J. Byrne, Fatigue crack growth at high temperature in the PM nickel base superalloy UDIMET 720 L1, ECF13, San Sebastian 2000 (2013) 0–7.

[182] B. ROEBUCK, M. LOVEDAY, M. BROOKS, Characterisation of Nimonic 90 by the use of miniaturised multiproperty mechanical and physical tests, Int. J. Fatigue 30 (2) (2008) 345–351. doi:10.1016/j.ijfatigue.2007.01.055.

[183] A. Pearce (Instron), Personal Communication (2014).

[184] S. PAHLAVANYALI, A. RAYMENT, B. ROEBUCK, G. DREW, C. RAE, Thermo-mechanical fatigue testing of superalloys using miniature specimens, Int. J. Fatigue 30 (2) (2008) 397–403. doi:10.1016/j.ijfatigue.2007.01.051.

[185] A. K. Roy, A. Venkatesh, V. Marthandam, A. Ghosh, Tensile Deformation of a Nickel-base Alloy at Elevated Temperatures, J. Mater. Eng. Perform. 17 (4) (2008) 607–611. doi:10.1007/s11665-007-9189-x.

[186] D. A. Woodford, L. F. Coffin, No TitleD. A. Woodford and L. F. Coffin, Jr: Proc. 4th Bolton Landing Conf. on 'The role of grain Boundaries in high temperature fatigue', 421; 1974, Baton Rouge, Claitors Pub. Div., in: 4th Bolt. Land. Conf. Role Grain Boundaries High Temp. Fatigue, 1974, p. 421.

[187] G. Onofrio, Fatigue crack growth of UDIMET 720 Li superalloy at elevated temperature, Int. J. Fatigue 23 (10) (2001) 887–895. doi:10.1016/S0142-1123(01)00053-6.

[188] L. Viskari, Oxygen Induced High Temperature Crack Growth in Ni-base Superalloys, Ph.D. thesis, Chalmers University of Technology (2011).

[189] D. E. J. Armstrong, E. Tarleton, Bend Testing of Silicon Microcantilevers from 21 to 770°C, JOM 67 (12) (2015) 2914–2920. doi:10.1007/s11837-015-1618-y.

[190] H.-J. Christ, K. Wackermann, U. Krupp, Effect of dynamic embrittlement on high temperature fatigue crack propagation in IN718 – experimental characterisation and mechanism-based modelling, Mater. High Temp. 33 (4-5) (2016) 528–535. doi:10.1080/09603409.2016.1187464.

[191] H. Kitaguchi, M. Moody, H. Li, H. Evans, M. Hardy, S. Lozano-Perez, An atom probe tomography study of the oxide–metal interface of an oxide intrusion ahead of a crack in a polycrystalline Ni-based superalloy, Scr. Mater. 97 (2015) 41–44. doi:10.1016/j.scriptamat.2014.10.025.

[192] A. A. N. Németh, D. J. Crudden, D. M. Collins, D. E. J. Armstrong, R. C. Reed, Novel Techniques to Assess Environmentally-Assisted Cracking in a Nickel-Based Superalloy, in: Superalloys 2016, John Wiley & Sons, Inc., Hoboken, NJ, USA, 2016, pp. 801–810. doi:10.1002/9781119075646.ch86.

[193] M. Rezende, L. Araújo, S. Gabriel, J. Dille, L. de Almeida, Oxidation assisted intergranular cracking under loading at dynamic strain aging temperatures in Inconel 718 superalloy, J. Alloys Compd. 643 (2015) 256–259. doi:10.1016/j.jallcom.2014.12.279.

[194] J. Telesman, T. Gabb, L. Ghosn, Separating the Influence of Environment from Stress Relaxation Effects on Dwell Fatigue Crack Growth in a Nickel-Base Disk Alloy, in: Superalloys 2016, John Wiley & Sons, Inc., Hoboken, NJ, USA, 2016, pp. 549–560. doi:10.1002/9781119075646.ch59.

[195] C. Stöcker, M. Zimmermann, H.-J. Christ, Z.-L. Zhan, C. Cornet, L. Zhao, M. Hardy, J. Tong, Microstructural characterisation and constitutive behaviour of alloy RR1000 under fatigue and creep–fatigue loading conditions, Mater. Sci. Eng. A 518 (1-2) (2009) 27–34. doi:10.1016/j.msea.2009.04.055.

[196] N. Iqbal, J. Rolph, R. Moat, D. Hughes, M. Hofmann, J. Kelleher, G. Baxter, P. J. Withers, M. Preuss, A Comparison of Residual Stress Development in Inertia Friction Welded Fine Grain and Coarse Grain Nickel-Base Superalloy, Metall. Mater. Trans. A 42 (13) (2011) 4056–4063. doi:10.1007/s11661-011-0802-0.

[197] A. J. Wilkinson, G. Meaden, D. J. Dingley, High-resolution elastic strain measurement from electron backscatter diffraction patterns: New levels of sensitivity, Ultramicroscopy 106 (4-5) (2006) 307–313. doi:10.1016/j.ultramic.2005.10.001.

[198] K. L. Moore, M. Schröder, C. R. M. Grovenor, Imaging Secondary Ion Mass Spectroscopy, in: Handb. Nanoscopy, Wiley-VCH Verlag GmbH & Co. KGaA, Weinheim, Germany, 2012, pp. 709–744. doi:10.1002/9783527641864.ch21.

[199] G. E. Dieter, Mechanical metallurgy., McGraw-Hill, New York, 1961. doi:10.5962/bhl.title.35895.

[200] C. Zener, J. H. Hollomon, Effect of Strain Rate Upon Plastic Flow of Steel, J. Appl. Phys. 15 (1) (1944) 22. doi:10.1063/1.1707363.

[201] P. Littlewood, T. Britton, A. Wilkinson, Geometrically necessary dislocation density distributions in Ti–6Al–4V deformed in tension, Acta Mater. 59 (2011) 6489–6500. doi:10.1016/j.actamat.2011.07.016.

[202] N. Briks, G. H. Meier, F. S. Pettit, High-Temperature Oxidation of Metals, Cambridge University Press, Cambridge, 2006. doi:10.1007/s13398-014-0173-7.2.

[203] M. Taylor, H. Evans, S. Stekovic, M. Hardy, The oxidation characteristics of the nickel-based superalloy, RR1000, at temperatures of 700–900°C, Mater. High Temp. 29 (2) (2012) 145–150. doi:10.3184/096034012X13341417107382.

[204] H. Li, J. Fisk, L.-B. Lim, S. Williams, P. Bowen, Thresholds of time dependent intergranular crack growth in a nickel disc alloy Alloy 720Li, MATEC Web Conf. 14 (2014) 10001. doi:10.1051/matecconf/20141410001.

[205] F. Abe, H. Araki, H. Yoshida, M. Okada, The role of aluminum and titanium on the oxidation process of a nickel-base superalloy in steam at 800C, Oxid. Met. 27 (1-2) (1987) 21–36. doi:10.1007/BF00656727.

[206] A. R. Wazzan, Lattice and Grain Boundary Self-Diffusion in Nickel, J. Appl. Phys. 36 (11) (1965) 3596–3599. doi:10.1063/1.1700021.

[207] V. Vitek, Y. Sodani, A theory of the temperature and strain rate dependence of the yield stress of L12 compounds in the anomalous regime, Scr. Metall. Mater. 25 (4) (1991) 939–944. doi:10.1016/0956-716X(91)90253-W.

[208] W. R. Upthegrove, M. Sinnott, Grain Boundary Self-Diffusion of Nickel, Trans. ASM 50 (1958) 1031–1046.

[209] J. L. W. Carter, N. Zhou, J. M. Sosa, P. A. Shade, A. L. Pilchak, M. W. Kuper, Y. Wang, H. L. Fraser, M. D. Uchic, M. J. Mills, Characterization of Strain Accumulation at Grain Boundaries of Nickel-Based Superalloys, Superalloys 2012 (2012) 43–52doi:10.1002/9781118516430.ch5.

[210] A. Soula, Y. Renollet, D. Boivin, J. Pouchou, D. Locq, P. Caron, Y. Brechet, Grain Boundary and Intragranular Deformations during High Temperature Creep of a PM Nickel-Based Superalloy, in: R. C. Reed, K. A. Green, P. Caron, T. Gabb, M. G. Fahrmann, E. S. Huron, S. A. Woodward (Eds.), Superalloys 2008 (Eleventh Int. Symp., TMS, Warrendale, Pa., 2008, pp. 387–394. doi:10.7449/2008/Superalloys_2008_387_394.

[211] G. Leverant, M. Gell, S. Hopkins, The effect of strain rate on the flow stress and dislocation behavior of a precipitation-hardened nickel-base alloy, Mater. Sci. Eng. 8 (3) (1971) 125–133. doi:10.1016/0025-5416(71)90050-4.
URL http://linkinghub.elsevier.com/retrieve/pii/0025541671900504

[212] P. Strunz, M. Petrenec, J. Polák, U. Gasser, G. Farkas, Formation and Dissolution of γ' Precipitates in IN792 Superalloy at Elevated Temperatures, Metals (Basel). 6 (12) (2016) 37. doi:10.3390/met6020037.

[213] E. Galindo-Nava, L. Connor, C. Rae, On the prediction of the yield stress of unimodal and multimodal γ' Nickel-base superalloys, Acta Mater. 98 (2015) 377–390. doi:10.1016/j.actamat.2015.07.048.

[214] R. Jiang, D. Bull, D. Proprentner, B. Shollock, P. Reed, Effects of oxygen-related damage on dwell-fatigue crack propagation in a P/M Ni-based superalloy: From 2D to 3D assessment, Int. J. Fatigue 99 (2017) 175–186. doi:10.1016/j.ijfatigue.2017.03.003.

[215] S. Cruchley, H. Evans, M. Taylor, An overview of the oxidation of Ni-based superalloys for turbine disc applications: surface condition, applied load and mechanical performance, Mater. High Temp. 3409 (2016) 1–11. doi:10.1080/09603409.2016.1171952.

[216] A. Németh, D. Crudden, D. Armstrong, D. Collins, K. Li, A. Wilkinson, C. Grovenor, R. Reed, Environmentally-assisted grain boundary attack as a mechanism of embrittlement in a nickel-based superalloy, Acta Mater. 126 (2017) 361–371. doi:10.1016/j.actamat.2016.12.039.

[217] S. Antonov, J. Huo, Q. Feng, D. Isheim, D. N. Seidman, R. C. Helmink, E. Sun, S. Tin, The effect of Nb on grain boundary segregation of B in high refractory Ni-based superalloys, Scr. Mater. 138 (2017) 35–38. doi:10.1016/j.scriptamat.2017.05.028.

[218] R. C. Reed, T. Tao, N. Warnken, Alloys-By-Design: Application to nickel-based single crystal superalloys, Acta Mater. 57 (2009) 5898–5913. doi:10.1016/j.actamat.2009.08.018.

[219] J. O. Andersson, T. Helander, L. Höglund, P. Shi, B. Sundman, Thermo-Calc & DICTRA, computational tools for materials science, Calphad Comput. Coupling Phase Diagrams Thermochem. 26 (2002) 273–312. doi:10.1016/S0364-5916(02)00037-8.

[220] C. A. Schneider, W. S. Rasband, K. W. Eliceiri, NIH Image to ImageJ: 25 years of image analysis, Nat. Methods 9 (2012) 671–675. doi:10.1038/nmeth.2089.

[221] D. M. Collins, D. J. Crudden, E. Alabort, T. Connolley, R. C. Reed, Time-resolved synchrotron diffractometry of phase transformations in high strength nickel-based superalloys, Acta Mater. 94 (2015) 244–256. doi:10.1016/j.actamat.2015.04.046.

[222] F. Wallow, E. Nembach, Synergisms of grain boundary and γ'-particle strengthening in nickel-base superalloys, Scr. Mater. 34 (1996) 499–505. doi:10.1016/S0956-716X(95)00548-A.

[223] L. A. Gypen, A. Deruyttere, Multi-component solid solution hardening - Part 1 Proposed model, J. Mater. Sci. 12 (5) (1977) 1028–1033. doi:10.1007/BF00540987.

[224] Y. Mishima, S. Ochiai, N. Hamao, M. Yodogawa, T. Suzuki, Solid Solution Hardening of Nickel -Role of Transition Metal and B-subgroup Solutes-, Trans. Japan Inst. Met. 27 (1986) 656–664. doi:10.2320/matertrans1960.27.656.

[225] D. Rooke, D. Cartwright, The compounding method applied to cracks in stiffened sheets, Eng. Fract. Mech. 8 (1976) 567–573. doi:10.1016/0013-7944(76)90010-2.

[226] S. T. Wlodek, The Oxidation of René 41 and Udimet 700, Trans. Metall. Soc. AIME 230 (1964) 1078–1090.

[227] D. Gustafsson, E. Lundström, High temperature fatigue crack growth behaviour of Inconel 718 under hold time and overload conditions, Int. J. Fatigue 48 (2013) 178–186. doi:10.1016/j.ijfatigue.2012.10.018.

[228] U. Krupp, K. Wackermann, H.-J. Christ, M. H. Colliander, K. Stiller, Intergranular Oxidation Effects During Dwell-Time Fatigue of High-Strength Superalloys, Oxid. Met. 88 (2017) 3–14. doi:10.1007/s11085-016-9707-z.

[229] S. Mannan, K. Samuel, P. Rodriguez, Influence of temperature and grain size on the tensile ductility of AISI 316 stainless steel, Mater. Sci. Eng. 68 (1985) 143–149. doi:10.1016/0025-5416(85)90403-3.

[230] S. Floreen, R. H. Kane, A critical strain model for the creep fracture of nickel-base superalloys, Metall. Trans. A 7 (1976) 1157–1160. doi:10.1007/BF02656598.

[231] S. R. Shatynski, The thermochemistry of transition metal carbides, Oxid. Met. 13 (1979) 105–118. doi:10.1007/BF00611975.

[232] G. H. Gessinger, M. J. Bomford, Powder Metallurgy of Superalloys, Int. Metall. Rev. 19 (1974) 51–76. doi:10.1179/imtlr.1974.19.1.51.

[233] B. Piekarski, Effect of Nb and Ti additions on microstructure, and identification of precipitates in stabilized Ni-Cr cast austenitic steels, Mater. Charact. 47 (2001) 181–186. doi:10.1016/S1044-5803(01)00166-8.

[234] M. F. Ashby, K. E. Easterling, A first report on diagrams for grain growth in welds, Acta Metall. 30 (1982) 1969–1978. doi:10.1016/0001-6160(82)90100-6.

[235] R. C. Reed, A. Mottura, D. J. Crudden, Alloys-by-design: Towards Optimization of Compositions of Nickel-Based Superalloys, in: Superalloys 2016, John Wiley & Sons, Inc., Hoboken, NJ, USA, 2016, pp. 13–23. doi:10.1002/9781119075646.ch2.

Appendix A

Stress-Strain Curves

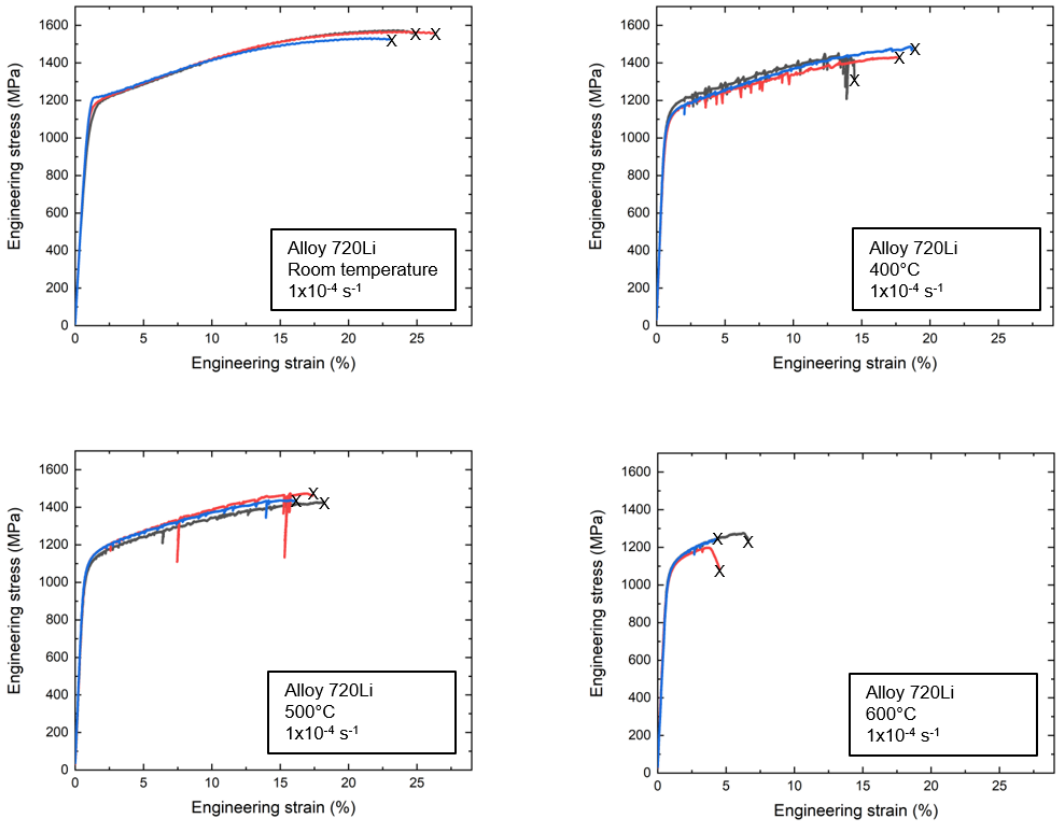


Fig. A.1 Individual stress-strain curves for alloy 720Li when tested in laboratory air with an constant LVDT displacement of 0.0005 mm/s corresponding to Fig. 3.6. The colors red, blue and black correspond to test repetitions under the same conditions. Strain was measured using DIC in the central 5 mm of the specimen.

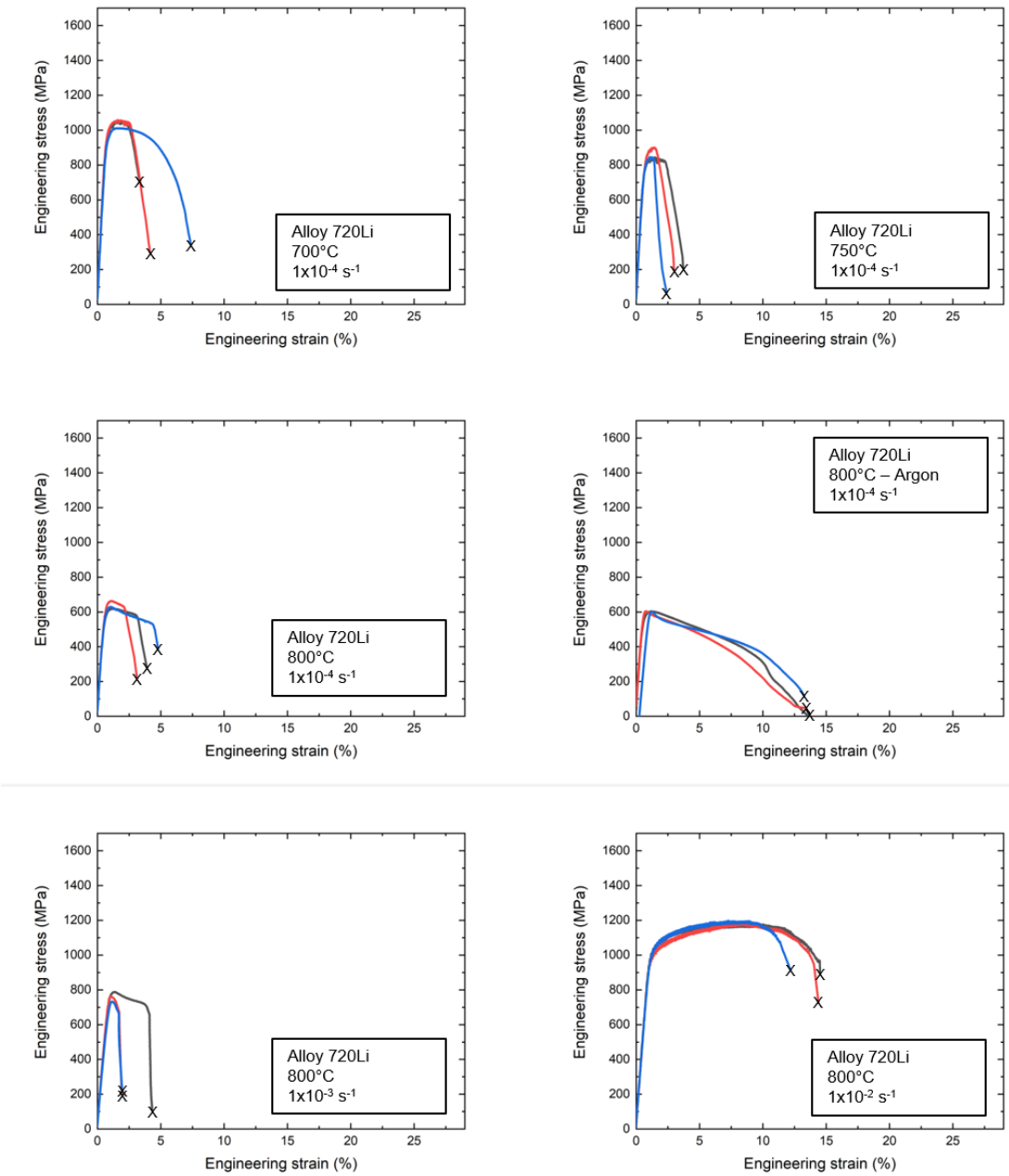


Fig. 1 (*Continued*) Individual stress-strain curves for alloy 720Li when tested in laboratory air with an constant LVDT displacement of 0.0005 mm/s corresponding to Fig. 3.6. The colors red, blue and black correspond to test repetitions under the same conditions. Strain was measured using DIC in the central 5 mm of the specimen.

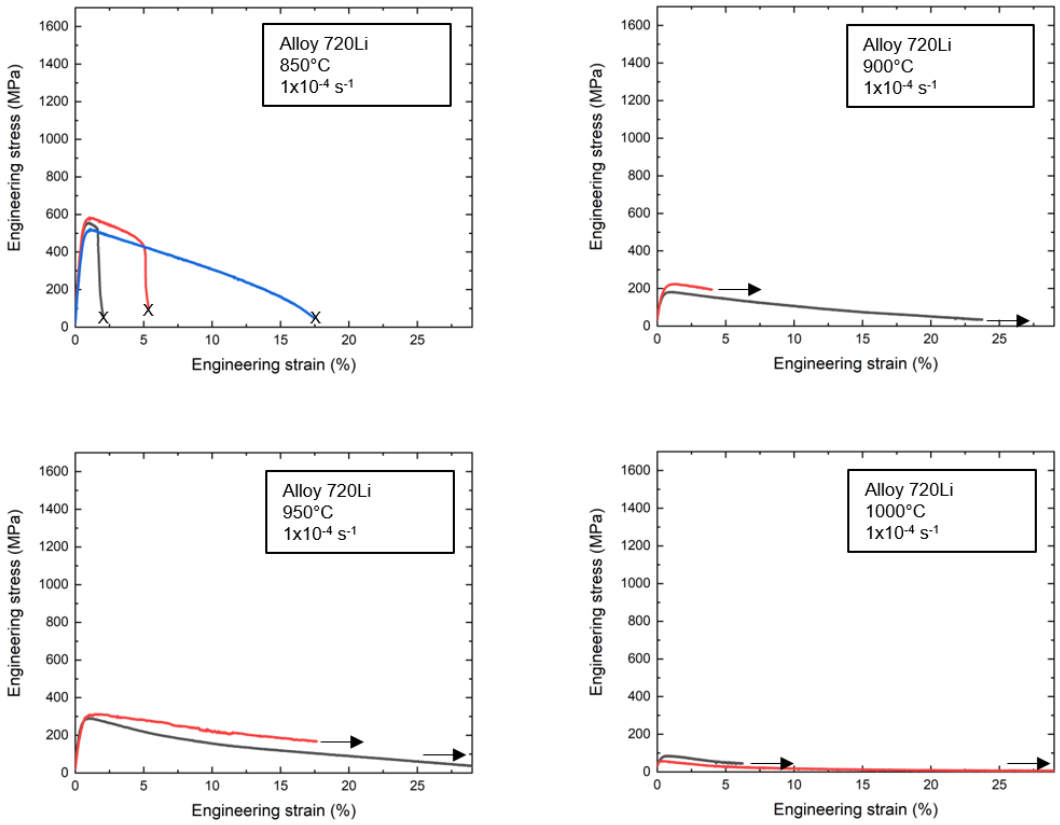


Fig. 1 (*Continued*) Individual stress-strain curves for alloy 720Li when tested in laboratory air with an constant LVDT displacement of 0.0005 mm/s corresponding to Fig. 3.6. The colors red, blue and black correspond to test repetitions under the same conditions. Strain was measured using DIC in the central 5 mm of the specimen.

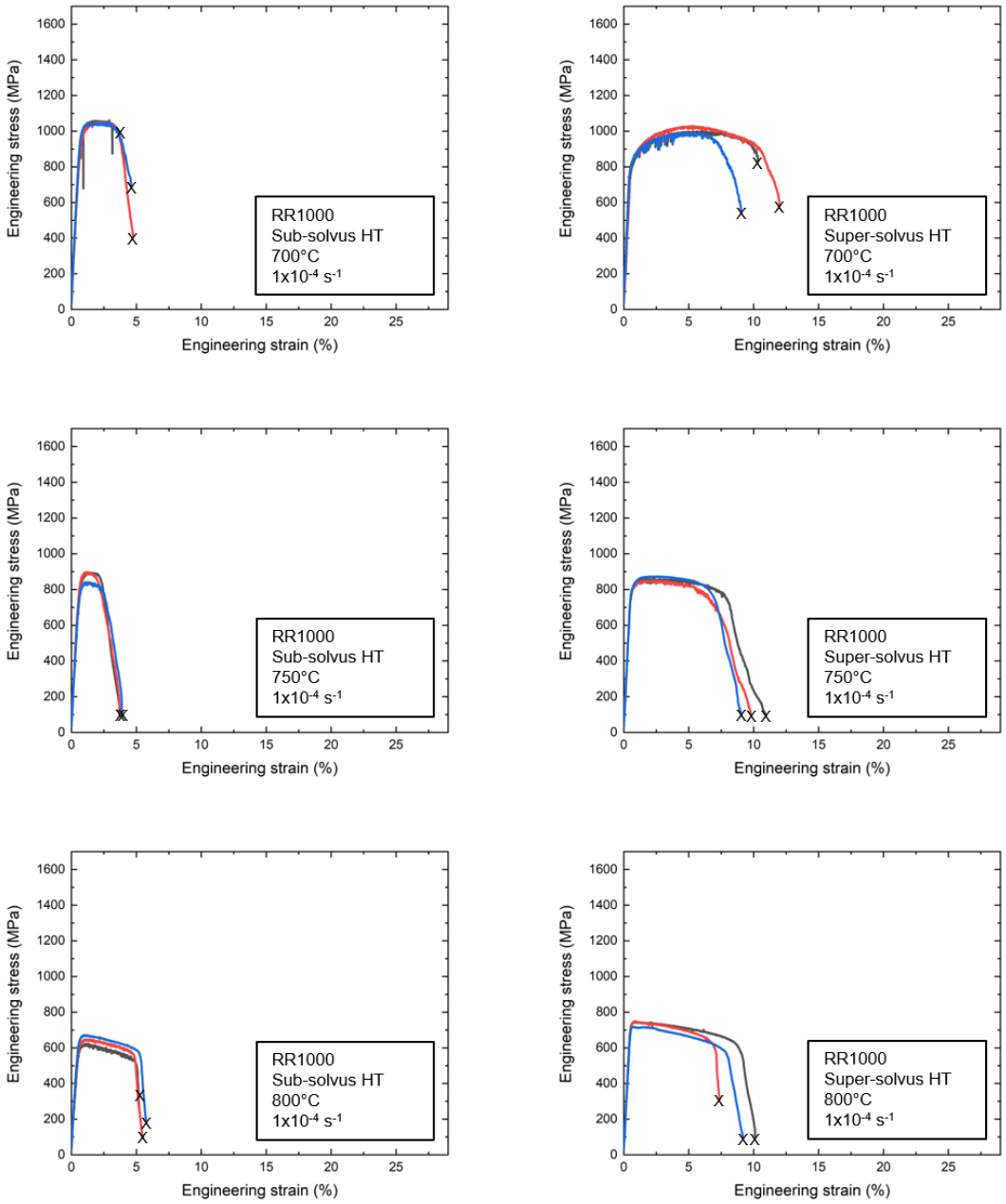


Fig. 2 Individual stress-strain curves for RR1000 when tested in laboratory air with an constant LVDT displacement of 0.0005 mm/s corresponding to Fig. 4.3. The colors red, blue and black correspond to test repetitions under the same conditions. Strain was measured using DIC in the central 5 mm of the specimen.

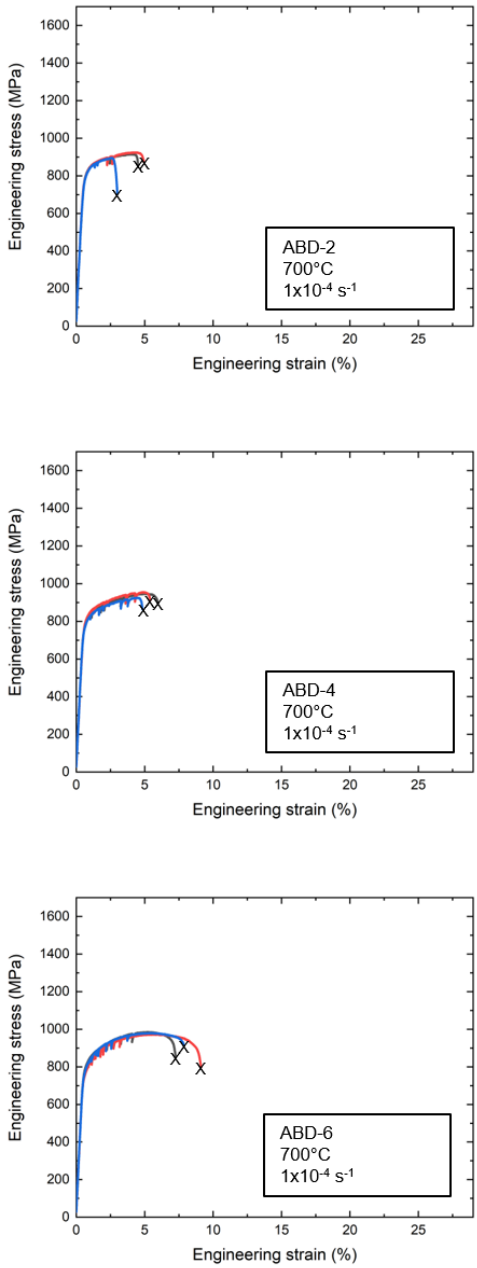


Fig. 3 Individual stress-strain curves for ABD-2, -4 and -6 when tested in laboratory air with an constant LVDT displacement of 0.0005 mm/s corresponding to Fig. 5.4. The colors red, blue and black correspond to test repetitions under the same conditions. Strain was measured using DIC in the central 5 mm of the specimen.

Appendix B

Individual STEM-EDS Elemental Maps

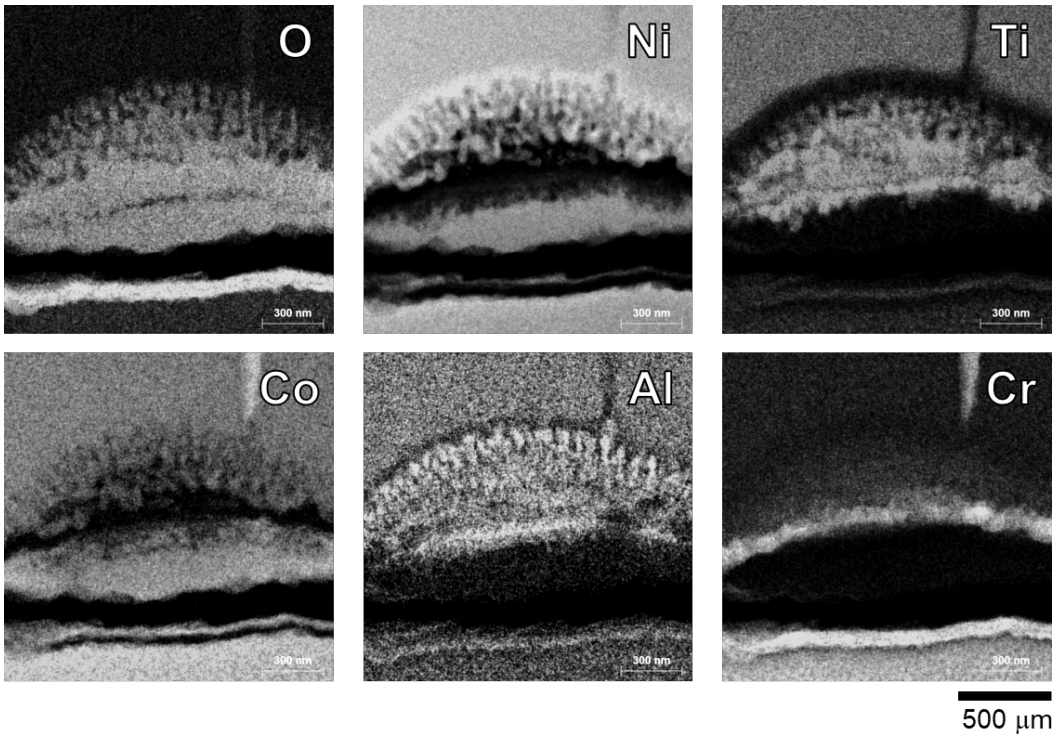


Fig. 1 Individual STEM-EDS elemental distribution maps of O and Ni showing the environmental damage occurring at the cracked γ/γ'-interface in alloy 720Li corresponding to Fig. 4.5.

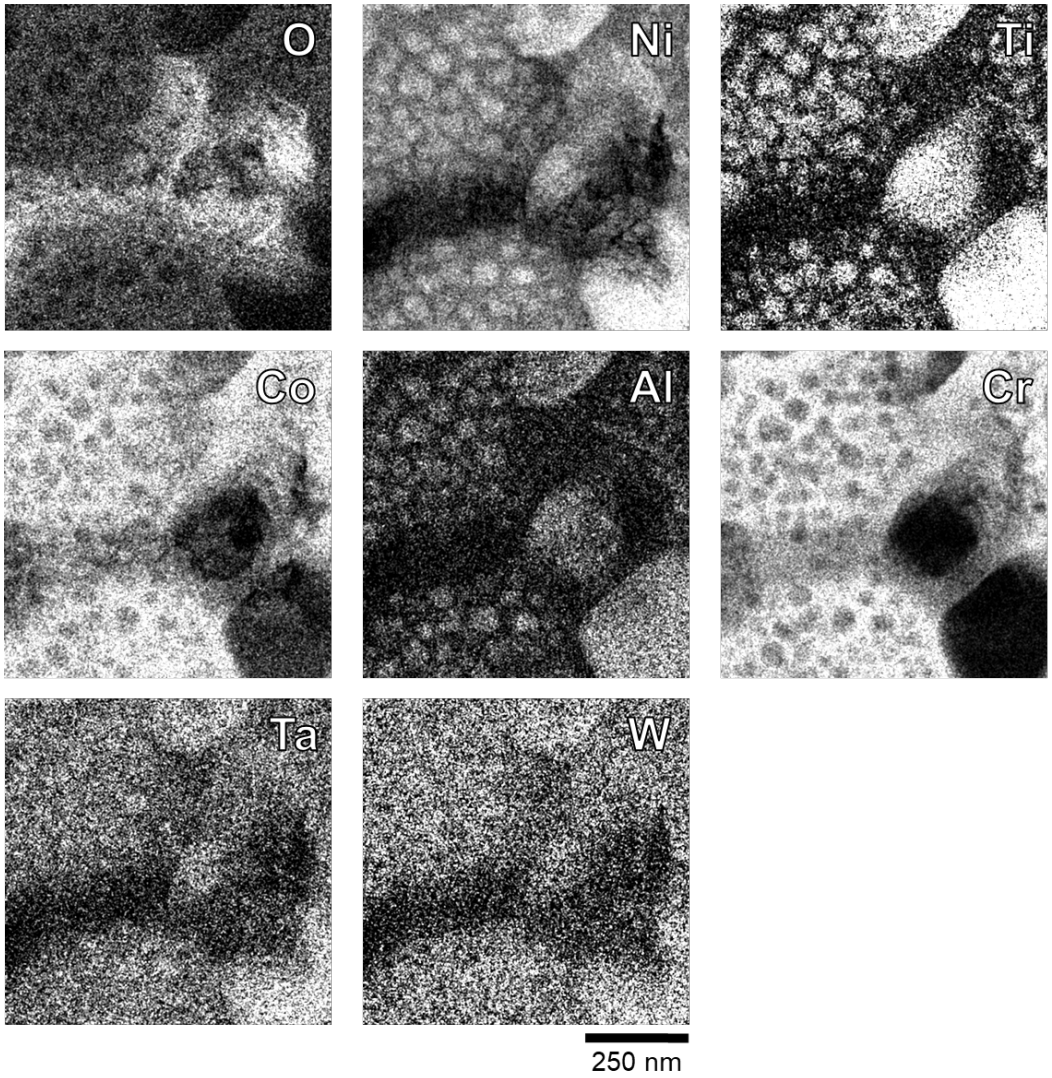


Fig. 2 Individual STEM-EDS elemental distribution maps of O, Ni, Ti, Co, Al and Cr showing the environmental damage at and ahead of a crack tip in ABD-2 corresponding to Fig. 5.10.

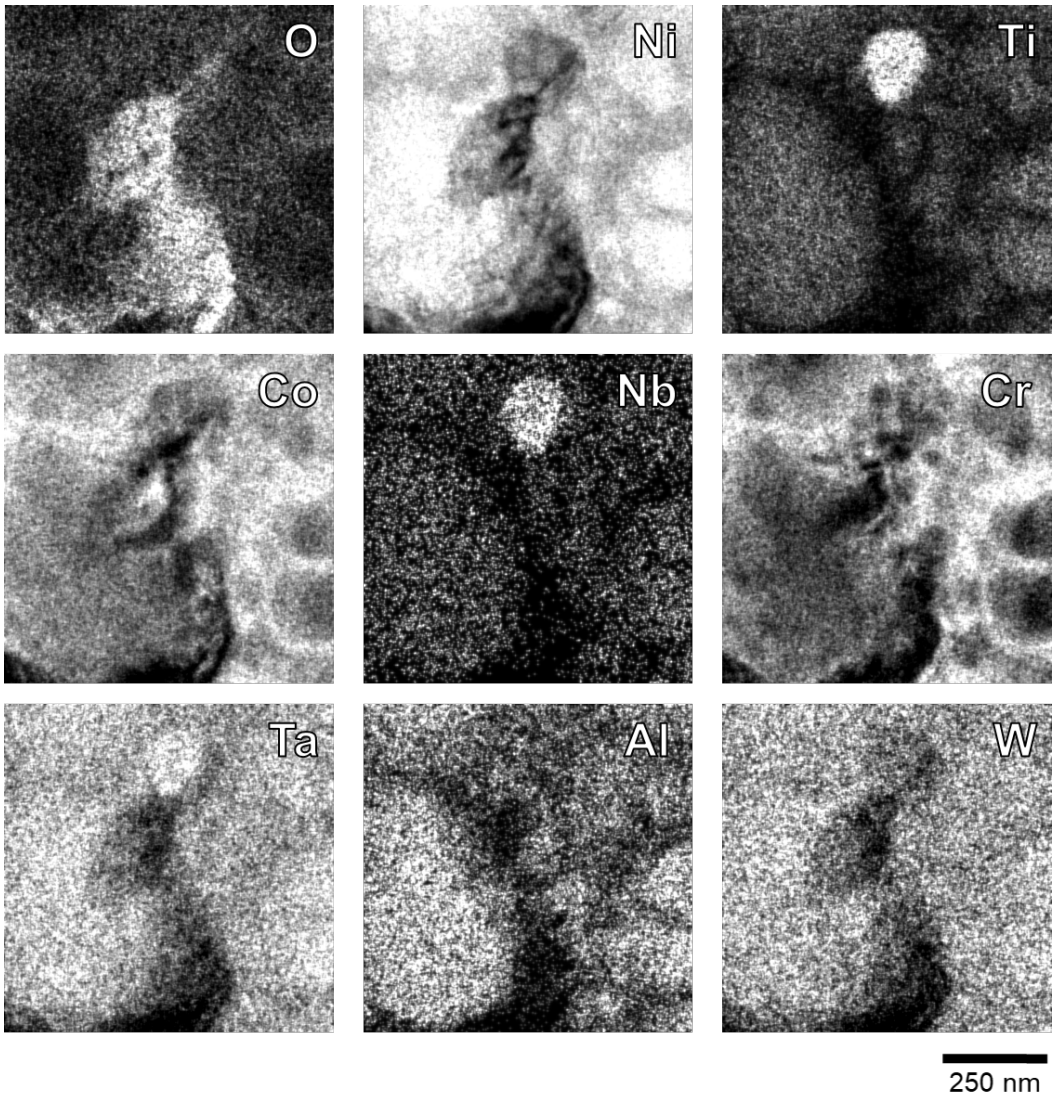


Fig. 3 Individual STEM-EDS elemental distribution maps of O, Ni, Ti, Co, Nb and Cr showing the environmental damage at and ahead of a crack tip in ABD-6 corresponding to Fig. 5.11.

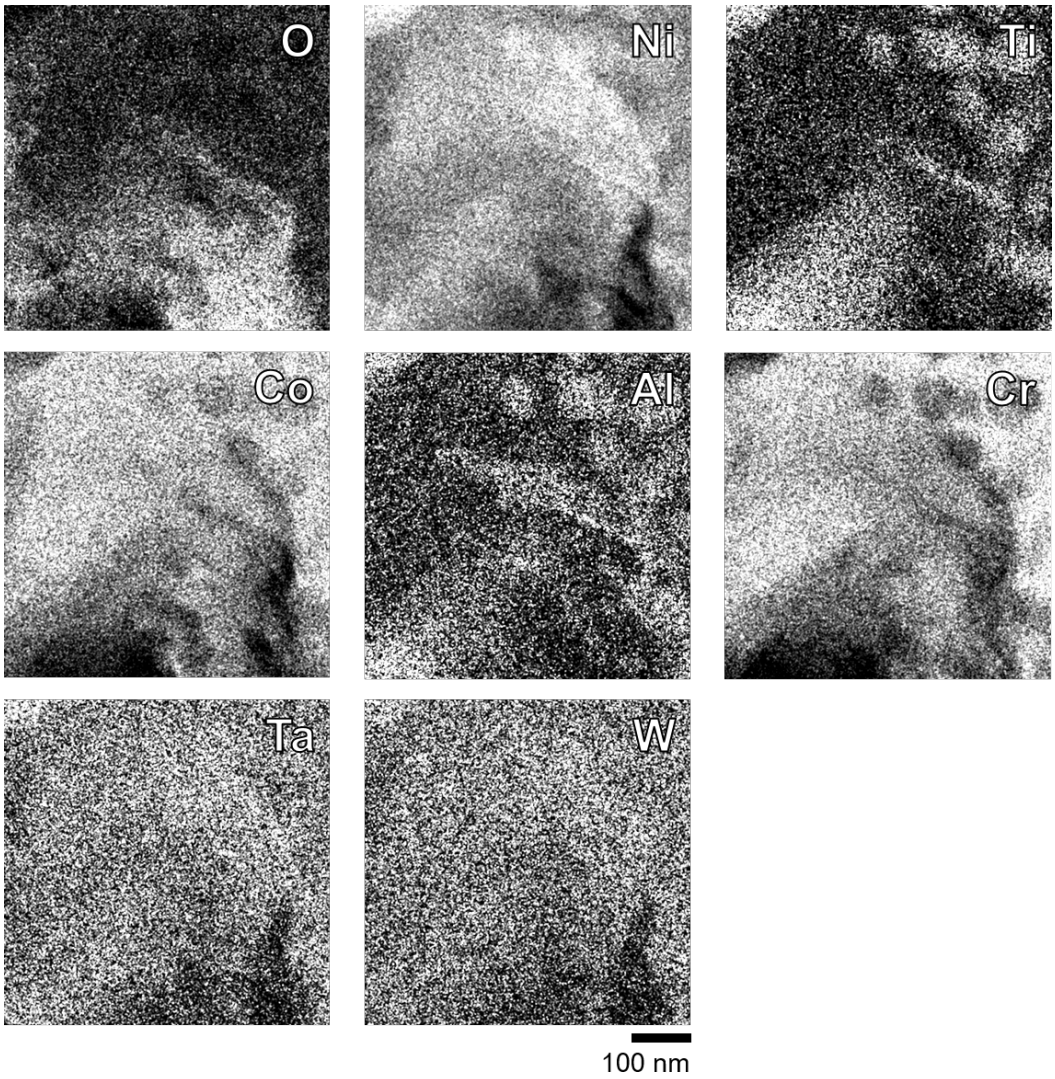


Fig. 4 Individual STEM-EDS elemental distribution maps of O, Ni, Ti, Co, Al and Cr showing the region closest to the undamaged grain boundary in ABD-2 corresponding to Fig. 5.12.